
Metamaterial and Plasmonic Microstructures for Controlling Infrared Properties

*A Thesis Submitted
in Partial Fulfilment of the Requirements
for the Degree of*
Doctor of Philosophy

by
RAGHWENDRA KUMAR



to the
**DEPARTMENT OF PHYSICS
INDIAN INSTITUTE OF TECHNOLOGY KANPUR,
INDIA, 208016
July, 2018**

Dedicated to
MY FAMILY
(Beloved Parents & Siblings)

STATEMENT

I hereby declare that the matter manifested in this thesis entitled "*Metamaterial and Plasmonic Microstructures for Controlling Infrared Properties*", is the result of research carried out by me in the Department of Physics, Indian Institute of Technology Kanpur, India under the supervision of Prof. S. Anantha Ramakrishna.

In keeping with the general practice of reporting scientific observations, due acknowledgement has been made wherever the work described is based on the findings of other investigators.

Raghwendra Kumar
RAGHWENDRA KUMAR

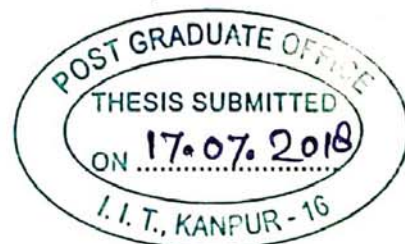
Roll No. 12109067
Department of Physics
IIT Kanpur, India, 208016

July 17, 2018




Dr. S. Anantha Ramakrishna
Professor
Department of Physics
Indian Institute of Technology Kanpur
Kanpur, 208016, India
Office : +91 512 2597449
Lab : +91 512 2596601
Email : sar@iitk.ac.in
Fax: +91-512-259 0914

CERTIFICATE



It is certified that the work contained in the thesis entitled "*Metamaterial and Plasmonic Microstructures for Controlling Infrared Properties*" by *Raghendra Kumar*, has been carried out under my supervision and that this work has not been submitted elsewhere for a degree.


17 July 2018
Prof. S. Anantha Ramakrishna
(Thesis Supervisor)

July 17, 2018

Acknowledgements

It has been a long journey since I started up the project to writing up the thesis, during that I have come across various interesting challenges, difficulties and successes. The challenges and difficulties are the parts and parcel of any project and without these, success will never be joyful. But it would have been impossible to take these challenges and surpass the difficulties without few hard-working companions and motivating mentors. It gives me immense pleasure to get an opportunity to officially thank all of them from the bottom of my heart.

First and foremost I would like to express my deep and utmost gratitude to my thesis supervisor Professor S. Anantha Ramakrishna for his valuable guidance, commitment, interest, sheer encouragement and endless patience. It was something more than independence and freedom of thought I have come across while working with him. It was the expertise I gained by virtue of his invaluable guidance and constant motivation in understanding scientific problems, designing experiments, building scientific equipments and rendering the manuscripts and which finally led me give my own modest contribution no matter how small it may be.

I am extremely grateful to my doctoral committee and I would like to show my gratitude to Prof. H. Wanare, Prof. Saurabh Mani Tripathi and Prof. Saikat Ghosh not only for their insightful comments, encouragement, assistance, and suggestions throughout my Ph.D. but also for their questions which encouraged me to explore my research and knowledge from various perspectives.

I am also thankful to Prof. Rajendra Prasad, Prof. Tarun Kanti Ghosh, Prof. Manoj K. Harbola, Prof. K.P. Rajeev, Prof. Krishnacharya Khare and Prof. Soumik Mukhopadhyay for teaching various foundation and advanced topics during the coursework. I owe my sincere gratitude to Prof. Kamal Poddar from the Department of Aerospace Engineering, IIT Kanpur for teaching me the LabView programming. His methodology and teaching style is really appreciable, and encouragement for writing a small programme from the beginning of the class helped me to build up the concept as well as writing my own code. Without his insightful teaching style,

it would not be possible for me to develop the two photon absorption laser writing system. I also want to convey my sincere thanks to all my teachers during my school and college life prior to IIT Kanpur. Through classroom teaching they shaped my mind, nurtured my thoughts and nourished my research potential.

I would also like to thank the Department of Physics, IIT Kanpur for providing me an excellent laboratory and other academic and non-academic facilities, and giving me the opportunity to write this dissertation. I would like to show my gratitude to all staff members of Physics office especially to Mr. Narayanan G., Mr. Arvind Verma, Mr. Maifus Khan and Ms. Pooja Sahu for their patience and support in overcoming various obstacles I have been facing through my academia. I would like to thank especially Mr. Arvind Misra for assisting me to resolve the various issues related to COMSOL software and Ubuntu operating system. I would like to thank Mr. Om Prakash and Mr. Shiv Sagar Singh from the department workshop for assisting me in designing and building up some parts for my experiments.

I enjoyed working in the group and I want to extend my sense of gratitude to my past and present labmates. I offer my special thanks to my labmates Dr. Sriram Guddala, Dr. Govind Dayal, Dr. Jhuma Dutta, Dr. Dheeraj Pratap, Dr. Gangadhar Behera, Dr. Anjani Kumar Tiwari, Dr. Vishnu Prasad Srivastva, Rajesh Kumar, Jitendra Kumar Pradhan, Abhinav Bhardwaj, Naorem Rameshwari, Kajal Chaudhary, Saleem Shaik for their friendly attitude, academic support, and helpful efforts to make the lab an enthusiastic place for research. I am indebted to all of them for providing a healthy atmosphere, stimulating and fun environment to learn and grow. I will always cherish the moments spent with them. My special thanks go to Dr. Sriram Guddala for familiarizing me with various instruments and techniques in the laboratory. I am lucky to have batchmates and friends like Anmol Thakur, Rabeet Singh, Khunsang Phukon, Alestine, Anil Kumar Singh and Ritu Gupta. However, I was not able to spend more time with them due to a busy schedule, but that much precious time I spent with them I will always cherish.

I am very thankful to IIT Kanpur for providing me the great research infrastructure and financial support, and CSIR India for the research fel-

lowship.

I express my profound thanks to Mrs. Kanchan (Ma'am), Kartik, Kanishk and Jyoti Bhabhi for providing a homely atmosphere and lively company on various occasions.

No words of appreciation could express my gratitude for my family, who have always been with me although they were miles away from me. Whatever I am today is because of their unconditional love, care, guidance, encouragement and moral support. To put in one line, the script of my success remains incomplete without their huge sacrifices. I would like to especially thank my elder sister (Full Kumari) and brother's in law (Rajnarayan Chaudhary) for standing with me throughout my career in sorrow as well as in joy moments, and for their unconditional love and moral supports.

Lastly but definitely not the least, I owe a debt of gratitude to the Almighty to sail the journey and made this possible by being with me all the time.

I wish to extend my thanks to all, whose help I have taken knowingly and unknowingly. Please forgive me if I have mistakenly forgotten to mention your name in the list.

Raghwendra Kumar

July 17, 2018

Synopsis

Name:	Raghwendra Kumar
Roll No.:	12109067
Degree for which submitted:	Doctor of Philosophy
Department:	Physics
Thesis title:	Metamaterial and Plasmonic Microstructures for Controlling Infrared Properties
Thesis supervisor:	Prof. S. Anantha Ramakrishna
Month and year of submission:	July, 2018

Recent advances in metamaterials and plasmonic structured materials have challenged many conventional notions in optics, and have given rise to new possibilities in photonic applications. Metamaterials are composite arrays of artificially designed metallodielectric micro/nanostructures of sub-wavelength sizes arranged typically in a periodic fashion and with exotic properties rarely or never met in nature. These can be considered as homogeneous bulk media described as effective media through effective medium parameters such as the relative electric permittivity and the relative magnetic permeability. Metamaterials offer a wide range of exceptional properties and functionalities such as negative refractive index, sub-wavelength imaging, cloaking, perfect absorption, etc., which are not found in naturally occurring materials. These exceptional properties are obtained by designing the sub-wavelength sized unit cell to have a resonance at specific frequencies, in the vicinity of which there is an enormous dis-

persion in the effective medium properties. The concept of negative refractive index at the first time was proposed by Veselago in 1968 [Veselago, Soviet physics uspekhi **10**, 509 (1968)], and that was experimentally demonstrated by Smith et al. in 2001 [Shelby et al., Science **292**, 5514 (2001)]. The complete absorption of the electromagnetic radiation can be enabled by adjusting the effective permittivity and the permeability to be optically impedance matched with the surrounding medium. Since Landy et al. [Phys. Rev. Lett **100** (20): 207402 (2008)] proposed and experimentally demonstrated the first metamaterial absorber at microwave frequencies, the operation frequency of metamaterials was quickly shifted to higher frequency from terahertz to mid-/near infrared and even to visible. The first experimental demonstration of a metamaterial perfect absorber in the mid-infrared regime of absorptivity around 97% at 6 μm wavelength was demonstrated by Padilla's group [Phys. Rev. Lett **104**: 207403 (2010)]. Even the metamaterial perfect absorber at optical regime has been demonstrated by the other group. However, Due to the metallic components in the metamaterials, plasmonic effects start playing an important role at optical frequencies. Spectrally selective, nearly perfect absorbers have received considerable attention due to their importance for RADAR stealth at micro-wave and terahertz frequencies, development of ultra-sensitive infrared detectors, micro-bolometer arrays, controllable thermal emitters for manipulating the black body emittance, thermo-photovoltaic application etc.

There can be confinement and propagation of electromagnetic waves at metal-dielectric interfaces as well as confinement and localization of electromagnetic waves at nanometric/micrometric-scales. The surface electromagnetic waves that propagate along the interface between a metal and a dielectric material and consist of surface charges are known as surface plasmon polaritons, and the electromagnetic waves that are localized around the nanometric/micrometric-scales sized particles/objects are known as localized surface plasmons. The excitation of surface plasmons depends critically on the penetration of the electromagnetic fields into the metal and is typically limited to visible or near infrared frequencies. Metals behave almost as perfect con-

ductors with almost zero skin depth at low frequencies. To understand the optical properties of structured metallic surfaces, which occur at lower frequencies (infrared to microwave), the concept of spoof surface plasmons was introduced by Sir John Pendry in 2004 [Pendry et al., *Science* **305**, 847 (2004)], and it was experimentally demonstrated by A. P. Hibbins et al. in 2005 [Hibbins et al., *Science* **308**, 670 (2005)]. Spoof surface plasmons are electromagnetic waves that are resonantly bound to periodically structured perfectly conducting surfaces. For example, electromagnetic waves can penetrate into a conducting film with periodic sub-wavelength sized holes through the holes and bind to the film through resonances excited in the holes and provide surface waves that appear similar to surface plasmon excitations on metallic surfaces. These structured conducting surfaces can support propagating as well as localized surface waves at lower frequencies even extending down to microwaves. A lot of optical phenomena such as extraordinary optical transmission, localization of electromagnetic waves around perfect conducting surfaces/corners, etc. have been explained on the basis of spoof surface plasmon at longer wavelengths. In this thesis, the concept of spoof surface plasmons has been used to explain the optical phenomena such as extraordinary optical transmission and absorption of electromagnetic waves through resonant excitation.

The work presented in this thesis targets the design, fabrication and characterization of metamaterial and plasmonic microstructures at infrared frequencies for different applications. Numerical simulations and experimental methods are used to tailor the electromagnetic responses of the structures at different wavelengths, and to understand the mechanism that allows such structures to exhibit the unique electromagnetic responses through different physical phenomena. One of the main motivations behind this thesis is the development of realistic metamaterial and plasmonic microstructures from the perspective of real-life applications. As a metamaterial absorber, we have shown that our proposed designs can be easily implemented for fabrication on industrial scales. In another proposed design as a plasmonic microstructured thin film, the

design can be exploited to enhance the performance of infrared photovoltaic detectors. We have also developed a low-cost two-photon absorption based laser writing lithography system using a sub-nanosecond laser for the fabrication of microstructures with complex shapes. The thesis is organized into Chapters as follows.

Chapter 1 contains the theoretical background of different physical phenomena observed in our system. Section 1.1 is dedicated to the basic introduction of light-matter interaction, starting from Maxwell's equations to the Lorentz-Drude model of dispersion. The concept of surface plasmons, excitation of surface plasmons using EM waves, concepts of localized surface plasmons and basic introduction to spoof surface plasmon polaritons are discussed in Section 1.2. The basic introduction of the Fabry Perot cavities, guided-mode resonance, Woods anomalies and Fano resonance are discussed in Sections 1.3, 1.4, 1.5 and 1.6, respectively. Finally, an overview of extraordinary optical transmission and metamaterials absorbers are given in Sections 1.7 and 1.8, respectively.

In **Chapter 2**, we present the details of the fabrication techniques, characterization tools and numerical simulations used for the work in this thesis. Section 2.1 contains the details of interference lithography for fabrication of nano/microstructures with different shapes which have been used in this thesis, and the details of metal/dielectric deposition and lift-off processes which were further carried out for fabrication of plasmonic two-dimensional hole arrays. The development of a home built two-photon absorption based laser lithography system is discussed in Section 2.2. Section 2.3 contains the methods of soft lithography from the fabrication of the master to embossing the stamp for fabrication of microstructures. The sample characterization methods such as AFM and FTIR are discussed in Section 2.4. The electromagnetic calculations based on finite element method using the COMSOL Multiphysics software are discussed in Section 2.5.

In **Chapter 3**, we have proposed and experimentally demonstrated a new design

to enhance the transmittance through periodically perforated sub-wavelength sized hole array in a gold film by mounting dielectric micro-domes on each hole. In comparison to the extraordinary transmission through an array of bare holes in the gold film, this structure showed a further enhanced transmission over a larger range of incident angles with much larger bandwidth at mid-wave infrared wavelengths. The structure was fabricated using laser interference lithography, a novel back-exposure with an ultra-violet laser, and lift-off process that left behind the micro-domes of dielectric, covering each of the holes in the gold film. A detailed study of the behaviour of these structures as a function of wavelength, state of polarization and incident angles is presented. The details of samples fabrication and characterization are presented in Section 3.1. The design and simulation details including the effect of different parameters such as shape, the height of the micro-dome, hole size, etc. on the transmittance spectra are presented in Section 3.2. Further, the results and discussions are presented in Section 3.3, and finally, conclusions are in Section 3.4. The work in this thesis has been published as Raghwendra Kumar and S. A. Ramakrishna, *Enhanced infrared transmission through sub-wavelength hole arrays in a thin gold film mounted with dielectric micro-domes*, J. Phys. D: Appl. Phys. **51**, (2018), 165104 (10pp).

Generally, metamaterial absorber is a tri-layered system, where the structured metallic layer is separated from a thick metal layer by inserting a dielectric layer (spacer) in between. However, this design is most suitable for rigid substrates, is not suitable for scaling to large areas and only a few studies have been reported on flexible substrates. In **Chapter 4**, We have proposed and demonstrated a very simple design of a bi-layer based metamaterial absorber suitable for very rough, flexible, rigid surfaces as well as for large area fabrication. The metamaterial absorbers were fabricated using laser interference lithography and soft lithography techniques. The details of the samples fabrication using laser interference lithography and soft lithography and structural and optical characterizations are presented in Section 4.1. A detailed analysis of the design, simulations, and effect of different parameters of the metamaterial

absorber is presented in Section 4.2. The result analysis and the origin of absorption have been drawn in Section 4.3, and finally conclusions are in Section 4.4. The work in this thesis has been published as Raghwendra Kumar, Amit K. Agarwal, S. Anantha Ramakrishna, *Development of a metamaterial structure for large area surfaces with specified infrared emissivity*, Opt. Eng. **57**(8), 087109 (2018).

In **Chapter 5**, we present a simple design of tri-layer on the structured photoresist based metamaterial absorber suitable for large area fabrication. In this design the spectral resonance can be tuned by controlling the thickness of different layers. The absorber was fabricated using laser interference lithography and physical vapour deposition techniques. The finite element method based simulations have been carried out to understand the origin of absorption as well as the asymmetric absorption profile generated due to the interference of bright and dark mode resonances. Experimental details including the sample fabrication and characterization are presented in Section 5.1. Effects of different geometrical parameters on electromagnetic responses of the metamaterial absorber understood using electromagnetic simulations are presented in Section 5.2. The physical origin of the absorption due to the excitation of different resonance modes is presented in Section 5.3, and finally, conclusions are in Section 5.4. This work is being submitted for publication as Raghwendra Kumar and S. A. Ramakrishna, *Tuning the resonances of a metamaterial absorber using Fano resonance*, (Under Preparation).

In **Chapter 6**, we present the development of a two-photon absorption based lithography system with sub-micrometer resolution using a sub-nanosecond pulsed laser. The system is optimized for different processing parameters such as average laser power, writing speed, laser spot dwell time, concentration of PI and truncation of the voxel by the substrate. New combinations of commercially available negative photoresists such as SU-8 and AR-N 4340 and the photoinitiator (2,4-Diethyl-9H-thioxanten-9-one) have been proposed and optimized for fabrication of microstructures. This system is comparably effective and has much higher capabilities for 2D structuring in terms of

the aspect ratio of the fabricated structures than conventional 2D laser micro writers. In Section 6.1, the introduction of two-photon absorption based lithography system including state of the art of the technique is presented. The basic introduction of TPA and TPP are presented in Sections 6.2 and 6.3, respectively. Section 6.4 contains the details of the photosensitive materials. Further, samples fabrication in different photosensitive materials and the role of truncation of the voxel by substrates in limiting the resolution and issues of adhesion on the substrates are explored in Section 6.5. Next, the characterization and calibration of the fabricated microstructures have been discussed in Section 6.6. Section 6.7 contains the details of theoretical estimation of the voxel dimensions, and finally, conclusions are in Section 6.8. This work has been published as Raghwendra Kumar and S. A. Ramakrishna, *Microstructuring by two-photon polymerization using a sub-nanosecond laser*, Current Science, **112**, 8, 25, (2017), p-1668-1674.

Publications

I. Related to this thesis

1. Microstructuring by two-photon polymerization using a sub-nanosecond laser,
Raghwendra Kumar and S. A. Ramakrishna; Current Science, **112**, 8, 25,
(2017), p-1668-1674.
2. Enhanced infrared transmission through subwavelength hole arrays in a thin
gold film mounted with dielectric micro-domes,
Raghwendra Kumar and S. A. Ramakrishna; J. Phys. D: Appl. Phys. **51**
(2018) 165104 (10pp).
3. Development of a metamaterial structure for large area surfaces with specified
infrared emissivity,
Raghwendra Kumar, Amit K. Agarwal and S. Anantha Ramakrishna;
Opt. Eng., **57**(8), 087109 (2018).
4. Tuning the resonances of a metamaterial absorber using Fano resonance,
Raghwendra Kumar and S. A. Ramakrishna; To be submitted.

II. Other publications

5. Thermally induced nonlinear optical absorption in metamaterial perfect absorbers,
Sriram Guddala, **Raghwendra Kumar** and S. Anantha Ramakrishna; Applied
Physics Letters **106**, 11 (2015), 111901.
6. Surface Plasmon Assisted Nonlinearity of Corrugated Gold Grating Structure,
Prince Gupta, **Raghwendra Kumar** and S. A. Ramakrishna; International Con-
ference on Fibre Optics and Photonics, OSA, **P1A-9**,(2016).
7. Studying Quantum Light Emission from Color Centers Embedded in Ultra-thin
Films SiC from Pulsed Laser Deposition,
Faraz Inam, **Raghwendra Kumar**, Naorem Rameshwari, Desmond Lau, Saikat
Ghosh, Brant C. Gibson, S. A. Ramakrishna and Stefania Castelletto; Interna-
tional Conference on Fibre Optics and Photonics, OSA, **P1A-11**,(2016).

Table of Contents

1	Theoretical background and recent activities	1
1.1	Light matter interaction	3
1.1.1	Maxwell's equations	3
1.1.2	Dielectric permittivity of metals (Drude model)	4
1.1.3	Lorentz-Drude model	6
1.2	Plasmons	7
1.2.1	Electromagnetic modes at the metal-dielectric interface	9
1.2.2	Excitation of surface plasmon polaritons	12
1.2.3	Estimation of the SPP resonance wavelength	14
1.2.4	Localized surface plasmons	15
1.2.5	Spoof surface plasmon polaritons	18
1.3	Fabry P�rot cavity	20
1.4	Guided mode resonance	22
1.5	Wood's anomaly	24
1.6	Fano resonance	26
1.7	Extraordinary optical transmission	28
1.7.1	Optimization of geometrical parameters for enhanced transmittance	31
1.8	Metamaterial absorber	36

1.8.1	Tri-layer metamaterial absorber	38
2	Fabrication, characterization and simulations methods	41
2.1	Laser interference lithography	43
2.1.1	Interference theory	44
2.1.2	Experimental set-up	47
2.1.3	Sample fabrication using laser interference lithography	48
2.1.4	Metal and dielectric deposition	51
2.1.5	Lift-off process	51
2.2	Two photon absorption lithography	55
2.2.1	Setup for two photon absorption lithography system	57
2.2.2	Putting all together	60
2.3	Soft lithography	61
2.3.1	General preparation for soft lithography	63
2.4	Sample characterization	65
2.4.1	Atomic force microscope	66
2.4.2	FTIR spectrometer	69
2.5	Numerical simulations	72
2.5.1	Modelling using COMSOL Multiphysics	73
2.5.2	A benchmark problem solved by COMSOL	74
3	Transmittance enhancement through sub-wavelength hole array using dielectric micro-domes	77
3.1	Experimental Details: Fabrication and Characterization	80
3.2	Electromagnetic simulations	88
3.2.1	Statistical analysis of the hole sizes	89

3.2.2	Effects of shape and size of dielectric structures	91
3.3	Results and discussions	96
3.4	Conclusions	103
4	Development of large area metamaterial structures for rough and flexible surfaces	105
4.1	Experimental details: Fabrication and Characterization	108
4.1.1	Sample fabrication using laser interference lithography	108
4.1.2	Sample fabrication using soft lithography	108
4.1.3	Sample characterizations	110
4.1.4	Fabrication of metamaterials on rough and flexible substrates	112
4.2	Electromagnetic simulations	116
4.3	Discussions	120
4.4	Conclusions	122
5	Tuning the resonances of a metamaterial absorber using Fano resonance	125
5.1	Experimental details: Fabrication and Characterization	128
5.1.1	Sample fabrication	128
5.1.2	Sample characterization	128
5.2	Electromagnetic simulations	131
5.3	Discussion	140
5.4	Conclusions	144
6	Microstructuring using two photon polymerization with a sub-nanosecond laser	147
6.1	Introduction	147

6.2	Fundamentals of two photon absorption	151
6.3	Two photon polymerization	154
6.4	Photosensitive materials	156
6.5	Sample fabrication	157
6.5.1	Role of voxel truncation in resolution and adhesion	160
6.6	Characterization and calibration of microstructures	162
6.7	Theoretical estimation of the voxel dimensions	164
6.8	Conclusions	168
7	Summary and future aspects	171
	Bibliography	195

List of Figures

1.1	The schematic diagram of surface plasmon oscillation at a single metal-dielectric interface.	9
1.2	Dispersion relation of SPPs propagating at the metal/glass and metal/air interfaces, and the dispersion relation of light in air and glass.	11
1.3	(a) Schematic diagram representation showing the excitation SPPs by a grating which provides the required momentum to the incidence light to fulfil the wave matching condition, (b) Graphical representation describes the requirement of extra momentum for excitation of SPPs. . .	13
1.4	Schematic diagram of LSPR on a sub-wavelength sized metallic sphere. Coherent oscillations in the free electrons of the metallic sphere are induced by the oscillating electric field of the incident light.	16
1.5	(a) Perforated metallic surface with a periodically square hole of sides a and periodicity d , which supports SSPPs, (b) Dispersion plot for the SSPPs on a structured surface. These figures are adopted from Ref. [29].	19
1.6	Illustration of the electric fields integrated with a surface mode in PEC surface. (a) In the absence of holes, the field cannot penetrate into the metal surfaces, and the light grazes the surface. (b) In the presence of sub-wavelength holes, the fields decay evanescently into the metal through holes, resulting in the formation of bound SPP-like waves, known as SSPPs. This figure is adopted from Ref. [30].	20
1.7	Schematic diagram of a Fabry-Perot cavity.	21

1.8	Schematic diagram illustrating the guided mode inside the guiding medium, where n_1 is the refractive index of the first medium, n_2 is the effective refractive index of the grating and guiding medium, and n_3 is the refractive index of the substrate.	23
1.9	Demonstration of Fano formula as the superposition of the Lorentzian line shape of a discrete level with flat continuum background.	27
1.10	Zero-order transmission spectrum through an Ag film perforated with nano-hole arrays. This figure is adopted from Ref. [59].	29
1.11	(a) Schematic diagram of a two-dimensional periodically perforated gold film with circular hole array. (b) The simulated transmittance spectrum corresponding to the circular hole array of $2\ \mu\text{m}$ periodicity and $1\ \mu\text{m}$ hole diameter in a thin gold film of thickness 40 nm on fused silica glass. The dotted square portion in the schematic represents a unit cell of the hole array.	31
1.12	Simulated transmittance spectra for different periodicities of the hole array.	32
1.13	Simulated transmittance spectra for different thickness of the gold film.	33
1.14	Simulated transmittance spectra for different diameters of the hole.	34
1.15	Transmission efficiency at the main peak wavelength versus hole diameter.	36
1.16	(a) Schematic diagram of a tri-layered (Au/ZnS/Au) metamaterial absorber, where t_1 , t_2 are the thickness of the ZnS, bottom gold layers, respectively; and h , d are the height and diameter of the top gold disk; and P is the periodicity of the unit cell. (b) The simulated absorbance, reflectance and transmittance spectra. The parameters used for simulation are $P = 2\ \mu\text{m}$, $d = 1\ \mu\text{m}$, $t_1 = 150\ \text{nm}$, $t_2 = 60\ \text{nm}$ and $t_3 = 100\ \text{nm}$	39

1.17	(a) Normalized electric field in the middle of the ZnS layer at resonance wavelength, (b) normalized electric field at resonance wavelength, (c) normalized magnetic field at resonance wavelength, (d) normalized current density as color map with its arrow volume plot at resonance wavelength.	40
2.1	Schematic representation of interference of two monochromatic and coherent waves with a simultaneous illustration of the resultant intensity distribution.	44
2.2	The energy density distribution patterns of the interference of two coherent beams in double exposure at different azimuthal angles of the sample holder (a) $\phi = 0^\circ$, (b) $\phi = 60^\circ$ and (c) $\phi = 90^\circ$	47
2.3	The photograph of the experimental set-up of two-beam laser interference lithography with a schematic diagram of the set-up in the inset, where the acronyms BS, L, M, SF, NDF stand for beam splitter, lens and mirror, spatial filter and neutral density filter, respectively.	48
2.4	Schematic diagram of the step-wise fabrication process of the one and two dimensional photoresist pattern using LIL.	50
2.5	AFM topographical map of the fabricated (a) one-dimensional, (b) two-dimensional grating pattern in photoresist.	50
2.6	Illustration of lift-off process steps: where (i) spin coating of photoresist on the substrate, (ii) structuring of the patterned in the photoresist using lithography, (iii) deposition of gold on the top of the structured film, (iv) removing the photoresist together with gold in acetone and (v) final patterned structures.	53
2.7	AFM topographical maps of the (a) photoresist disk array, (b) hole array fabricated from a sharp photoresist pillar array on a fused silica substrate, (c) hole array fabricated from a sharp photoresist pillar array on a silicon substrate (d) hole array fabricated from a conical shape photoresist pillar array on a glass substrate.	54

2.8	Screenshot image of the front panel of the software used for operating the system in manual data fitting mode.	59
2.9	(a) Schematic diagram of the TPALS, (b) Photograph of the same system where L is the sub-nanosecond laser, LD is laser driver, LC is laser controller, IM is inverted microscope, C is CCD camera, AOM is AO modulator, 3DPS is 3D piezo nano positioning stage and SH is sample holder.	61
2.10	(a) AFM topographical map across the one edge of the scratched line on the gold film, and the line profile plot across the cut is shown as the inset, (b) FESEM cross-sectional image of a tri-layer deposited sample.	66
2.11	Schematic diagram of a typical AFM in the working state where the reflected light from the back of the cantilever is collected in PSPD. (b) The plot of Lennard-Jones potential versus distance between the tip and sample. The shaded portions corresponding to the different working regions represent the different modes of operation of the AFM.	67
2.12	Schematic diagram of a FTIR spectrometer.	71
2.13	(a) Schematic diagram of the unit cell of square hole array in an optically thin metal film. (b) Transmittance spectra (red-reported & black-simulated) of the corresponding square hole array at normal incidence. The parameters used for simulation: periodicity of the hole array, the size of the hole and the thickness of the gold film are 400 nm, 160 nm and 40 nm, respectively.	75
3.1	The cross-sectional view of the unit cell of the micro-dome mounted sub-wavelength hole array. P is the periodicity of the hole array, d is the diameter of the hole, and t and h are the thickness of the gold layer and height of the micro-dome, respectively.	79
3.2	Schematic diagram of the sample fabrication steps.	81

3.3	(a) AFM topographical map of the perforated gold film on fused silica substrate; (b) 3D view of figure (a). The measured thickness of the gold film, diagonal of the square, periodicity of hole array are 40 ± 4 nm, 1.0 ± 0.05 μm and 2.1 ± 0.03 μm , respectively.	83
3.4	(a) AFM topographical map of the perforated gold film mounted with SU-8 micro-domes before melt flow process; (b) 3D view of figure (a).	83
3.5	(a) AFM topographical map of the perforated gold film mounted with SU-8 micro-domes after melt flow process; (b) 3D view of figure (a). The measured periodicity of micro-dome array, height of the SU-8 micro-dome are 2.1 ± 0.03 μm and 0.4 ± 0.02 μm , respectively.	83
3.6	Optical microscopy image of the SU-8 micro-domes mounted sample taken in transmission mode using $100\times$ objective lens.	84
3.7	Optical microscopy image of the SU-8 micro-domes mounted sample taken in reflection mode using $100\times$ objective lens.	84
3.8	Diffraction pattern through the periodically perforated gold film when each hole is mounted with US-8 micro-dome.	85
3.9	(a) Measured infrared normalized transmittance spectra of the perforated gold film (i); when coated with an SU-8 layer before UV curing (ii); and when SU-8 micro-domes are mounted on the holes of the gold film (iii).	86
3.10	Transmittance through the periodically perforated gold film mounted with SU-8 micro-domes on each hole. Measured transmittance spectra at different incident angles ($0^\circ \leq \theta \leq 30^\circ$) for (a) the TE polarized light and, (b) the TM polarized light.	86
3.11	Reflectance from the periodically perforated gold film when SU-8 micro-domes are mounted on the holes. Measured reflectance spectra at different incident angles ($0^\circ \leq \theta \leq 30^\circ$) for the (a) TE polarized light and, (b) TM polarized light. The measured reflectance spectra are normalized with reflectance from a smooth gold film at the corresponding polarizations and incident angles.	87

3.12	Absorption spectra at different incident angles ($0^\circ \leq \theta \leq 30^\circ$) for the (a) TE polarized polarization and (b) TM polarization. In each case, the absorption is obtained from the measured transmittance (T) and reflectance (R) as $A = 1 - T - R$	87
3.13	Statistical distribution of hole sizes in the perforated gold film.	89
3.14	(a) Simulated transmittance through the different sizes of the hole in the perforated gold film and weighted average transmittance (black line) through different sizes of the hole. (b) simulated transmittance through the different sizes of the hole in perforated gold film mounted with SU-8 micro-domes and weighted average transmittance (black line) through different sizes of the hole mounted with SU-8 micro-domes. A residual layer of SU-8 of thickness 200 nm was assumed to be present on the gold film in calculation with the micro-dome.	90
3.15	Simulated transmittance spectra at different incident angles ($0^\circ \leq \theta \leq 25^\circ$) through the hole array mounted with the SU-8 micro-dome and having residual layer of SU-8 of thickness 200 nm on the gold film, and the corresponding angular weighted transmittance (black line) at different incident angles (a) TE polarization (b) TM polarization. The parameters used for simulations: thickness of the gold film, the periodicity of the hole array and height of the micro-dome are 40 nm, 2.1 μ m and 400 nm, respectively.	91
3.16	Simulated transmittance spectra corresponding to the conical and cylindrical SU-8 microstructure mounted on the holes of the perforated gold film with 200 nm residual layer of SU-8. The parameters used for simulations are: thickness of the gold film, the periodicity of the hole array, thickness of residual SU-8 layer and height of the cylindrical microstructure and conical microstructure are 40 nm, 2.1 μ m, 200 nm, 400 nm and 400 nm respectively.	92
3.17	Simulated transmittance spectra of the perforated gold film mounted with different heights of the micro-dome with residual layer of SU-8 of thickness 200 nm on the gold film.	92

3.18	Simulated weighted average transmittance through different sizes of the hole in the gold film without mounting of micro-dome (red line), and with mounting the micro-domes on the holes with a residual layer of SU-8 of thickness 200 nm (black line). The parameters used for simulations are: thickness of the gold layer = 40 nm, array lattice constant = $2.1\ \mu\text{m}$ and height of the micro-dome = $0.4\ \mu\text{m}$	93
3.19	Square of the absolute value of electric field for (a) perforated gold film, (b) hole array mounted with micro-dome without the residual layer of SU-8, (c) hole array mounted with micro-dome with residual layer of SU-8 of thickness 100 nm on the gold film, (d) hole array mounted with micro-dome with a residual layer of SU-8 of thickness 500 nm, and the inset transmittance spectra through the hole array with 500 nm residual SU-8 layer with and without the micro-domes.	94
3.20	Simulated transmittance spectra of the periodically perforated gold film mounted with the micro-dome on each hole with a residual layer of SU-8 of thickness 200 nm at different incident angles ($0^\circ \leq \theta \leq 30^\circ$) for the (a) TE polarization, and (b) TM polarization. The simulated spectra are not averaged over the hole sizes or angles here to understand the angle dependency.	95
3.21	Simulated reflectance spectra of the periodically perforated gold film mounted with SU-8 micro-dome on each hole with a residual layer of SU-8 of thickness 200 nm at different incident angles ($0^\circ \leq \theta \leq 30^\circ$) for the (a) TE polarization, and (b) TM polarization.	95
3.22	Simulated absorption spectra at different incident angles ($0^\circ \leq \theta \leq 30^\circ$) for the (a) TE polarized polarization and (b) TM polarized polarization. In each case, the absorption is obtained from the measured transmittance (T) and reflectance (R) as $A = 1 - T - R$	96
3.23	Normalized electric fields at incident angles $\theta = 0^\circ$ (a, c) and $\theta = 30^\circ$ (b, d) for the TM (a, b) and TE (c, d) polarizations. The corresponding color bars for the field strengths are shown to the right of each plot. . .	100

3.24	Color maps of the normalized time average power with Poynting vector field lines at incident angles $\theta = 0^\circ$ (a, c) and $\theta = 30^\circ$ (b, d) for the TM (a, b) and TE (c, d) polarizations. The corresponding color bars for the strength of time average power are shown to the right of each plot. . . .	101
4.1	Schematic diagram of the unit cell of the metamaterial. In the diagram, p is periodicity of the disk array, h is the height of the photoresist disk, d is diameter of the disk, t_2 and t_1 are thickness of the ZnS and Au layers, respectively.	107
4.2	AFM topographical map of a two-dimensional disk array, (a) before the deposition of the (ZnS/Au) layers, (b) after the deposition of the (ZnS/Au) layers. The measured height of the disk, periodicity of the disk array, ZnS layer thickness and top gold layer thickness are 500 ± 30 nm, $3.0 \pm 0.03 \mu\text{m}$, 300 ± 20 nm, 40 ± 5 nm, respectively.	109
4.3	SEM image of the sample whose AFM topographical map is shown in the figure 4.2(b), and the inset shows an enlarged and tilted view of a small portion of the sample.	109
4.4	Schematic diagram depicting the steps in the fabrication of the metamaterial using soft lithography and deposition.	111
4.5	Measured reflectance spectra of the metamaterial for the (a) TE polarization and (b) TM polarization at different incident angles.	112
4.6	(a) Optical microscope image of an unpolished Si wafer at $5\times$ magnification (b) 3D view of AFM topographical map of the unpolished Si wafer, (c) optical microscope image of the disk array made of UV curable polymer fabricated on the unpolished Si wafer viewed at $100\times$ magnification (d) optical microscope image of the fabricated metamaterial on the unpolished Si wafer viewed at $100\times$ magnification. The corresponding measured reflectance spectrum is shown in the inset. . . .	113

4.7	(a) Photograph of the emery paper with grit size of $220\ \mu\text{m}$, (b) Optical microscope image of the metamaterial fabricated on the emery paper viewed at $100\times$ magnification with the measured reflectance spectra in the inset. (c) Photograph of the metamaterial showing its flexibility fabricated on emery paper, (d) optical microscope image at $5\times$ magnification of the Al sheet, (e) optical microscope image of the metamaterial fabricated on the Al sheet at $100\times$ magnification with the measured reflectance spectra in the inset. (f) optical microscope of the metamaterial fabricated on the kapton sheet at $100\times$ magnification with the measured reflectance spectra in the inset.	114
4.8	(a) Photograph of the metamaterial fabricated over large areas on a glass substrate. A centimeter scale has been shown beside the fabricated sample to show the dimension of the fabricated area. (b) measured reflectance spectra of the metamaterial, (c) LWIR camera infrared image of the metamaterial held in by hand.	115
4.9	(a) Simulated reflectance, transmittance and absorbance spectra of the metamaterial at normal incidence, (b) color map of the normalized magnetic field at the resonant wavelength $6.4\ \mu\text{m}$ and (c) color map of the normalized electric field at the resonant wavelength $6.4\ \mu\text{m}$. The parameters used in the simulations: periodicity of the disk array, disk height, diameter of the disk, thickness of the ZnS layer and thickness of the Au layer are $3.0\ \mu\text{m}$, $0.5\ \mu\text{m}$, $1.68\ \mu\text{m}$, $300\ \text{nm}$ and $40\ \text{nm}$, respectively. . .	117
4.10	Simulated reflectance spectra for the (a) TE polarization and (b) TM polarization at different incident angles. The parameters used for simulations: periodicity of the disk array, height of the disk, diameter of the disk, thickness of the ZnS layer and thickness of the Au layer are $3.0\ \mu\text{m}$, $0.5\ \mu\text{m}$, $1.68\ \mu\text{m}$, $300\ \text{nm}$ and $40\ \text{nm}$, respectively.	118
4.11	Simulated (a) reflectance, (b) transmittance and (c) absorbance spectra at normal incidence for different diameters of the photoresist disk. The parameters used for simulations: periodicity of the disk array, height of the disk, thickness of the ZnS layer and thickness of the Au layer are $3.0\ \mu\text{m}$, $0.5\ \mu\text{m}$, $300\ \text{nm}$ and $40\ \text{nm}$, respectively.	119

4.12	Simulated (a) reflectance, (b) transmittance and (c) absorbance spectra at normal incidence for different periodicities of the photoresist disk array. The parameters used for simulations: height of the disk, diameter of the disk, thickness of the ZnS layer and thickness of the Au layer are $0.5\ \mu\text{m}$, $1.68\ \mu\text{m}$, $300\ \text{nm}$ and $40\ \text{nm}$, respectively.	119
4.13	Simulated (a) reflectance, (b) transmittance and (c) absorbance spectra at normal incidence for different thickness of the ZnS layer. The parameters used for simulations: periodicity of the disk array, height of the disk, diameter of the disk and thickness of the Au layer are $3.0\ \mu\text{m}$, $0.5\ \mu\text{m}$, $1.68\ \mu\text{m}$ and $40\ \text{nm}$, respectively.	120
5.1	Schematic diagram of the unit cell of the metamaterial absorber with illustration of different existing modes, where the gap between gold layers on the top of photoresist pillar and on the ZnS layer on the silicon substrate is g	127
5.2	AFM topographical maps of the fabricated sample (a) before tri-layer deposition, (b) after tri-layer deposition, and the inset in each figure shows a 3D view of the corresponding images.	129
5.3	SEM image of the fabricated sample after the tri-layer deposition, the inset shows an enlarged and tilted view of a portion of the sample. . . .	130
5.4	The measured reflectance spectra of the fabricated sample for the (a) TE polarization, (b) TM polarization at different incident angles. . . .	131
5.5	(a) Simulated reflectance, transmittance and absorbance spectra corresponding to the metamaterial absorber, (b–e) color plot of the normalized magnetic field at resonant wavelengths $9.1\ \mu\text{m}$, $6.4\ \mu\text{m}$, $9.6\ \mu\text{m}$, $10.0\ \mu\text{m}$. Parameters used for simulations: periodicity of the disk array, height of the disk, diameter of the disk, thickness of the bottom Au layer, thickness of the ZnS layer and thickness of the top Au layer are $2.8\ \mu\text{m}$, $0.5\ \mu\text{m}$, $1.68\ \mu\text{m}$, $160\ \text{nm}$, $300\ \text{nm}$ and $30\ \text{nm}$, respectively. . .	132

- 5.6 (a) Simulated reflectance, transmittance and absorbance spectra corresponding to the metamaterial absorber without top Au and ZnS layers on the disk, where the schematic diagram of the unit cell without the top gold and ZnS layers on the top of photoresist disk is shown in the inset, (b) color plot of the normalized time average power with Poynting vector field lines at resonant wavelength $9.1 \mu\text{m}$, (c–d) color plot of the normalized magnetic field at the resonant wavelength of $9.1 \mu\text{m}$ and $10.0 \mu\text{m}$. Parameters used for simulations: periodicity of the disk array, height of the disk, diameter of the disk, thickness of the bottom Au layer, thickness of the ZnS layer and thickness of the top Au layer are $2.8 \mu\text{m}$, $0.5 \mu\text{m}$, $1.68 \mu\text{m}$, 160 nm , 300 nm and 30 nm , respectively. 134
- 5.7 Simulated reflectance, transmittance and absorbance spectra at normal incidence for the different periodicity of the photoresist disk array. The parameters used for simulations: disk height, disk diameter, bottom Au layer thickness, ZnS layer thickness and top Au layer thickness are $0.5 \mu\text{m}$, $1.68 \mu\text{m}$, 160 nm , 300 nm and 30 nm , respectively. 135
- 5.8 Color plots of the normalized magnetic field at resonance wavelength (a) $\lambda = 8.8 \mu\text{m}$, (b) $\lambda = 13.7 \mu\text{m}$ and (c) $\lambda = 10.3 \mu\text{m}$. The arrow volume plots of the time average power flow at resonance wavelength (d) $\lambda = 8.8 \mu\text{m}$, (e) $\lambda = 13.7 \mu\text{m}$, and (f) $\lambda = 10.3 \mu\text{m}$ 136
- 5.9 The simulated reflectance spectra of the fabricated sample for the (a) TE polarization, (b) TM polarization at different incident angles. The parameters used for simulations: disk height, disk diameter, bottom Au layer thickness, ZnS layer thickness and top Au layer thickness are $0.5 \mu\text{m}$, $1.68 \mu\text{m}$, 155 nm , 300 nm and 30 nm , respectively. 137
- 5.10 The simulated (a) reflectance, (b) transmittance and (c) absorbance spectra of the tri-layered metamaterial for different values of g as 10 nm , 15 nm , 20 nm , 25 nm and 30 nm . The other parameters such as disk height, disk diameter, ZnS layer thickness and top Au layer thickness are $0.5 \mu\text{m}$, $1.68 \mu\text{m}$, 300 nm and 30 nm , respectively. 138

5.11	Simulated reflectance spectrum (black line) with Fano fit (red line). The parameters used for simulations: periodicity of the disk array, disk height, disk diameter, bottom layer Au thickness, ZnS layer thickness and top layer Au thickness are 2.8 μm , 0.5 μm , 1.68 μm , 160 nm, 300 nm and 30 nm, respectively.	139
5.12	Fano fitted reflectance spectra of the corresponding individual resonance.	139
6.1	(a) Mechanism of two photon absorption when photons are simultaneously excited. An illustration of the methods for increasing the probability of two photon absorption by increasing the density of photons by (b) spatial confinement using objectives with high numerical aperture and by (c) temporal confinement of photons using pulse laser.	152
6.2	(a) Comparison of the spatial full width at half maximum of a Gaussian shaped beam intensity and its squared (I^2) profile, (b) schematic explaining a threshold intensity for photosensitive materials with a threshold assumed to be at horizontal dashed line. As the peak intensity gets closer to the threshold from above, the voxel width decreases.	154
6.3	3D view of AFM topographical maps of (a) 2D grating and (b) 2D micro disk array fabricated in SU-8. The experimental parameters used for fabrication of these microstructures are: 1.2 mW laser average power, 100 $\mu\text{m/s}$ writing speed, 10 kHz rep rate and 0.8 NA objective.	157
6.4	Optical microscopy images of (a) logo of IIT Kanpur fabricated in SU-8, (b) an array of micro-pillars of height 6 μm fabricated in SU-8, (c) 2D disk array fabricated in AR-N 4340. All these microstructures are fabricated using the parameters: 1.2 mW laser average power, 100 $\mu\text{m/s}$ writing speed, 10 kHz rep rate and 0.8 NA objective.	158
6.5	AFM topographical map of a 2D grating fabricated using 100 \times oil immersion objective in SU-8, (b) the line profile of the selected portion of the micro-line in the sample, and FWHM of the corresponding line profile is around 500 nm. (c) 3D view of optical profiler image of the pillar array fabricated in SU-8.	159

6.6	AFM topographical map of a 2D grating fabricated using $50\times$ magnification objective in ma-N 1405 negative photoresist, (b) 3D view of figure (a). This grating is fabricated using parameters: 1.2 mW laser average power, $1000\text{ }\mu\text{m/s}$ writing speed, 10 kHz rep rate and 0.8 NA objective.	159
6.7	(a) Schematic diagram illustrating the truncation of the voxel by the substrate, (b) AFM topographical map of the pillars at a different height from the substrate. (c) 3D view of the AFM topographical map of the figure (b).	161
6.8	(a) Optical microscope image of the SU-8 pillar array topple down on the substrate during the development process, (b) Optical image of distorted micro-lines.	161
6.9	(a) 2D AFM topographical map of the SU-8 pillar array topple down on the substrate during the development process. (b) 3D AFM topographical view of the figure (a).	162
6.10	AFM topographical maps of (a) micro-lines array fabricated in the SU-8 at constant writing speed $100\text{ }\mu\text{m/s}$ with decreasing peak intensity of 5.7 GW/cm^2 to 2.5 GW/cm^2 (from left to the right) and micro-lines array fabricated in the SU-8 at constant peak intensity 4.6 GW/cm^2 with increasing writing speed of 300 to $1600\text{ }\mu\text{m/s}$ (from left to the right). The corresponding line profiles of the AFM maps are shown beneath the individual map.	164
6.11	Line width (of Figs. 6.10 (a) and (b)) versus (a) peak intensity, (b) writing speed. Data points represent FWHM of the corresponding line profiles, while error bars show the variance in the line width.	164
6.12	Schematic diagram used for visualization of the voxel formation in our TPALS.	165

6.13	(a) Evolution of voxel width with dwell time and average laser power, (b) Evolution of voxel width with scanning speed and average laser power (c) Change in voxel width with the numerical aperture (NA) of the objectives and dwell time. The parameters used to plot these figures λ , NA , n , f , P_{av} , E'_{th} , are 532 nm, 0.8, 10 kHz, 1.2 mW and $6.6 \times 10^{-73} W^2/m^4$, respectively.	167
7.1	Micro-lines array fabricated at different average powers without the PI and with a different weighted concentration of the PI in AR-N 4340 photoresist.	183

Chapter 1

Theoretical background and recent activities

Advancements in micro/nano fabrication techniques and theoretical knowledge are driving innovations in designer structured systems which display unique and useful electromagnetic and optical properties. The possibility of manipulation of the electromagnetic properties with the designer material systems has attracted the attention of researchers from different interdisciplinary areas and opened up a wide variety of applications in many fields such as plasmonics [1, 2], photonics [3, 4], metamaterials [5, 6], biosensors [7, 8], solar cells [9, 10], photonic crystals [11, 12], etc. These designer material systems show unexpected optical and electrical properties, which are different from that of the composite bulk materials.

The field of plasmonics, which is the study of electromagnetic response in structured metallic systems has gained wide interest from researchers in many disciplines due to the tunability of the optical responses by varying the geometrical designs of the structured surfaces. The focusing and confining light to sub-wavelength scale dimensions are an inherent feature of plasmonic systems, which have been exploited to develop many new devices. In some cases, the electromagnetic responses of the individual unit of plasmonic systems are different from that of their collective arrangement,

particularly in the periodic fashion. The enhanced transmission through periodically arranged sub-wavelength hole array known as extraordinary optical transmission is one of the examples where the effect of the periodic arrangement in the structural design is critically important.

Metamaterials have novel electromagnetic properties, which are rarely or never found in the naturally available materials. Usually, metamaterials consist of artificial micro/nanostructures of size much smaller than the operating wavelength of electromagnetic radiation. We now have the capability to tailor the effective permittivity, effective permeability and the refractive index of a medium through the design and geometry of the structures. A medium can exhibit negative refraction and unique reversed electromagnetic properties if it has a simultaneously negative permittivity and negative permeability at a particular frequency as discussed by Veselago in 1968 [13]. Among the numerous applications of metamaterials, the concept of perfect absorption of electromagnetic waves got particular attention because of various possible applications such as bolometers [14], thermal emitters [15], sensors [7, 8, 16], etc.

In this chapter, the theoretical background needed to understand this thesis is outlined. The basic introduction of light-matter interaction, starting from Maxwell's equations to the Lorentz model of dispersion is discussed in Section 1.1. The concept of surface plasmons, excitation of surface plasmons using EM waves, concepts of localized surface plasmons and basic introduction to spoof surface plasmon polaritons are discussed in Section 1.2. To understand the physical phenomena happening in our systems, the basic introductions of the Fabry Perot cavity, guided mode resonance, Wood's anomalies, and Fano resonance are discussed in Sections 1.3, 1.4, 1.5 and 1.6, respectively. Finally, an overview of extraordinary optical transmission and metamaterials absorbers are given in Sections 1.7 and 1.8, respectively.

1.1 Light matter interaction

1.1.1 Maxwell's equations

Generally, the most electromagnetic phenomena are governed by Maxwell's equations, which are a set of equations describing the inter-relationship among fields, sources, and material properties. The interactions of the metallic micro/nanostructures with electromagnetic radiation can be described within the classical framework of Maxwell's equations on the macroscopic level. The advantage of this macroscopic approach is that details of the fundamental interactions between charged particles inside the media and electromagnetic fields need not be taken into account. The rapidly varying microscopic fields are averaged over distances much larger than the underlying microstructure. In the differential form, these equations evolve in space and time and can be written as

$$\nabla \cdot \mathbf{D} = \rho_{free}, \quad (1.1)$$

$$\nabla \cdot \mathbf{B} = 0, \quad (1.2)$$

$$\nabla \times \mathbf{E} = -\frac{\partial \mathbf{B}}{\partial t}, \quad (1.3)$$

$$\nabla \times \mathbf{H} = \mathbf{J}_{free} + \frac{\partial \mathbf{D}}{\partial t}. \quad (1.4)$$

where \mathbf{E} and \mathbf{H} are the macroscopic electric and the magnetic field, \mathbf{D} is the dielectric displacement, \mathbf{B} is the macroscopic magnetic induction or magnetic flux density, and ρ_{free} and \mathbf{J}_{free} are the macroscopic free external charge and current densities, respectively. The \mathbf{D} and \mathbf{B} are linearly proportional to the \mathbf{E} and \mathbf{H} , respectively in linear and isotropic media can be written as:

$$\mathbf{D} = \epsilon \mathbf{E} = \epsilon_r \epsilon_0 \mathbf{E} = \epsilon_0 (1 + \chi_e) \mathbf{E} = \epsilon_0 \mathbf{E} + \mathbf{P}, \quad (1.5)$$

$$\mathbf{B} = \mu \mathbf{H} = \mu_r \mu_0 \mathbf{H} = \mu_0 (1 + \chi_m) \mathbf{H} = \mu_0 \mathbf{H} + \mathbf{M}. \quad (1.6)$$

where $\epsilon_0 = 8.854 \times 10^{-12}$ F/m, $\mu_0 = 4\pi \times 10^{-7}$ H/m are the dielectric permittivity and dielectric permeability of the free space, and ϵ_r , μ_r are the relative permittivity and the relative permeability of the medium, respectively. \mathbf{P} and \mathbf{M} are polarization and magnetization induced by the electric field and the magnetic field inside the medium, respectively. Since we are dealing with non-magnetic materials, so we will put $\mu_r = 1$ for our work.

1.1.2 Dielectric permittivity of metals (Drude model)

The physical quantity that describes the interaction of the electromagnetic fields with a medium is known as the dielectric function (dielectric permittivity or constant), which is frequency dependent. The permittivity of a metal mainly depends on the number of free electrons present in the metal. Electrons in the outer shell orbits are loosely bounded by the Coulomb force causing the electrons to move freely within the volume of the metal. The Drude model is developed on the basis of the assumption of a simple plasma model, where it is assumed that the metal can be described as a gas of free, independent electrons. It effectively models the conductivity, dispersion of the alkali, alkaline-earth as well as noble metals (S-shell electrons). Under the influence of an external time varying electric field the equation of motion of a free electron having mass m and charge $-e$ can be described as:

$$m \frac{\partial^2 \mathbf{r}(t)}{\partial t^2} + m\gamma \frac{\partial \mathbf{r}(t)}{\partial t} = -e\mathbf{E}_0 \exp(-i\omega t), \quad (1.7)$$

where $\mathbf{r}(t)$ is displacement of the electron, and γ phenomenologically describes the rate of dissipation due to collisions and various phenomena and is related to the relaxation time τ for the free electron as $\gamma=1/\tau$. Since the driving electric field varies harmonically as $e^{-i\omega t}$, so the corresponding electron's responses as it's displacement ($\mathbf{r}(t)$) also varies

harmonically as $e^{-i\omega t}$. Therefore, after putting $\mathbf{r}(t) = r_0 e^{-i\omega t}$ in Eq. 1.7, we get

$$\mathbf{r}(t) = \frac{e}{m(\omega^2 + i\gamma\omega)} E_0 e^{-i\omega t}. \quad (1.8)$$

The macroscopic polarization (\mathbf{P}) induced by displaced electrons is explicitly given by

$$\mathbf{P} = -Ner = \frac{Ne^2}{m(\omega^2 + i\gamma\omega)} E_0 e^{-i\omega t}, \quad (1.9)$$

where N is the number density of electrons. So the dielectric displacement can be written as,

$$\mathbf{D} = \epsilon_0 \mathbf{E} + \mathbf{P} = \epsilon_0 \left(1 - \frac{\omega_p^2}{\omega^2 + i\gamma\omega} \right) \mathbf{E}, \quad (1.10)$$

where $\omega_p^2 = Ne^2/m_e\epsilon_0$ is the plasma frequency of the free electron gas. Thus using equations 1.5 and 1.10, the dielectric permittivity of the medium can be expressed as:

$$\epsilon(\omega) = 1 - \frac{\omega_p^2}{\omega(\omega + i\gamma)} = 1 - \frac{\omega_p^2\tau}{\omega(\omega\tau + i)}. \quad (1.11)$$

In the case of $\omega\tau \gg 1$, the collision interval time, $\tau \sim 1 \times 10^{-14} \text{s}$ typically for metals,

$$n^2 = \epsilon(\omega) = 1 - \frac{\omega_p^2}{\omega^2}, \quad (1.12)$$

and for $\omega < \omega_p$, which means that the refractive index n takes a purely imaginary value. This also means that the incident light is reflected by the surface of the metals as light does not propagate inside the metal. Since $\omega\tau \gg 1$ is valid for most of the metals, so they have high reflectivity and shiny appearance.

The Drude model is a reasonably accurate and valid model for dielectric constants of most of the metals at visible to infrared (IR) frequencies. However, in the case of silver, gold, and copper, the dielectric constants calculated by this model exhibit significant discrepancies with experimental measurements [17] due to the inter-band (d- shell) and intra-band transition. The discrepancies were seen at higher frequencies,

where the bound electrons also start responding to the driving electric fields.

1.1.3 Lorentz-Drude model

In the Lorentz model, It was assumed that the optical behavior of materials can be dominated by the inter-band transitions of the electrons and the conduction band is assumed to be empty for a dielectric or metal, whereas the Drude model was totally based on the intra-band motion of electrons. Usually, the intra-band effects are referred to free-electron effects, and inter-band effects are referred to bound-electron effects. The dielectric function of metals based on inter-band transition effect is given by

$$\epsilon_L(\omega) = 1 + \frac{\omega_p^2}{(\omega_0^2 - \omega^2) - i\omega\gamma}, \quad (1.13)$$

where ω_0 and γ are the oscillator resonant frequency and resonance bandwidth, respectively. The subscript L is used in ϵ to represent the Lorentz model. The dielectric function based on multiple inter-band transitions is given by

$$\epsilon_L(\omega) = 1 + \sum_{j=1}^k \frac{f_j \omega_p^2}{(\omega_j^2 - \omega^2) + i\omega\gamma_j}, \quad (1.14)$$

where ω_p is the plasma frequency, k is the number of oscillators with frequency ω_j . γ_j , f_j and ω_j are the damping, oscillator strength and oscillation frequency of the j^{th} oscillator.

The Drude and Lorentz models can be combined in a single one which takes into account both intra-band and inter-band contributions [18]. The hybrid Lorentz-Drude (LD) model provides a dielectric function having an excellent correlation with the experimentally measured dielectric functions of many metals like silver (Ag) over a wide range of frequencies. The Lorentz-Drude model is described by the following

dielectric function:

$$\epsilon_{LD}(\omega) = \epsilon_{Drude}(\omega) + \sum_{j=1}^k \frac{f_j \omega_p^2}{(\omega_j^2 - \omega^2) + i\omega\gamma_j}. \quad (1.15)$$

The general form of the Lorentz-Drude dielectric permittivity can be written as

$$\epsilon_{LD}(\omega) = \epsilon_\infty - \frac{\omega_p^2}{\omega^2 + i\gamma\omega} + \sum_{j=1}^k \frac{f_j \omega_p^2}{(\omega_j^2 - \omega^2) + i\omega\gamma_j}. \quad (1.16)$$

The complex refractive indices of the gold, silicon, ZnS and fused silica used in this thesis are taken from Refs. [19], [20], [21] and [22], respectively. Refractive index of the SU-8 used in this thesis is taken as $1.561 + 0.0024i$ [23], the refractive index of the photoresist (ma-P 1205) is taken as 1.58 [24].

1.2 Plasmons

The plasmon is a quantum of plasma oscillations [25], similar to the photon as the quantum of electromagnetic oscillations. It is also defined as the quantum of collective oscillation of free electrons in solids. The collective oscillations can occur in the volume of solids as well as on the surfaces of solids. If they occur inside the bulk solids, they are known as volume plasmons, and if they occur the surface then they are known as surface plasmons. Plasmonic effects are obtained in metals when they are excited with frequency lesser than their plasma frequency because of their free-electron gas like behaviour. When the surface waves enter into resonance with free radiation, i.e. photons then coupled oscillations appear and the coupled state of surface plasmon and photon is known as the surface plasmon polariton (SPP). The equation of the motion of such plasma oscillations can be described by combining the curl Eqns. 1.3 and 1.4.

$$\nabla \times \nabla \times \mathbf{E} = -\mu_0 \frac{\partial^2 \mathbf{D}}{\partial t^2}. \quad (1.17)$$

If the source of excitation is a plane wave $\mathbf{E} = E_0 e^{i(kx - \omega t)}$, we obtain

$$\mathbf{k}(\mathbf{k} \cdot \mathbf{E}) - k^2 \mathbf{E} = -\epsilon(k, \omega) \frac{\omega^2}{c^2} \mathbf{E}, \quad (1.18)$$

and for the longitudinal wave, $\mathbf{k}(\mathbf{k} \cdot \mathbf{E}) = k^2 \mathbf{E}$ leads to

$$\epsilon(k, \omega) = 0. \quad (1.19)$$

For transverse mode, $\mathbf{k} \cdot \mathbf{E} = 0$ leads to

$$k^2 = \epsilon(k, \omega) \frac{\omega^2}{c^2}, \quad (1.20)$$

where ω is the frequency of the excitation source, c is speed of light in free space, and k is the wavevector of plasmon polaritons. For frequencies close to ω_p , the damping coefficient (γ) can be neglected, and the dielectric permittivity $\epsilon(\omega)$ can be written as,

$$\epsilon(\omega) = 1 - \frac{\omega_p^2}{\omega^2}. \quad (1.21)$$

After combining Eqs. 1.20 and 1.21, the $k(\omega)$ can be expressed as

$$k(\omega) = (1/c) \sqrt{\omega^2 - \omega_p^2}. \quad (1.22)$$

For $\omega \gg \omega_p$, the metal behaves like a dielectric material, and waves propagate with group velocity $v_g = d\omega/dk < c$. When $\omega = \omega_p$, where for low damping $k(\omega) = 0$, and the electrons oscillate collectively against the fixed background of positive atom cores with the plasmon frequency throughout the medium. For $\omega < \omega_p$, $k(\omega)$ is imaginary, hence there is no propagation of electromagnetic waves, and the waves decay evanescently inside the metal. The corresponding electric fields of the propagating wave along the surface decay exponentially on both sides normal to the metal-dielectric interface. The waves propagating along the surface of the metal are the surface plasmons [1].

Physically, surface plasmons are electromagnetic excitations propagating at the interface between a dielectric and a metal, and evanescently confined in the perpendicular direction to the interface, when these surface waves coupled with the free radiation i.e. photons known as the surface plasmon polaritons (SPPs). To understand the physical aspects of the surface plasmons polaritons, we will discuss the wave propagation at a smooth interface between semi-infinite metallic and dielectric media.

1.2.1 Electromagnetic modes at the metal-dielectric interface

The schematic diagram of the smooth metal-dielectric interface is shown in Fig. 1.1, where the part $z > 0$ is filled with a dielectric medium of dielectric permittivity ϵ_d , and the part $z < 0$ as a metal with dielectric permittivity of $\epsilon_m = \epsilon_{mr} + i\epsilon_{mi}$. In the schematic diagram, the charge oscillation and field profiles are shown by symbolic representation of charges (+ and -) and with curved arrow lines inside the metal and dielectric medium. The time-harmonic fields at frequency ω in the two media for the

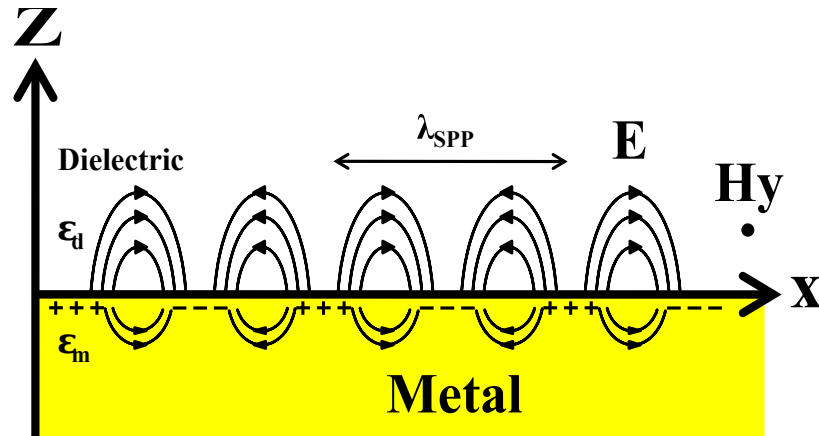


Figure 1.1: The schematic diagram of surface plasmon oscillation at a single metal-dielectric interface.

the TM polarized light (magnetic field along the y-axis) can be written as;

for $z > 0$,

$$H_y^d(z) = A_d e^{i(\beta x - \omega t)} e^{-k_z^d z}, \quad (1.23)$$

$$E_x^d(z) = i A_d \frac{1}{\omega \epsilon_0 \epsilon_d} k_z^d e^{i(\beta x - \omega t)} e^{-k_z^d z}, \quad (1.24)$$

$$E_z^d(z) = -A_d \frac{\beta}{\omega \epsilon_0 \epsilon_d} e^{i(\beta x - \omega t)} e^{-k_z^d z}, \quad (1.25)$$

and for $z < 0$,

$$H_y^m(z) = A_m e^{i(\beta x - \omega t)} e^{k_z^m z}, \quad (1.26)$$

$$E_x^m(z) = -i A_m \frac{1}{\omega \epsilon_0 \epsilon_m} k_z^m e^{i(\beta x - \omega t)} e^{k_z^m z}, \quad (1.27)$$

$$E_z^m(z) = -A_m \frac{\beta}{\omega \epsilon_0 \epsilon_m} e^{i(\beta x - \omega t)} e^{k_z^m z}, \quad (1.28)$$

where, $(k_z^d)^2 = \beta^2 - k_0^2 \epsilon_d$ and $(k_z^m)^2 = \beta^2 - k_0^2 \epsilon_m$. The above equations can be solved by imposing the conditions of continuity from above and the Maxwell's Eqs. 1.1 and 1.4 in absence of charges and currents ($\rho = 0, J = 0$). According to the continuity conditions, the tangential components of the magnetic field (H_y) and the electric field (E_x) at the interface $z = 0$ are given as

$$H_y^d(0) - H_y^m(0) = 0, \quad (1.29)$$

$$\frac{k_z^d}{\omega \epsilon_d} H_y^d(0) + \frac{k_z^m}{\omega \epsilon_m} H_y^m(0) = 0. \quad (1.30)$$

For these equations to have a non-trivial solution, the determinant must be zero. Thus we get $A_d = A_m$ and

$$\frac{k_z^d}{k_z^m} = -\frac{\epsilon_d}{\epsilon_m}. \quad (1.31)$$

After putting the values of k_z^d and k_z^m into Eq 1.31, the dispersion relation for propagating waves at the interface can be written as,

$$\beta = k_x = k_0 \sqrt{\frac{\epsilon_d \epsilon_m}{\epsilon_d + \epsilon_m}}. \quad (1.32)$$

From Eq. 1.31, it is clear that the real parts of ϵ_d and ϵ_m must have opposite signs because k_z^d and k_z^m have opposite signs, and hence $\epsilon_m + \epsilon_d < 0$, and this has to be satisfied for the existence of surface plasmons on the metal-dielectric interface. The SPP dispersion plots at air/gold and glass/gold interfaces are shown in Fig. 1.2. On

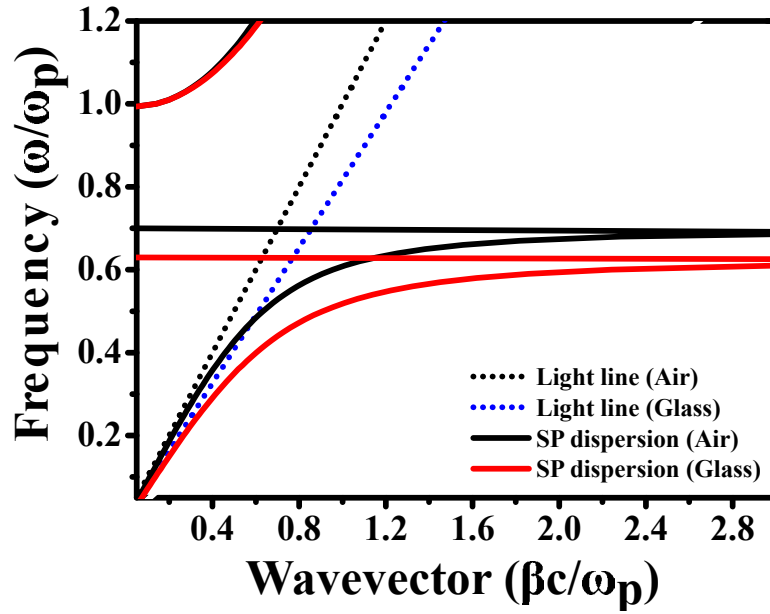


Figure 1.2: Dispersion relation of SPPs propagating at the metal/glass and metal/air interfaces, and the dispersion relation of light in air and glass.

the metal/dielectric or metal/air interface, the transverse confinement of SPPs field is determined by $e^{-|k_z^i||z|}$ for $i = (m, d)$. The decay lengths of the SPPs field in the direction normal to the surface are;

$$|z_m| = 1/|k_z^m| = \frac{c}{\omega} \sqrt{\frac{\epsilon_d + \epsilon_{mr}}{\epsilon_{mr}^2}}, \quad (1.33)$$

and

$$|z_d| = 1/|k_z^d| = \frac{c}{\omega} \sqrt{\frac{\epsilon_d + \epsilon_{mr}}{\epsilon_d^2}}. \quad (1.34)$$

The amplitude of the propagating surface plasmon decreases as $e^{-2\text{Im}(\beta)x}$, and the surface plasmon propagation length along the interface is given as [2]

$$L_{SPP} = \frac{1}{2\text{Im}(\beta)} = \frac{c}{\omega} \left(\frac{\epsilon_d + \epsilon_{mr}}{\epsilon_d \epsilon_{mr}} \right)^{3/2} \frac{(\epsilon_{mr})^2}{\epsilon_{mi}}. \quad (1.35)$$

The propagation length L_{SPP} of surface plasmons is typically between 10 μm and 100 μm at visible frequencies.

Similarly, for the TE polarized light, the field equations in two media are solved by imposing the conditions of continuity of the tangential magnetic field (H_x) and the electric field (E_y) at the interface $z = 0$, which leads to the requirement of $A_d = A_m$ and

$$A_d(k_z^d + k_z^m) = 0. \quad (1.36)$$

Since confinement of the field to the surface requires $\text{Re}(k_z^d) > 0$ and $\text{Re}(k_z^m) > 0$, this condition is only satisfied if $A_d = 0$. Hence the above equation implies that $A_d = A_m = 0$, from which we conclude that no surface plasmons modes exist for the TE polarization.

1.2.2 Excitation of surface plasmon polaritons

The dispersion relation of surface plasmon polaritons at smooth metal/dielectric interfaces has been discussed in the previous Subsection 1.2.1. From the dispersion plot of the SPP at the smooth metal/dielectric interface (see Fig. 1.2), it is clear that for a given frequency the momentum of incident light is less than that of the SPP wave at the interface. For excitation of the SPPs at the interface, the momentum of the incident light must be equal to the momentum of SPP. The black straight dotted line shows the light line in the air, whereas the red straight dotted line shows the light line in the glass. The corresponding SPP curve at the metal/air and metal/glass interfaces are shown by the solid black and red line, respectively. The difference between the

momentum (Δk) of the SPP and that of light for a particular frequency is given by $K_{SP} - K_{light}$. To couple the incident light to the SPP, there is a need to increase the momentum of the incident light using a suitable coupler. There are various kinds of coupler configurations such as prism coupler, grating coupler, fibre and wave-guide coupler that have been adopted to provide the necessary extra momentum to the incident light [1,2]. It has been shown that the coupling of incident light with the SPP can be achieved by either photon tunnelling in the total internal reflection geometry or diffraction effect. In this thesis, momentum transfer via diffraction grating has been used to couple the incident light to SPPs.

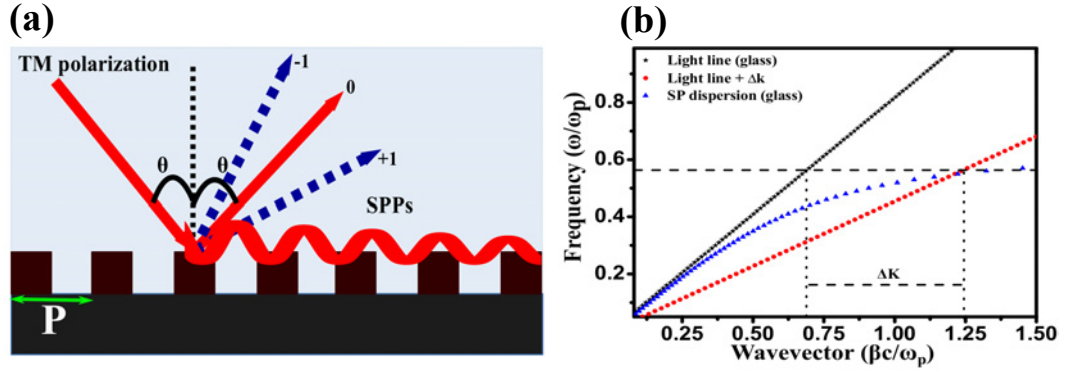


Figure 1.3: (a) Schematic diagram representation showing the excitation SPPs by a grating which provides the required momentum to the incidence light to fulfil the wave matching condition, (b) Graphical representation describes the requirement of extra momentum for excitation of SPPs.

The schematic presentation of a grating coupler is shown in Fig. 1.3(a), in which a one dimensional metallic grating of periodicity (P) and dielectric permittivity ϵ_m is used to couple the incident light to SPPs. When an EM wave with wavevector k_0 and frequency (ω) is incident on the surface of the grating, the wave gets diffracted into various orders along with the specularly reflected light. The diffracted wave from the grating provides an extra momentum to the incident wave Δk , and satisfies the momentum matching condition. The momentum matching condition for SPs can be expressed as

$$k_{spp} = k_{in} + \Delta k, \quad (1.37)$$

where k_{spp} is the wavevector of SPP given by $\omega/c\sqrt{\epsilon_d\epsilon_m/(\epsilon_d + \epsilon_m)}$, k_{in} is the x component of the wavevector of the incident light given by $k_{in} = k_0 \sin \theta$, and Δk is the change in the diffracted wavevector, which is $\pm m2\pi/P$ for a one-dimensional grating, where m is a positive integer and represents the different diffraction orders. There is an increment in the wavelength of SPP with a decreasing angle of incidence of light for coupling to negative diffraction orders and vice versa for coupling to positive diffraction orders.

1.2.3 Estimation of the SPP resonance wavelength

For a one-dimensional grating, the momentum matching condition for the TM polarized light (when an electric field is perpendicular to the grating lines) at oblique incident can be expressed as

$$\vec{k}_{spp} = k_0 \sin \theta_{in} \hat{e} \pm m \frac{2\pi}{P} \hat{e}. \quad (1.38)$$

In the case of two-dimensional structures, the momentum matching condition for the TM polarization at oblique angle incident can be expressed as

$$\vec{k}_{spp} = k_{in} \hat{e} \pm m \frac{2\pi}{P} \hat{e}_1 \pm n \frac{2\pi}{P} \hat{e}_2, \quad (1.39)$$

where $k_{in} = k_0 n_s \sin \theta_{in} \cos \phi \hat{x} + k_0 n_s \sin \theta_{in} \sin \phi \hat{y}$, in which $k_0, \theta_{in}, \phi, n_s$ are the incident wavevector in air, angle of incidence and azimuthal angle, refractive index of the surrounding medium, respectively. The unit vectors \hat{e}_1 and \hat{e}_2 are along the lattice vectors, and the unit vector \hat{e} along the incident wavevector that lies in the plane of incidence. P is the periodicity of the unit cell (assumed to be the same in both the x - and y -directions), and m and n are positive integers corresponding to the different diffraction orders along the \hat{e}_1 and \hat{e}_2 directions.

By considering the momentum matching condition for different structures the SPP resonance wavelength at the different interface can be calculated. Using Eq. 1.32,

the momentum matching condition can be written as;

$$|\vec{k}_{spp}| = |k_{in}\hat{e} \pm m\frac{2\pi}{P}\hat{e}_1 \pm n\frac{2\pi}{P}\hat{e}_2| = k_0\sqrt{\frac{\epsilon_d\epsilon_m}{\epsilon_d + \epsilon_m}}, \quad (1.40)$$

where ϵ_m , ϵ_d are permittivity of the metal and dielectric material, respectively. The SPP resonance wavelength of two-dimensional structured film at oblique incidence, and for square and triangular lattice arrays are given by Eqs. 1.41 and Eqn 1.42:

$$\lambda_{square} = \frac{P}{\sqrt{m^2 + n^2}} Re\left\{ \sqrt{\frac{\epsilon_m\epsilon_d}{\epsilon_m + \epsilon_d}} - \sqrt{\epsilon_d}\sin\theta \right\}, \quad (1.41)$$

and

$$\lambda_{triangular} = \frac{P}{\sqrt{\frac{4}{3}(m^2 + mn + n^2)}} Re\left\{ \sqrt{\frac{\epsilon_m\epsilon_d}{\epsilon_m + \epsilon_d}} - \sqrt{\epsilon_d}\sin\theta \right\}. \quad (1.42)$$

1.2.4 Localized surface plasmons

SPPs are propagating excitation of conduction electrons at the metal-dielectric interface whereas localized surface plasmons (LSPs) are non-propagating excitation of the conduction electrons localized in metallic nano/micro-structures of a size comparable to or smaller than the wavelength of light used to excite the plasmons. If frequency of the incident radiation matches with the frequency of the charges oscillation in the nano/micro-structures, then there is a huge enhancement in the scattering amplitude due to the resonance condition, and this is known as localized surface plasmon resonance (LSPR). There is requirement of special phase matching techniques for excitation of the propagating surface plasmon resonance whereas the LSPR can be excited by illuminating light directly on the metallic nano/micro-structures or particles. The LSPR frequency can be tuned by the changing the geometry of nano/micro-structures or particles as well as the local surrounding medium around the nano/micro-structures or particles, and it is primarily controlled through the free electron density of the nano/micro-

structures or particles material. The most common plasmonic metals, such as gold, silver and copper have free electron densities in the range of $10^{22} - 10^{23} \text{ cm}^{-3}$ with corresponding LSPR in the visible regime. The corresponding LSPR at low frequency regimes is known as localized spoof surface plasmon resonance. Due to the LSPR there is a huge amplification in fields both inside (usually small) and in the near-field zone outside the metallic nano/micro-structures or particles. Fig. 1.4 schematically shows the coherent oscillations in the free electrons of a metallic sphere induced by the oscillating electric field of the incident light. When the metallic sphere is illuminated by light with resonance wavelength, the induced oscillating electric dipoles increase scattering and absorption compared to the dielectric sphere of similar size. If the size of the metallic sphere is lesser than that of the wavelength of incident light absorption dominates whereas if the size of the sphere is greater than that of the wavelength of incident light scattering dominates. The conduction electrons of metallic sphere follow the direction of applied electric field and displaced opposite to it as shown in Fig. 1.4 schematically. The near field is localized near the surface in direction and opposite to applied electric field.

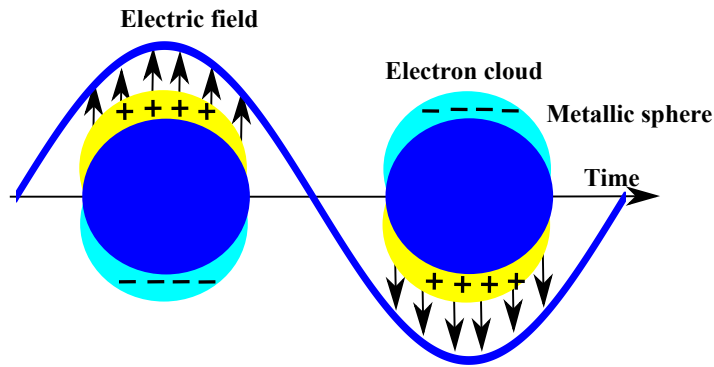


Figure 1.4: Schematic diagram of LSPR on a sub-wavelength sized metallic sphere. Coherent oscillations in the free electrons of the metallic sphere are induced by the oscillating electric field of the incident light.

Estimation of a universal resonance condition for the LSPR is difficult due to the direct dependence on the geometrical details. However, for symmetric objects like a

spherical cell, the resonance condition can be estimated in the quasi-static limit (size $\ll \lambda$), when the particle is much smaller than the wavelength of incident radiation in the surrounding medium. Assuming a uniform polarization of a spherical particle, the polarizability [26] is

$$\alpha = 4\pi a^3 \frac{\epsilon_m - \epsilon_d}{\epsilon_m + 2\epsilon_d}, \quad (1.43)$$

where a is the radius of the sphere, ϵ_m and ϵ_d are the permittivities of the metallic sphere and surrounding dielectric medium, respectively. Due to the LSPR, the non-propagating evanescent field amplitudes can be orders of magnitude greater than that of the incident illumination. At resonance, the polarizability experiences a resonant enhancement, and under that condition the $|\epsilon_m + 2\epsilon_d|$ is a minimum, and for the case of small $\text{Im}[\epsilon]$ around the resonance simplifies to

$$\text{Re}[\epsilon(\omega)] = -2\epsilon_d. \quad (1.44)$$

This relationship is called the Fröhlich condition [27]. The corresponding cross sections for scattering (C_{sc}), and absorption (C_{abs}) and can be calculated using the Poynting-vector formulation and can be expressed as [28]:

$$C_{sca} = \frac{k^4}{6\pi} |\alpha|^2 = \frac{8\pi}{3} k^4 a^6 \left[\frac{\epsilon_m - \epsilon_d}{\epsilon_m + 2\epsilon_d} \right]^2, \quad (1.45)$$

$$C_{abs} = k \text{Im}[\alpha] = 4\pi k a^3 \text{Im} \left[\frac{\epsilon_m - \epsilon_d}{\epsilon_m + 2\epsilon_d} \right]. \quad (1.46)$$

For small particles with $a \ll \lambda$, there is an efficient absorption due to the scaling with a^3 compared to the scattering that is scaling with a^6 . The more general expression of extinction cross section ($C_{ext} = C_{abs} + C_{sca}$) for the metallic sphere of volume V in the quasi-static limit of dielectric permittivity $\epsilon_m = \epsilon_{mr} + i\epsilon_{mi}$ is expressed as

$$C_{ext} = 9 \frac{\omega}{c} \epsilon_m^{3/2} V \frac{\epsilon_{mi}}{[\epsilon_{mr} + 2\epsilon_d]^2 + \epsilon_{mi}^2}. \quad (1.47)$$

LSPR has potential applications in many fields such as photovoltaics, bio-imaging and photo-thermal therapy, bio-sensing, etc, due to its dependency on the shape, size and materials of the sub-wavelength sized nano/micro-structures or particles as well as on their surrounding medium.

1.2.5 Spoof surface plasmon polaritons

The concept of spoof surface plasmon polaritons (SSPPs) was first introduced by Sir John Pendry in the year 2004 [29]. As the name suggests, spoof surface plasmon polaritons, also known as the designer surface plasmon polaritons are the electromagnetic waves propagating at the metal/dielectric interface, and up to a certain extent mimic the behaviour of SPPs which exist at the UV-visible-NIR frequencies. Metals in these frequencies band behave as plasmas with negative permittivity below the plasma frequency, but with further reduced frequencies at far-infrared, terahertz, and microwave regimes, they start behaving like a perfect electric conductor (PEC) with zero skin depth. As we have seen in Fig. 1.1 of the previous Section 1.2, a finite penetration of the surface waves into the metals is necessary for the existence of the SPPs. Thus, no SPPs exist at lower far-infrared, terahertz, and microwave frequencies. In the year 2004, Pendry et al. [29] theoretically showed the existence of SPPs-like mode, the so-called SSPPs by structuring periodic sub-wavelength holes array in a metallic surface at lower frequencies. Fig. 1.5(a) shows the schematic of the perforated metal film with a square sub-wavelength hole array of side a and periodicity d . In this treatment, it was assumed that the fundamental mode which decays least in the holes plays a dominant role among the several wave-guide modes. Since, $a < d \ll \lambda_0$ where λ_0 is the wavelength of incident radiation in free space, the incident waves are insensitive to the details of the surface and the perforated surface is regarded to have an effective response. By equating the instantaneous energy flow inside and outside of the surface, the dispersion relation of the SSPPs is given as [29]

$$k_{||} = \frac{1}{c} \sqrt{\omega^2 + \frac{1}{\omega_p^2 - \omega^2} \frac{64a^4\omega^2}{\pi^4 d^4}}, \quad (1.48)$$

where $k_{||}$ is the wavevector of the SSPPs along the interface, ω is the frequency of incident radiation. The plasma frequency $\omega_p = \frac{\pi c}{a\sqrt{\epsilon_h\mu_h}}$ in which ϵ_h and μ_h are equivalent permittivity and permeability of the perforated metal sheet, respectively. Fig. 1.5(b) shows the dispersion plot for the SSPPs on a structured surface. It is quite similar to the dispersion plot of SPPs in the visible-NIR regime even though their origins are different.

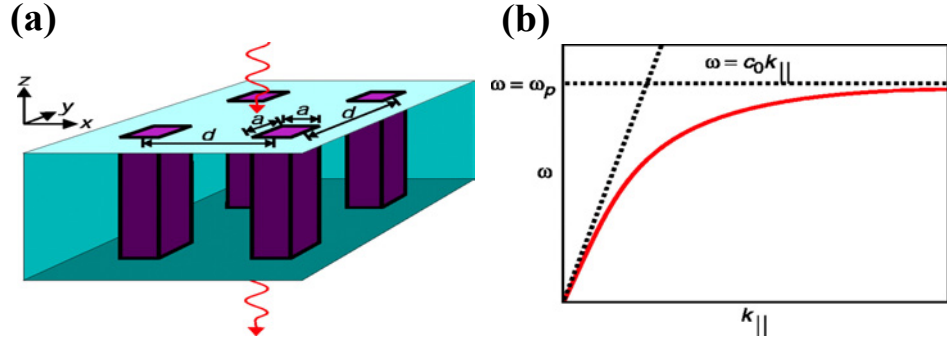


Figure 1.5: (a) Perforated metallic surface with a periodically square hole of sides a and periodicity d , which supports SSPPs, (b) Dispersion plot for the SSPPs on a structured surface. These figures are adopted from Ref. [29].

In the year 2005, this behaviour of SSPPs was experimentally verified by Hibbins et al. In the experiment, the cylindrical brass rods were carefully arranged on a flat brass plate and tightly clamped together like one-dimensional grating, and it was shown that the coupling of incident light to spoof surface plasmons for the TM polarization, and got the similar reflectance spectra as that of SPR in the visible-NIR frequencies regime. Besides sub-wavelength holes array in the metal film at visible-NIR frequencies, other periodic structures such as grating-like structures with blocks or grooves in which bound states of electromagnetic fields can exist are also able to support SSPPs [30].

A schematic depiction of the electric fields associated with a surface mode in perfect PEC surface is shown in Fig. 1.6(a), whereas in the absence of holes the field cannot penetrate into the metal and the light grazes the surface. But the inclusion of

sub-wavelength holes allows the fields to evanescently decay into the PEC surface, couples the wave to the surface resulting in the formation of bound SPP-like waves. The sub-wavelength hole arrays allow the electric field of surface waves to penetrate into the metal surface and provide an effective surface like that of metal at visible-NIR frequencies which sustain the SPPs. SSPPs with sub-wavelength transverse confinement have been found both in periodic perforated plane metal surfaces [31] and in a varieties of structured wave-guide configurations [32]. The concept of localized spoof surface plasmons has been also reported, and it is similar to the localized surface plasmon in the visible regime [33–35].

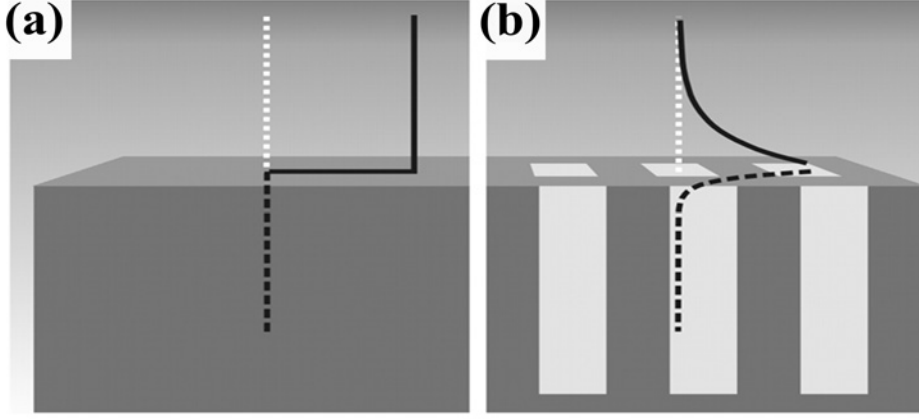


Figure 1.6: Illustration of the electric fields integrated with a surface mode in PEC surface. (a) In the absence of holes, the field cannot penetrate into the metal surfaces, and the light grazes the surface. (b) In the presence of sub-wavelength holes, the fields decay evanescently into the metal through holes, resulting in the formation of bound SPP-like waves, known as SSPPs. This figure is adopted from Ref. [30].

1.3 Fabry Pérot cavity

The Fabry Pérot cavity is an arrangement of two usually high reflecting mirrors (with small transmissivity) to cause light to be confined in a region of space [36]. The incoming light makes multiple round-trips inside the cavity and give rise to a series of partial reflections. The different outgoing partial waves interfere with each other give rise to an interference pattern. The transmission through such a cavity exhibits

sharp resonances as a function of wavelength, the angle of incidence, cavity length and refractive index n of the material in the cavity. The output field is the superposition of all the transmitted partial waves

$$E_t = E_1 t_1 t_2 \left[1 + r_1 r_2 e^{i\phi} + (r_1 r_2 e^{i\phi})^2 + \dots \right] = E_1 t_1 t_2 \frac{1 - (r_1 r_2 e^{i\phi})^n}{1 - r_1 r_2 e^{i\phi}}. \quad (1.49)$$

The phase difference (ϕ) between each successive reflected partial wave is given by

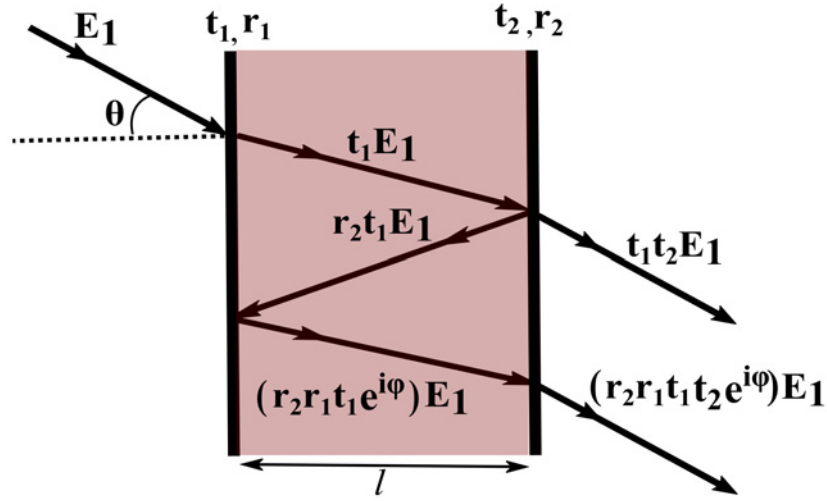


Figure 1.7: Schematic diagram of a Fabry-Perot cavity.

$$\phi = \left(\frac{2\pi}{\lambda} \right) 2nl \cos \theta. \quad (1.50)$$

The transmittance through the Fabry P rot interferometer is $T_{cavity} = |E_t|^2 / |E_0|^2$:

$$T_{cavity} = \frac{t_1^2 t_2^2}{(1 - r_1 r_2 e^{i\phi})(1 - r_1 r_2 e^{-i\phi})}. \quad (1.51)$$

After using $\cos 2\theta = 1 - 2\sin^2 \theta$, and $R_i = r_i^2 = 1 - t_i^2 = 1 - T_i$, R_1 and R_2 are the reflectance of first and second mirrors, and for identical mirrors $R_1 = R_2$ we can write

$$T_{cavity} = \frac{(1 - R)^2}{1 + R^2 - 2R^2 \cos \phi} = \frac{1}{1 + Q_R \sin^2(\phi/2)}, \quad (1.52)$$

where $Q_R = 4R/(1 - R)^2$ is defined as the quality factor of the cavity. Maximum transmission ($T_{cavity} = 1$) occurs when the optical path length difference ($2nl\cos\theta$) between each transmitted beam is an integral multiple of the wavelength. In the absence of absorption, reflectance from the cavity is the complement of the transmittance through the cavity, such that $T_{cavity} + R_{cavity} = 1$, and hence the reflectance from the cavity can be expressed as

$$R_{cavity} = 1 - \frac{1}{1 + Q_R \sin^2(\phi/2)}. \quad (1.53)$$

1.4 Guided mode resonance

Guided mode resonance or waveguide mode resonance (GMR) is an optical phenomenon where the guided modes of an optical waveguide are excited via the diffracted mode of a periodic grating [37, 38]. It is a combined effect of the diffraction and waveguiding, when a diffraction grating and slab waveguide are brought into proximity and the angle of a diffracted mode matches the angle of a guided mode. Such guided modes are also called “leaky modes” [39]. Fig. 1.8 shows the schematic diagram of a wave coupling into the guided mode, in which the diffracted wave by grating couples into the guiding mode in the guiding medium. GMR has been used in various applications such as narrow band/pass tunable filters, EO modulators, and switches, wavelength division multiplexing, chemical and environmental sensors, MEMS-tunable display pixels and filters, leaky-mode nanoplasmonics and omnidirectional absorbers and reflectors [39–43].

We know that from the grating equation

$$n_2 \sin[\theta(m)] = n_1 \sin\theta_{inc} - m \frac{\lambda_0}{\Lambda} \sin\phi, \quad (1.54)$$

where $\lambda_0, \Lambda, \theta_{inc}, n_1, n_2, m, \theta(m), \phi$ are the wavelength of the incident light in vacuum, grating period, the angle of incidence, refractive index of the surrounding medium, pos-

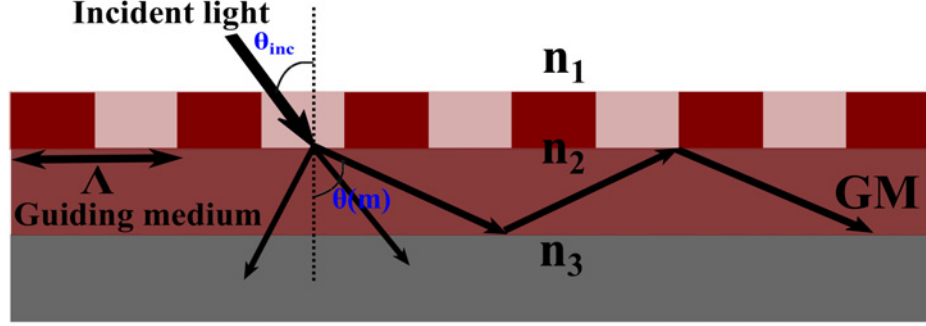


Figure 1.8: Schematic diagram illustrating the guided mode inside the guiding medium, where n_1 is the refractive index of the first medium, n_2 is the effective refractive index of the grating and guiding medium, and n_3 is the refractive index of the substrate.

itive integer representing the diffraction order, the effective refractive index of guiding medium, angle of diffraction of the m th mode and azimuthal angle, respectively.

The corresponding wavevector of the guided wave can be written as

$$\beta_m = k_0 n_{eff} = k_0 n_2 \sin[\theta(m)], \quad (1.55)$$

where β_m, k_0, n_{eff} are propagating wavevector inside the waveguide layer, the wavevector of the incident light, effective refractive index inside the guiding layer faced by guided mode wave, respectively.

Hence, the effective refractive index can be expressed as

$$n_{eff} = n_1 \sin \theta_{inc} - m \frac{\lambda_0}{\Lambda} \sin \phi. \quad (1.56)$$

The waveguiding can only occur if the effective refractive index of the guided mode is greater than that of the surrounding media and less than that of the core itself [44].

So, the conditions for n_{eff} to allow a guided mode

$$\max[n_1, n_3] \leq n_{eff} \leq n_2. \quad (1.57)$$

The regions of resonance for guided mode resonance can be obtained by combining Eqs 1.56 and 1.57.

$$\max[n_1, n_3] \leq n_1 \sin \theta_{inc} - m \frac{\lambda_0}{\Lambda} \sin \phi \leq n_2. \quad (1.58)$$

When such a structure is illuminated with incident light, a part of the light is directly transmitted and a part is diffracted and subsequently trapped in the waveguide layer. Some of the trapped light is re-diffracted outwards and interferes destructively/constructively with the transmitted part of the light beam.

1.5 Wood's anomaly

In the year 1902, Wood observed a set of bright and dark bands in the reflection spectrum of a diffraction grating, and the nature of these bands was unaccounted by the existing theory. As these could not be explained by the grating theory, they were termed Wood's anomalies. These were only observed in the case of TM polarization, and for particular sets of incident angles and wavelengths. In the year 1907, Rayleigh proposed a theoretical treatment of the Wood's anomalies and it was based upon an expansion of the diffracted field in terms of outgoing plane waves, and allowed coupling between the diffracted orders by means of surface boundary conditions. However, due to the oversimplification of the grating grooves as shallow compared to the wavelength of incident light, the theoretical model was not able to explain the Wood's anomalies exactly. Many years later, Fano explained the Wood's anomalies as the interaction of surface waves with the incident light. He assumed that a diffracted wave at grazing angles travels along the grating surface, and if the wave travels to the adjacent grooves in phase with the incident light, a resonance condition develops and results in the anomalous behaviour of the diffracted waves. This condition is mathematically defined

as

$$\frac{P \sin \theta_0}{\lambda} \mp \frac{P}{\lambda_p} = m, \quad (1.59)$$

where λ, λ_p are the wavelength of the incident wave and the diffracted wave propagating along the grating surface, respectively. P, θ_0 and m are the periodicity of the grating, the angle of incidence and positive integers representing different diffraction orders, respectively. The existence of the surface plasmons was postulated by Ritchie in 1957, and the behaviour of the surface plasmons was quite matching with the diffracted wave propagating along the grating surface as predicted by Fano. The coupling of the incident light to surface plasmons wave takes place only for the TM polarization and only when the surface is rough. Since the grating surface can be considered as periodic roughness, coupling of the incident TM light occurs when the tangential component of the incident wavevector k_0 plus the wavevector associated with the grating k_g matches the wavevector of the surface plasmons. Hence, Eq. 1.59 is nothing but the coupling condition of the incident light to surface plasmons on a one-dimensional grating.

The wavelengths corresponding to the Wood's anomalies modes for two dimensional grating structures with a square lattice array can be calculated as

$$\lambda_{WA} = \frac{P}{\sqrt{m^2 + n^2}} \sqrt{\epsilon_d}. \quad (1.60)$$

It was observed that the Wood's anomaly appears in the perfect conductor as well as in real metals with finite conductivity. This means WAs are purely geometry and surrounding medium dependent phenomena, whereas SPPs strongly depend upon the dielectric permittivity of the metal as well as on the dielectric permittivity of the surrounding medium.

1.6 Fano resonance

Fano resonance (FR) a resonance with a distinctly asymmetric shape, was experimentally observed by Beutler in 1935 in the absorption profile of noble gases [45]. It was theoretically described in quantum auto-ionizing states of atoms in 1961 by Ugo Fano [46], and hence known as Fano resonance. It was understood on the basis of the overlapping of a discrete state with a continuum of states, where destructive and constructive interferences take place at close energy positions and result in the asymmetric profile [46]. Initially, this phenomenon was studied for quantum systems. The interference effect in a classical system of coupled oscillators also shows asymmetric line profile, and has been extensively used in mechanical systems [47, 48]. Recently, Fano resonance has been successfully applied to explain a large number of phenomena such as the energy-dependent line profile of absorption in molecular systems [49], strong coupling between Mie and Bragg scattering in photonic crystals [50], asymmetric response of terahertz metamaterials [51–55], bilayer graphene nanostructures in different systems [56].

Now, the field of plasmonics has become one of the most active platforms for the applications of Fano resonance due to its application to generate coherent effects such as SPPs. In plasmonic systems, the relevant interaction parameters can be tuned by changing the geometry and composition of nanostructures, which enables the generation of FRs with sharp dispersion. In these systems, the FRs occur due to the interference of the bright mode (super-radiant) and sharp dark mode (sub-radiant) resonances, which depends on the designs and geometry of the systems. Detailed descriptions of the Fano resonance and its influence in many plasmonic micro/nano-structures can be found in recent reviews [51, 57].

Fano used a perturbation approach to explain the asymmetric resonance observed in the noble gases. He considered the coupling between discrete bound states, which

is degenerate in energy with a continuum of states. He obtained the formula for the shape of the asymmetric resonance profile of the scattering cross section as

$$\sigma = \frac{(\epsilon + q)^2}{\epsilon^2 + 1}, \quad (1.61)$$

where q is asymmetric shape parameter and ϵ is reduced energy defined by $2(E - E_F)/\Gamma$. E_F is resonant energy and Γ is the width of the asymmetric profile. This asymmetric Fano profile can be considered as the superposition of a Lorentzian line shape of discrete level with a flat continuum background. The Fano profile reduces to the symmetric Breit-Wigner or Lorentzian profile for either very large ($|q| \rightarrow \infty$) or very small ($|q| \rightarrow 0$) asymmetry parameter. The Eq. 1.61 can be written as a superposition of different states

$$\frac{(q^2 - 1)}{\epsilon^2 + 1} + \frac{2q\epsilon}{\epsilon^2 + 1} + 1 = \frac{(\epsilon + q)^2}{\epsilon^2 + 1}. \quad (1.62)$$

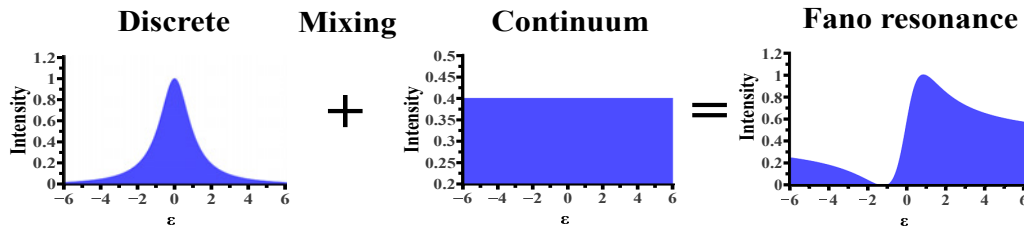


Figure 1.9: Demonstration of Fano formula as the superposition of the Lorentzian line shape of a discrete level with flat continuum background.

Fig. 1.9 shows the schematic demonstration of the Fano asymmetric line profile as a superposition of the discrete lever with a continuum background. The mathematical representation of the corresponding states is given in Eq 1.62. Here the plus sign represents the mixing of discrete and continuum states.

1.7 Extraordinary optical transmission

In 1944, Bethe in his seminal paper entitled *Theory of Diffraction by Small Holes*, investigated the transmittance of electromagnetic waves through a sub-wavelength hole in an infinitely thin perfectly conducting plate [58]. He found that, to a first approximation, the normalized-to-area transmittance through the sub-wavelength hole is

$$T \approx \frac{64}{27\pi^2} \left(\frac{r}{\lambda} \right)^4, \quad (1.63)$$

where λ and r are the wavelength of the incident light and radius of the hole, respectively. Hence, the transmittance of light through the sub-wavelength hole ($\lambda \ll r$) in a perfectly conducting film is negligibly small. The problem was solved for a single hole in a PEC sheet, the scale invariance property of Maxwell's equations makes it applicable to light in visible and near infrared frequencies range. But in 1998, Ebbesen et al. surprisingly discovered an unexpectedly large optical transmission through a silver film perforated periodically with array of sub-wavelength sized holes [59]. This can be treated as one of most important findings in the field of optics in the last two decades. This effect was termed the extraordinary transmission (EOT) of light. Since the discovery of this effect, it was realized that the spectral frequencies of the appeared resonances coincided with the corresponding surface plasmon resonance (SPR) of the structured surface [60]. This link between EOT and SPR was confirmed by subsequent theoretical and experimental works, and now it is widely accepted that the origin of the EOT lies in the excitation of those surface electromagnetic (EM) modes [61–63]. Direct experimental evidence of the role of SPP excitations has also been demonstrated [64,65]. EOT has been shown to have many potential applications such as in nano-photonic devices, chemical and biological sensors [66,67], sub-wavelength photolithography [68], near-field optics [69], etc. The first experimental zero-order transmission spectrum through a periodically perforated 200 nm thick silver film with 150 nm hole size and

0.9 μm lattice periodicity reported by Ebbesen et al. in 1998 is shown in Fig. 1.10. The spectrum shows a number of distinct features. At wavelength $\lambda = 326$ nm the narrow bulk silver plasmon peak is observed which disappears as the film becomes thicker. The others peaks can be explained by surface plasmon resonance wavelength using Eq. 1.41. Here, for the normal incident Eq. 1.41 can be written as

$$\lambda_{peak} = \frac{P}{\sqrt{m^2 + n^2}} \text{Re} \left\{ \sqrt{\frac{\epsilon_m \epsilon_d}{\epsilon_m + \epsilon_d}} \right\}, \quad (1.64)$$

where ϵ_m , ϵ_d are permittivity of the metal and dielectric material, respectively. P is the periodicity of the hole array (assumed to be the same in both the x-and y-directions), and m and n are positive integers corresponding to the different diffraction orders along array axes. The minima of the transmission spectrum corresponding to the Rayleigh-Wood's anomalies, and can be explained using Eq. 1.60.

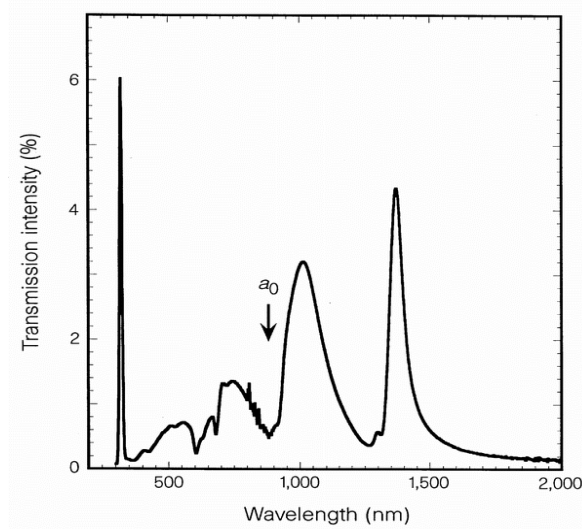


Figure 1.10: Zero-order transmission spectrum through an Ag film perforated with nano-hole arrays. This figure is adopted from Ref. [59].

The excitation of surface plasmons depends critically on the penetration of the electromagnetic fields into the metal and is typically limited to visible or near infrared frequencies. Metals behave almost as perfect conductors with almost zero skin depth at low frequencies (Mid IR to microwave) and a flat conducting surface does not support

surface plasmons [1, 70]. To understand the extraordinary transmission that occurs at lower frequencies (far infrared, terahertz or microwave), the concept of spoof surface plasmons was developed [29, 71]. Spoof surface plasmons are electromagnetic waves that are resonantly bound to periodically structured perfectly conducting surfaces. For example, electromagnetic waves can penetrate through the holes in conducting film perforated with periodic sub-wavelength sized holes and bind to the film through resonances excited in the holes and provide for surface waves that appear similar to surface plasmon excitation on metals. These structured conducting surfaces can support propagating as well as localized surface waves at lower frequencies even extending down to microwaves [30]. The concept of spoof surface plasmons polaritons and their experimental evidence of existence have already been discussed in Subsection 1.2.5.

To understand the origin of transmittance through sub-wavelength hole array, we did finite element based simulations. However, the details simulation methods are discussed in the next Chapter. Since we have worked at infrared frequencies regime, therefore the corresponding designs and simulations were done for the same spectral bands. Fig. 1.11 show the schematic diagram with simulated transmittance spectrum of a two-dimensional periodically perforated gold film with an array of a circular hole on the fused silica substrate. The square portion in the schematic diagram represents the unit cell of the hole array. The geometrical parameters used for simulations: as periodicity of the hole array, diameter of the hole and thickness of the gold film are $2\ \mu\text{m}$, $1\ \mu\text{m}$, and $40\ \text{nm}$, respectively. The data corresponding to the refractive indices of gold and fused silica are taken from Refs [19] and [22], respectively. Color maps corresponding to the square of normalized electric and magnetic field at resonance wavelength are shown in Fig. 1.11(c) and Fig. 1.11(d), respectively. Due to infrared regimes, all the transmission peaks and dips can be explained using the concepts of spoof surface plasmon resonance and Wood's anomalies resonances, respectively.

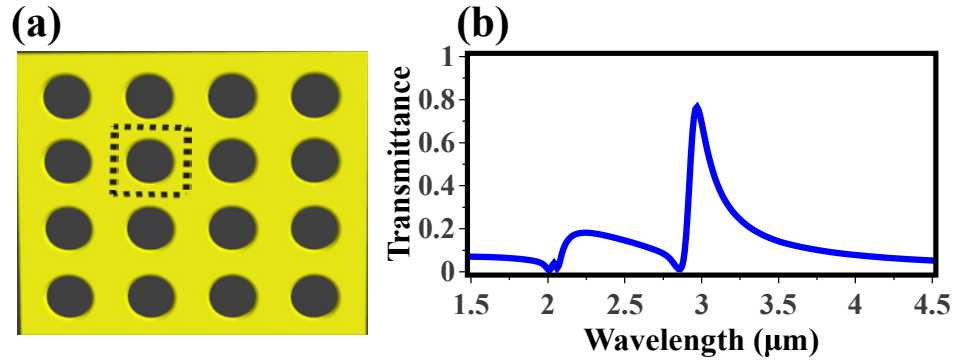


Figure 1.11: (a) Schematic diagram of a two-dimensional periodically perforated gold film with circular hole array. (b) The simulated transmittance spectrum corresponding to the circular hole array of $2\ \mu\text{m}$ periodicity and $1\ \mu\text{m}$ hole diameter in a thin gold film of thickness $40\ \text{nm}$ on fused silica glass. The dotted square portion in the schematic represents a unit cell of the hole array.

1.7.1 Optimization of geometrical parameters for enhanced transmittance

The transmittance through sub-wavelength hole array depends on a number of different geometrical parameters such as periodicity of the hole array, size of the hole, thickness of the metal film. So it is necessary to have an optimized set of geometrical parameters for maximum transmittance through the hole array. Keeping in the view of the optimum geometrical parameters, we did simulations with changing the different geometrical parameters and find out the optimum parameters for enhanced transmittance. In this paragraph, we will discuss the optimization details of the geometrical parameters. Due to the direct dependence of the transmission peak wavelength on periodicity, it is easier to find out the optimal periodicity to enhance the performance of devices at a specific wavelength. Hole sizes can be optimized using the transmission efficiency curve of the corresponding design.

Effect of periodicity

The numerically calculated transmittance spectra for different periodicities of the hole array is shown in Fig. 1.12. It is clear that with an increasing periodicity of the hole array, the peak resonances are shifting towards longer wavelengths. To check the effect of periodicity, the other parameters such as the thickness of the gold film, hole diameter and the refractive index of the substrate are kept constant. These results are consistent with the previously reported results in the different literatures [72, 73]. The linear dependency of the resonance wavelength on periodicities of the hole array can be understood from the surface plasmon resonance wavelength from Eq. 1.64.

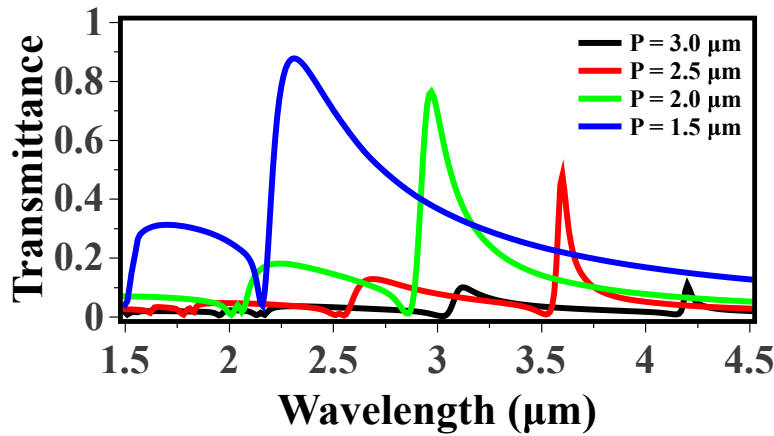


Figure 1.12: Simulated transmittance spectra for different periodicities of the hole array.

Effect of metal film thickness

The metal film thickness plays an important role in the coupling of incident light with SPPs, particularly at lower thickness. In the view of SPPs excitation, the metal film should be as thick as possible. However, the thicker metal means higher reflection as well as absorption losses and lower transmission, so there should be some trade-off for the metal thickness to get optimum transmittance. The numerically calculated transmittance spectra for different thickness of the gold film is shown in Fig. 1.13.

To check the effect of the thickness of the gold film, the other parameters such as; periodicity of the hole array, diameter of the hole and substrate refractive index are kept constant. It is clearly shown that with increasing the thickness of the metal film, transmittance values decrease, and it remains almost constant for the thickness 60 nm and 80 nm, and further started decreasing with decreasing the thickness of the gold film. This is because the thickness 60 nm is about twice of the SPP penetration depth (δ_m) into the gold layer as the penetration depth of SPP in the range of (1 - 6 μm) is 30 nm. These observations indicate that for better SPP enhancement, the thickness of the gold should not be less than $2\delta_m$.

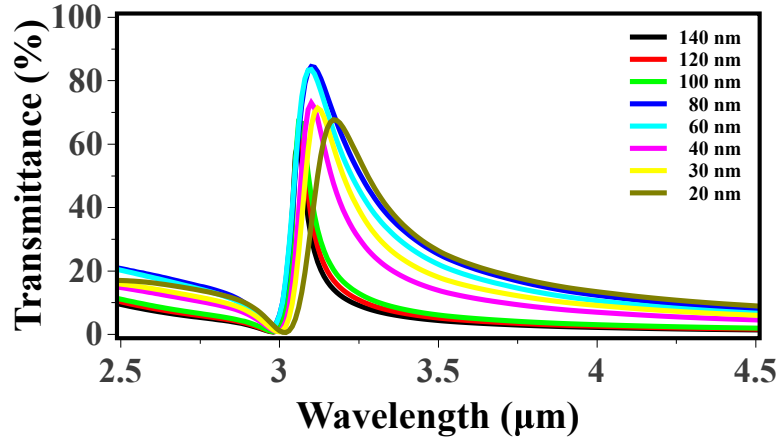


Figure 1.13: Simulated transmittance spectra for different thickness of the gold film.

There is redshift in the main peak of transmittance spectra with the decreasing the thickness of the metal film and it dominates for the lower thickness especially when it decreases from 60 to 20 nm. This phenomenon is also observed in previously reported works [74]. This phenomenon can be understood from Eq. 1.64, the resonance wavelength λ_{SPR} is directly proportional to $\sqrt{\epsilon_m \epsilon_d / (\epsilon_m + \epsilon_d)}$. In the real situation, metal is not like what we assumed as semi-infinite. Thus the dielectric permittivity of the metal (ϵ_m) is averaged by the dielectric permittivity of the background material (Air in this case), and implying that the metal film is less metallic. With decreasing the thickness of the metal layer, the averaging effect starts playing a more important role, and the averaged material that is combined material, which is less metallic compared to

the real metal. The real part of the combined permittivity is negative and hence it will be more for a thinner film after averaging. Therefore the peak wavelength λ_{SPR} shows a redshift when the metal film becomes thinner. The averaging effect of permittivity will have a considerable influence on the transmittance peak wavelength only when the metal film is thin enough.

Effect of hole size

Fig. 1.14 show the simulated transmittance spectra for different sizes of the hole. It is clearly shown that as long as the periodicity remains constant, the main peak transmission wavelength exhibits very small differences when the size of the hole increases from 0.6 to 1.2 μm . But the absolute transmittance varies a lot for different sizes of the hole. Larger hole results in the higher transmittance. This indicates that the size of hole array will not considerably affect the main peak transmission wavelength, but will have a major influence on the absolute transmission value. To find the optimum diameter of the hole size, a new term transmission efficiency. The geometrical parameters corresponding the maximum transmission efficiency corresponds to the optimum geometrical parameters.

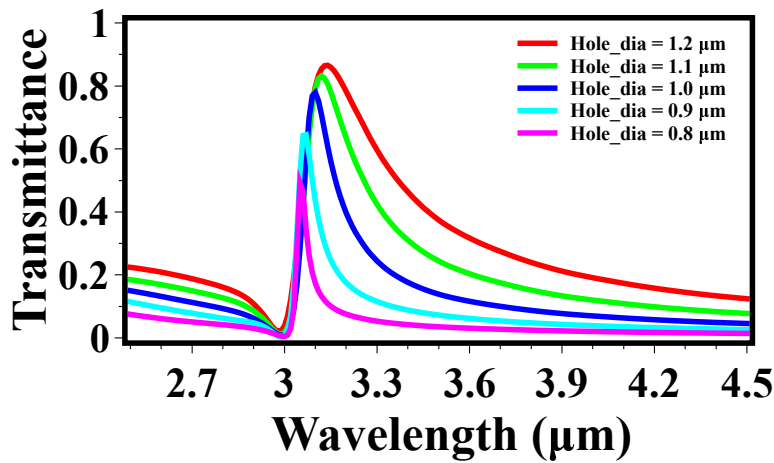


Figure 1.14: Simulated transmittance spectra for different diameters of the hole.

Transmission efficiency

To efficiently enhance the performance of a photodetector using EOT structures, the optimum values of different parameters like periodicity of the hole array, size of the hole and thickness of the metal film are extremely important. Since the transmittance peak wavelength directly depends on the periodicity of the hole array, an optimal periodicity can be easily found to enhance the performance of photodetector at a specific wavelength. It is easy to find out the optimal value of the film thickness keeping in mind of metallic losses and thickness requirements for the particular application. To determine the optimal value of the hole size for the best performance of a device, one needs to find the transmission efficiency through the hole array, which is defined as:

$$\eta = \frac{T}{F}, \quad (1.65)$$

where T is the normalized transmittance through the perforated film. F is the filling fraction defined as the ratio of areas of the hole to that of the unit cell of the perforated metal film. The transmission efficiency at the main peak wavelength versus the hole diameter of the sample is shown in Fig.1.15. It is clearly shown that when the hole side is around half of the periodicity, the highest transmission efficiency will be achieved. Thus the optimal transmitted light can facilitate more absorption of the light in the active material of detectors, and hence the quantum efficiency of the photodetector can be greatly enhanced by mounting the EOT structures on detectors active surfaces. Once, the parameters are optimized, the transmittance efficiency can be maximized. There are only a few studies on trying to further enhance the transmittance through the sub-wavelength hole arrays. We have proposed a new design in this thesis that can be used to enhance the transmittance through such sub wavelength hole array.

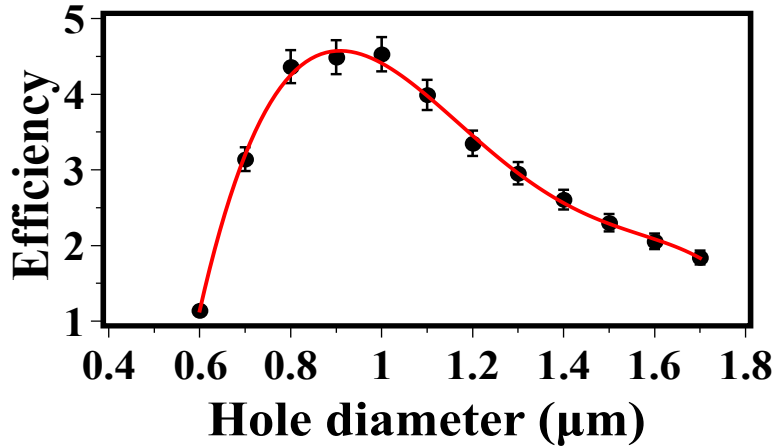


Figure 1.15: Transmission efficiency at the main peak wavelength versus hole diameter.

1.8 Metamaterial absorber

Metamaterials have been inspiring researchers across the globe due to their exotic properties such as complete absorption of electromagnetic waves [75–79], negative refraction [80], invisibility cloaking [81], and sub-diffraction limited imaging using super lenses [82], etc. Electromagnetic (EM) metamaterials are artificial nano/micro-structured composites of sub-wavelength metallic and dielectric elements and exhibit exotic EM responses those are not available in natural materials [13]. These composites usually consist of identical structured unit cells, arranged typically in a periodic fashion, and can be considered as bulk homogeneous media described as an effective medium through effective medium parameters [5]. The structures are designed to be resonant at specific frequencies so that the strong dispersion of the material parameters in the neighbourhood of the resonances can be utilized to obtain various exotic phenomena which are not found with the naturally occurring materials. In particular, metamaterial absorbers have attracted more interest of researchers due to their almost scale-invariant nature of responses.

Metamaterial absorbers can be realized using different physical mechanisms such as anti-reflection coating, resonant/impedance matching [77, 83–86], localized surface

plasmons resonance, Ohmic losses in the visible regime and lossy dielectric in the microwave regime, cavity resonance [87], guided mode resonance [88], etc. A typical metamaterial absorber has a tri-layer structure, with a structured top conducting layer separated by a continuous dielectric layer from a bottom conducting layer. The absorption depends on the electric resonance of the top layer and the impedance matching arises from the magnetic resonance created by current distributions on the top resonating structure and the bottom conducting layer (image charges and currents) which are anti-parallel. The thickness of the dielectric layer determines the capacitance for the LC resonance and the impedance matching for coupling maximum radiation into the resonant structure.

A perfect metamaterial absorber with nearly perfect absorption by simultaneous excitation of electric and magnetic resonances to realize the impedance match with the surrounding medium was first proposed by Landy et al. in 2008 [75]. After that, a lot of absorbers based on different physical mechanisms have been demonstrated theoretically and experimentally in a wide spectral range [77, 89–91]. Most of these metamaterial absorbers consist of a tri-layered structure of a sandwiched dielectric layer between metal films (structured and continuous). The main purpose of metamaterial absorber is to reduce undesired reflections and to increase absorption within the given spectral range. Spectrally selective perfect/highly intense absorbers have received considerable attention due to their importance for RADAR stealth at microwave and terahertz frequencies, development of sensitive infrared detectors, micro-bolometer arrays [14], controllable thermal emitters for manipulating the black body emittance [15] and thermophotovoltaic applications [92] at infrared frequencies, etc. Over the past few years, the metamaterial absorbers have been extensively researched for different frequencies.

1.8.1 Tri-layer metamaterial absorber

To understand the physical phenomena happening in the typical tri-layer metamaterial absorber, we did FEM based simulations. However, the details of the simulation methods are presented in the next Chapter but for convenience, the corresponding results of a tri-layer metamaterial absorber have been shown here. Fig. 1.16(a) shows a schematic diagram of a unit cell of the tri-layered metamaterial absorber, which consists of a gold circular disk separated from a continuous gold film by a thin ZnS layer. In the tri-layered metamaterial absorber, the top structured metallic layer along with bottom metallic layer provides electric response by coupling to the incident electric field at a certain resonance frequency. The generation of current in the bottom metal layer is anti-parallel to that of in the top metallic layer provides magnetic response. An incident time-varying magnetic field couples to the magnetic response generated by the anti-parallel currents flowing via top metallic layer to bottom metallic layer. The individual electric and magnetic response can be tailored by the tuning the design parameters such as the thickness of the dielectric layer and periodicity as well as the structural design of the top metallic layer. The impedance matching condition in the tri-layered metamaterial absorber can be understood from the Fresnel's equation for the layer media. As we know that from the Fresnel's equation, the reflectance from a magneto-dielectric medium at normal incidence can be written as

$$R(\omega) = \left| \frac{Z(\omega) - Z_0}{Z(\omega) + Z_0} \right|^2, \quad (1.66)$$

where $Z(\omega) = \sqrt{\mu(\omega)/\epsilon(\omega)}$ is the impedance of the magneto-dielectric material, and $Z_0 = \sqrt{\mu_0/\epsilon_0}$ is the impedance of the free space. Since in this configuration the metallic layer provides zero transmittance, the absorbance (A) can be easily calculated as $A(\omega) = 1 - R(\omega)$. For a particular design, the design parameters can be tuned in such a way that at a particular frequency their electric and magnetic responses enables

a condition in which effective impedance of the designed structured matches with that of the surrounding medium i.e. $Z(\omega) = Z_0$. This condition implies the complete absorption of the electromagnetic radiation. In the case of impedance matching the reflectance becomes zero, it can be understood for Eq. 1.66, and hence, absorbance is maximum.

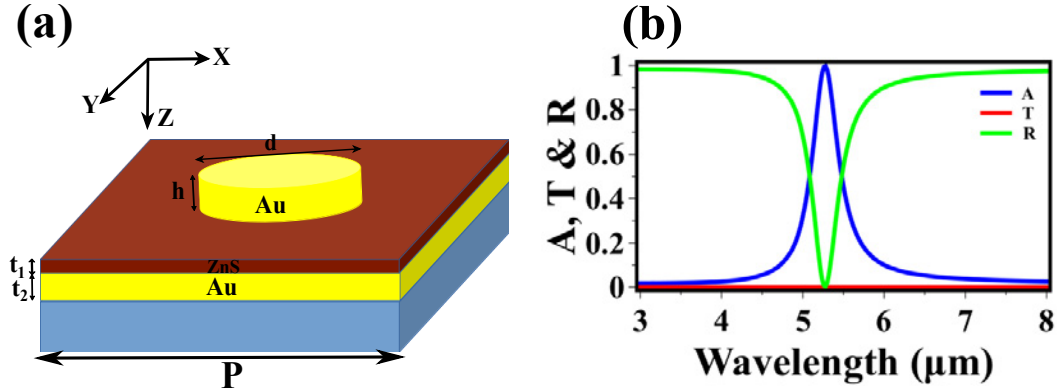


Figure 1.16: (a) Schematic diagram of a tri-layered (Au/ZnS/Au) metamaterial absorber, where t_1 , t_2 are the thickness of the ZnS, bottom gold layers, respectively; and h , d are the height and diameter of the top gold disk; and P is the periodicity of the unit cell. (b) The simulated absorbance, reflectance and transmittance spectra. The parameters used for simulation are $P = 2\mu\text{m}$, $d = 1\mu\text{m}$, $t_1 = 150\text{ nm}$, $t_2 = 60\text{ nm}$ and $t_3 = 100\text{ nm}$.

Fig. 1.16(b) shows the simulated electromagnetic response of the tri-layer metamaterial absorber. The geometrical parameters used for the simulation are $P = 2\mu\text{m}$, $d = 1\mu\text{m}$, $t_1 = 150\text{ nm}$, $t_2 = 60\text{ nm}$ and $t_3 = 100\text{ nm}$. The data corresponding to dispersive refractive indices of the gold and the ZnS are taken from Refs. [19] and [21], respectively. It is clear that there is a complete absorption of the electromagnetic waves at the resonant wavelength. The excitation of an electric dipole due to the disk in the ZnS layer is clearly shown in Fig. 1.17(a), whereas the extent of the localized electric field in the ZnS is clearly shown in Fig. 1.17(b). The localization of the magnetic field in the ZnS layer is shown in Fig. 1.17(c) which is caused by the oppositely oriented current sheets on the disk and the ground plane[Fig. 1.17(d)].

It is clear that the simultaneous excitation of the electric and magnetic resonances at a particular frequency is responsible for the complete absorption of the elec-

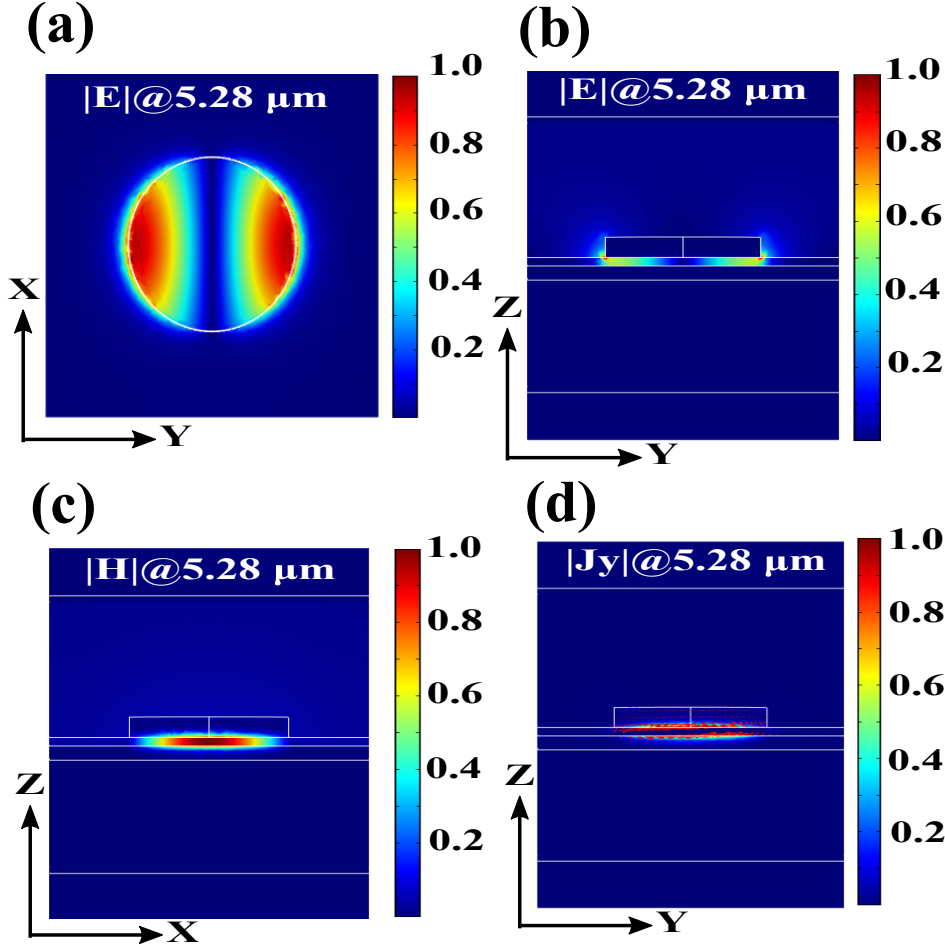


Figure 1.17: (a) Normalized electric field in the middle of the ZnS layer at resonance wavelength, (b) normalized electric field at resonance wavelength, (c) normalized magnetic field at resonance wavelength, (d) normalized current density as color map with its arrow volume plot at resonance wavelength.

tromagnetic waves. The resonance position can be shifted by tuning the geometrical parameters as well as the refractive index of the dielectric layer (in this case ZnS). The shift can be understood by noting the change in capacitance formed between the disk and the ground plane as well as between the two nearest disks at the resonance frequency, $\omega_0 = 1/\sqrt{LC}$ where L is inductance and C is the effective capacitance of the structure. In this thesis, metamaterial absorbers based on the cavity and localized surface plasmons have been designed and fabricated. Fano-like resonance is observed in the metamaterial absorber based on the cavity and guided mode resonance in this thesis.

Chapter 2

Fabrication, characterization and simulation methods

The photonics/optics communities have invested much efforts into micro/nano structuring techniques due to their critical requirements in various applications such as plasmonics [1, 2], photonic devices [3, 4], metamaterials [5, 6], biosensors [7, 8], solar cells [9, 10], photonic crystals [11, 12], etc. In turn, the fields of plasmonics and metamaterials have seen tremendous advancement due to the availability of such micro/nano structuring techniques [93]. There are several techniques such as electron beam lithography (EBL) [94], focused ion beam lithography (FIB) [95], photolithography [94] and many more, which are used for fabrication of micro/nano structures for metamaterials and plasmonics. In particular photolithography, including X-ray lithography [96], ultraviolet lithography [97], laser interference lithography [98], nano-sphere lithography [99, 100] and multi photon absorption based lithography [101] have been showing extreme capabilities of fabricating even very complex micro/nano-structures for different applications. However, many applications of the plasmonic and metamaterial devices are still lagging due to the non-availability of rapid and cost-effective fabrication tool over the large areas. Hence, techniques for the rapid fabrication of micro/nano structures over a large area need to be developed further. Laser interference lithogra-

phy [102] and soft lithography [103, 104] are two maskless and cost-effective techniques that can be used for fabrication of micro/nano structures over the large areas.

Laser interference lithography is a rapid and maskless photolithography technique, in which an interference pattern of laser light is recorded on the photosensitive materials. It can take very short times for exposure and developments depending on the laser and sensitivity of the photosensitive materials. In contrast to other techniques, laser interference lithography takes advantages of the periodic patterns generated by the superimposition of two or more coherent laser beams to define one-dimensional, two-dimensional, or even three-dimensional nano/micro structures. A variety of periodic patterns can be generated using the multi-beams interference lithography and can be used for fabrication of the different shapes micro/nano structures over a large area [98, 105, 106].

Only a few micro/nano fabrication techniques like conventional laser writing, FIB and EBL have seen a partial success in the fabrication of 3D micro/nano-structures. Micro-stereo lithography is an alternative technique for 3D micro fabrication, but has its limitations in terms of spatial resolution and writing speed. In contrast to this, multi-photon lithography has shown a great advantage over other techniques due to the localized nature of polymerization that is employed for the fabrication of highly complex 3D microstructures with a spatial resolution even smaller than 100 nm beyond the diffraction limit using tightly focused laser beams [107, 108].

Although photolithography is the dominant technique for large area and rapid fabrication, it is not always the best and/or the only option for all applications. It is an expensive technique, and poorly suited for patterning over non planar and flexible surfaces. It is directly applicable only to a limited set of photosensitive materials. Soft lithography techniques share a common feature of using a patterned elastomer as a stamp/mold which can be used to generate micro/nano structures over even non planar and flexible surfaces as the stamp is not rigid. It offers access to a broader range

of materials, as well as experimental simplicity and flexibility in forming different types of test patterns. Masters are typically fabricated by other lithographic processes like photolithography, EBL, FIB in order to define a stamp pattern. Stamps are generally made by curing of polydimethylsiloxane (PDMS) onto a master.

In this chapter, we present the details of fabrication techniques and characterization tools used for the work in this thesis. The details of interference lithography for the fabrication of different shapes nano/micro-structure are discussed in Section 2.1. This Section also contains the details of metal deposition and lift-off processes that were carried out for fabrication of plasmonic two-dimensional hole arrays. The details of the development of a home built two-photon absorption lithography system is discussed in Section 2.2. The methods of soft lithography; fabrication of the master, stamp and its implementations for fabrication of nano/micro structures are discussed in Section 2.3. The sample characterization methods are discussed in Section 2.4. The numerical simulations for electromagnetic calculations carried out using the COMSOL Multi-physics software based on finite element method are discussed in Section 2.5.

2.1 Laser interference lithography

Laser interference lithography (LIL) is a technique to produce periodic structures using interfering of two or more highly-coherent laser beams. Typically, a laser beam from a source is divided and recombined, forming a periodic intensity pattern that is recorded by the exposure of photosensitive material coated substrates. The photoresist patterns fabricated with LIL are a platform for further fabrication of nano/micro-structures and are building blocks for devices. LIL has two advantages over other lithography techniques: (1) it does not require a photo-mask, so patterns with various sizes and shapes can be easily fabricated by changing the configuration of the system, and (2) its resolution is limited only by the wavelength used. The disadvantage is that principally

periodic structures with well define symmetry can be only fabricated by this technique. On the basis of the arrangement of optical components, the LIL has been categorized in two types: (1) Lloyd's mirror interferometer based LIL system, which is used for fabrication of high resolution structures, and (2) multi beam interference based LIL system which is used for large area fabrication. In this thesis, two beam interference based LIL system has been used to fabricate micro-scale periodic structures.

2.1.1 Interference theory

In two beam interference based LIL system, two coherent and monochromatic collimated laser beams created by the equal splitting of a single highly coherent and monochromatic laser beam is used for fabrication of nano/micro structures. In order to realize the interference pattern created by the superposition of the two laser beams, we consider two plane polarized waves having wave vector \vec{k}_1 and \vec{k}_2 incident at angles θ_1 and θ_2 with respect to the normal at screen where the interference pattern is recorded, respectively. Fig. 2.1 shows a schematic diagram of the interference of two plane polarized electromagnetic (EM) waves.

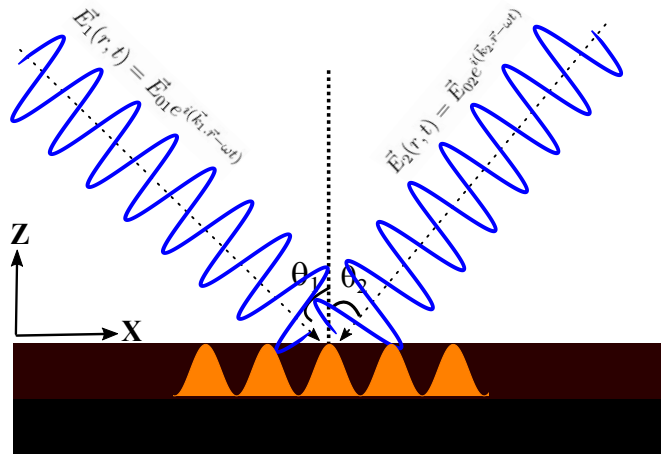


Figure 2.1: Schematic representation of interference of two monochromatic and coherent waves with a simultaneous illustration of the resultant intensity distribution.

The electric fields associated with corresponding EM waves can be written as;

$$\vec{E}_1(r, t) = E_{01} e^{i(\vec{k}_1 \cdot \vec{r} - \omega t)} \hat{e}, \quad (2.1) \quad \vec{E}_2(r, t) = E_{02} e^{i(\vec{k}_2 \cdot \vec{r} - \omega t)} \hat{e}, \quad (2.2)$$

where E_{01} and E_{02} are the electric field amplitudes, ω is the angular frequency, $\vec{k}_1 = \hat{x}k_{x1} + \hat{z}k_{z1}$ and $\vec{k}_2 = \hat{x}k_{x2} + \hat{z}k_{z2}$, are the corresponding wavevectors. \hat{e} is the unit vector along the polarization of the electric fields.

According to the principle of superposition, the resultant electric field will be the vector sum of the individual electric fields of the corresponding waves, and can be written as

$$\vec{E}_{total}(r, t) = \vec{E}_1(r, t) + \vec{E}_2(r, t) = (\vec{E}_{01} e^{i(\vec{k}_1 \cdot \vec{r})} + \vec{E}_{02} e^{i(\vec{k}_2 \cdot \vec{r})}) e^{-i\omega t} \hat{e}. \quad (2.3)$$

There is no physical detector that can measure the electric field of the EM wave directly, and all the photodetectors are “square-law” detectors. Therefore, the physical quantity that can be experimentally observed is the time-average intensity of light, i.e

$$I_{total} = \left\langle \vec{E}_{total} \cdot \vec{E}_{total}^* \right\rangle, \quad (2.4)$$

since,

$$I_1 = \left\langle |\vec{E}_1|^2 \right\rangle, \quad I_2 = \left\langle |\vec{E}_2|^2 \right\rangle, \quad \left\langle \vec{E}_1 \cdot \vec{E}_2^* \right\rangle = \left\langle \vec{E}_{01} \cdot \vec{E}_{02}^* \right\rangle e^{i[(\vec{k}_1 - \vec{k}_2) \cdot \vec{r}]} \text{ and} \\ \left\langle \vec{E}_2 \cdot \vec{E}_1^* \right\rangle = \left\langle \vec{E}_{02} \cdot \vec{E}_{01}^* \right\rangle e^{-i[(\vec{k}_1 - \vec{k}_2) \cdot \vec{r}]}.$$

Therefore, the time average intensity can be expressed as

$$I_{total} = I_1 + I_2 + \sqrt{I_1 I_2} \cos \gamma, \quad (2.5)$$

where $\gamma = (\vec{k}_2 - \vec{k}_1) \cdot \vec{r}$ is the phase difference between the two beams at a particular place due to the angle between the two beams. Since we have assumed that both beams have equal intensity, i.e. $I_1 = I_2 = I_0$. So, the resultant intensity distribution at $z = 0$ can be expressed as

$$I_{total} = 4I_0 \cos^2\left(\frac{(k_{x2} - k_{x1})x}{2}\right), \quad (2.6)$$

where $k_{x2} = k \sin \theta_2$ and $k_{x1} = -k \sin \theta_1$.

Since the intensity profile of the two superposed beams is proportional to the square of a cosine function, and hence the maximum and minimum of intensity will be decided by the phase factor that is an integral multiple of π , which helps in the determination of the fringe position. The position of the n^{th} fringe from the centre can be expressed as $x_n = n\lambda/(\sin \theta_1 + \sin \theta_2)$, where n is positive integers. In the case of $\theta_1 = \theta_2 = \theta$, the distance between consecutive fringes i.e. the periodicity (P) of the fringes is $x_{n+1} - x_n = \lambda/2 \sin \theta$.

In the laser interference lithography process, the interference pattern is recorded in a photosensitive material (photoresist), typically coated on hard substrates. Hence the amount of energy delivered to the photoresist coated substrate in time t is given by $u = 4I_0 \cos^2\left(\frac{(k_{x2} - k_{x1})x}{2}\right)t$.

The two-dimensional interference patterns of different shapes can also be created and recorded on the photoresist coated substrate by either interfering of more than two beams at a time or with multiple exposures to the two laser beams. The multi-beam exposure at the same time requires more optical components to fabricate two-dimensional structures. More optical components increase the complexity as well as reduce the power of beams on the photoresist film which increases the exposure time. To avoid such complexity of the system, two beam LIL with multiple exposures process was used to fabricate high quality micro/nano structures for various applications. First, the photoresist coated substrate is exposed for time t_1 , and further for the time t_2 after rotation by an angle ϕ , which is shown schematically in Fig. 2.3. The amount of energy per unit area delivered to the photoresist film in this process for fabrication of

two-dimensional patterned structures is given by

$$U = 4I_0 \left\{ \cos^2 \left[\frac{(k_{x2} - k_{x1})x}{2} \right] t_1 + \cos^2 \left[\frac{(k_{x2} - k_{x1})(x \cos \phi + y \sin \phi)}{2} \right] t_2 \right\}. \quad (2.7)$$

Fig. 2.2 shows the simulated density profile of the resultant time average power corresponding to the interfering waves for different rotational angles. Fig. 2.2(a) corresponds to the single exposure or at $\phi = 0^\circ$ rotation angle, whereas Figs. 2.2(b) and (c) correspond to double exposures at rotation angles $\phi = 60^\circ$ and $\phi = 90^\circ$, respectively.

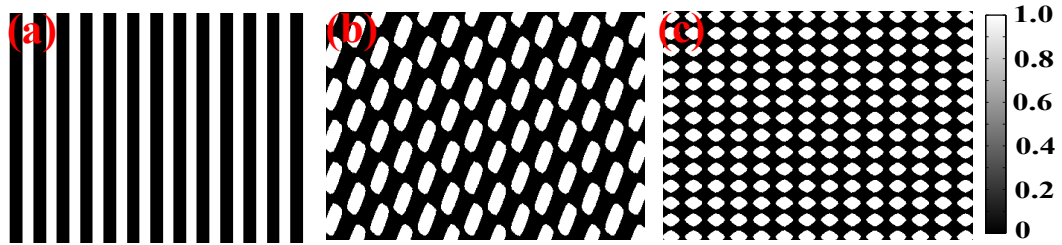


Figure 2.2: The energy density distribution patterns of the interference of two coherent beams in double exposure at different azimuthal angles of the sample holder (a) $\phi = 0^\circ$, (b) $\phi = 60^\circ$ and (c) $\phi = 90^\circ$.

2.1.2 Experimental set-up

Fig. 2.3 shows the experimental set-up of a two-beam LIL. It comprises of a He-Cd laser (Kimmon Koha, Japan) operating at a wavelength of 442 nm and having coherence length 10 cm, a spatial filter (consisting of a convex lens with 6 mm focal length and a pinhole with a diameter of $30 \mu\text{m}$), a 50:50 cube beam splitter, a couple of high reflecting mirrors, a convex lens and sample holder mounted on a rotating frame. The spatial filter is used to clean up the laser beam by removing high spatial-frequency noise from the laser beam. The convex lens in combination with the spatial filter lens is used to expand and collimate the beam for uniform exposure on the samples. The 50:50 cube beam splitter is used to split the single laser beam into two beams of equal

optical intensity. The mirrors are used to guide the laser beam up-to sample holder. A rotating frame attached with the sample holder which is mounted on a rail to adjust the angle between the interfering beams is used to rotate the sample azimuthally for fabrication of two-dimensional structures with different shapes. The laser power can be control using a variable neutral density filter to optimize the laser dose on the photoresist. Here a neutral density filter has been used in the path of laser beam behind the spatial filter. In the photograph, the red arrow line is drawn to illustrate the path of the laser beam. The acronyms used for different components in the system are given in the caption of the figure.

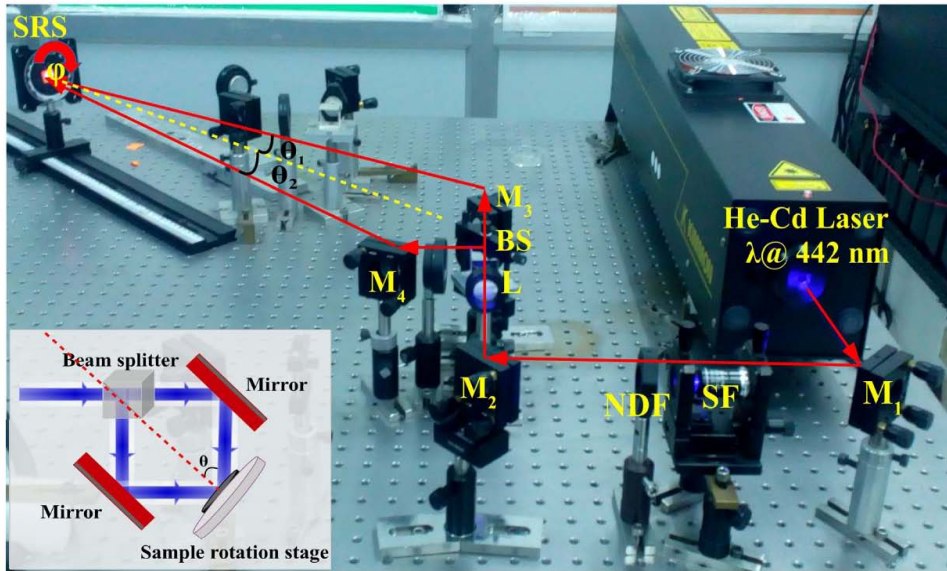


Figure 2.3: The photograph of the experimental set-up of two-beam laser interference lithography with a schematic diagram of the set-up in the inset, where the acronyms BS, L, M, SF, NDF stand for beam splitter, lens and mirror, spatial filter and neutral density filter, respectively.

2.1.3 Sample fabrication using laser interference lithography

Laser interference lithography system was used to fabricate the various patterns of the photoresist on different substrates. The quality of the fabricated samples depend on the various parameters such as the proper interference of the beams, exact location of

the sample in the overlapping region of the laser beams, exposure time, development time in developer.

The following steps are involved in the fabrication of the photoresist pattern:

1. The substrates were cleaned properly by following the standard cleaning procedures.
2. The positive photoresist (maP-1205, Micro-resist Technology, Germany) was spin coated on the clean substrates at 3000 revolution per minute (RPM) for 45 seconds. The thickness of the photoresist depends on the speed of the motor in spin coater and viscosity of the photoresist.
3. The coated samples were pre-baked at 80°C on a hot plate for 1 minute.
4. The pre-baked samples were exposed to the LIL system for 3 minutes. The exposure time may vary for different thickness of the photoresist. Single exposure results in one dimensional grating pattern whereas the double exposures at different rotational angle results in a two-dimensional pattern, and the type of pattern depends on the rotation angle. A square array of two-dimensional disks is patterned by double exposure at 0° and 90° rotation angles.
5. The exposed samples were developed in the developer (maD-331, Micro-resist Technology, Germany) and rinsed with DI water.
6. The washed samples were dried by flowing dry nitrogen gas over them.

The schematic diagram illustrating the fabrication steps of the photoresist patterns is shown in Fig. 2.4. The one dimensional grating pattern is fabricated in a single exposure and followed by development and drying, whereas the two-dimensional grating pattern is fabricated in two consecutive exposures at $\phi = 0^\circ$ and $\phi = 90^\circ$ rotation angles and followed by development and drying procedures. The AFM topographical

maps of the fabricated one dimensional grating and two- dimensional disk array in the photoresist are shown in Figs. 2.5(a) and (b), respectively.

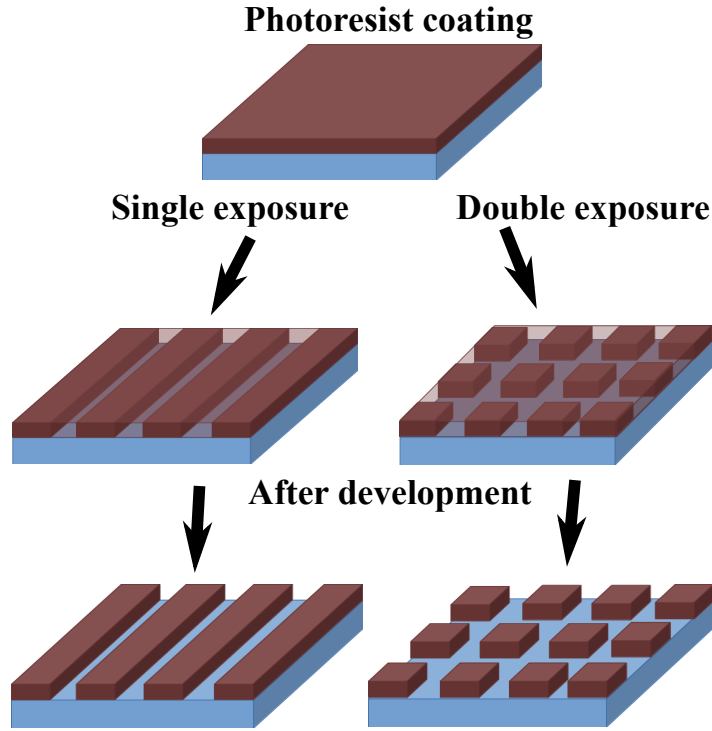


Figure 2.4: Schematic diagram of the step-wise fabrication process of the one and two dimensional photoresist pattern using LIL.

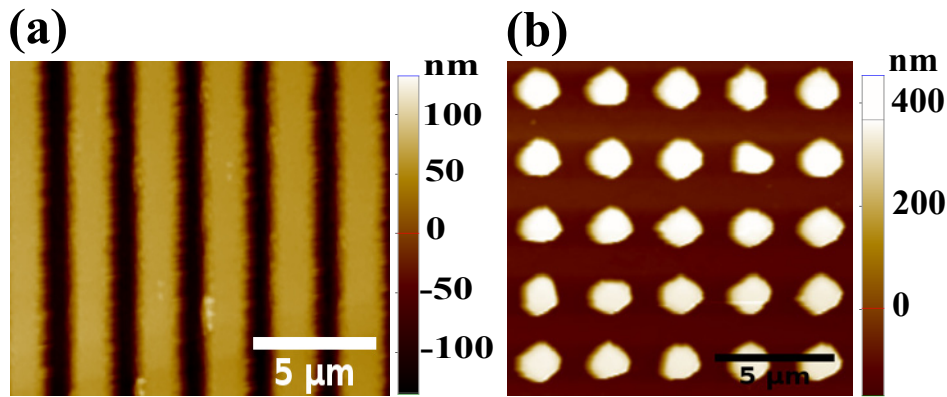


Figure 2.5: AFM topographical map of the fabricated (a) one-dimensional, (b) two-dimensional grating pattern in photoresist.

2.1.4 Metal and dielectric deposition

In this thesis, the thermal evaporation technique was used to deposit the metal/dielectric materials required for fabrication of plasmonic and metamaterial structures. The thermal evaporation technique involves heating of a solid material inside a high vacuum chamber to a temperature which produces some vapour pressure. Usually, resistive heating or an electron beam is used for heating. The material is heated until fusion by means of an electrical current passing through a filament or metal sheet where the target material is mounted in boat or crucible. The evaporated material condenses on the substrate as a thin film due to the low temperature at the substrate. The thickness of the deposited material is monitored by using quartz crystal which is mounted inside the vacuum chamber to receive deposited materials in real time. The crystal's oscillation frequency starts decreasing with increasing the mass of crystal as deposited on it, and the electronic instrument attached to the crystal reads the changes in frequency and convert those changes in frequency into the thickness data simultaneously that help in the determination of the accumulated thickness of the deposited material and also show the instantaneous rate of deposition. In our system, two pumps are being used to achieve the high vacuum, one is a rotary pump (RP) to obtain rough vacuum up to 10^{-3} mbar and the diffusion pump (DP) which is used to obtain the high vacuum up-to 10^{-6} mbar.

2.1.5 Lift-off process

A lift-off process is commonly used to pattern metal or dielectric films in the nano/micrometric structuring using a sacrificial material layer. In this process, the required pattern is fabricated using standard lithography in photoresist, the so-called sacrificial material, on a substrate. During deposition, the materials layer covers the total area of the substrates including the patterned and non-patterned. In the lift-off process, the

photoresist under the film is dissolved and washed away with a solvent, and leaving only the film which was deposited directly on the substrate. The photoresist can be removed using acetone or the appropriate resist removal solvent which enters through the gap between the metal/dielectric layer on the photoresist and the metal/dielectric layer on the substrate. Some resists do not completely dissolve in acetone or in usual organic solvents. So the special measures should be taken for those resists. Sometimes due to the thick metal/dielectric layer or conical shape of the fabricated structure in the resist, the gap between the metal/dielectric layers on top of photoresist and the substrate becomes very small and sometimes completely blocked, which does not allow the solvent to come in contact with the resist, so the thickness of the metal/dielectric layer, as well as the shape of the structures, are very important. The thickness of the metal/dielectric layer should be in accordance to the height of photoresist to avoid the complete blocking of the gap between the layer on the top of resist and the layer on substrates for proper lift-off.

There are some critical points regarding the proper lift-off.

- Thickness of the metal/dielectric layer: the thickness of metal/dielectric film must be lesser than $1/3$ of the height of the photoresist pillar/disk.
- The undercut profile: the photoresist structures with undercut profile are preferred for proper lift-off, which helps to retain the gap between the metal/dielectric layers deposited on the top of photoresist structures and on the substrate portions.
- Flatness of the top surface: the photoresist disk or pillar should have a flat top surface to sustain the metal/dielectric layer that helps in to retain the gap which allows to enter the solvent and come in contact with photoresist.

The step-wise fabrication of hole array using the lift-off process is shown in Fig. 2.6 where the substrate was spin-coated with photoresist and follow by lithographically

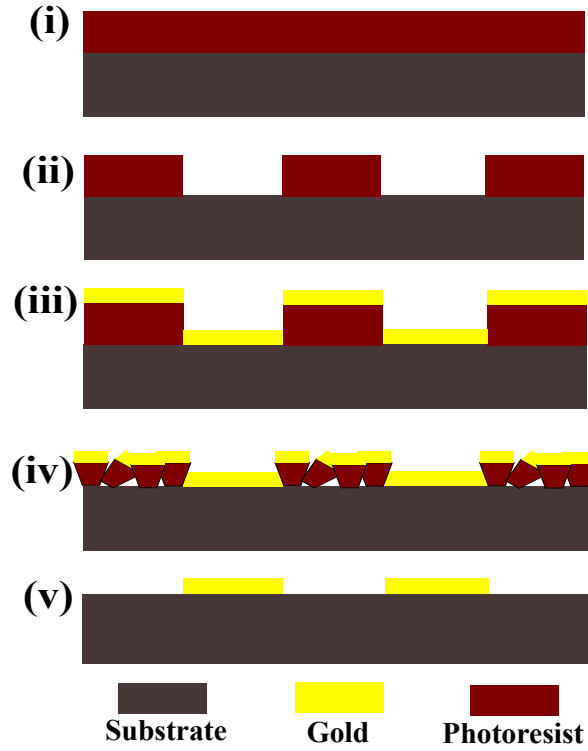


Figure 2.6: Illustration of lift-off process steps: where (i) spin coating of photoresist on the substrate, (ii) structuring of the patterned in the photoresist using lithography, (iii) deposition of gold on the top of the structured film, (iv) removing the photoresist together with gold in acetone and (v) final patterned structures.

structuring, gold deposition, dissolving in acetone and washing in DI water subsequently.

Fig. 2.7(a) shows the AFM topographical map of the photoresist disk array fabricated on a silicon substrate. The height of the photoresist disk is around 200 nm and the thickness of the deposited gold film is 40 nm. The similar photoresist pattern was on the fused silica substrate, but the photoresist pattern on the glass substrates had a conical shape. Here the different shapes of the photoresist pattern on the silicon substrate and glass substrate have been used to understand the difficulties in proper and uniform lift-off. The height of the pillar and thickness of the metal film is sufficient for lift-off. Fig. 2.7(b) and (c) show the AFM topographical maps of the microstructured pattern fabricated using lift-off process from a sharp photoresist pillar array fabricated on the fused silica and silicon substrates, respectively, whereas Fig. 2.7(d) shows the AFM topographical map of the microstructured pattern fabricated using lift-off process

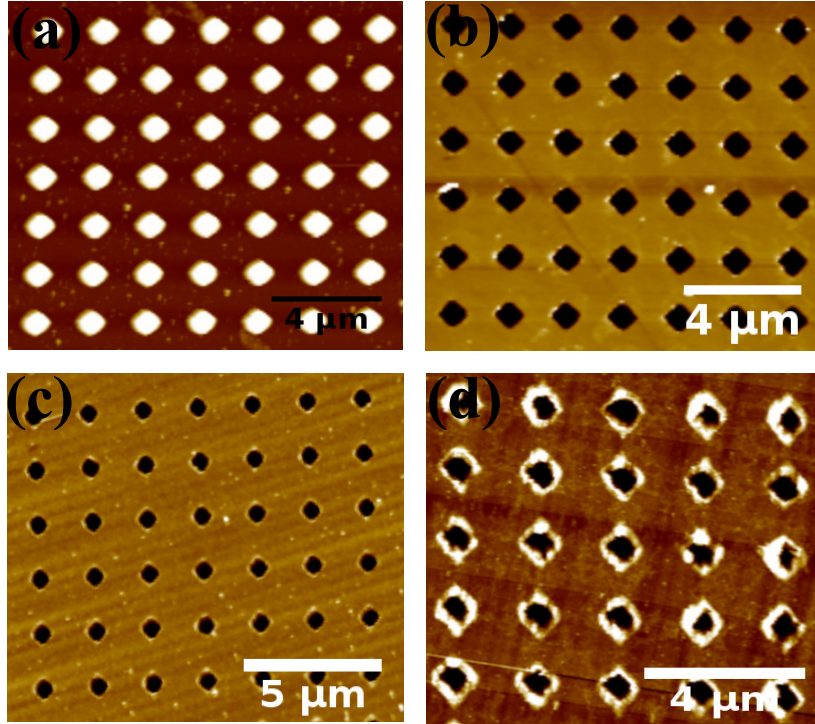


Figure 2.7: AFM topographical maps of the (a) photoresist disk array, (b) hole array fabricated from a sharp photoresist pillar array on a fused silica substrate, (c) hole array fabricated from a sharp photoresist pillar array on a silicon substrate (d) hole array fabricated from a conical shape photoresist pillar array on a glass substrate.

from a conical photoresist pillar array fabricated on the glass substrate. It is clear that there is a clean and neat lift-off in the case of (b) and (c), whereas the lift-off in (d) is not smooth, which is caused by the profile of the photoresist disk. During gold layer deposition, the gold completely covered the microstructures due to the conical shape photoresist pillar in the case of (d), which did not allow acetone to enter through the bottom side of the pillar due to the complete blockage of the gap. Gold layer on the top of the conical disk is of similar thickness as that on the sides of the conical pillar, but the gold film at the top of the conical disk gets easily torn, allowing to enter acetone from the top and which dissolve the photoresist, and gold on side portion left with the gold on the substrate.

2.2 Two photon absorption lithography

Lithographic techniques for fabrication of complex three-dimensional (3D) nano/micro-structures with high resolution are essential in many fields, such as photonics [109–111], metamaterials [108, 112, 113], microelectronics [114], microfluidics [115–119], electronic communications [120], and microelectromechanical systems (MEMS) [121, 122], and also increasingly in biotechnology and biomedicine (BioMEMS) [123–125]. These fields make high demands on miniaturization and integration of 3D nano/micro structures. This, in turn, leads to the development of various nano/micro fabrication technologies like deep UV lithography [126], electron/ion beam lithography [127, 128], nano imprint lithography (NIL) [129] micro stereolithography [130], ink-jet printing [131] and self-assembly [132] and many others. However, these technologies have encountered many problems such as incapable to fabricate complex real 3D micro/nano structures, particularly rapidly and over large areas. Two-photon absorption lithography technique is based on a voxel-by-voxel method of fabrication and has great advantages in the manufacturing of arbitrarily shaped three dimensional (3D) micro/nano-structures of various materials such as polymers, hybrid materials, metallic structures and organically modified ceramics (Ormocer) with sub-diffraction limited resolution almost down to 100 nm [133–136].

Two photon absorption lithography technique was developed after the experimental confirmation of two photon absorption by Kaiser et al. [137] that was actually theoretically proposed by Göppert Mayer in 1931 [138]. Two photon absorption lithography started to be applied to fabricate 3D micro/nano structures since 1997 when the first 3D spiral microstructure with a diameter of $\sim 7 \mu\text{m}$ was fabricated by Maruo et al. [139]. In 2001, Satoshi et al. fabricated a micro-bull structure with feature size of 120 nm which is far beyond the diffraction limit [140]. The micro-bull structure was fabricated using a femtosecond laser of wavelength 780 nm and with 1 numerical

aperture (NA) objective. The feature size (120 nm) of the micro bull was lesser than the calculated Abbe's diffraction limit, i.e., 390 nm using $d = \lambda/(2NA)$. It was a historic moment, and after which various applications of two photon absorption lithography sprang up in the different fields such as photonic crystals [111, 141], microfluidic devices [142, 143], biomedical science [123, 144], metamaterials [145] and so on.

The resolution of structures fabricated by two photon absorption lithography is mostly influenced by two major factors, namely the properties of the photo polymerizable material, such as two photon absorption coefficient at the corresponding wavelength, and the process parameters like exposure time, laser dose, amount of truncation, the numerical aperture of the lens and the writing speed. Thus, the resolution is always specific to the particular set of laser-material combination, and it always varies with the change of either of them from the combination. A threshold polymerization and dwell time is fixed for all photosensitive materials and it has to be overcome to initiate the polymerization. Due to the existence of a well defined polymerization threshold, a resolution far beyond the diffraction limit can be achieved with optimal fabrication conditions and parameters. The best resolution is obtained by working with the laser intensities close to the polymerization threshold within minimum dwell time [133]. There is an influence of radical quenchers on the resolution and the smallest reported resolutions with and without adding of radical quenchers with resin are 25 nm [146] and 45 nm [135], respectively.

The most widely used laser type for two photon absorption lithography is the Ti:sapphire laser with femtosecond pulses, typically at a wavelength of 780 nm. Although femtosecond pulsed lasers are efficient for two photon polymerization, due to the high cost associated, 2PP has been limited in utilization for industrial as well as on large-scale production. This can be offset by using picosecond or sub-nanosecond lasers along with photoinitiators of large two-photon absorption cross-sections to obtain sub-wavelength resolution. There are only a handful of results reported by different groups using picosecond or sub-nanosecond lasers [147, 148]. These results pave the way for

low-cost fabrication systems and moving towards industrial rapid production systems. The requirement of the low-cost fabrication system can be fulfilled by the development of new classes of photosensitive materials with large two photon absorption coefficient, which can enable two photon polymerization even with nanosecond/subnanosecond pulse lasers. However, a series of multiphoton absorbing materials have been reported by different groups [149,150], but their compatibility needs to be verified for two photon polymerization individually or in combination with photoinitiators.

In this Section, we present the background to our development of a two photon absorption lithography system (TPALS) using a sub-nanosecond laser operating at 532 nm wavelength. The further details of optimization of different fabrication parameters and fabrication in different resins are discussed in Chapter 6.

2.2.1 Setup for two photon absorption lithography system

TPALS developed in our laboratory was assembled with different components purchased from different companies.

The following are the main components of the system:

- **Diode-pumped solid-state laser**

It is a sub-nanosecond laser of 700 ps pulse width (Wedge-532-1064, Bright Solutions, Italy), with simultaneous output at 532 and 1064 nm wavelengths. Only 532 nm wavelength was used for this thesis work. It is a very compact in size, easy to handle and air-cooled laser. It can operate over a range of repetition rates varying from 1 Hz to 100 kHz. This is a high power laser, average output power at 532 nm is around 1.2 W and at 1064 nm is 1.6 W. Typically a lower power of about a hundred milliwatt ($\sim 100\text{mW}$) is sufficient for the TPP.

- **3D Piezo nano positioning stage**

A piezoelectric XYZ (3D) nano-positioning stage (PI E-725, Physik Instrumente,

Germany) is used to precise control of the movement of the samples placed on it with respect to the fixed focal plane and fixed focal point. It is mounted on the microscope stage. It has $200\ \mu\text{m} \times 200\ \mu\text{m} \times 200\ \mu\text{m}$ travel range along the XYZ axes, and 0.5 nm closed loop resolution. It is based on the capacitive feedback sensor which provides higher linearity and long-term stability than the piezoresistive sensor. Due to the parallel kinematics in all axes, the simultaneous control over all the axes is possible. It is compatible with LabView software as well as with text-based programming languages like Python, etc. and having USB, Ethernet and RS-232 communication interfaces.

- **Inverted Microscope**

An inverted microscope (Eclipse Ti-s, Nikon) is used in our system to focus the laser beam on the sample, to generate the image and to view the process in real time. The samples can be viewed through oculars or CCD camera attached to the microscope. The illumination source is placed on the top of the microscope which is used for illumination of the samples from the top, objectives are mounted below the microscope stage in the upward direction. The microscope contains a backport through which laser beam is sent to the objective lens which is used to focus the laser beam on the sample as well as for imaging. A dichroic mirror is fixed in the turret at 45° inclination to reflect the laser beam into the objective lens to focus on the sample. There are some mechanical reasons to select the inverted microscope over the upright microscope: (a) In the inverted microscope position of the stage is fixed and the objective can be moved up and down along the optical axis. This makes the focal plane less likely to drift in the vertical direction compared to an upright microscope, where an entire stage is capable of moving in this direction and can gradually drift up or down with extended periods of time. (b) There is more space between the condenser and objective lens as compared to the upright microscope to fit the nano positioning stage on the microscope stage.

- **Acousto-optic modulator**

It is very important to control the laser beam instantaneously during fabrication of samples, and it is not possible to have rapid switching with a mechanical shutter. To control the laser beam quickly, an acousto-optic modulator (IntrAction Corporation, USA) was used in the path of the laser beam which works as an optical switch for our system. The first order diffracted beam is used for fabrication of the sample.

- **Interfacing software**

The software for controlling the stage as well as the AOM was written in Labview programme. Two Labview programmes were written, one programme is used to control the stage motion by manual feeding the coordinates and the other one is used to control the stage by feeding the data extracted from AutoCAD design. Fig. 2.1 shows the screenshot image of the front panel of the software used for controlling the position of the stage by feeding the data manually. There are some parameters in the program which are set as default such as interface, Autozero, system number, AOM details, so there is no need to change them.



Figure 2.8: Screenshot image of the front panel of the software used for operating the system in manual data fitting mode.

2.2.2 Putting all together

Fig. 2.9(a) and (b) show the schematic diagram and photograph of the TPALS, respectively. The acronyms used for indication of the components in the photograph are mentioned in the caption of the figure. All components are mounted on a floating vibration-free table (Newport Corp., USA) to prevent vibrational disturbances during fabrication. A dichroic mirror is used to reject the laser output at 1064 nm wavelength and use the 532 nm wavelength only. The AO modulator is used in the path of the laser beam and aligned at Bragg's angle that diffracts the beam into three components $(-1,0,1)$, and a pinhole is used to select the first order $(+1)$ diffracted beam which is used for fabrication. This selected laser beam by a pinhole is guided to the microscope turret which contains a high reflecting mirror that guides the beam to enter into the microscope objective which is used to focus the laser beam at sample placed on a sample holder. The sample holder is mounted on the 3D nano-positioning stage where samples are clipped with the holder to avoid mechanical disturbance during fabrication. A Charge-Coupled Device (CCD) camera is used to view the samples and for the live observation of the writing process.

The operation procedures of the system have been discussed in the Appendix-A. This system can be operated in manual and auto data feeding mode. Users have to follow the steps mentioned in the operation procedures either for manual or auto data feeding mode.

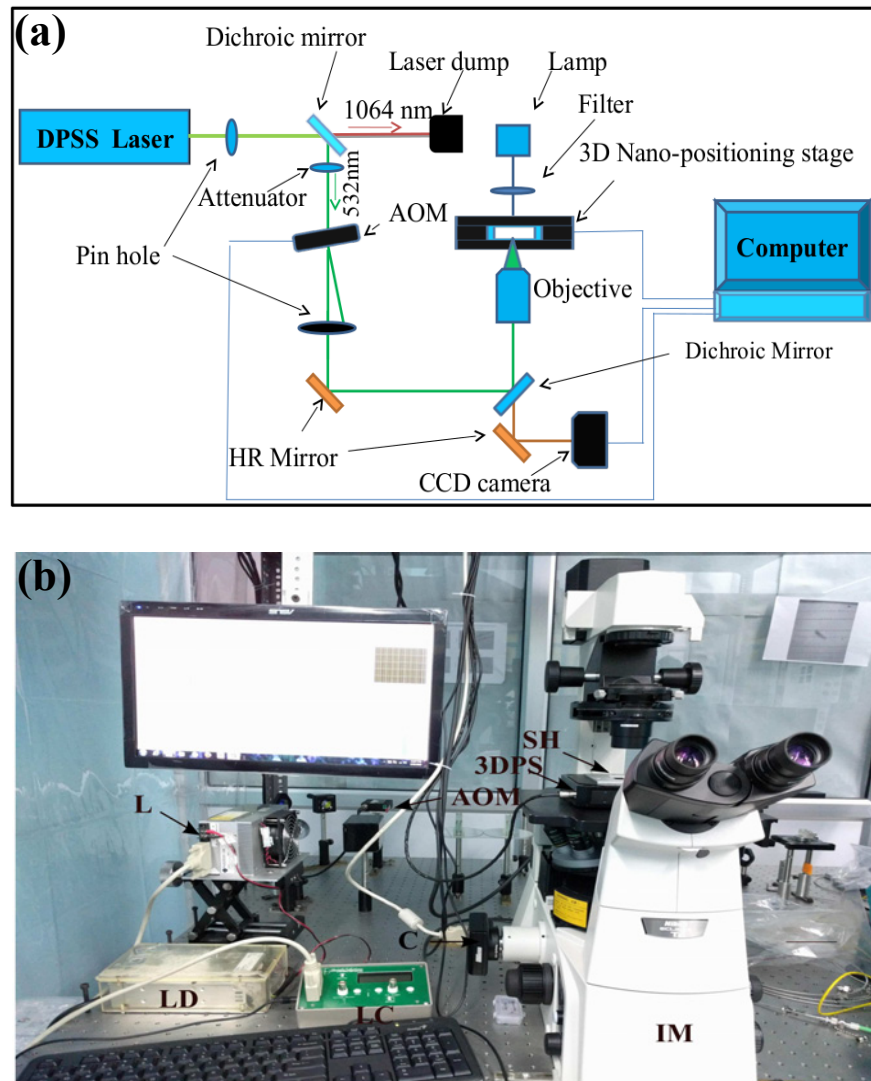


Figure 2.9: (a) Schematic diagram of the TPALS, (b) Photograph of the same system where L is the sub-nanosecond laser, LD is laser driver, LC is laser controller, IM is inverted microscope, C is CCD camera, AOM is AO modulator, 3DPS is 3D piezo nano positioning stage and SH is sample holder.

2.3 Soft lithography

Soft lithography is a category of nano/micro fabrication techniques, in which a stamp/mold made from a “soft” material is used for fabrication of nano/micro structures. It was pioneered specifically by G.M. Whitesides and co-workers, at Harvard University [103,151]. Soft lithography techniques are convenient, inexpensive, straightforward to use, accessible to a wide range of users. It is a non-photolithographic approach suitable for

nano/micro-fabrication by replication of nano/micro structures. The mold/stamp is made from an elastomer, generally polydimethylsiloxane (PDMS) due to certain special features associated with the material.

1. PDMS is elastic in nature which enables it to make conformal contact with even non-planar substrates due to minimally applied pressure.
2. It is mostly transparent in UV which makes it suitable for UV-imprint lithography.
3. It is commercially available in bulk and moderate in price which enables its use for rapid prototyping.

Soft lithography offers the following advantage over the other popularly known lithographic techniques like photolithography, e-beam lithography etc.

- Significantly cheaper for mass production compared to the other lithographic techniques, as it does not require clean room facilities to produce high resolution structures, apart from this no need for special equipment.
- It is suitable for planar or non-planar surfaces that makes it appealing over the other techniques like photolithography where there is a requirement of a very clean, flat surface, as usually the image transfer occurs from one plane to another and parts of a curved surface will be out of focus during exposure.
- In terms of resolution, soft lithography is very efficient and competitive, and the feature resolution obtained here can easily exceed the resolution limits of standard photolithography. This is because the physical contact process does not involve the diffraction limit that e-beam and photo-lithographic techniques necessary face.

2.3.1 General preparation for soft lithography

The soft lithography process occurs in three steps [152]. the first step consists of a master pattern fabrication on a substrate, the second one is the preparation of stamp/mold and the last one is embossing the pattern using the stamp/mold.

Master fabrication

The fabrication process for the “master” usually involves the use of conventional processes like photolithography, e-beam lithography, and i-beam lithography to produce the required pattern on a hard substrate. According to the requirements, it may be possible to use some inexpensive techniques for fabrication of the master like LIL or readily available master with sub-micron features size can be obtained from data storage devices such as compact discs (CDs) and digital versatile discs (DVDs). This is particularly if some periodic features with single symmetries are desired.

Molds/Stamp fabrication

Generally, elastomer material used for preparation of the mold/stamp is PDMS which is a silicone-based organic polymer. It is a non-toxic material along with very good transparency in the UV to visible range. This makes it possible to cure the resin through PDMS mold/stamp itself. Sylgard 184 is a commercially available PDMS, obtainable in a kit containing the base resin and curing agent separately.

Following are the steps for preparing of stamp/mold.

- **Dispensing:**

Generally, base and curing agents are taken in the 10:1 ratio in a plastic cup.

The dispensing is irrespective of the order of base and curing agent. A small

difference in the amounts of base and curing agent used does not affect the final result much. Use of less amounts of curing agent makes the stamp softer whereas as the excess amounts of the curing agents do not make the stamp any harder.

- **Mixing:**

The base and the curing agent should be properly and thoroughly mixed by stirring for a couple of minutes as recommended. During the mixing, typically air bubbles get trapped inside and incorporated into the mixture.

- **Degassing:**

The air bubbles entrapped in the process can be removed by degassing in a mild vacuum ~ 300 mbar for a few minutes. We typically used desiccator for this process.

- **Pouring:**

Special care should be taken during the pouring of the mixture onto the master to minimize the formation of air bubbles. If needed, the degassing process should be repeated until the solution is completely free of any visible air bubbles.

- **Curing:**

PDMS is cured by keeping it at the temperature of about 70°C . It can be done either by placing the poured PDMS with the master pattern on a hot plate/oven or even by leaving it at room temperature for a long time. Generally, it is cured for 6 hours at 70°C on a hot plate or in an oven, and takes 24 hours at room temperature, to properly harden. It should be noted that the PDMS is slightly hardening in the fabrication process as ages.

- **Peel off:**

For peeling off the stamp, first it is recommended to cut away the extra portions of the cured silicone from all sides. After cutting from all sides, the rest portion so-called stamp can be gently peeled off from any corner and separated from the master pattern.

Embossing using stamp

A drop of a liquid pre-polymer such as polyurethane or monomeric solution is poured onto a substrate, and the PDMS mold is gently placed over the polymer in contact with the substrate and pressed softly so that contact of the mold with the substrate can be made. After that, the system is placed under the UV lamp for 15 minutes for curing. After curing, the PDMS stamp is carefully peeled off from the substrate which leaves behind the replica of the master as a polymeric structure on the substrate.

2.4 Sample characterization

The surface topography of the fabricated samples and thickness of the different deposited materials were investigated by an atomic force microscopy (AFM, Xe 70, Park System, S. Korea, and WITec, Germany) and a field emission scanning electron microscope (FESEM: Zeiss Supra 40VP). To optically characterize the samples an optical microscope (Olympus, BX51) was used. The thickness measurements of the deposited material were carried out either by cutting the sample into two parts and examining the cross-sectional view or by scratching the deposited materials up-to substrate using sharp edge of a blade and scanning over the scratched region corner side using AFM. The samples were scanned over the scratched line in such a way that the half portion of the scan area falls in the substrate side and rest half on the film side. This technique typically works for a thin film of soft material like gold or aluminium. Fig. 2.10(a) shows the AFM topographical image of the gold coated sample which is scratched up-to the substrate to measure the thickness of the film. The line profile of the corresponding scan over the boundary is shown as the inset in the figure. The measured thickness of the deposited films using the AFM was cross-checked using FESEM by scanning the cross section of the samples. Fig. 2.10(b) show the FESEM scanned cross-sectional image of a sample used to measure the thickness of the deposited films.

The Infrared properties of the samples were characterized using a Fourier transform infrared spectrometer (FTIR, Cary 660, Agilent Technologies).

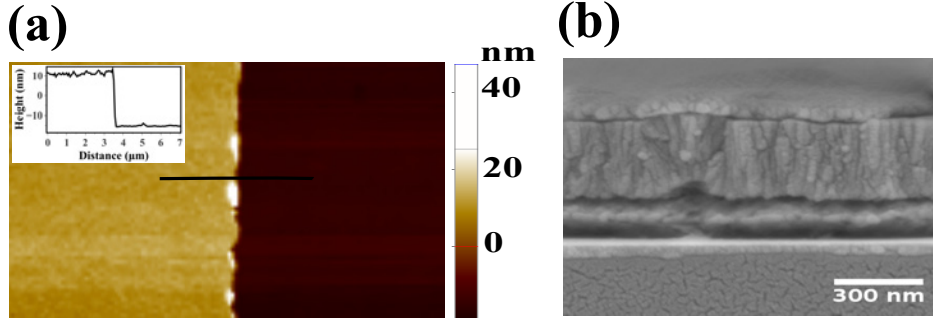


Figure 2.10: (a) AFM topographical map across the one edge of the scratched line on the gold film, and the line profile plot across the cut is shown as the inset, (b) FESEM cross-sectional image of a tri-layer deposited sample.

2.4.1 Atomic force microscope

Atomic force microscopy (AFM) is a type of scanning probe microscopy (SPM) where a physical probe is scanned over samples. The scanning tunnelling microscope (STM) is the forefather of all scanning probe microscopes and was invented by Gerd Binnig and Heinrich Rohrer in 1982. The AFM was also invented by Gerd Binnig and et al. in 1986. STM is based on the concept of quantum tunnelling of electrons between the probe and samples whereas the AFM is based on the van der Waals forces acting between probe and sample. The forces can be either attractive or repulsive, depending on the distance between the probe and sample.

The probe represents a fabricated cantilever with a sharp tip at one end, which is brought into interaction with the sample surfaces. Generally, V-shaped and pyramidal shape cantilevers are used for probing the samples due to their low mechanical resistance to the vertical deflection, and high resistance to the lateral torsion. These cantilevers are made of silicon (Si) or silicon nitride (Si_3N_4). Dimensions and specification of the cantilevers are varied with the manufacturers and systems. We have used cantilevers with a pyramidal tip of 3-6 μm height and 10-20 nm tip diameter in

the Park system, and cantilever with pyramidal tip of 10-15 μm height and ~ 10 nm diameter in WITec system. There is a deflection of the cantilever during the scanning due to the surface morphology of the samples. To measure the deflection in the cantilever, laser light is reflected off from the back side of the cantilever and collected on a position sensitive quadrant photodiode (PSPD). The PSPD is divided into four parts, shown in Fig. 2.11(a). The topography of the sample is obtained by scanning the probe over the region of interest. The deflection in the cantilever is monitored by the PSPD. The PSPD is connected to a feedback loop which controls the height of tip above the sample surface by maintaining the position of the laser spot on the PSPD which helps to generate an accurate topographical map of the surface feature.

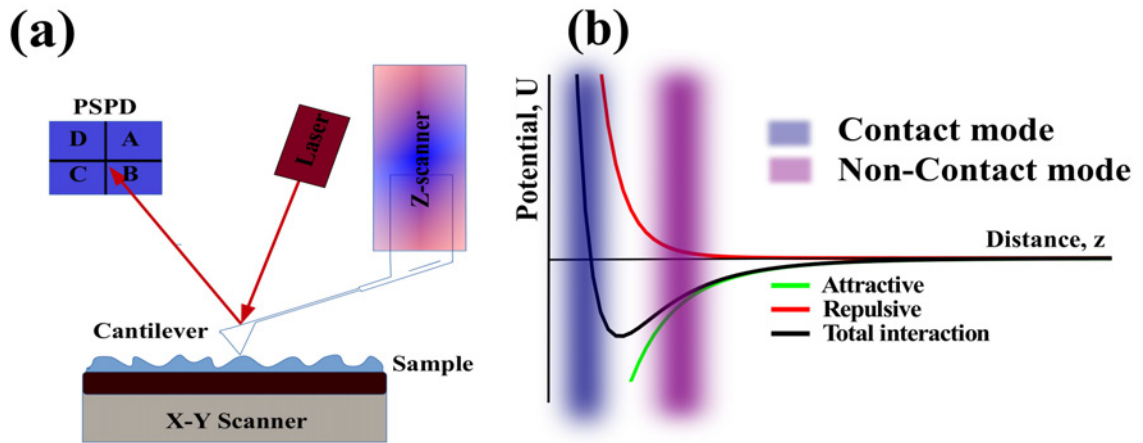


Figure 2.11: Schematic diagram of a typical AFM in the working state where the reflected light from the back of the cantilever is collected in PSPD. (b) The plot of Lennard-Jones potential versus distance between the tip and sample. The shaded portions corresponding to the different working regions represent the different modes of operation of the AFM.

Generally, there are two primary modes of operation of an AFM.

- **Contact mode:**

Fig. 2.11(b) shows the plot of Lennard-Jones potential versus distance between the tip and sample. If the distance between the tip and sample is of the order of few angstroms, then there will be a strong repulsive force between them, and the working mode in this range is regarded as the contact mode of operation. In this

mode, the tip is softly in physical contact with the sample. The tip is scanned over the sample either in constant height mode or constant distance (separation) mode. In this mode, it is necessary to have a soft cantilever so that it can even deflect by very small forces, and should have high enough resonant frequency to avoid the deflection by vibrational instabilities. Silicon Nitride tips are used for this mode. Higher resolution is possible in this mode because of the physical contact with the sample surface.

- **Non-contact mode:**

If the distance between tip and sample is of the order of few nanometers then, there will be an attractive force between them, and working mode in this range is regarded as the non-contact mode. In this mode, there is a minimum interaction between tip and sample, and generally, silicon tips are used. This mode is also known as non-destructive mode because there is not even soft physical contact of the tip with the sample surface and a very low force is exerted on the sample. However, there is a lower lateral resolution due to the larger separation between the tip and sample.

Possible applications of AFM:

- Roughness analysis of samples
- Crystallite analysis at the nanometer scale
- Temperature dependent topography of the sample.
- Use for indentation
- Thickness measurements of thin film
- Phase information of chemical samples

- Young's modulus measurements of samples

Advantages of AFM:

- It does not require any vacuum and/or special preparation of sample (carbon or metallic coating) that is required in the scanning electron microscope and even in STM.
- It can image both conducting and non-conducting samples, including polymers, ceramics, composites, glass and biological samples.
- It can work in a liquid environment which enables scanning even of biological samples without damaging the system.
- The high resolution AFM is even comparable to that of scanning tunnelling microscopy and transmission electron microscopy.

Disadvantages of AFM:

- The measurement speed of an AFM is much slower than that of an optical microscope or electron microscope.
- Due to the finite tip size, it is very difficult and sometimes impossible to measure narrow and deep features and those with steep slopes. The convolution effect due to the shape of the tip and sample profile may result in measurement errors.
- There are possibility of image artefacts, which could be induced by an unsuitable tip or damaged tip, a poor operating environment, or even sometimes by the sample itself.

2.4.2 FTIR spectrometer

A FTIR spectrometer is an instrument used to acquire the Near InfraRed (NIR) to Far InfraRed (FIR) spectra. Unlike a dispersive instrument (grating monochromator or spectrograph), FTIR spectrometer collects all wavelengths simultaneously using

a Michelson interferometer. In the FTIR method, infrared spectra are obtained by Fourier Transform of the interferogram of a sample collected by the interferometer. The FTIR spectrometer collects and digitizes the interferogram of a sample, performs the Fourier transform, and displays the corresponding infrared spectrum. It is preferred over the dispersive instrument due to applicability over large bands of frequencies in infrared, capability for high spectral resolution, suitability for even weak signals and its high spectral accuracy. The signal to noise ratio can be enhanced by using more scans.

The schematic diagram of a FTIR spectrometer is shown in Fig. 2.12. The broadband infrared beam generated from a thermal source is passed through an interferometer, where the beam is divided into two parts (1) reflected beam from the splitter, and (2) transmitted through the splitter. The reflected beam from the splitter is again reflected from a fixed mirror and passed through the splitter towards the sample compartment where is the transmitted beam through the splitter, is reflected by a movable mirror and again reflected by the splitter towards the sample compartment, where beams interfere. The interference condition depends on the total optical path difference between the two beams. If the movable mirror is displaced by Δ distance, then the total path difference is 2Δ as both mirrors were placed at equal distance from the beam splitter. For the constructive interference, the phase difference between the two beams should satisfy the condition of $2\Delta = n\lambda$, and for destructive interference, the phase difference between the two beams should satisfy the condition of $2\Delta = (n+1/2)\lambda$ where $n = 0, 1, 2, 3, \dots$. The interfering beams interact with the sample and the resultant response is collected in the detector which generates an interferogram, that is the intensity versus displacement of the moving mirror. The computer converts this interferogram into the spectrum using fast Fourier Transformation algorithm.

The IR properties of our samples were investigated by a FTIR spectrometer (Agilent, Model Cary 660) with an attached IR microscope (Agilent, Model Cary 610). The angle-dependent reflectance spectra were measured using a reflection accessory

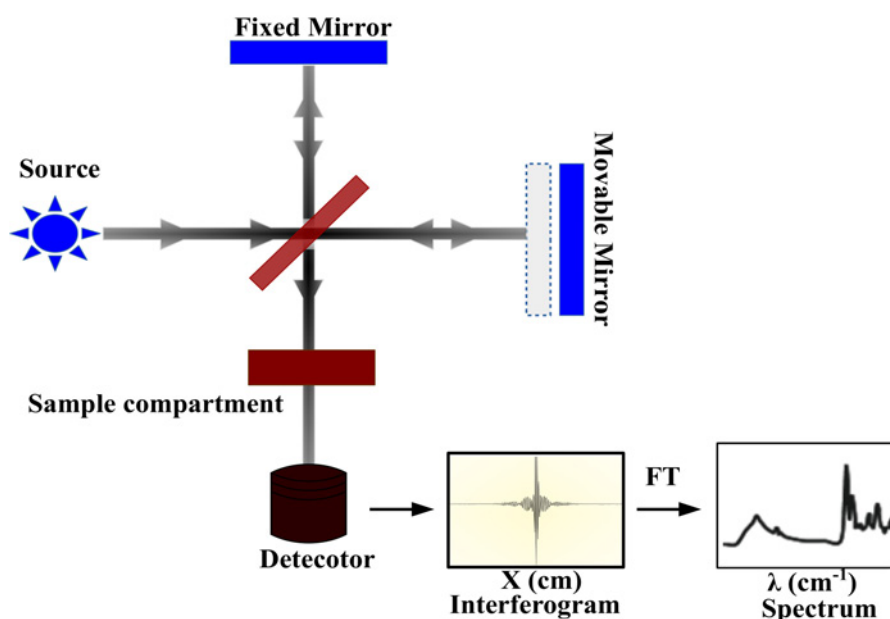


Figure 2.12: Schematic diagram of a FTIR spectrometer.

(Make: Harrick seagull). This spectrometer has two detectors; one is liquid nitrogen cooled Mercury Cadmium Telluride (MCT) detector mounted on the microscope, and other is an uncooled Deuterated Triglycine Sulfate (DTGS) detector mounted in the spectrometer. Both detectors have different spectral range, and it is $2.5\ \mu\text{m}$ to $14\ \mu\text{m}$ for MCT detector and $1.66\ \mu\text{m}$ to $25\ \mu\text{m}$ for the DTGS detector. The incident angle and polarization dependent reflectance spectra were measured using the DTGS detector. Due to the limited space on the sample holder attached with reflection accessory, the bigger samples were characterized using the MCT detector with an attached IR microscope.

In the spectrometer, the IR beam is focused on the sample using a parabolic mirror, so there is a finite angular width of the incident beam which can be calculated by measuring the curvature of the mirror, and the distance between the mirror and its focal plane. It was calculated in our spectrometer, and the calculated value of the half of the angular width is around 5° . In the case of the microscope, the angular width

is even larger than that of in spectrometer due to the objective ($10\times$) lens, and it is around 14° ($NA = 0.5$). The spectral resolution in the spectrometer can be set from 4 cm^{-1} to 16 cm^{-1} at intervals of 4 cm^{-1} . In our measurement, it was set at 4 cm^{-1} .

2.5 Numerical simulations

Due to the artificially designed structures of metamaterials and plasmonics, there is a complex geometry in almost all the designs. Hence, it becomes difficult to solve the Maxwell's equations analytically for any of the cases and thus numerical techniques become necessary. There are various numerical techniques implemented on high-speed computers such as finite difference time domain (FDTD), finite element method (FEM), computer simulation technology (CST), finite difference method (FDM), mesh free method, etc. to solve the Maxwell's equation for complex geometries. In this thesis, a commercial software package COMSOL Multiphysics 4.4 [153] based on the FEM was used to model the metamaterial and plasmonic structures.

The FEM is used to solve the problems which are described by ordinary differential equations /partial differential equations with appropriate boundary/initial conditions. It provides greater flexibility to model complex geometrical systems and can handle general boundary conditions and variable material properties.

Some important steps involved in the general calculation using FEM methods are as follows:

1. Discretization of real continuum or structure into domains or elements
2. Identification of primary unknown quantities
3. Implementation of interpolation functions and the derivation of interpolated functions to interconnect the physical quantities over domain nodes
4. Derivation of elementary equations

5. Solutions for primary and secondary equations
6. Postprocessing and interpretation of results

2.5.1 Modelling using COMSOL Multiphysics

COMSOL Multiphysics can be used to model highly complex physical problems with mechanical, chemical, electromagnetic, thermal phenomena.

There are some important steps to model any physical problems:

1. Selection of appropriate working dimension and appropriate module such as acoustics, heat transfer, optics, plasma, radio frequency and so on
2. Drawing the geometry of the system domain
3. Filling the domain with material parameters
4. Applying the appropriate boundary conditions
5. Setting the study parameters such as frequency, wavelength, etc.
6. Meshing or discretization of the domain
7. Running the model
8. Results analysis

In this thesis work, full wave three-dimensional numerical simulations using the radio frequency (RF) module were carried out to understand the underlying physics behind the different electromagnetic properties shown by the designed structures. COMSOL Multiphysics uses FEM to solve the EM fields in the modelling domain under the assumption that the fields are varying sinusoidally in time at a particular frequency, and all the material properties vary linearly with respect to the field strength. The

governing Maxwell's equations in 3D reduce to:

$$\nabla \times (\mu_r^{-1} \nabla \times E) - \frac{\omega^2}{c_0^2} (\epsilon_r - \frac{i\sigma}{\omega\epsilon_0}) E = 0,$$

where μ_r , ϵ_r and σ are relative permeability, relative permittivity and electrical conductivity, respectively.

The other quantities like magnetic fields, currents, and power flows etc. can be derived from the electric field. This equation can be formulated as an equation of eigenvalue problem and the solved for eigenvalues(resonance frequencies) of the system.

There are some important steps which have to be followed in designing the module, analysing and understanding the output results are mentioned in the Appendix-B.

2.5.2 A benchmark problem solved by COMSOL

To check the validity of our model, an extraordinary optical transmission through hole arrays in optically thin metal films reported by Rodrigo et al. [154] using FDTD simulation software was taken as a benchmark problem. In the paper, they have shown the effect of different thickness of the gold film, different refractive index of the substrate and the surrounding medium with the medium inside the hole on the transmittance. The geometrical parameters such as the periodicity of the square hole array and the width of the hole are taken as 400 nm and 160 nm, respectively. The varying thickness of the gold film was considered in simulation as 16 nm, 20 nm, 40 nm, 80 nm and 160 nm to check the effect on the transmittance. It has been shown that as the thickness decreases, the coupling of light with short-range surface plasmons redshifts the extraordinary optical transmission peak to longer wavelengths.

To check the accuracy of our model, we simulate the design described in the paper for a particular thickness of the gold film at normal incidence using COMSOL Multi-

physics software. Perfectly matched layers were used along the propagation direction (z-direction) to prevent the reflection of the waves from the top and bottom domain boundaries. Periodic boundary conditions were used along the x and y directions to simulate an infinite array of unit cells to reduce the complexity of the simulation. All parameters such as refractive indices of the substrates and gold and geometrical parameters were taken from the quoted paper. The schematic diagram of the unit cell is shown in Fig. 2.13(a). The corresponding reported transmittance spectrum (red in color) and simulated transmittance spectrum (black in color) at normal incidence of the design are shown in Fig. 2.13(b).

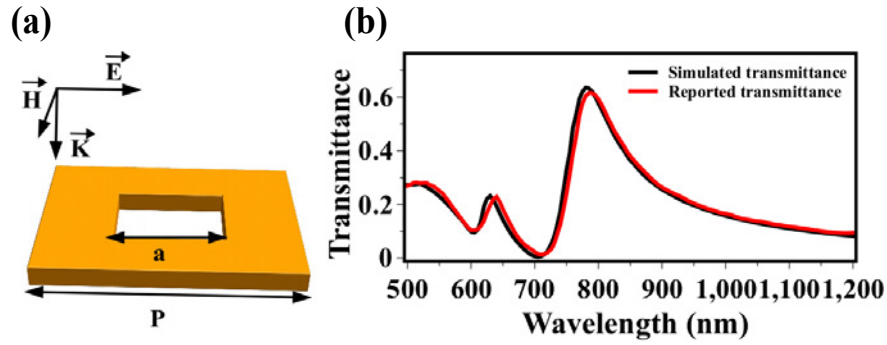


Figure 2.13: (a) Schematic diagram of the unit cell of square hole array in an optically thin metal film. (b) Transmittance spectra (red-reported & black-simulated) of the corresponding square hole array at normal incidence. The parameters used for simulation: periodicity of the hole array, the size of the hole and the thickness of the gold film are 400 nm, 160 nm and 40 nm, respectively.

The simulated transmittance spectrum at normal incidence obtained by using COMSOL Multiphysics software for the 40 nm thick metal film in the respective wavelength range is consistent with simulated transmittance spectra using FDTD software for the same thickness of the gold film as it is shown in Fig. 1(a) of the reported paper. The peak amplitude and position are almost matching with their reported simulated transmittance spectrum.

Chapter 3

Transmittance enhancement through sub-wavelength hole array using dielectric micro-domes

Since the discovery of the extraordinary optical transmission by Ebbesen et al. in 1998 [59], it has found numerous applications in the fields of nano-photonic devices, chemical and biological sensors [66, 67], sub-wavelength photolithography [68], near-field optics [69], etc. Different theoretical mechanisms have been developed to explain this effect, but the concept of excitation of surface plasmons polaritons has been widely accepted among the scientific communities. Direct experimental evidence of the role of SPP excitations has been also demonstrated [64, 65]. However, the excitation of SPPs typically limited to visible or near infrared frequencies due to the requirement of bounding the EM modes to the surface of metal while propagation that needs a finite penetration of EM waves into it. Metals behave almost as perfect conductors with almost zero skin depth at lower frequencies, and a flat conducting surface does not support surface plasmons [1, 70]. To understand the extraordinary transmission that occurs at lower frequencies, the concept of SPs-like wave so-called spoof surface plasmons was developed [29, 71].

The periodically perforated metallic thin film with sub-wavelength hole arrays that show extraordinary optical transmission (EOT) effect has also been of interest for use as electrically conducting, optically transparent couplers for optoelectronic devices and detectors [155]. The metallic film provides a nearly uniform conducting contact over the front surface of a device while simultaneously allowing the incident radiation to couple into the device. Further, the near-fields of the resonant micro/nano-structures are highly enhanced and localized within the photonic device. This can immensely enhance the photo-absorption or photo conductivity. Krishna et al. have reported up to 30% enhancement in the detectivity of an InAs quantum dot infrared photodetector with a perforated metal film integrated on top of the detector's active region [156]. The perforated metallic film was designed to have resonance within the excitation frequency band of the active material or quantum dots to enhance the response optimally. In the case of type-2 super-lattice structures used for IR and THz detectors [157], the photo-response at normal incidence (transverse polarization) is almost nil due to the selection rules of light absorption [158]. This limitation can be overcome by using plasmonic structures [159] or metamaterials [160] for coupling in the radiation to the super-lattice structure through the scattered near-fields whereby the polarization selectivity can be avoided. The rather modest transmittance (20-30%) obtained in EOT and the absorptive losses in the metals have limited the use of these devices. We note here various attempts to enhance the transmittance by filling the holes with other materials [161], by coating the top surface with a high refractive index material with a crater-like structure on top of the holes [162], using buried metal grating structures fabricated using a metal-assisted chemical etching process [163] or by an array of coaxial-apertures instead of simple holes [164, 165].

In our study, we show that the transmittance through sub-wavelength hole array can be further enhanced by mounting dielectric micro-dome structures on each hole. In contrast to mounted metallic pillars or structures that suffer from immense Ohmic losses [166], our adaptation increases the EOT amplitude as well as the bandwidth.

The dielectric micro-domes mounted on sub-wavelength holes in the thin metal film work as scatterers which scattered the incidence electromagnetic radiation and help in coupling of the incident radiation with the surface plasmon generated on the thin gold film. Transmittance through sub-wavelength holes array depends on the coupling of incident radiation and more coupling implies more transmittance. Thus, the transmittance through the sub-wavelength hole array is enhanced by mounting the dielectric micro-domes on the holes. This enables enhanced transmittance simultaneously along with large localization of the near-fields within the substrate, which suggests the potential use for infrared detectors if active-layers are deposited on the substrate. The enhanced sensitivity can be really important for the detectors and imaging devices in the 3-5 micrometer band, particularly for super lattice semiconductor quantum well devices that do not absorb normally incident light. The schematic diagram of cross-section of the unit cell of the proposed design of sub-wavelength hole array mounted with dielectric micro-dome is shown in Fig. 3.1. It consists of a hole in the gold film mounted with SU-8 micro-dome on the fused silica substrate. The COMSOL Multiphysics software was used to estimate the geometrical parameters needed for fabrication of the structures. A novel fabrication process based on LIL and lift-off processes involving a back exposure using UV laser is developed to obtain dielectric micro-domes made of SU-8 that are almost lens-like (although sub-wavelength in size) and mounted on each hole of the periodically perforated gold film.

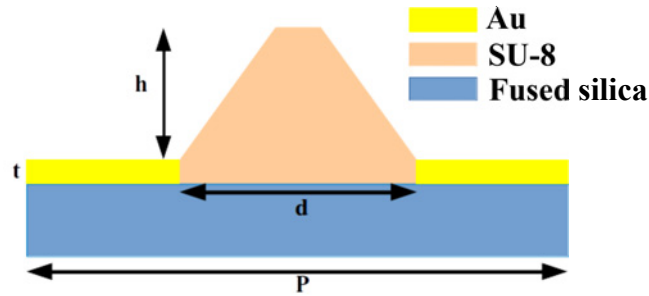


Figure 3.1: The cross-sectional view of the unit cell of the micro-dome mounted sub-wavelength hole array. P is the periodicity of the hole array, d is the diameter of the hole, and t and h are the thickness of the gold layer and height of the micro-dome, respectively.

Chapter is organized as follows: The details of samples fabrication and characterization are discussed in Section 3.1. The design and simulation details including the statistical analysis of the hole sizes and effects of shape and size of dielectric structures on the transmittance spectra of the microstructures are discussed in Section 3.2. Further, the results and discussions are discussed in Section 3.3, and finally conclusions are in Section 3.4.

3.1 Experimental Details: Fabrication and Characterization

Laser interference lithography and ultra-violet (UV) laser exposure were used to fabricate the samples. The samples were fabricated with keeping in mind of the optimized parameters for enhanced transmittance at a particular wavelength. A two-dimensional square array of photoresist pillars was fabricated using LIL by following the same procedures as mentioned in the sample fabrication procedures in Section 2.1 of the Chapter 2. After that, the samples were coated with 40 nm thick gold using thermal evaporation in a vacuum ($\sim 10^{-6}$ mbar) and followed by lift-off process in acetone that left behind hole arrays in the gold film on the substrate.

A negative photoresist (SU-8-2002, MicroChem Corp., USA) was used to fabricate the dielectric micro-domes mounted on the holes of the gold film. SU-8 was spin coated at 4000 RPM for 45 s on the perforated gold film, and pre-baked at 65 °C and 85 °C for 2 minutes and 3 minutes, respectively. The SU-8 coated samples were exposed through the perforated gold film from the substrate side by a UV laser (Frequad-C, Oxide Corporation, Japan) of wavelength 266 nm and power 50 mW for 1 minute. The gold film with an array of holes acts as a mask that allows the laser to pass only through the holes, which leads to polymerization of the SU-8 only at the locations of the holes. After post-baking at 65 °C and 85 °C for 3 minutes and 5 minutes, respectively, the

development of the polymerized structures was carried out in propylene glycol methyl ether acetate (PGMEA) for 20 s, followed by washing in isopropyl alcohol (IPA) for 1 minute. During development, the unexposed portions of the SU-8 dissolve out, leaving behind the cross-linked polymer as micro-domes mounted on the holes of the perforated gold film. A melt flow technique was used to smoothen the surface of the SU-8: the sample was heated at 105 °C on a hot plate for 3 minutes, whereby the SU-8 softens, and the surface smoothen out due to surface tension. Highly smooth and uniform micro-domes were achieved in this manner.

The schematic diagram of the step-wise fabrication of the samples is shown in Fig. 3.2. A thin film of positive photoresist was spin coated on cleaned fused silica and followed by LIL and development in the developer, that left behind the fused silica substrate with a two-dimensional photoresist pillar array. After that, the samples were thermally coated with 40 nm thick gold. A lift-off process was carried out to fabricate the hole arrays in the gold film. Next, the SU-8 photoresist was spin coated on the top of the perforated gold film, and a back exposure of the coated samples was carried out using UV laser from the substrate side. The exposed portions of the photoresist get polymerized and rest of the portions get washed away in the developer (PGMEA, Sigma Aldrich), thus a perforated gold film mounted with SU-8 micro-dome over the holes was fabricated.

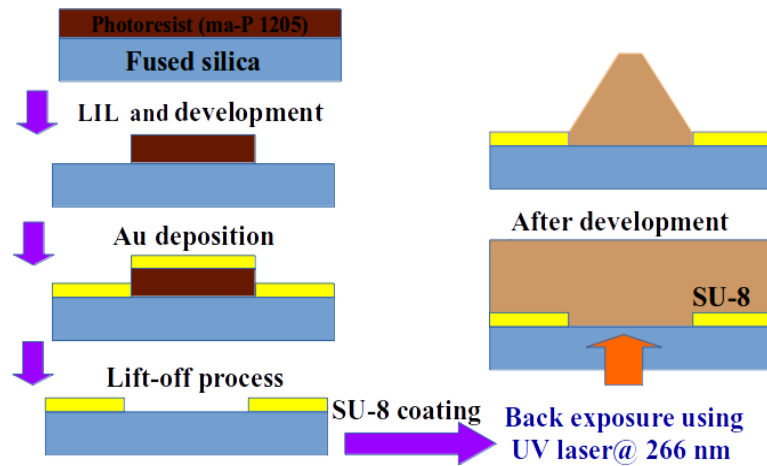


Figure 3.2: Schematic diagram of the sample fabrication steps.

An atomic force microscope (Park XE-70, S. Korea) was used to structurally characterize the samples. Fig. 3.3(a) and (b) show the AFM topographical maps of the perforated gold film on the fused silica substrate and its 3D view, respectively. A nominal thickness of 40 nm for the gold film was measured by the AFM. The gold layer has square holes rotated by 45° from the axes of the square array, with $1.0\ \mu\text{m}$ diagonal length and $2.1\ \mu\text{m}$ periodicity. The holes have slightly rounded corners and have some small variation in their shapes and sizes that are inherent to the fabrication process. The statistical distribution of the hole sizes (diagonal of the square) is shown in Fig. 3.13.

The sample shown in Fig. 3.3 was used to fabricate the SU-8 micro-domes. The AFM topographical map of the perforated gold film mounted with SU-8 micro-domes before melt-flow and its 3D view are shown in Figs. 3.4(a) and (b), respectively. It is clear that the micro-domes are having very rough surfaces. The *rms* roughness measured using AFM is $\sim 9\ \text{nm}$. Figs. 3.5(a) and (b) show the AFM topographical map of the SU-8 micro-domes mounted perforated gold film and its 3D view, respectively after the melt-flow on a hot plate at 105°C for 3 minutes. The micro-domes are of $0.4\ \mu\text{m}$ in height and of $1.0\ \mu\text{m}$ full width at half maxima. The micro-domes are very uniform and smooth throughout the sample after the melt flow process with an *rms* roughness of about 2 nm compared to $\sim 9\ \text{nm}$ before the melt flow. Figs. 3.6 and 3.7 show the optical microscopy images of the SU-8 micro-dome mounted sample taken using $100\times$ objective lens in transmittance and reflection mode, respectively. The uniformity of sample can be seen through the optical microscopy images of the sample in transmission as well as in reflection mode. In transmission mode image all the holes appear bright whereas in reflection mode image all holes are dark. Fig. 3.8 shows the diffraction pattern through the SU-8 micro-domes mounted sample using He-Neon laser of 633 nm wavelength.

A FTIR spectrometer was used to investigate the optical properties of the samples. Polarization dependent transmittance (T) and reflectance (R) spectra were mea-

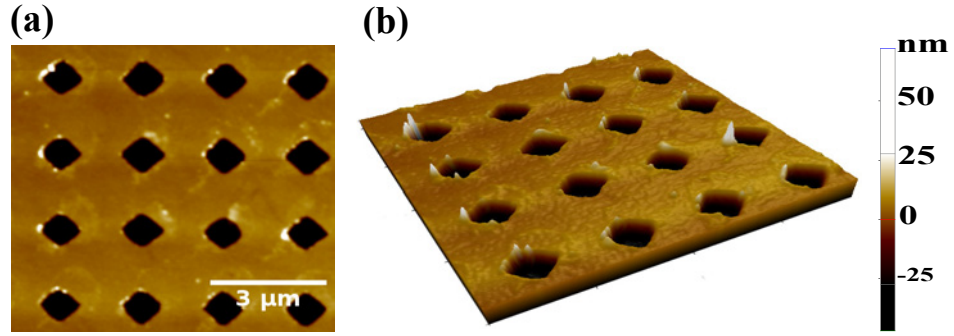


Figure 3.3: (a) AFM topographical map of the perforated gold film on fused silica substrate; (b) 3D view of figure (a). The measured thickness of the gold film, diagonal of the square, periodicity of hole array are 40 ± 4 nm, 1.0 ± 0.05 μm and 2.1 ± 0.03 μm, respectively.

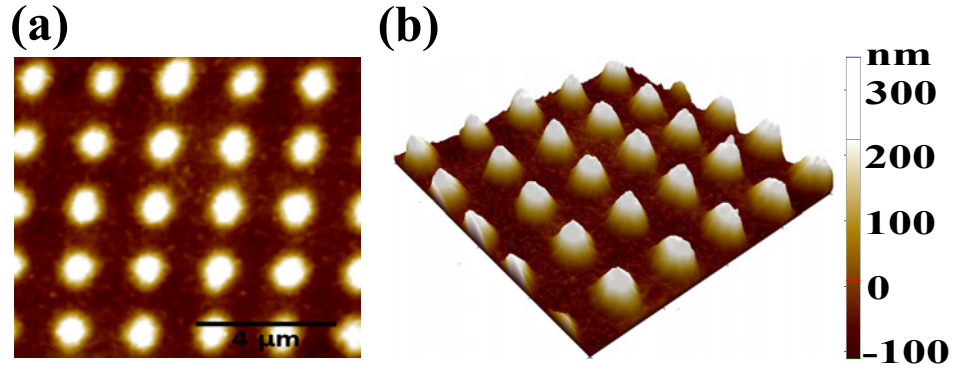


Figure 3.4: (a) AFM topographical map of the perforated gold film mounted with SU-8 micro-domes before melt flow process; (b) 3D view of figure (a).

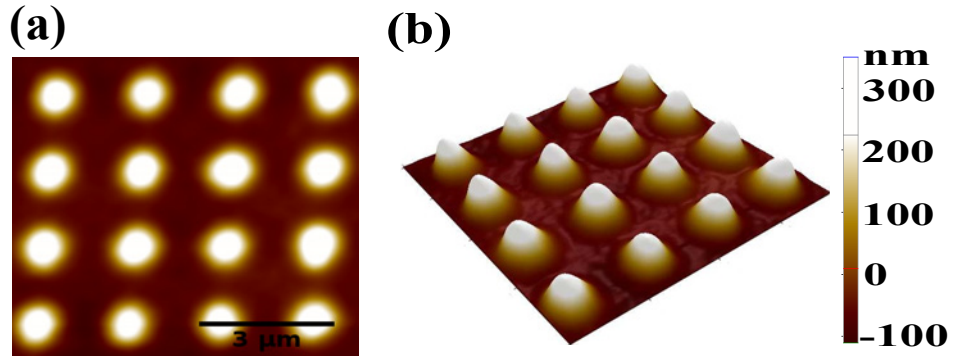


Figure 3.5: (a) AFM topographical map of the perforated gold film mounted with SU-8 micro-domes after melt flow process; (b) 3D view of figure (a). The measured periodicity of micro-dome array, height of the SU-8 micro-dome are 2.1 ± 0.03 μm and 0.4 ± 0.02 μm, respectively.

sured by inserting wire grid polarizers in the input beam path. The incident angle dependent reflectance spectra were measured using a reflection accessory (Make: Har-rick seagull). The transmittance was normalized with respect to the transmittance of

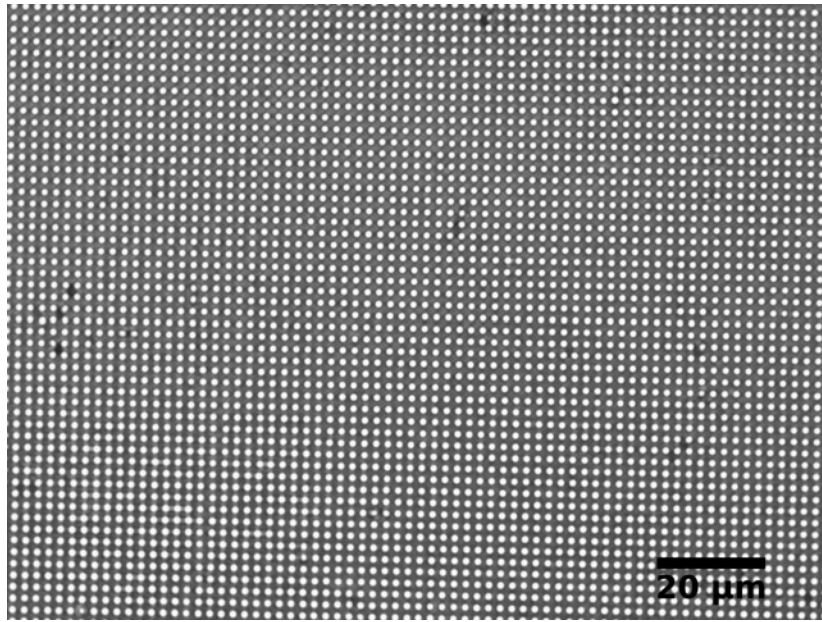


Figure 3.6: Optical microscopy image of the SU-8 micro-domes mounted sample taken in transmission mode using 100 \times objective lens.

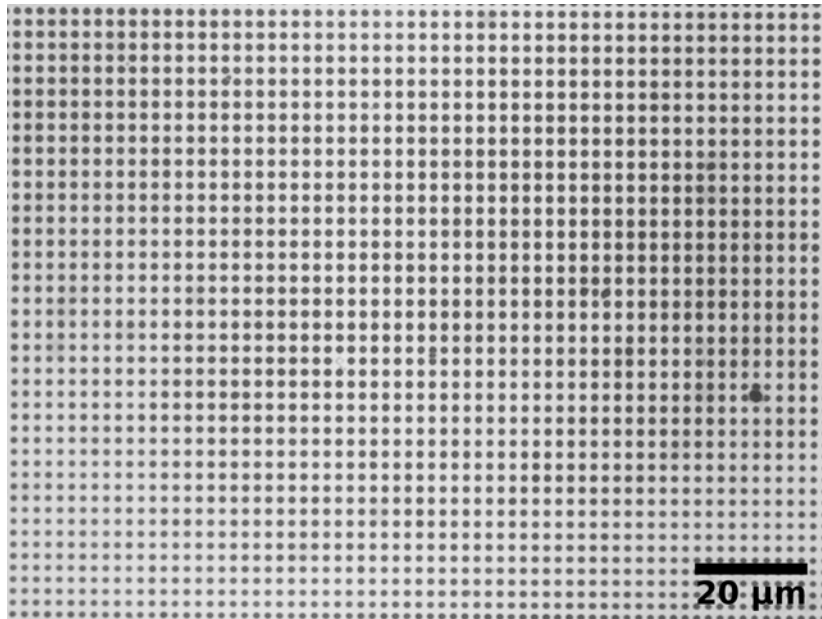


Figure 3.7: Optical microscopy image of the SU-8 micro-domes mounted sample taken in reflection mode using 100 \times objective lens.

fused silica at the corresponding polarizations and incident angles, while the reflectance was normalized with respect to the reflectance from a smooth gold film. Since, fused silica is transparent over the wavelength ranges from 200 nm to 4.5 μm . So, we have

used this as a substrate to ensure the back exposure for fabrication of SU-8 microdomes over the holes using the UV laser operating at 266 nm wavelength, and also due to their transparency in the long wavelength infrared (LWIR) band. To measure the actual transmittance through the perforated gold film, it was normalized with respect to the transmittance through the fused silica. The absorption (A) was calculated as, $A = 1 - R - T$ from the reflection and transmission at any specified wavelength and angle.

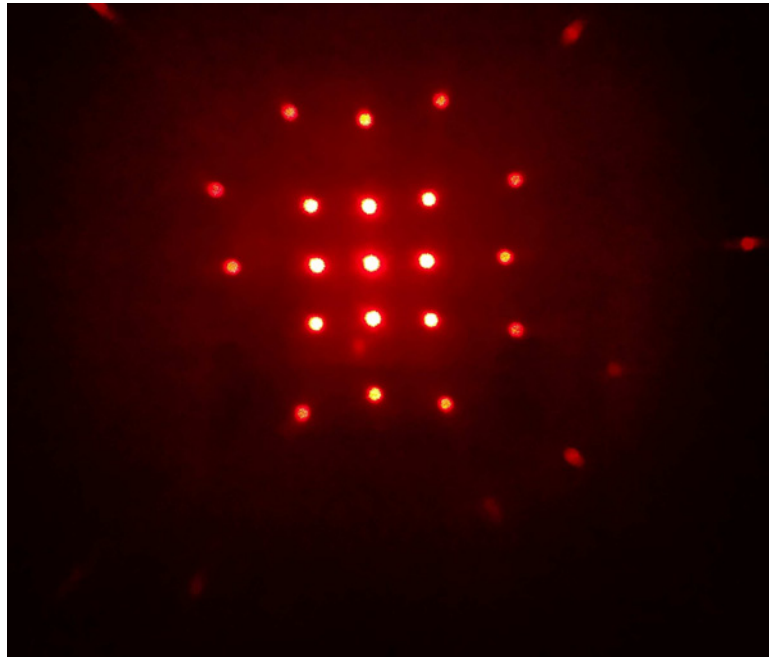


Figure 3.8: Diffraction pattern through the periodically perforated gold film when each hole is mounted with US-8 micro-dome.

Fig. 3.9 shows the measured transmittance spectra (at normal incidence of light) of (i) the bare perforated gold film, (ii) when uniformly coated with an SU-8 thin film (before UV exposure), and (iii) when the holes are mounted with the SU-8 micro-domes. The transmittance spectrum of the uncoated perforated gold film shows a peak transmittance of about 39% at a wavelength of $3.2 \mu\text{m}$. The main effect in the transmission spectrum due to the coating of the SU-8 film (before UV exposure) is a red-shift of the fundamental peak to a wavelength of $3.75 \mu\text{m}$, coupled with a small broadening of the peak. The spectrum also shows a couple of minor peaks with 15% and 14%

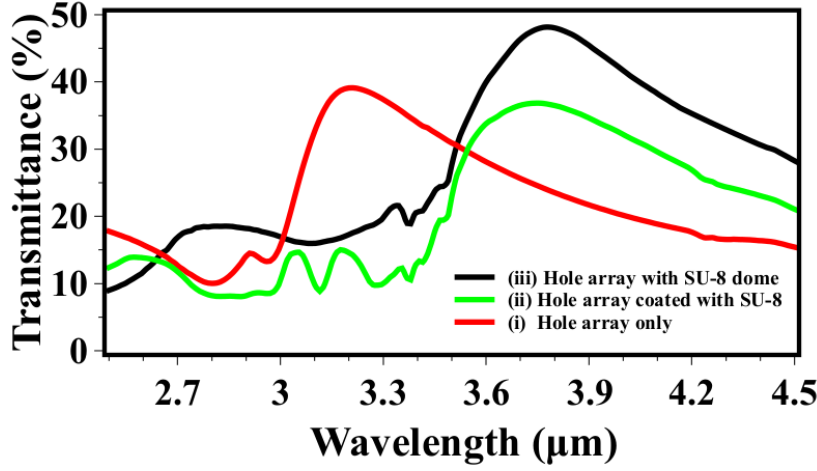


Figure 3.9: (a) Measured infrared normalized transmittance spectra of the perforated gold film (i); when coated with an SU-8 layer before UV curing (ii); and when SU-8 micro-domes are mounted on the holes of the gold film (iii).

transmittance at $3.17 \mu\text{m}$ and $3.04 \mu\text{m}$. The transmission spectrum of the hole array mounted with SU-8 micro-domes has a fundamental peak at $3.75 \mu\text{m}$ with an enhanced transmittance of about 48%. A minor peak with a transmittance of 19% at $2.8 \mu\text{m}$ is also seen. The spectral features between $3.3 \mu\text{m}$ - $3.5 \mu\text{m}$ (shown by the grey area) in the measured transmittance (Fig. 3.9 and Fig. 3.10(a, b)), reflectance (Fig. 3.11(a, b)) and absorbance (Fig. 3.12(a, b)) arise due to the absorption bands of cyclopentanone present in the SU-8 photoresist [167].

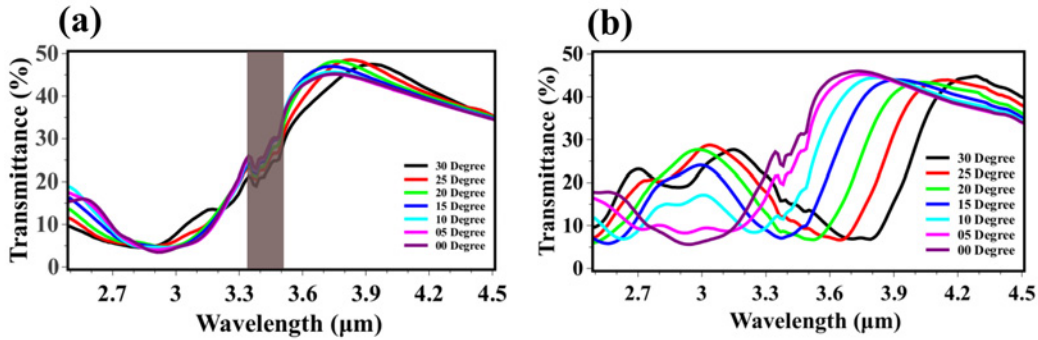


Figure 3.10: Transmittance through the periodically perforated gold film mounted with SU-8 micro-domes on each hole. Measured transmittance spectra at different incident angles ($0^\circ \leq \theta \leq 30^\circ$) for (a) the TE polarized light and, (b) the TM polarized light.

Figs. 3.10(a) and (b) show the measured transmittance spectra of the samples for different polarizations (TE and TM) of the light incident at different incident angles

($0^\circ \leq \theta \leq 30^\circ$). For the TE polarized light, there are only slight variations in the spectra, with small shifts in the wavelengths of the transmission peaks and dips occurring with increasing the angle of incidence. In the case of the TM polarization, however, there are large shifts of the transmission peaks and dips to longer wavelengths with increasing the angle of incidence. The higher order ($\pm 1, \pm 1$) transmittance peak appears to split up at large angles of incidence. Rotation of the sample about its normal can also lead to wavelength shifts of the resonances, due to the square shaped holes that are rotated by 45° from the arrays axes.

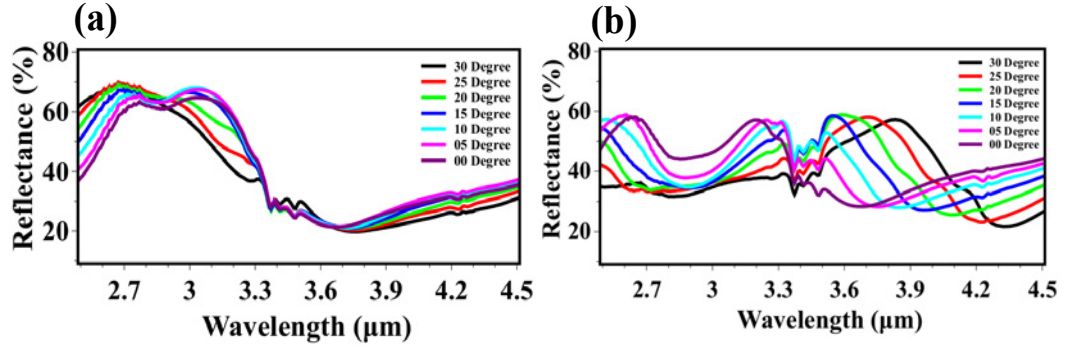


Figure 3.11: Reflectance from the periodically perforated gold film when SU-8 microdomes are mounted on the holes. Measured reflectance spectra at different incident angles ($0^\circ \leq \theta \leq 30^\circ$) for the (a) TE polarized light and, (b) TM polarized light. The measured reflectance spectra are normalized with reflectance from a smooth gold film at the corresponding polarizations and incident angles.

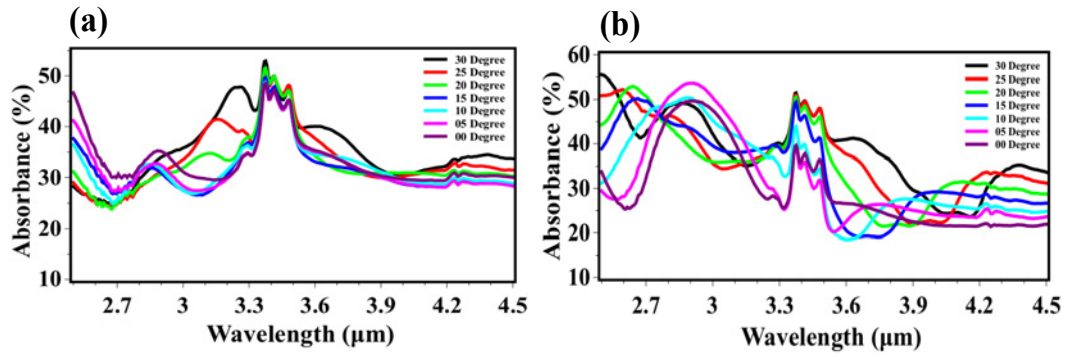


Figure 3.12: Absorption spectra at different incident angles ($0^\circ \leq \theta \leq 30^\circ$) for the (a) TE polarized polarization and (b) TM polarization. In each case, the absorption is obtained from the measured transmittance (T) and reflectance (R) as $A = 1 - T - R$.

The measured reflectance spectra for the TE and TM polarizations of incident

light of the micro-dome mounted samples are shown in Fig. 3.11(a) and (b), respectively. The reflection spectra were measured with the light incident on the air side of the sample. The reflection spectra are complementary to the transmission spectra. At normal incidence, the measured reflection spectra exhibit two minima located at about $3.7\ \mu\text{m}$ and $2.9\ \mu\text{m}$ for the TE and TM polarizations, respectively. In the case of the TE polarization, there is a slight change in magnitude as well as in wavelength of fundamental and higher order minima. But, in the case of TM polarization, there is a shift towards longer wavelengths in fundamental order minima and slight change in wavelength in higher order minima with increasing the angle of incidence (Fig. 3.11(b)).

The absorbance spectra calculated from the corresponding transmittance [Fig. 3.10] and reflectance [Fig. 3.11] spectra for the TE and TM polarizations are shown in Fig. 3.12. There is an enhancement in the fundamental order absorption peak and decrement in higher order absorption peak with increasing the angle of incidence in the case of TE polarization. But, in the case of TM polarization, there is an enhancement in fundamental order absorption peak and decrement in the higher order absorption peak with increasing the angle of incidence. In addition to the increment in the fundamental and decrement in the higher order absorption mode, both modes are shifting towards the longer wavelengths with increasing the angle of incidence. The material absorption peaks of the cyclopentanone show up prominently in the absorption spectra.

3.2 Electromagnetic simulations

The COMSOL Multiphysics software was used to calculate the electromagnetic fields in the structure to understand the origin of the EOT better. Periodic boundary conditions were used along the x and y directions to simulate an infinite array of unit cells to reduce the complexity of the simulation. Perfectly matched layers (PML) were used

along the propagation direction (z -direction) to prevent the reflection of the waves from the top and bottom domain boundaries. The dispersive refractive indices (real and imaginary parts) of evaporated gold and fused silica were taken from Refs [19, 22] and [22], respectively. The SU-8 was assumed to have a complex refractive index of $1.561 + 0.0024i$ [23]. A lot of simulations were performed with changing the different parameters to find out the optimum transmittance, and it is verified that our a new design of the sub-wavelength hole array mounted with dielectric micro-domes can be used to further enhance the transmittance.

3.2.1 Statistical analysis of the hole sizes

Generally, the structures fabricated using LIL and lift-off process do not have a uniform hole size across the sample. The non-uniformity in the hole sizes can cause broadening of spectra or lead to the shift of spectral peaks, and it becomes difficult to match the experimental results with that of simulations or analytical. To find out the distribution of dimension of the holes, the diagonal of more than 100 holes of the sample were measured over a large area. The corresponding statistical distribution of the hole sizes of the perforated gold film is shown in Fig. 3.13. The statistical distribution suggests that the most of the holes have diagonal around $1\ \mu m$.

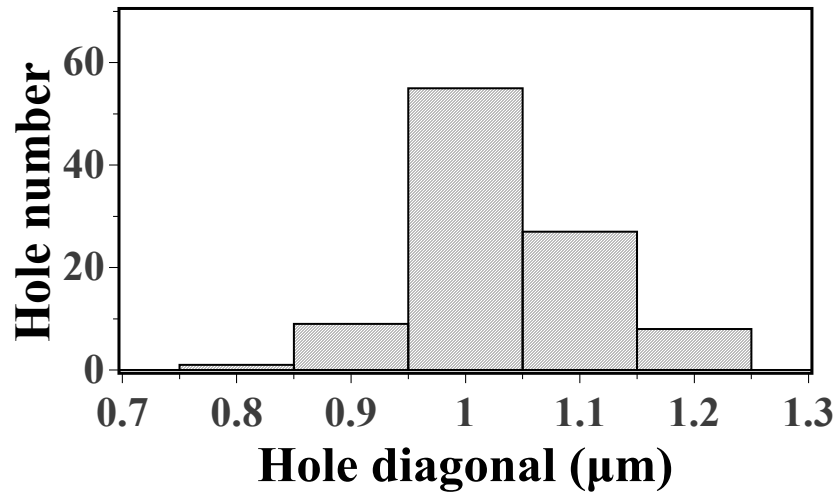


Figure 3.13: Statistical distribution of hole sizes in the perforated gold film.

The weighted average transmittance was numerically calculated over the transmittance through different sizes of the holes to take into account of the structural inhomogeneity of the sample. Figs. 3.14(a) and (b) show the transmittance spectra of different sizes of the holes without and with SU-8 micro-domes, respectively. The black spectrum in Fig. 3.14(a) and (b) corresponds to the weighted average transmittance through different sizes of the hole. In addition to inhomogeneity and shapes of the fabricated structures, some broadening of the transmittance peak also arises due to the angular width of the incident beam caused by the parabolic mirror in the FTIR spectrometer. Figs. 3.15(a) and (b) show the calculated angular weighted average transmittance (black line) through sub-wavelength hole array mounted with SU-8 micro-domes at different incident angles for the TE and TM polarizations, respectively. The weighted average angular transmittance was calculated by assuming the incident beam as a Gaussian with 5° angular widths. It is clear that the non zero base-line in measured transmittance is caused by the angular width of the incident beam.

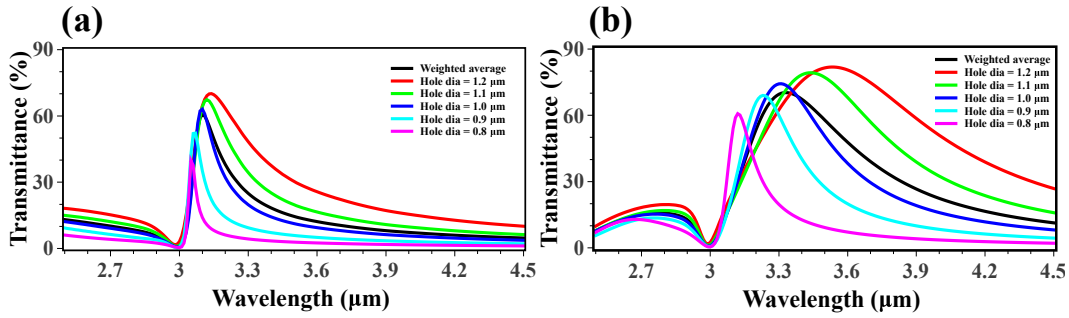


Figure 3.14: (a) Simulated transmittance through the different sizes of the hole in the perforated gold film and weighted average transmittance (black line) through different sizes of the hole. (b) simulated transmittance through the different sizes of the hole in perforated gold film mounted with SU-8 micro-domes and weighted average transmittance (black line) through different sizes of the hole mounted with SU-8 micro-domes. A residual layer of SU-8 of thickness 200 nm was assumed to be present on the gold film in calculation with the micro-dome.

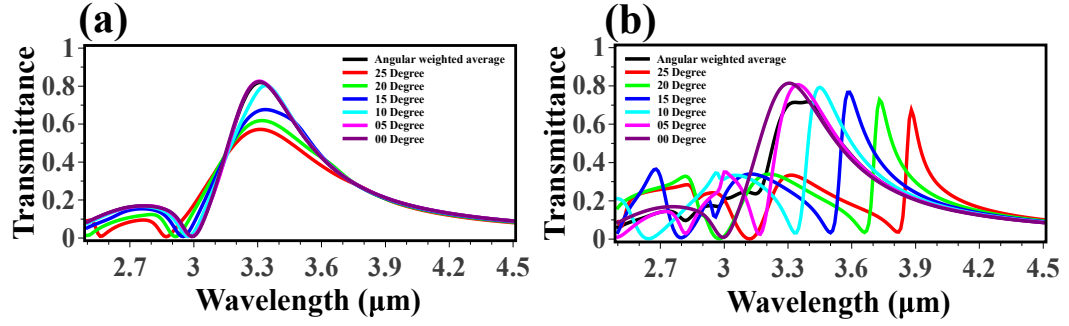


Figure 3.15: Simulated transmittance spectra at different incident angles ($0^\circ \leq \theta \leq 25^\circ$) through the hole array mounted with the SU-8 micro-dome and having residual layer of SU-8 of thickness 200 nm on the gold film, and the corresponding angular weighted transmittance (black line) at different incident angles (a) TE polarization (b) TM polarization. The parameters used for simulations: thickness of the gold film, the periodicity of the hole array and height of the micro-dome are 40 nm, 2.1 μm and 400 nm, respectively.

3.2.2 Effects of shape and size of dielectric structures

Fig. 3.16 shows the simulated comparative transmittance spectra corresponding to the conical and cylindrical microstructures mounted on the holes of the periodically gold film with 200 nm residual layer of SU-8. It is clearly shown that the transmittance enhancement is higher in the case of conical microstructure than for the cylindrical ones. However, there is a slight shift in resonance towards longer wavelengths and broadening in the resonance band in the case of cylindrical microstructure. Fig. 3.17 shows the simulated transmittance spectra corresponding to different heights of the micro-dome. With the increase in the height of the micro-dome, there is a slight shift in resonance towards longer wavelengths whereas amplitude of the transmittance remains almost constant.

Fig. 3.18 shows the simulated weighted averaged transmittance through different hole sizes varying from 0.6 to 1.2 μm without the SU-8 micro-dome (red line) and with SU-8 micro-domes (black line). A layer of 200 nm was assumed in simulation on the top of the gold film as a residual layer left behind after the development process. These weighted average transmittances had already been shown in Fig. 3.14 by the black line.

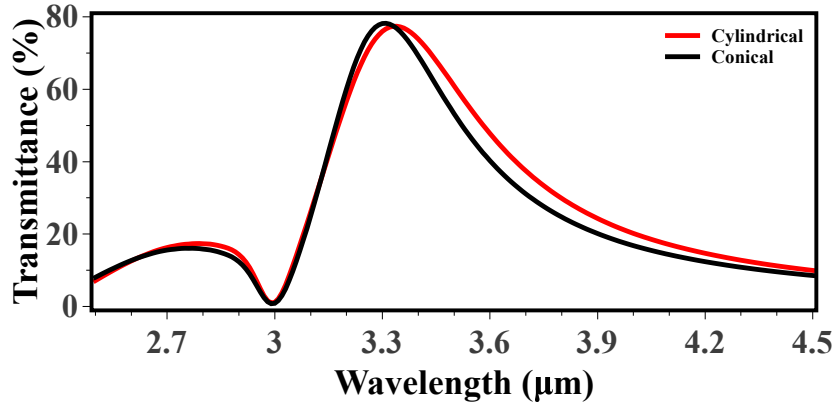


Figure 3.16: Simulated transmittance spectra corresponding to the conical and cylindrical SU-8 microstructure mounted on the holes of the perforated gold film with 200 nm residual layer of SU-8. The parameters used for simulations are: thickness of the gold film, the periodicity of the hole array, thickness of residual SU-8 layer and height of the cylindrical microstructure and conical microstructure are 40 nm, 2.1 μm, 200 nm, 400 nm and 400 nm respectively.

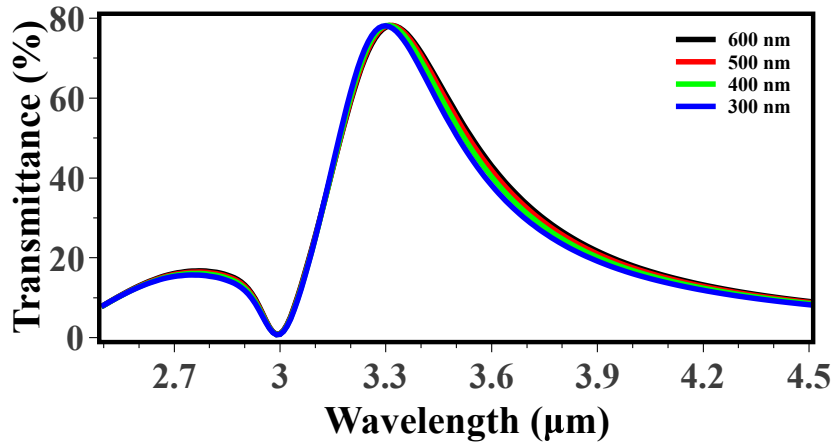


Figure 3.17: Simulated transmittance spectra of the perforated gold film mounted with different heights of the micro-dome with residual layer of SU-8 of thickness 200 nm on the gold film.

To check the contribution of the SU-8 residual layer left behind on the gold film to the localized electric fields as well as to the transmittance, the color maps of the square of absolute value of the electric fields has been plotted. Fig. 3.19 shows the color maps of the square of the absolute value of electric field at the resonance wavelength for different cases of the hole array with and without the SU-8 micro-dome, and with different thickness of the residual layer of the SU-8 assumed to be present on the gold film. The corresponding scale bar of the square of absolute value of electric field is

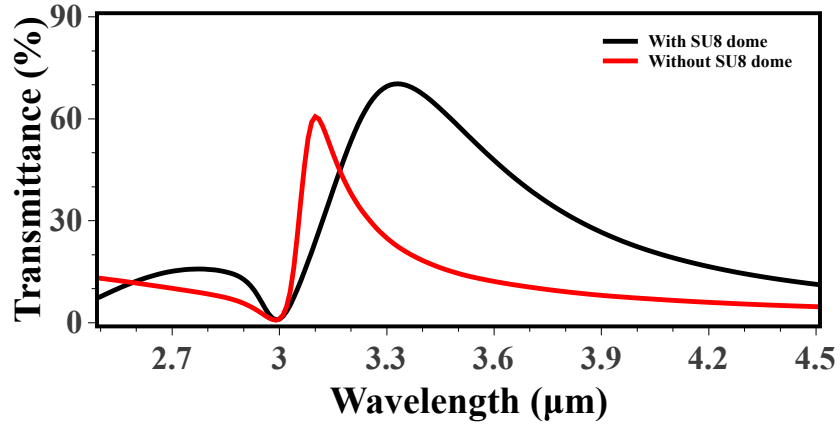


Figure 3.18: Simulated weighted average transmittance through different sizes of the hole in the gold film without mounting of micro-dome (red line), and with mounting the micro-domes on the holes with a residual layer of SU-8 of thickness 200 nm (black line). The parameters used for simulations are: thickness of the gold layer = 40 nm, array lattice constant = $2.1 \mu\text{m}$ and height of the micro-dome = $0.4 \mu\text{m}$.

shown to the right of each figure. Evolution of the localized near-field intensity can be seen by the maximum value of the corresponding scale bar for the different cases. We can see that an SU-8 film thickness of 500 nm no longer makes any contributions to the enhancement of the transmittance which is clear from the inset of Fig. 3.19(d). The measured enhancement appeared to be well described when the SU-8 layer thickness is taken to be about 200 nm. So we considered the 200 nm thickness of the SU-8 layer in simulations.

Figs. 3.20(a) and (b) show the measured transmittance spectra of the samples for different polarizations (TE and TM) of the light incident at different incident angles ($0^\circ \leq \theta \leq 30^\circ$). For the TE polarized light, there are only slight variations in the spectra, with small shifts in the wavelengths of the transmission peaks and dips occurring with increasing the angle of incidence. In the case of the TM polarization, however, there are large shifts of the transmission peaks and dips to longer wavelengths with increasing the angle of incidence. The higher order ($\pm 1, \pm 1$) transmittance peak appears to split up at large of incident angles. Rotation of the sample about its normal can also lead to wavelength shifts of the resonances, due to the square shaped holes

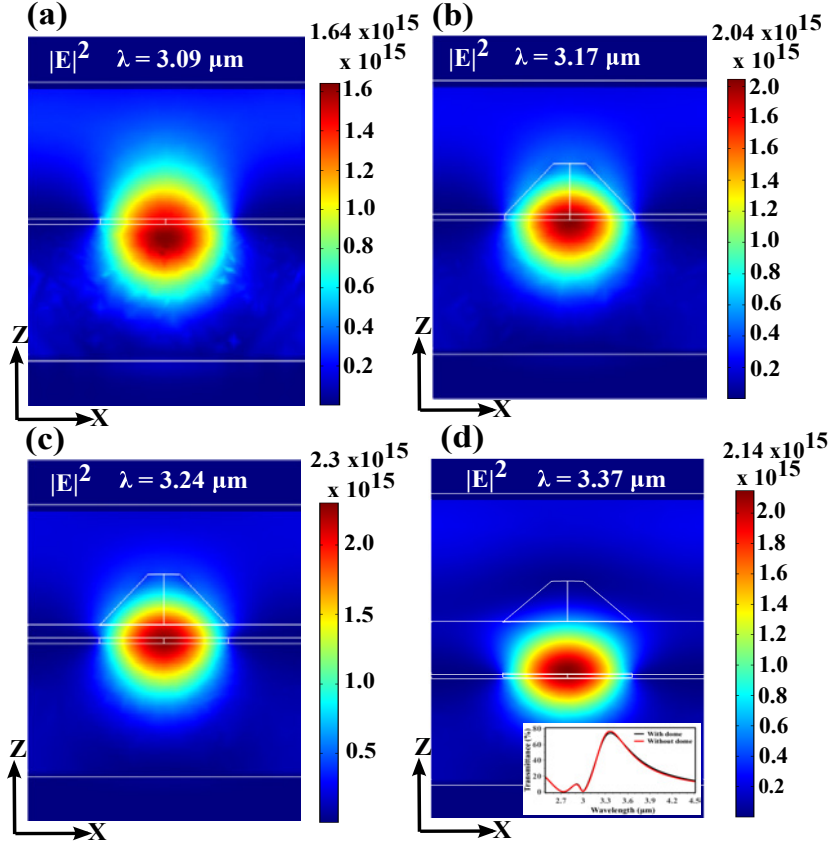


Figure 3.19: Square of the absolute value of electric field for (a) perforated gold film, (b) hole array mounted with micro-dome without the residual layer of SU-8, (c) hole array mounted with micro-dome with residual layer of SU-8 of thickness 100 nm on the gold film, (d) hole array mounted with micro-dome with a residual layer of SU-8 of thickness 500 nm, and the inset transmittance spectra through the hole array with 500 nm residual SU-8 layer with and without the micro-domes.

that are rotated from the arrays axes.

The corresponding simulated reflectance spectra for the TE and TM polarizations of the micro-dome mounted samples are shown in Fig. 3.21. At normal incidence, the simulated reflection spectra exhibit two minima located at about $3.3 \mu\text{m}$ and $2.8 \mu\text{m}$ for the TE and TM polarizations respectively (Fig. 3.21). In the case of the TE polarization, the higher order minimum monotonically decreases and the fundamental order minimum fluctuates in magnitude as well as in wavelength (Fig. 3.21(a)). But, in the case of TM polarization, there is a shift towards longer wavelengths in the fundamental as well as the higher order mode with increasing the angle of incidence

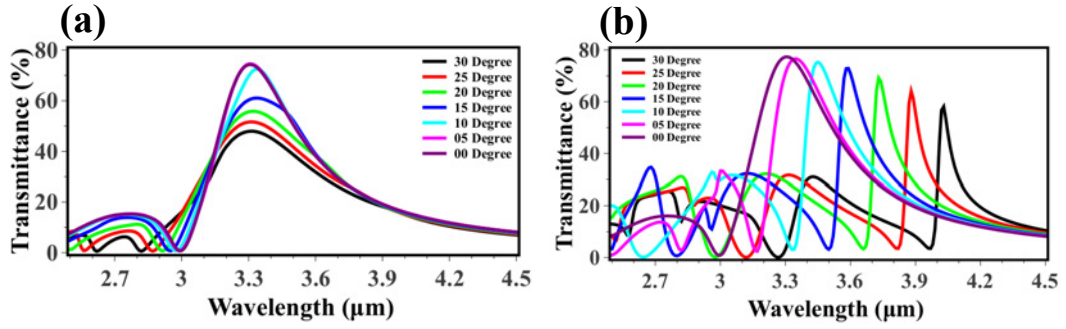


Figure 3.20: Simulated transmittance spectra of the periodically perforated gold film mounted with the micro-dome on each hole with a residual layer of SU-8 of thickness 200 nm at different incident angles ($0^\circ \leq \theta \leq 30^\circ$) for the (a) TE polarization, and (b) TM polarization. The simulated spectra are not averaged over the hole sizes or angles here to understand the angle dependency.

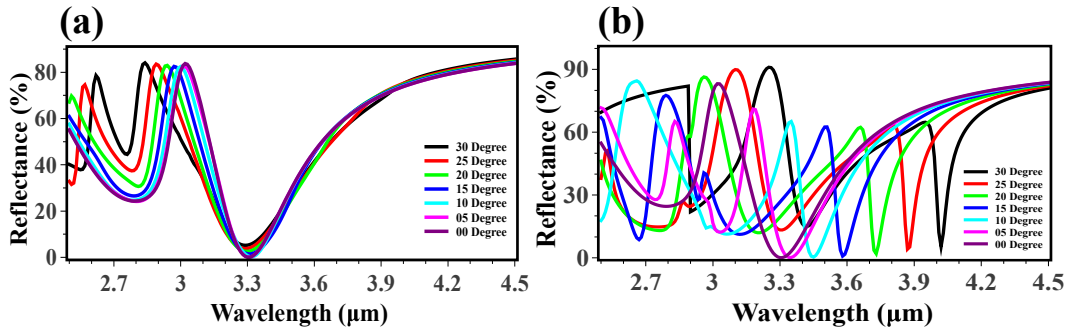


Figure 3.21: Simulated reflectance spectra of the periodically perforated gold film mounted with SU-8 micro-dome on each hole with a residual layer of SU-8 of thickness 200 nm at different incident angles ($0^\circ \leq \theta \leq 30^\circ$) for the (a) TE polarization, and (b) TM polarization.

(Fig. 3.21(b)).

The absorbance spectra calculated from the corresponding transmittance [Fig. 3.20] and reflectance [Fig. 3.21] spectra for the TE and TM polarizations are shown in Fig. 3.22. The fundamental order absorption peak is enhanced and the higher order absorption peak is decreased with increasing the angle of incidence in the case of TE polarization. But, in the case of TM polarization, the fundamental order absorption peak is enhanced while the higher order absorption peak is decreased with increasing the angle of incidence. In addition to the increment in the fundamental and decrement in the higher order absorption mode, both modes are shifting towards longer

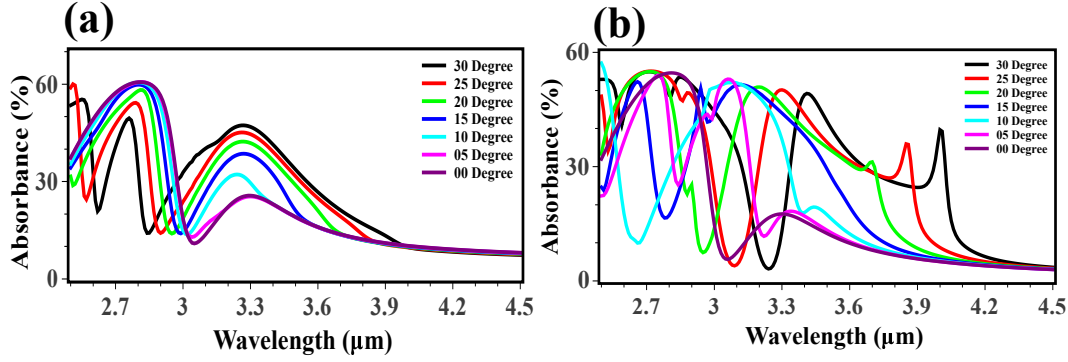


Figure 3.22: Simulated absorption spectra at different incident angles ($0^\circ \leq \theta \leq 30^\circ$) for the (a) TE polarized polarization and (b) TM polarized polarization. In each case, the absorption is obtained from the measured transmittance (T) and reflectance (R) as $A = 1 - T - R$.

wavelengths with increasing the angle of incidence.

3.3 Results and discussions

The simulated transmittance spectra have almost the same peak positions but had much narrower bandwidths. On the closer examination, we found that the bandwidth can increase drastically due to the (i) increased size of holes, (ii) angle of incidence for the TM polarization, (iii) a thin layer of SU-8 left over the gold film and (iv) reduced thickness of the gold film. We measured the distribution of hole sizes obtained by our process from AFM images. To understand these effects, we computed the transmittance for the array of various hole sizes, different angle of incidence and polarizations and carried out the average of these transmittances by considering the distribution of hole sizes, and incident beam as a Gaussian of 5° angular widths caused by the parabolic mirror in the FTIR spectrometer. We expect no contribution from interference effects as the different sizes would be randomly positioned in the sample. If the holes of a particular size were arranged periodically, then the response from different sizes of hole arrangement would have a slightly different result, and may be the resultant would give slightly different responses of the interference effects. The inherent broadening in the

measurement becomes clearly apparent. The non zero base line for the transmittance also arises due to the distributions of incident angles.

Fig. 3.16 shows the simulated transmittance spectra of the conical and cylindrical microstructure mounted on the holes of the periodically perforated gold film with 200 nm residual layer of SU-8. There is a slight change in amplitude of the transmittance as well as in resonance wavelength. The shift to longer wavelengths in the resonance in the case of a cylindrical micro-dome is due to the capacitive load caused by the increase in refractive index of the surrounding medium. The volume of the cylinder microstructure is more than that of the conical microstructure, and hence there is an increase in the overall effective refractive index of the surrounding medium. So it causes a resonance shift to longer wavelengths.

The height dependent simulated transmittance spectra of the micro-domes are shown in Fig. 3.17. There is a slight shift in resonance towards longer wavelengths due to the capacitive load caused by the change in the refractive index of the surrounding medium. The filling fraction of the high refractive index material (SU-8) in comparison of air increases due to a rise in the height of the micro-domes, and hence results in an overall increment in the effective refractive index of the surrounding medium. However, the transmittance amplitude remains almost constant even with increasing the height of the micro-dome. With increase in the height of the micro-dome, the effective refractive index on the top of perforated film increases, so more light is reflected due to the mismatch in refractive index with the surrounding medium. Hence, with an increase in height micro-dome, the transmission amplitude remains almost constant.

The simulated transmittance spectrum (Fig. 3.18) averaged over the hole size distribution shows a good correspondence with the measured transmittance spectrum (Fig. 3.9). There is a significant enhancement of transmittance peak as well as the bandwidth and the longer wavelengths shift in transmission peak due to the mounted SU-8 micro-domes. However, the magnitude of the transmittance in the simulation

is more than that of the measured transmittance, while the bandwidth is somewhat narrower. These differences are due to the inhomogeneous broadening caused by the varying sizes of the holes and the average over the excitation angles. The edges of the holes are also rough due to the lift-off process, which is known to increase the absorption and broaden the peaks.

In Fig. 3.18(a), the transmittance spectrum of the bare perforated gold film shows a primary peak with 39% transmittance at wavelength $3.2 \mu\text{m}$ that we call the fundamental peak. This arises from the coupling of the incident light to the (0, 1) or (1, 0) waveguide mode of the hole, and is primarily responsible for the spoof surface plasmon polariton (SSPP). It should be noted that light with any polarization at normal incidence will couple to both the (0, 1) and (1, 0) waveguide modes due to the rotated square holes (45° with respect to the array axes). When the hole array is coated with the continuous SU-8 film, it is observed that the transmission peak gets red shifted to a wavelength of $3.75 \mu\text{m}$. This arises due to the capacitive loading of the resonance caused by the larger refractive index of the SU-8. The transmittance peak decreases to 36.5% due to the larger mismatch in the refractive indices of air and the SU-8 coating. The peaks at shorter wavelengths ($3.04 \mu\text{m}$ and $3.17 \mu\text{m}$) arise due to Fabry-Pérot resonances in the SU-8 layer and disappear when the unexposed portions of the SU-8 film are washed off in the development process.

The transmission spectrum when the holes are mounted with the SU-8 domes consists of two main peaks: the peak at the wavelength of $3.75 \mu\text{m}$ with about 48% transmittance is caused by the fundamental waveguide mode (0,1 or 1,0) while the peak at the wavelength of $2.8 \mu\text{m}$ with 19% transmittance is caused by coupling to the higher order (1,1) mode. Thus, there is a gross enhancement by about 9% in the fundamental order transmission peak apart from the broadening of the peak. Now enhanced transmittance occurs at least over the $3 - 4.5 \mu\text{m}$ band. The dip in the transmittance wavelength around $\lambda = 2.9 \mu\text{m}$ is ascribed to the Wood's anomaly, which is caused due to the absorption of the diffracted wave as it propagates in the

plane of the perforated film. This enhancement of the transmittance can be principally attributed to the scattering of light from the SU-8 micro-domes, which causes the light to get coupled to the modes of the perforated holes in the near-field.

We note here that the full amount of SU-8 film may not be washed away properly due to the development of scattered near field of the holes. To account for this, we assumed that some amount of SU-8 was left behind on the gold film apart from the region of the holes and computed transmittance and near field in that case (Fig. 3.19(a – d)). It is found that the small thickness (50 - 200 nm) of SU-8 can give rise to an immense broadening of the transmittance. From the electromagnetic near-field calculations, we can see that an SU-8 film thickness of 500 nm no longer makes any contributions to the enhancement in transmittance. But, experimentally measured enhancement that appears to be well described when the thickness of the SU-8 layer is taken to be 200 nm. We note here that there are uncertainties in the refractive index of the SU-8. We used $n = 1.561 + 0.0024i$ and that can also be a source of some broadening.

Fig. 3.10(a) and 3.20(a) show the measured and simulated transmittance spectra for the TE polarized light at different angles of incidence ($0^\circ \leq \theta \leq 30^\circ$). The fundamental transmittance peak is measured to increase up to $\sim 20^\circ$ angle of incidence and starts decreasing and shifts towards longer wavelengths with a further increase of incident angles. The dip in the transmittance (Fig. 3.10(a)) shifts only slightly towards lower wavelengths with increasing the angle of incidence and the magnitude of the transmittance changes only slightly. There is very little shift in transmittance because of the lack of dispersion of the localized resonant mode, and only some retardation induced shifts can be present. The SU-8 micro-domes scatter the incident light which couple with SPP generated on the gold film, in addition to that it may couple with the radiation into the holes via the near-fields of the micro-domes. The scattered near-fields have only a weak dependence on the angle of incidence as the micro-domes are sub-wavelength in size. This coupling can also be another reason for the very slight shift

of transmission peak with increasing the incident angles. The simulated fundamental transmittance peak value (Fig. 3.20(c)) decreases with increasing angle of incidence.

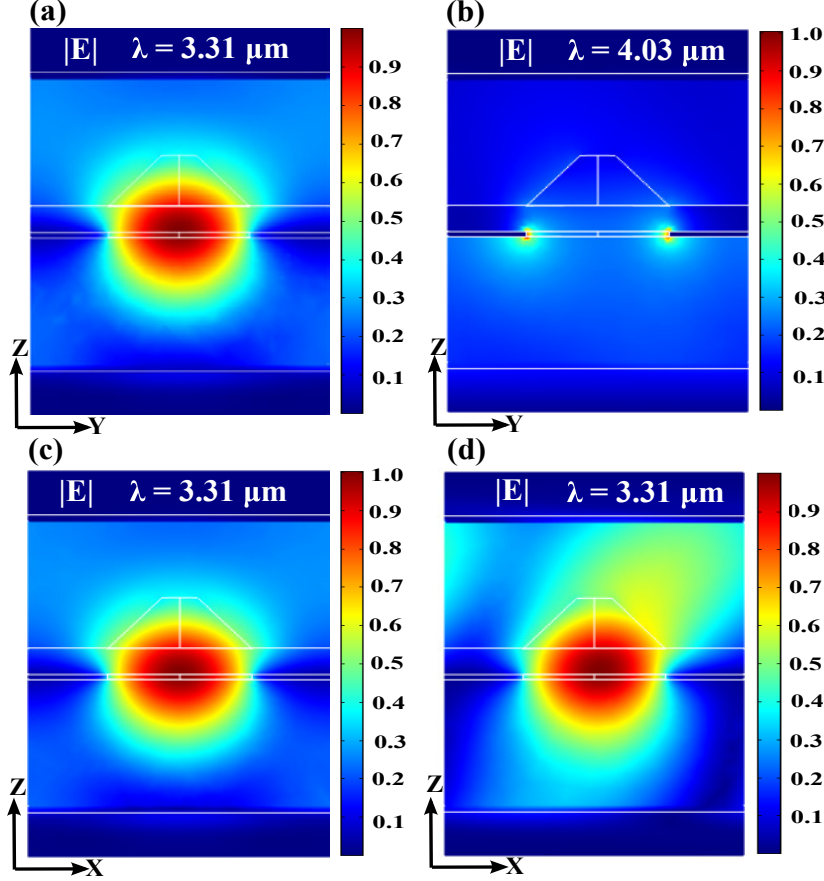


Figure 3.23: Normalized electric fields at incident angles $\theta = 0^\circ$ (a, c) and $\theta = 30^\circ$ (b, d) for the TM (a, b) and TE (c, d) polarizations. The corresponding color bars for the field strengths are shown to the right of each plot.

In the case of TM polarized light (Figs. 3.10(b) and 3.20(b)), there is a shift of the transmission peaks to longer wavelengths corresponding to the fundamental and higher order modes. These shifts are due to the coupling of the incident light to SPP via the diffracted modes. The transmission peak at the lower wavelength (corresponding to the excitation of the higher order mode) splits with increasing the angle of incidence. The splitting in the higher order mode can be understood by the dispersion of the SSPP propagating at the interface between the perforated metal film and the substrate. The

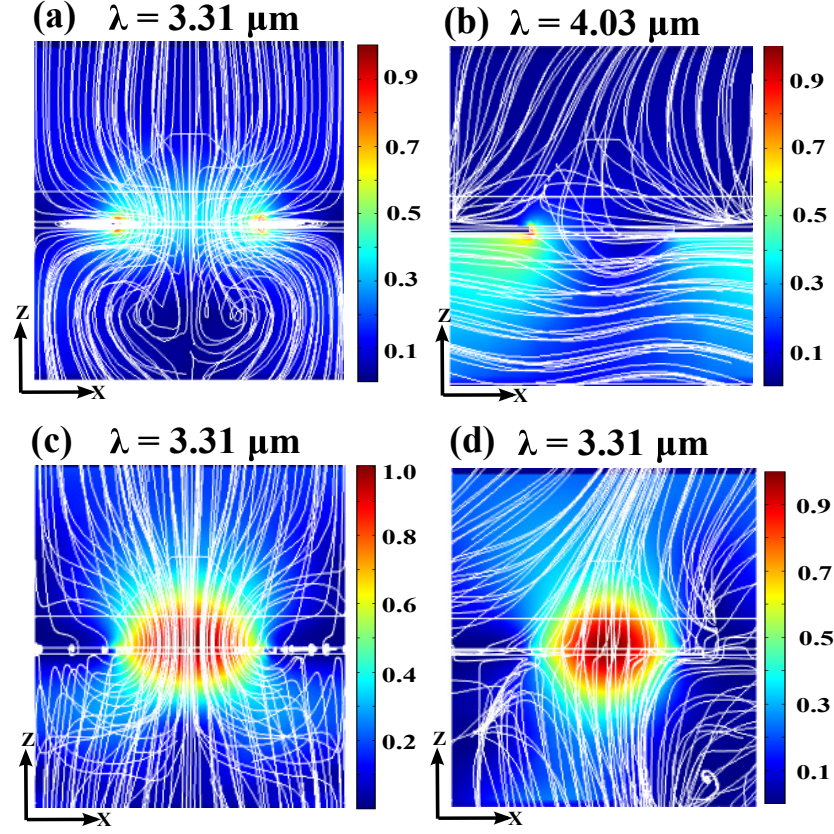


Figure 3.24: Color maps of the normalized time average power with Poynting vector field lines at incident angles $\theta = 0^\circ$ (a, c) and $\theta = 30^\circ$ (b, d) for the TM (a, b) and TE (c, d) polarizations. The corresponding color bars for the strength of time average power are shown to the right of each plot.

wave vector of the SSPP excited by the diffracted modes can be written as

$$\vec{k}_{sp} = (k_0 \sin \theta \pm m2\pi/p)\hat{x} + (\pm n2\pi/p)\hat{y}, \quad (3.1)$$

where, $n_s = \sqrt{\epsilon_s}$ is the refractive index of the substrate, $|k_{sp}| \approx 2\pi n_s/\lambda_{sp}$, $k_0 = 2\pi/\lambda$, p is the period of the hole array and θ is the angle of incidence for the TM polarized light [1] and, m and n are diffraction order along x and y directions, respectively. The electric field has a component along the x -axis and causes a lifting of the degeneracy of the modes propagating along the positive and negative x -directions [168]. Hence, for $\theta > 0$, the second order diffracted mode $(\pm 1, \pm 1)$ splits into two modes $(-1, \pm 1)$ and $(+1, \pm 1)$. The corresponding resonance wavelengths for the degeneracy lifted modes are

$\lambda_{2-} = n_s / \sqrt{(1/p - \sin \theta / \lambda_0)^2 + 1/p^2}$ and $\lambda_{2+} = n_s / \sqrt{(1/p + \sin \theta / \lambda_0)^2 + 1/p^2}$, where λ_0 is the resonance wavelength for normal incidence. With increasing incident angle, the $\sin \theta / \lambda_0$ term in λ_{2-} and λ_{2+} leads to larger and shorter wavelength shifts for the $(-1, \pm 1)$ and $(+1, \pm 1)$ modes, respectively. This is confirmed by the experimental and simulation results as shown in Figs. 3.10(b) and 3.20(b).

The localized electric fields corresponding to the fundamental order mode with the highest transmittance peak were calculated and plotted in Fig. 3.23 at incident angles of $\theta = 0^\circ$ (a, c) and $\theta = 30^\circ$ (b, d) for the TM (a, b) and the TE (c, d) polarizations. The guidance provided to the electromagnetic waves at normal incidence by the micro-dome mounted on the holes of perforated film is clearly seen in the streamline maps of the power-flow shown in Fig. 3.24. The near-field distribution of the light is highly localized just below each micro-dome within the substrate. The extent of localization of the fields inside the substrate depends on the hole size in the film and axially extends out (along with the z-direction) with increasing size of the holes. The transversely localized fields can be changed using the different sizes of the micro-dome mounted on the holes. There is a large decrease in the localized electric fields in the case of TM polarization as the angle of incidence increases. Here the parallel component of the electric field responsible for coupling of SSPP to the micro-domes decreases with increasing angle of incidence and hence the localized electric fields as well as the transmittance decrease. Plots of the normalized magnitude of Poynting vector fields (color scale) and Poynting vector fields lines are shown in Fig. 3.24 at the incident angles of $\theta = 0^\circ$ (a, c) and $\theta = 30^\circ$ (b, d) for the TM (a, b) and the TE (c, d) polarizations. The Poynting vector field lines (Figs. 3.24(a, c)) when light is normally incident indicate that there is strong transmission associated with the coupling of SSPPs through the SU-8 micro-domes, whereas at $\theta = 30^\circ$ (b, d), a much weaker transmittance is associated with a lower coupling of SSPPs through the SU-8 micro-domes. At $\theta = 30^\circ$, very few vector field lines couple through the micro-domes for the TM polarized light (Fig. 3.24(b)) because of the magnitude of the parallel component of the electric field, which causes the

generation of SSPP at the metal-dielectric interface decreases with increasing the angle of incidence as noted while discussing the fields above. In the case of TE polarization, the magnitude of the parallel component of the electric field, which coupled to the waveguide modes at the metal-dielectric interface is independent of incident angles, and hence larger number of vector lines couple through the micro-domes even at large incident angles (Fig. 3.24(d)).

3.4 Conclusions

We have experimentally and numerically demonstrated that periodically perforated gold film mounted with dielectric micro-domes shows an enhanced transmittance over a broader frequency bandwidth with more localized near-fields at mid-wave infrared wavelengths ($3 - 4.5 \mu\text{m}$) compared to those of with only the bare holes in the gold film. The micro-domes work as scatters that scatter the incident light and help in coupling of more incident light compared to bare holes (without micro-domes) to SPPs generated on the perforated gold film which are responsible for extraordinary transmission through the perforated gold film. Thus, the more light is transmitted through the micro-domes mounted perforated gold film compared to the bare (only hole array) perforated gold film. The micro-domes have an almost lens-like action in enhancing the coupling of radiation at larger angles, and over a broader bandwidth of frequencies. These effects, however, have to describe more appropriately as due to the scattered fields, since the coupling is via the near-fields of the sub-wavelength sized micro-domes. This enables the enhanced transmittance simultaneously along with large localization of the near-fields within the substrate. An inexpensive LIL and a novel back-exposure using UV laser techniques are used to fabricate the samples over areas of 0.5 cm^2 . The fabricated samples are structurally characterized using an AFM and optically using a FTIR spectrometer. COMSOL Multiphysics software is used to verify the experimental results and understand the mechanisms for the enhanced transmission. The

discrepancies between the experimental and simulation results caused due to the structural inhomogeneity and angular divergence of the laser beam in the spectrometer are discussed and understood. The micro-domes mounted structures show a peak transmission of $\sim 48\%$, which is an enhancement of about 9% over the peak transmission through the bare holes array (without the micro-domes mounted samples). Additional features that appear at smaller wavelengths, such as the splitting in higher order transmittance peaks with increasing incident angles, are also understood in terms of the SSPPs. Such enhanced coupling is important for device applications in infrared detection, particularly in super lattice semiconductor quantum well devices, that do not allow coupling to normally incident light. The enhanced bandwidth and the spatial region of the intensely localized near-fields near the coupling layer can be designed for specific material response and geometry of the detectors, respectively for improving their sensitivity and response.

Chapter 4

Development of large area metamaterial structures for rough and flexible surfaces

The design and development of various metamaterial-based absorbers dedicated to the different potential applications from optical frequencies to microwave regimes have been reported by different groups across the globe. The most traditional tri-layer metamaterial absorbers are generally fabricated on clean and neat smooth rigid substrates. Many difficulties arise when these absorbers are applied to rough and curved surfaces. The requirement of smooth and rigid substrates with conventional micro fabrication procedures hampers the developments of metamaterial absorbers in real applications to some extent. Rendering flexibility to metamaterials can make it even possible to wrap them around curved objects of any shape. As such, metamaterial functionality on conformable rough and flexible surfaces opens up a whole new domain. Hence, researchers have been attempting to develop highly flexible and reversibly deformable electronic devices and metamaterial absorbers on rough and flexible surfaces which could offer new applications in wearable devices and systems. For instance, flexible metamaterial absorbers must be bendable for attachment to nonplanar or curved surfaces. In the

last few years, several attempts have been made to design flexible MAs on different substrates [90,169,170]. But, still the fabrication on very rough surfaces is a challenge due to which it is lagging behind in real applications because the practical surfaces are not smooth as those used in the laboratory.

In the tri-layer metamaterial absorber, a structured top conducting layer separated by a continuous dielectric layer from a bottom conducting layer. The thickness of the dielectric layer determines the capacitance for the LC resonance and determines the impedance matching for coupling maximum radiation into the resonant structure. The impedance matching condition implies complete/perfect absorption of electromagnetic radiation at corresponding frequencies. For several applications such as for camouflage, one does not need absorptivities/emissivities close to unity, but it is rather desirable to achieve a range of emissivities between 0.1 to 0.9. In this context, we realized that considerable simplification was possible as the requirement of optimal impedance matching could be relaxed for such systems. Hence we envisaged a simpler bi-layered resonant structure that could yield a resonant absorption peak at infrared frequencies resulting in high absorptivity/emissivity bands.

In this Chapter, a resonant metamaterial for controlling the emissivity/absorptivity at infrared frequencies is designed and fabricated using LIL and soft lithography techniques. The metamaterial consists of a bi-layer of conducting (gold) and dielectric (ZnS) thin films on a structured polymer (disk array), and depends on a cavity and localized surface plasmon resonances of the structure to produce high absorptivity. Schematic diagram of cross-section of the unit cell of the metamaterial absorber is shown in Fig. 4.1. The corresponding geometrical parameters are explained in the caption of the figure. COMSOL Multiphysics software is used to computationally design the structure and to understand the origin of the absorption and to check the effect of various structural parameters on the absorption. The simplified design of the metamaterial is compatible with sequential patterning and deposition processes, that does not require lift-off or etching processes, which makes the process applicable to manufacture

metamaterial surfaces on large areas. Further, it is shown that the process is applicable for the fabrication of metamaterial structures on even very rough and flexible surfaces such as emery paper and rough aluminium sheets. AFM and FTIR spectrometer have been used for measuring the structural and infrared spectral properties of the fabricated samples, respectively. Optical microscope has been used to structurally characterize the fabricated samples and substrates to check the roughness. LWIR camera has been used to capture the infrared image of the metamaterial absorber fabricated on large areas.

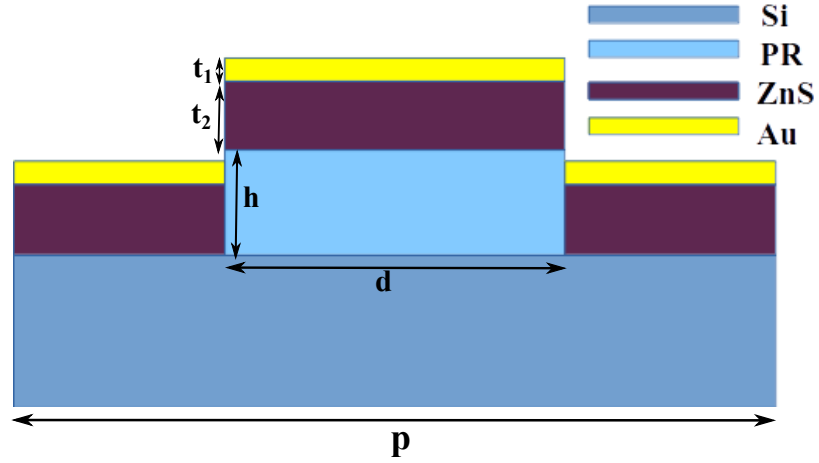


Figure 4.1: Schematic diagram of the unit cell of the metamaterial. In the diagram, p is periodicity of the disk array, h is the height of the photoresist disk, d is diameter of the disk, t_2 and t_1 are thickness of the ZnS and Au layers, respectively.

Chapter is divided into four Sections: Section 4.1 describes the details of samples fabrication using LIL & soft lithography and structural & optical characterization. Section 4.2 describes the design and simulation details of the metamaterial absorber, for examples as the dependence of reflectance, transmittance and absorbance on different parameters like the thickness of ZnS layer, pillar diameters and periodicity of the disk array. Further, the results and discussions are presented in Section 4.3 which discuss the origin of the absorption and effects of different structural parameters on the absorption, and conclusions are drawn in Section 4.4.

4.1 Experimental details: Fabrication and Characterization

4.1.1 Sample fabrication using laser interference lithography

The details of the LIL with schematic diagram and the fabrication procedures have been discussed in Chapter 2. It was used here to fabricate a disk array of photoresist on a polished silicon substrate. This could be directly used for deposition and fabrication of the absorber, or alternatively, it could be used as a master for replicating the structure on other substrates and surfaces by soft lithography techniques. A thin film of a positive photoresist was spin coated on polished cleaned silicon substrate (polished on one side) at 3000 RPM for 45 s and pre-baked at 85 °C for 60 s. The coated samples were exposed twice to a two-beam interference pattern created by a He-Cd laser. The first and second exposures were carried out for the equal periods of 3 minutes with a rotation of the sample by 90° about the substrate normal in between the exposures to create a square array of disks. The exposed samples were subsequently developed in a developer (ma D-331) for 20 s, rinsed with de-ionized water and dried by flowing dry nitrogen gas. The process left behind a square array of photoresist disks on top of the silicon substrate. Subsequently, the samples were sequentially coated with 300 nm thick ZnS film and a 40 nm thick gold using thermal evaporation in a vacuum of 10^{-6} mbar. The thickness of the films was nominally determined during deposition using a quartz crystal monitor.

4.1.2 Sample fabrication using soft lithography

The soft lithography process can be separated into two parts: one is the fabrication of a elastomeric stamp, and the other is transferring the features to the substrates

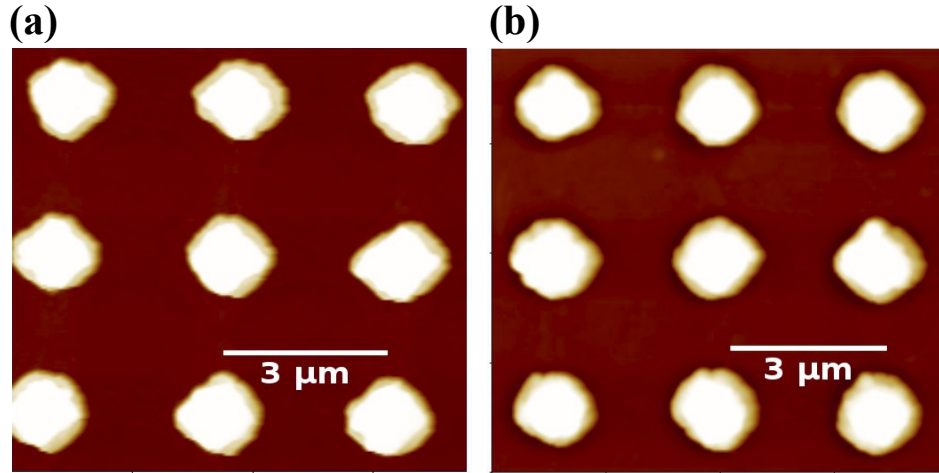


Figure 4.2: AFM topographical map of a two-dimensional disk array, (a) before the deposition of the (ZnS/Au) layers, (b) after the deposition of the (ZnS/Au) layers. The measured height of the disk, periodicity of the disk array, ZnS layer thickness and top gold layer thickness are 500 ± 30 nm, 3.0 ± 0.03 μm , 300 ± 20 nm, 40 ± 5 nm, respectively.

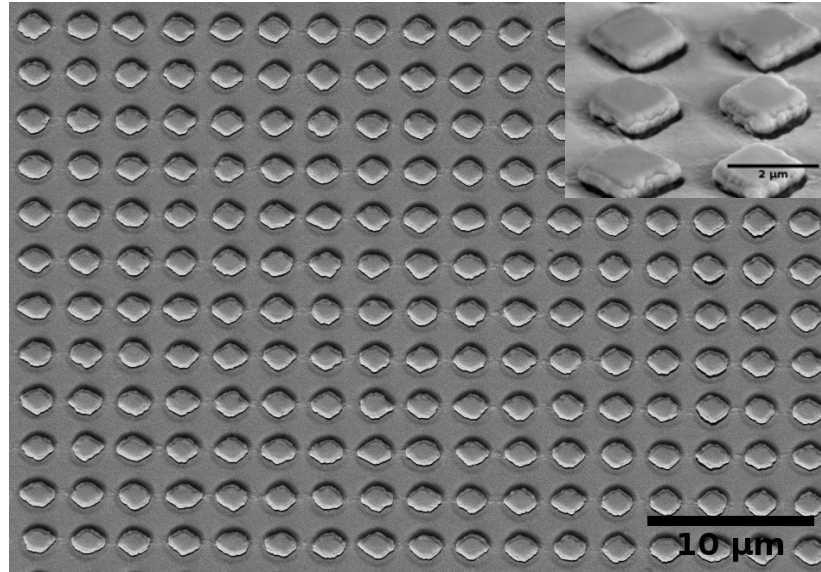


Figure 4.3: SEM image of the sample whose AFM topographical map is shown in the figure 4.2(b), and the inset shows an enlarged and tilted view of a small portion of the sample.

using the stamp [103, 151]. The fabrication steps of the metamaterial absorbers using soft lithography are illustrated in Fig. 4.4, where the master was fabricated using LIL as mentioned in Section 4.1. A two-dimensional photoresist disk array was used as the master. For fabrication of the stamp, a solution of polydimethylsiloxane (PDMS)

mixed with silicone elastomer (Sylgard 184, Dow Corning) was cast over the master patterned surface placed in a Petri dish and degassed in a vacuum desiccator to remove the bubbles formed during the mixing until all the bubbles get removed, and then cured for six hours at 60 °C on a hot plate. After the curing of the PDMS, it was peeled off from the master that left behind a negative impression of the disks as holes on the PDMS block.

Next, the fabricated PDMS stamp was used to fabricate the replica of photoresist disk array on a substrate by pouring a drop (~ 0.1 ml) of UV curable polymer (NOA 61, Norland Adhesive INC.) on the substrate and placing the stamp gently on the liquid which gets sucked into the micro holes in the PDMS stamp. The polymer, with the PDMS stamp in place was cured under an ultra-violet mercury lamp for 15 minutes. After curing, the PDMS stamp was removed and the substrate was left behind with an array of polymer disks.

For fabrication of the metamaterial absorbers, the samples fabricated using soft lithographically were coated with 300 nm thick ZnS and 40 nm thick gold consecutively using thermal evaporation in a vacuum of about 10^{-6} mbar.

4.1.3 Sample characterizations

Atomic force microscope, scanning electron microscope and optical microscope were used to structurally characterize the samples. The nominal thickness of the ZnS layer and gold layer measured using AFM are 300 nm and 40 nm, respectively. The thickness of the ZnS layer and the gold film were also cross-checked using the SEM cross-sectional images of the samples. AFM topographical maps of the fabricated samples on the polished silicon wafer before and after the deposition of ZnS and Au are shown in Figs. 4.2(a) and (b), respectively. AFM topographical map of the unpolished silicon substrate is shown in Fig. 4.6(b). SEM image of the fabricated sample whose AFM is

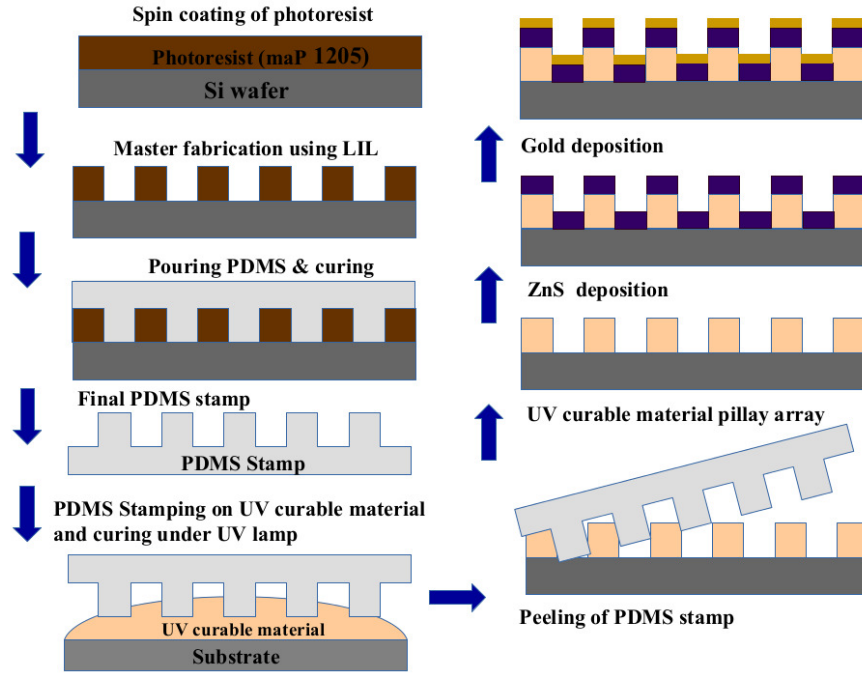


Figure 4.4: Schematic diagram depicting the steps in the fabrication of the metamaterial using soft lithography and deposition.

in the figure 4.2(b) is shown in Fig. 4.3, whereas the inset shows an enlarged and tilted view of a portion of the sample. The uniformity and smoothness of the fabricated sample on the silicon substrate over a large area can be seen through the SEM image (Fig. 4.3).

The infrared properties of the fabricated samples were measured by a FTIR spectrometer. Polarization dependent reflectance spectra were measured by inserting infrared wire grid polarizers. The angle dependent reflectance spectra were measured using a reflection accessory. Primarily the reflectance was measured as the transmittance through almost all the samples was negligibly small due to their absorbing nature, or in the case of silicon substrates polished on one surface, due to the scattering from the unpolished rough surface on the other side. The reflectance spectra were normalized with respect to the reflectance from a smooth gold film. The angle and polarization dependent reflectance spectra were measured using uncooled detector (DTGS) mounted in the spectrometer. The rest of the measured reflectance spectra

were taken using liquid nitrogen cooled detector (MCT) mounted on the microscope attached to the spectrometer. The dips in the measured reflectance spectra using MCT detector at $4.2\ \mu\text{m}$ and $6\ \mu\text{m}$ correspond to the absorption band of the CO_2 and water vapour, respectively present in the atmosphere.

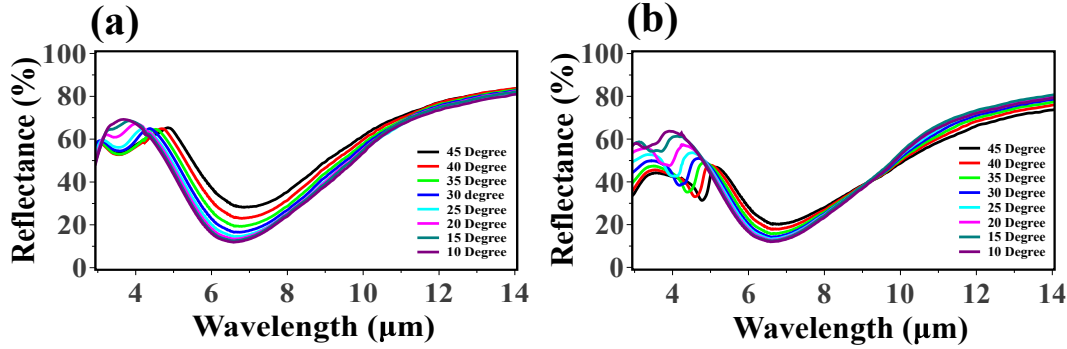


Figure 4.5: Measured reflectance spectra of the metamaterial for the (a) TE polarization and (b) TM polarization at different incident angles.

4.1.4 Fabrication of metamaterials on rough and flexible substrates

Soft lithography technique was used to fabricate the metamaterial absorber on rough as well as flexible substrates over large areas. Using the soft lithography method, it is possible to fabricate the disk array on rough substrates by exploiting the wetting nature of the UV curable polymer. Upon placing a drop of the polymer on a rough surface, due to wetting, the liquid fills up all the cavities and trenches of the surface below and forms a smooth surface above due to surface tension. Thus, the PDMS stamp could be used via UV curing to replicate the disk arrays on literally any rough surface which the liquid polymer solution would wet. For example, the optical microscope image and AFM topographical map of the rough surface of an unpolished silicon substrate are shown in Figs. 4.6(a) and (b), respectively. The crystal facets of the polycrystalline silicon is clearly visible in these images. The optical microscope image of the disk array

fabricated with the UV curable polymer is shown in Fig. 4.6(c). The micro-disk arrays form uniformly without any distortion throughout the sample. The roughness on the larger scale is apparent from the interference patterns due to reflections from silicon below the polymer and the surface of the polymer. The lighter regions correspond here to deeper trenches. These interference effects cannot be seen once the sample is coated with ZnS and gold [optical microscope image shown in Fig. 4.6(d)].

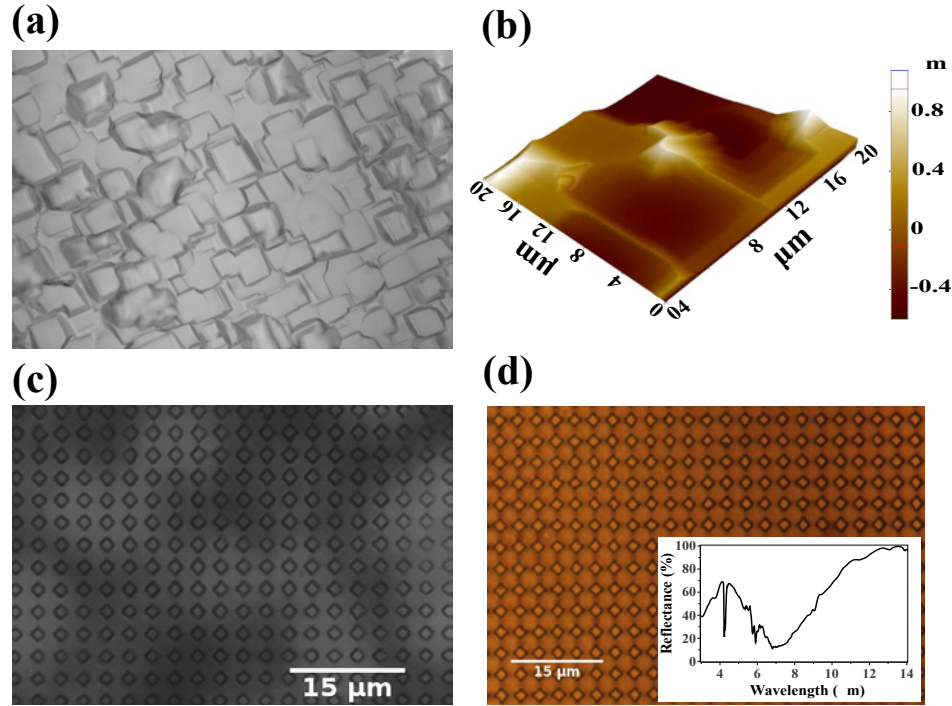


Figure 4.6: (a) Optical microscope image of an unpolished Si wafer at $5\times$ magnification (b) 3D view of AFM topographical map of the unpolished Si wafer, (c) optical microscope image of the disk array made of UV curable polymer fabricated on the unpolished Si wafer viewed at $100\times$ magnification (d) optical microscope image of the fabricated metamaterial on the unpolished Si wafer viewed at $100\times$ magnification. The corresponding measured reflectance spectrum is shown in the inset.

The same wetting property of the liquid polymer solution was exploited to fabricate the metamaterial absorber on extremely rough surfaces, for example, an emery paper with a grit size of $220\text{ }\mu\text{m}$ and on rough aluminium sheet. The optical images of the surfaces of the emery paper and the aluminium sheet are shown in Figs. 4.7(a) and (d), respectively. The fabricated metamaterial absorbers on the emery paper, on the aluminium sheet and on the polyimide sheet are shown in Figs. 4.7(b), (e) and (f),

respectively along with the corresponding measured reflectance spectrum in the inset, which was measured using the MCT detector. The flexible nature of the samples is demonstrated in Fig. 4.7(c), where the sample made on the emery paper has been rolled to have a radius of curvature of about a centimeter. The sample made on the kapton sheet is also highly flexible. As the substrate plays almost no role in this system other than to support the structure mechanically, the resonant wavelength and absorption band of the metamaterial absorber fabricated on different substrates are independent of the substrate used.

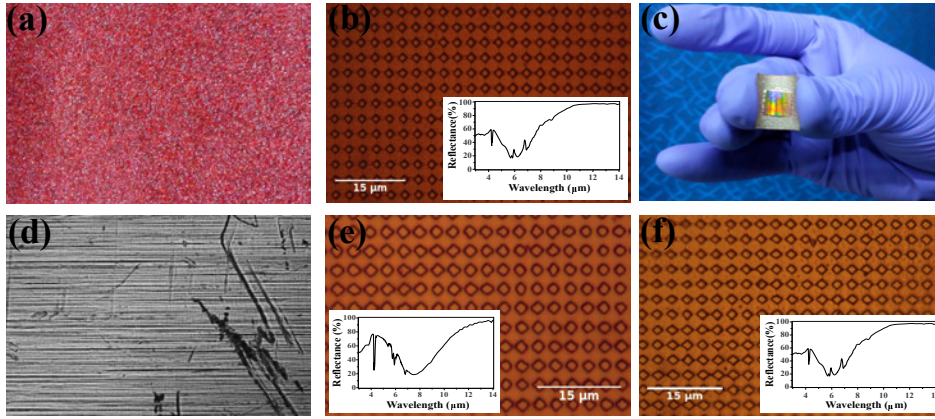


Figure 4.7: (a) Photograph of the emery paper with grit size of 220 μm , (b) Optical microscope image of the metamaterial fabricated on the emery paper viewed at 100 \times magnification with the measured reflectance spectra in the inset. (c) Photograph of the metamaterial showing its flexibility fabricated on emery paper, (d) optical microscope image at 5 \times magnification of the Al sheet, (e) optical microscope image of the metamaterial fabricated on the Al sheet at 100 \times magnification with the measured reflectance spectra in the inset. (f) optical microscope of the metamaterial fabricated on the kapton sheet at 100 \times magnification with the measured reflectance spectra in the inset.

The metamaterial absorber was fabricated over a large area of about 100 cm^2 [See Fig. 4.8(a)] using soft lithography and physical vapour deposition techniques on a glass substrate. The corresponding measured reflection spectrum of the sample is shown in Fig. 4.8(b). The structures were fabricated over a large area by repeating the soft lithography over the same substrate in the adjacent area using a PDMS stamp of about 1 cm^2 area. The resulting structures over a larger area were used to create another

larger PDMS stamp with an area of about 9 cm^2 , which was further used to fabricate the metamaterial absorber over even larger areas by repetitive stamping. The challenge in these cases was to minimize the blank area in between the adjacent stampings as the liquid polymer solution tends to run over to adjacent patterned areas. The blank areas give rise to stitch lines which will not have the desired infrared properties. This is brought out clearly in the infrared image of the large area sample at LWIR wavelengths (Fig. 4.8c), where the stitch lines appear bright because of their higher emissivity while the structured areas are dark due to their low emissivity (high reflectivity) in the 8-12 μm band. The sample is almost indistinguishable from the background.

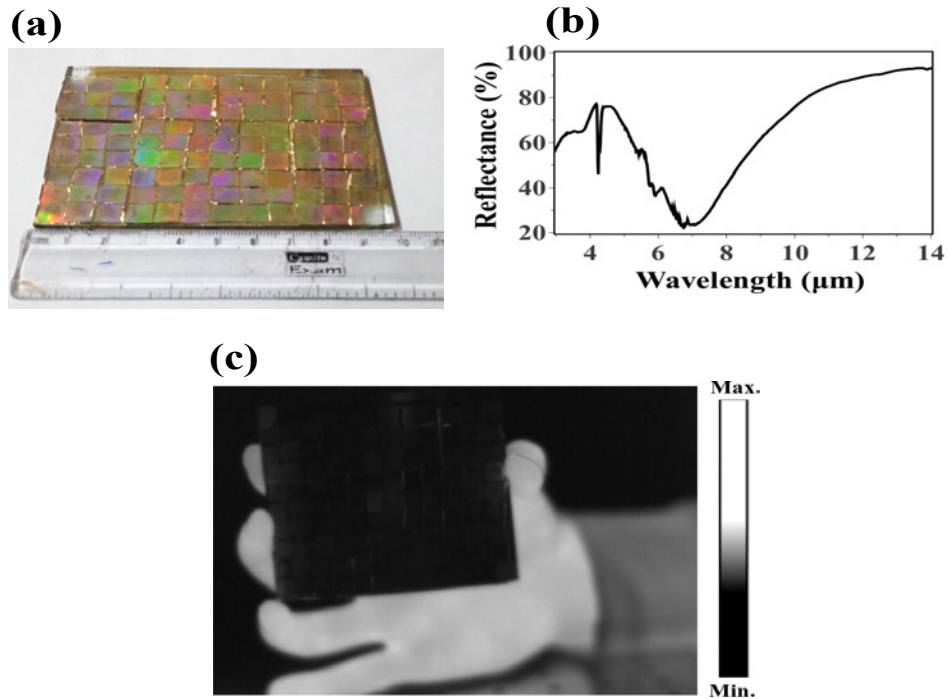


Figure 4.8: (a) Photograph of the metamaterial fabricated over large areas on a glass substrate. A centimeter scale has been shown beside the fabricated sample to show the dimension of the fabricated area. (b) measured reflectance spectra of the metamaterial, (c) LWIR camera infrared image of the metamaterial held in by hand.

4.2 Electromagnetic simulations

The structure consists of polymer micro-disks on a substrate on which thin films of a dielectric (ZnS) and a conductor (gold) are sequentially deposited in a snowfall deposition as shown schematically in Fig. 4.9(a). The structural dimensions used for simulations correspond to the sample, whose AFM image is shown in Fig. 4.2(b) (see Section 4.1 on fabrication). The unit cell consists of a polymer disk with a height of 500 nm on a silicon substrate, with consecutive layers of 300 nm thick ZnS and 40 nm thick gold on the top of both the polymer disk as well as on the parts of the silicon substrate not covered by the disk. In essence, the structure consists of two disks of gold and ZnS placed on the polymer disk with continuous thin films of gold and ZnS containing holes filled with the polymer/photoresist at a lower level on the substrate.

The COMSOL Multiphysics software was used to calculate the electromagnetic fields in the structure. Periodic boundary conditions were used along the transverse x and y directions to simulate an infinite array of unit cells to reduce the complexity of the simulation. Perfectly matched layers (PML) were used along the propagation direction (z -direction) to prevent the reflection of the waves from the top and bottom domain boundaries. The dispersive refractive indices (real and imaginary parts) of evaporated gold, ZnS and silicon were taken from Refs [19,21] and [20], respectively. The refractive index of the photoresist in simulations is chosen to be 1.58. The transmittance (T) and reflectance (R) of the structure are calculated by using port conditions at a plane above the structure in the air and below the structure in the silicon substrate. The absorbance is calculated using energy conservation as $A = 1 - R - T$ at each wavelength.

The simulated reflectance, transmittance and absorbance spectra of the metamaterial are shown in Fig. 4.9(a). The normalized magnetic and electric fields at the resonant wavelength with maximum absorption at $6.4 \mu\text{m}$ are shown as color maps

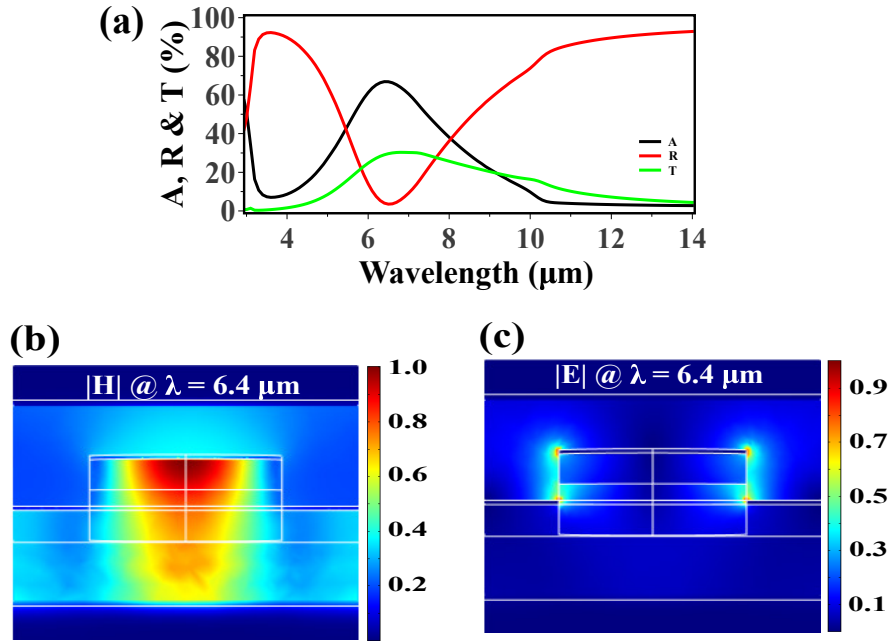


Figure 4.9: (a) Simulated reflectance, transmittance and absorbance spectra of the metamaterial at normal incidence, (b) color map of the normalized magnetic field at the resonant wavelength $6.4 \mu\text{m}$ and (c) color map of the normalized electric field at the resonant wavelength $6.4 \mu\text{m}$. The parameters used in the simulations: periodicity of the disk array, disk height, diameter of the disk, thickness of the ZnS layer and thickness of the Au layer are $3.0 \mu\text{m}$, $0.5 \mu\text{m}$, $1.68 \mu\text{m}$, 300 nm and 40 nm , respectively.

in Figs. 4.9(b) and (c), respectively. At resonance, the magnetic fields are large near the top gold disk and extend almost up to the Si substrate while the electric fields are highly localized at the periphery of the top gold disk and at the edge of the holes in the continuous gold film below. The electric field distribution (Fig. 4.9c) at $6.4 \mu\text{m}$ is localized around the edge of the gold disk on top of the disk and at the edge of the holes in the gold film, indicating that this absorption arises due to the LSPR. A cavity is formed between the gold film on the top of the disk and the silicon substrate that confines the electromagnetic field and causes the absorption of electromagnetic energy. The confinement of the EM wave in the cavity can be ascertained from the field distributions shown in Fig. 4.9(b). It is clear that the EM energy is being absorbed by the combined effect of the LSPR and cavity mode resonance. The resonance also manifests in a large transmittance (extraordinary transmittance) of the radiation into the silicon substrate. This will typically be absorbed if the substrate were an infrared absorbing

material with some amount of structure optimization required so that the reflectance is not affected.

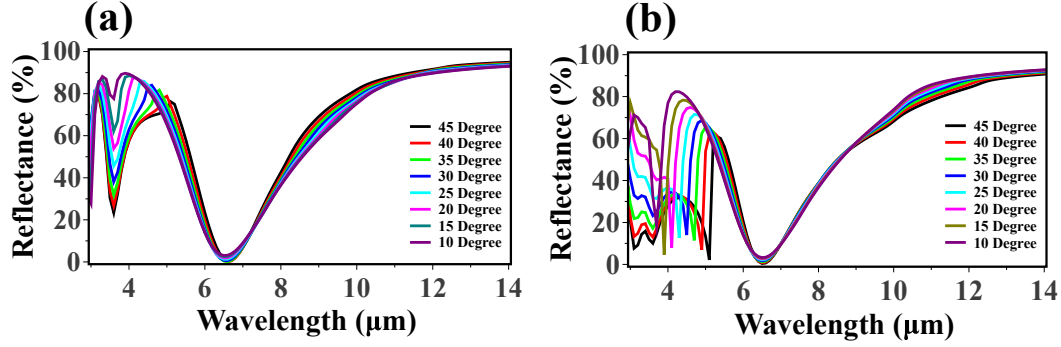


Figure 4.10: Simulated reflectance spectra for the (a) TE polarization and (b) TM polarization at different incident angles. The parameters used for simulations: periodicity of the disk array, height of the disk, diameter of the disk, thickness of the ZnS layer and thickness of the Au layer are $3.0\ \mu\text{m}$, $0.5\ \mu\text{m}$, $1.68\ \mu\text{m}$, $300\ \text{nm}$ and $40\ \text{nm}$, respectively.

We next investigate the dependence of the absorption in the structure with the incident angle and the polarizations. The simulated reflectance spectra of the metamaterial absorber for the TE and TM polarizations at different incident angles are shown in Figs. 4.10(a) and (b), respectively. At non-zero angle of incidence, there is an appearance of an extra dip in the reflectance spectra at shorter wavelength around $3.6\ \mu\text{m}$ in the case of TE and TM polarizations, and it shifts towards longer wavelengths with increasing angle of incidence in the case of TM polarization, whereas there is no such shift in case of the TE polarization. At wavelength $3.6\ \mu\text{m}$, the electric fields are mostly distributed at the interface between gold and ZnS layer, which corresponds to the propagating spoof surface plasmon polariton at the interface [29]. However the main resonance causing the minimum in reflectivity at $6.4\ \mu\text{m}$ remains unaffected with the change of angle of incidence in both polarizations.

We now describe the effects of the geometric parameters of the structure on the absorption. Fig. 4.11 shows the simulated reflectance, transmittance and absorbance spectra at normal incidence for different photoresist disk diameters. The resonance

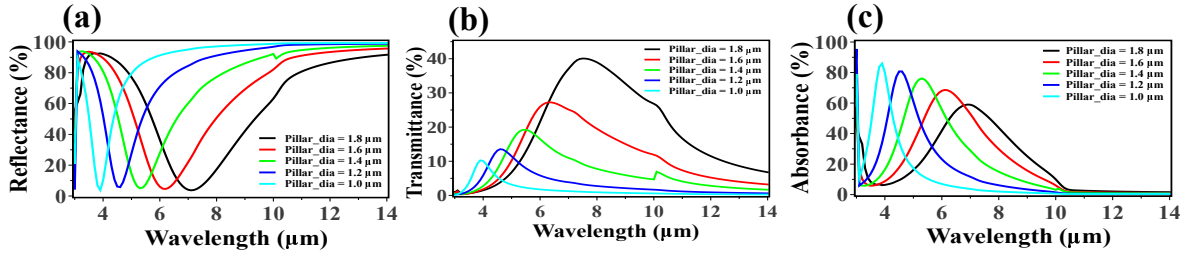


Figure 4.11: Simulated (a) reflectance, (b) transmittance and (c) absorbance spectra at normal incidence for different diameters of the photoresist disk. The parameters used for simulations: periodicity of the disk array, height of the disk, thickness of the ZnS layer and thickness of the Au layer are $3.0 \mu\text{m}$, $0.5 \mu\text{m}$, 300 nm and 40 nm , respectively.

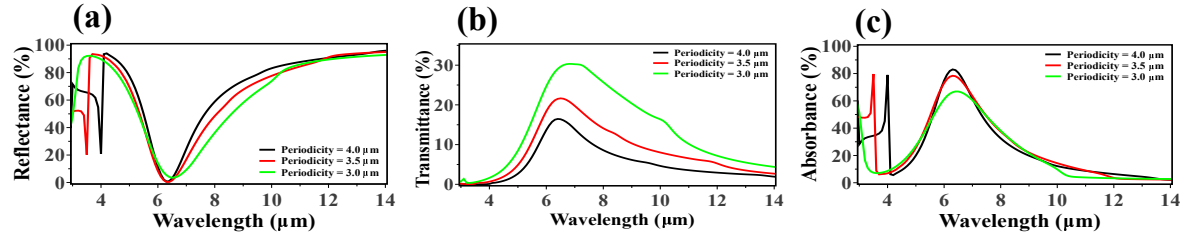


Figure 4.12: Simulated (a) reflectance, (b) transmittance and (c) absorbance spectra at normal incidence for different periodicities of the photoresist disk array. The parameters used for simulations: height of the disk, diameter of the disk, thickness of the ZnS layer and thickness of the Au layer are $0.5 \mu\text{m}$, $1.68 \mu\text{m}$, 300 nm and 40 nm , respectively.

shifts to longer wavelengths with increasing diameter of the disk. There is an increment in transmittance and decrement in absorbance with increasing diameter, but the minima in the reflectance spectra remain almost constant. Fig. 4.12 shows the simulated reflectance, transmittance and absorbance spectra for different periodicities of the disk array at normal incidence. There is an increment in the transmittance and decrement in the absorbance with decrease in the periodicity of the disk array. The minima in reflectance spectra remain almost constant and do not shift with an increasing periodicity of the disk array. The sharp dips in the reflectance spectra at smaller wavelengths when the wavelength typically match the periodicity corresponding to the Wood's anomaly [171] arising due to the periodic nature of the metallic structure. We will now finally describe the effects of the thickness of the ZnS layer to elucidate its role. Fig. 4.13 shows the simulated reflectance, transmittance and absorbance spec-

tra at normal incidence for different thickness of the ZnS layer. The resonance shifts towards longer wavelengths with increasing thickness of the ZnS layer. Extra peaks appear in the broad resonance bands of reflectance, transmittance and absorbance at longer wavelengths $7.2 \mu\text{m}$ and $10.3 \mu\text{m}$ with decreasing the thickness of the ZnS layer.

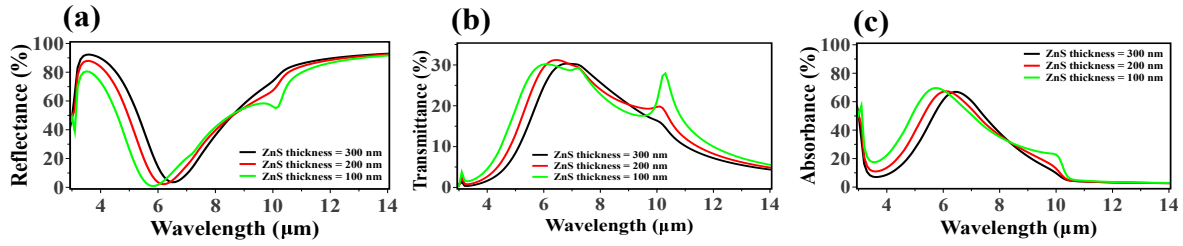


Figure 4.13: Simulated (a) reflectance, (b) transmittance and (c) absorbance spectra at normal incidence for different thickness of the ZnS layer. The parameters used for simulations: periodicity of the disk array, height of the disk, diameter of the disk and thickness of the Au layer are $3.0 \mu\text{m}$, $0.5 \mu\text{m}$, $1.68 \mu\text{m}$ and 40 nm , respectively.

4.3 Discussions

The simulated reflectance spectra (Figs. 4.10a, b) show a good correspondence with the measured reflectance spectra (Figs. 4.5a, b) for the TE polarization (Figs. 4.10a, 4.5a) and TM polarization (Figs. 4.10b, 4.5b) at different incident angles. The magnitude of the dip in the measured reflectance spectra is lesser than that of predicted in the simulations. The measured reflectance bandwidth is also substantially larger than that of in the simulated reflectance spectra which clearly points to

1. Inhomogeneous broadening of the resonance caused by the slightly varying sizes and shapes of the photoresist disks. These variations would be expected to arise in both LIL and imprint lithography techniques.
2. Averaging over the angular response due to the approximately 10° and 14° angular widths of the infrared beam in the FTIR when the DTGS detector and MCT detector are used respectively.

3. Possible effects of a thin layer of polymer left over on the substrates. [172]

Also note that we have considered the finite transmittance through the silicon substrate in the simulations whereas in the experiments, we have used single sided polished silicon substrate and the transmittance through the sample cannot be measured. In the case of TE polarization (Figs. 4.10a, 4.5a) with increasing the angle of incidence, the magnitude of the electric field remains constant and hence there is no wavelength shift in reflectance minima at wavelength $3.6 \mu\text{m}$, whereas it is shifted towards longer wavelengths in the case of TM polarization due to change in the magnitude of the electric field with increasing angle of incidence. In the case of TM polarization (Figs. 4.10b, 4.5b), the reflectance minima at wavelength $3.6 \mu\text{m}$ shifts towards the longer wavelengths corresponds to the coupling of the incident light to SSP via the diffracted modes. The wavevector of the SSPP excited by the diffracted modes can be written as

$$\vec{k}_{sp} = (k_0 \sin \theta \pm m2\pi/p)\hat{x} + (\pm n2\pi/p)\hat{y}, \quad (4.1)$$

where, $n_s = \sqrt{\epsilon_s}$ is the refractive index of the ZnS, $|k_{sp}| \approx 2\pi n_s/\lambda_{sp}$, $k_0 = 2\pi/\lambda$, p is the period of the disk array and θ is the angle of incidence for the TM polarized light [2] and, m and n are diffraction order along x and y directions, respectively.

The LSPR highly depends on the size, shape and material of the plasmonic particles and environment around them [173]. Fig. 4.11 shows the simulated reflectance, transmittance and absorbance spectra for different diameters of the photoresist disks. The gold disk on the top of the photoresist disk as well as hole size in the gold film are equal to the size of photoresist disk. Hence, the resonant wavelength changes with the diameter of the photoresist disk and shifts towards longer wavelengths with increasing disk diameter. Similarly as the size of hole in the gold film increases, the transmittance through the hole increases and causes decrement in the absorbance. The LSPR is almost independent of the periodicity of the nano particles or nano structures which is clear from Fig. 4.12. Thus, the resonance is almost independent of the periodicity of

the disk array. Due to the increase in the fill fraction of the holes in the gold film at smaller periodicities, the transmittance through the holes increases. Hence, absorbance increases with increasing the periodicity of the disk array.

The LSPR depends highly on the effective refractive index of the surrounding medium. With an increase in the thickness of the ZnS layer, there is an increase in the capacitive load, which cause the resonance to shift to longer wavelengths. Fig. 4.13 shows the simulated reflectance, transmittance and absorbance spectra for different thickness of the ZnS layer on the top of the disk. With decreasing the thickness of the ZnS layer, extra peaks appear in the absorption spectrum at wavelengths of $7.2\ \mu\text{m}$ and $10.3\ \mu\text{m}$. The peaks at $10.3\ \mu\text{m}$ and $7.2\ \mu\text{m}$ correspond to the partially propagating spoof surface plasmon at the interface of gold and Si substrate coupled through the diffraction modes $(\pm 1, 0)$ or $(0, \pm 1)$ and higher order modes $(\pm 1, \pm 1)$, respectively. The peaks disappear with increasing the thickness of the ZnS layer due to an increase in the distance between the gold layer and Si substrate.

4.4 Conclusions

We have proposed a very simple design of metamaterial absorber with band selective emissivity that is suitable for large area fabrication. FEM based simulations were used to design the structure and to understand the mechanisms for the absorption. We have shown that the adopted soft lithography based imprint technique is suitable for large areas and for rapid fabrication directly on hard or flexible substrates with arbitrary roughness. The soft lithographic structuring of a UV curable polymer is followed by vacuum deposition of thin films making the process very inexpensive and optimal for fabrication over large areas as it eliminates lift-off and etching process for developing the structure. Our approach can easily be adopted for the roll to roll fabrication on flexible sheets. Thus, a method for rapid production of designer metamaterials for

emissivity control over large area has been presented here. Another advantage of this structure is that it reduces the fabrication complexity by separating out the structuring and deposition processes and making them sequential, as well as avoiding expensive lift-off and etching processes.

Chapter 5

Tuning the resonances of a metamaterial absorber using Fano resonance

In Chapter 4, we have discussed a simple design of metamaterial absorber based on the localized spoof surface plasmons and cavity mode resonances, where the resonance was highly depending on the size of the disk, cavity length and refractive index of the surrounding medium. In this Chapter, a simple design of metamaterial absorber based on the combined effect of the cavity mode, guided mode and Wood's anomalies is presented, where the resonance can be tuned by controlling the thickness of the metal and dielectric layers instead of changing the dimensions of structures. Due to the excitation of several modes simultaneously, Fano resonance is observed in the system, which is caused by the interference of bright and dark mode arises in the system. In the earlier design, photoresist disk array was followed by bi-layer (Au/ZnS) deposition, whereas in this design the photoresist disk array is followed by tri-layer deposition. Due to the tri-layer deposition on the photoresist disk array, there is a formation of a cavity between the gold layer on the top of photoresist and substrate, and a wave-guide between the gold layers on the substrate and the ZnS layer. Wood's anomalies are also

observed in the system due to grazing of the diffracted light which is caused by the 2-D grating along the interface of the gold/substrate.

Generally, Fano resonance is used to describe asymmetric resonance [46,57], which arises due to the constructive and destructive interference of discrete resonance states with broadband continuum states. This phenomenon and the underlying mechanism, being common and appearing in many domains of physical sciences, are found in a variety of micro/nano-structures such as plasmonics and metamaterials [51,174], photonic crystals [50,175,176], quantum dots [177], etc. The asymmetric Fano resonance profile promises a variety of applications in a wide range of photonic devices, such as sensors [178,179], optical filters [180], switches [181], detectors [49,182], non-linear devices [183] and slow-light devices [184], etc. In the last few years, with advancements in micro/nano fabrication techniques and the development of integration techniques, Fano resonance has been widely investigated in micro/nano fabricated structures [51,174,176,185–188].

Fano resonance in metamaterial absorbers has also been observed earlier. Conventional metamaterial absorbers are tri-layer and are based on impedance matched which enables the complete absorption of the electromagnetic radiations at particular frequencies. The metamaterial perfect absorbers based on impedance matched resonances typically involve a complex design, and the fabrication tolerances are quite severe. However, for many infrared applications, such as solar thermal devices or thermal camouflage, control of the emissivity and the absorptivity is required over very large surfaces ranging from few square meters to even square kilometers. It is a great manufacturing challenge to produce metamaterials that have complex micrometric or even sub-micrometric structures containing metallic as well as dielectric constituents over these large areas with good fidelity and in realistic time scales.

In this work, we present a novel resonant metamaterial absorber for controllable emissivity/absorptivity at infrared frequencies, fabricated using laser interference

lithography technique and physical vapour deposition technique. The metamaterial absorber consists of a tri-layer of Au/ZnS/Au thin films on photoresist disk array and depends on a cavity and guided mode resonance (GMR) of the structure to produce high absorption. The schematic diagram of the unit cell of the metamaterial absorber with illustration of different existing modes is shown in Fig. 5.1. We have computationally designed the structures using the commercial COMSOL Multiphysics software to understand the origin of the absorption. The simplified design of the metamaterial allows for sequential patterning and deposition processes without lift-off or etching processes involved, making the process applicable to the manufacturing of large area metamaterial surfaces.

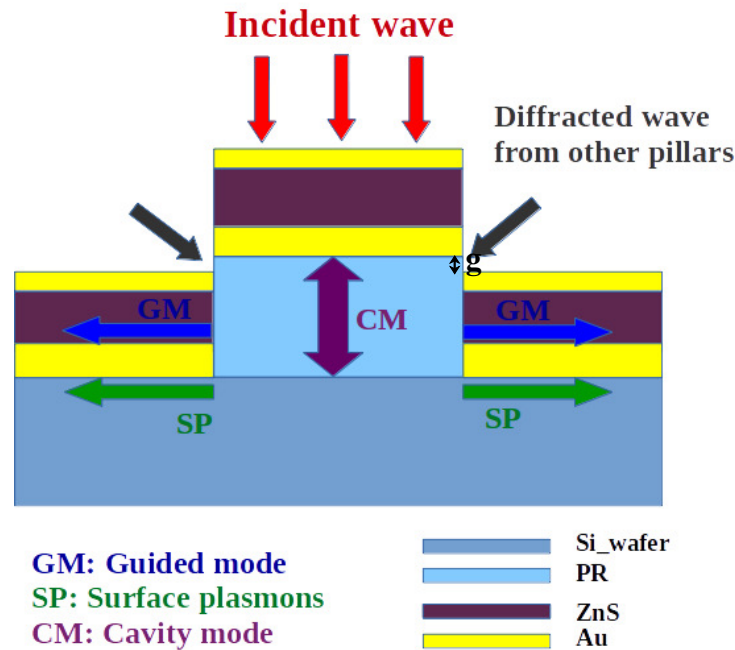


Figure 5.1: Schematic diagram of the unit cell of the metamaterial absorber with illustration of different existing modes, where the gap between gold layers on the top of photoresist pillar and on the ZnS layer on the silicon substrate is g .

Chapter is organized as follows: experimental details, including the fabrication and characterization of the samples, are discussed in Section 5.1. The details of electromagnetic simulations of the metamaterial absorber including the effect of the different parameters are discussed in Section 5.2. The physical origin of the absorption due to the

cavity and guided mode resonance is discussed in Section 5.3, and finally conclusions are drawn in Section 5.4.

5.1 Experimental details: Fabrication and Characterization

5.1.1 Sample fabrication

Laser interference lithography is used to fabricate a photoresist disk array on a polished silicon substrate. A thin film of a positive photoresist was spin coated on a cleaned polished silicon substrate (polished on one side) at 3000 RPM for 45 s and pre-baked at 85 °C for 60 s. The coated samples were exposed twice to a two-beam interference pattern created by a He-Cd laser of power 30 mW, a wavelength of 442 nm and the coherence length of 10 cm. The first and second exposures were carried out for the equal time of 3 minutes with a rotation of the sample by 90 ° in between the exposures to create a square array of disks. The exposed samples were subsequently developed in a developer (ma D-331) for 20 s, rinsed with de-ionized water and dried by flowing dry nitrogen gas. The process left behind a square array of photoresist disks on top of the silicon substrate. Subsequently, the samples were coated with 160 nm thick gold, 300 nm thick ZnS and 30 nm thick gold sequentially using thermal evaporation in a vacuum of 10^{-6} mbar. The thickness of the films was nominally determined during deposition using a quartz crystal monitor.

5.1.2 Sample characterization

AFM and FESEM were used to structurally characterize the samples. The nominal thickness of the bottom gold layer, ZnS layer and the top gold layer, measured using

AFM, are 160 ± 8 nm, 300 ± 20 nm and 30 ± 5 nm, respectively. The measured periodicity of the disk array, disk height and disk diameter using the AFM are 2.8 ± 0.1 μm , 0.5 ± 0.08 μm , 1.68 ± 0.04 μm , respectively. AFM topographical maps of the fabricated samples on a polished silicon wafer before and after the deposition of Au/ZnS/Au are shown in Figs. 5.2(a) and (b), respectively. The FESEM image of the fabricated sample after the deposition of tri-layer is shown in Fig. 5.3 with an enlarged and tilted view of a portion of the sample in the inset. The top portion of the photoresist disk was flat before the tri-layer deposition, and after tri-layer deposition, it becomes slightly conical in shape, as it can be seen from the AFM topographical maps before and after the tri-layer deposition (Figs. 5.2(a) and (b)) as well as from the FESEM image (Fig. 5.3).

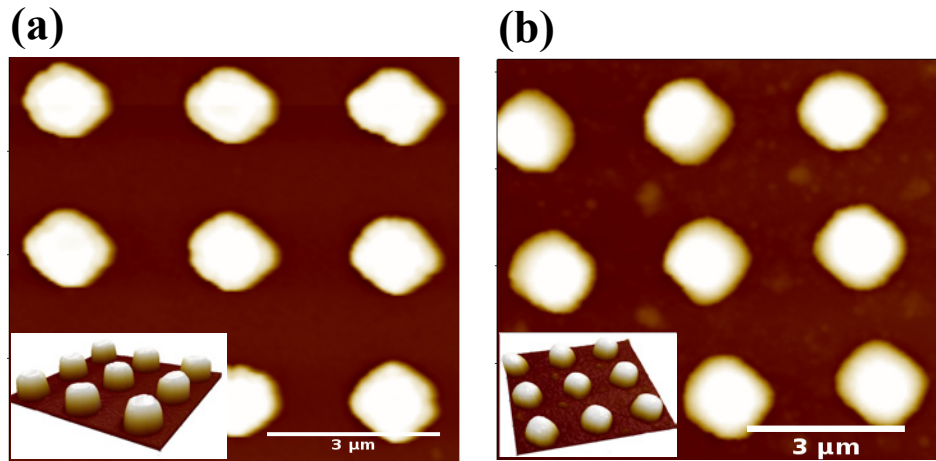


Figure 5.2: AFM topographical maps of the fabricated sample (a) before tri-layer deposition, (b) after tri-layer deposition, and the inset in each figure shows a 3D view of the corresponding images.

The infrared properties of the fabricated samples were measured by a FTIR spectrometer. Polarization dependent reflectance spectra were measured by inserting infrared wire grid polarizers and the angle-dependent reflectance spectra were measured using a reflection accessory (Harrick seagull made). Primarily the reflectance was measured as the transmittance through the samples was negligibly small as the silicon substrate was polished only on one side due which the scattering from the unpolished

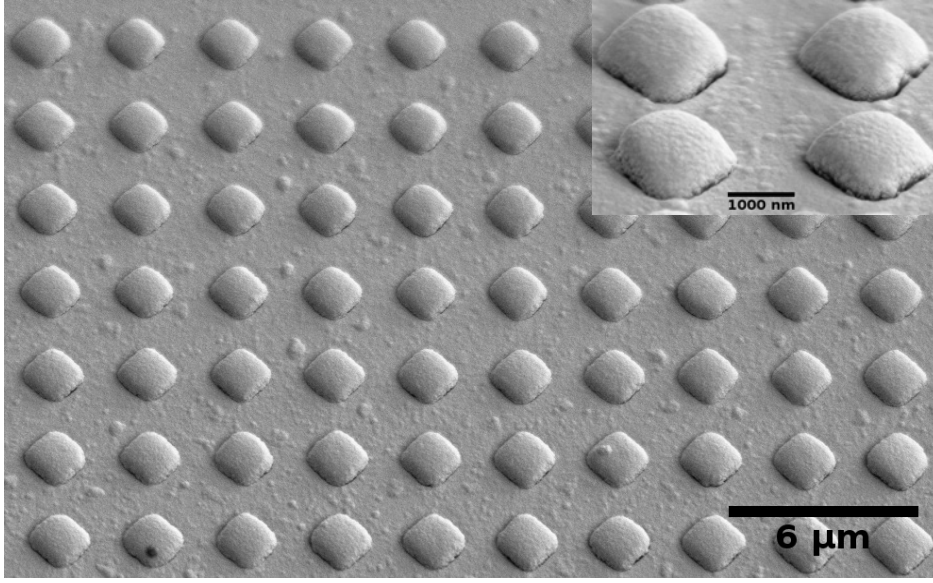


Figure 5.3: SEM image of the fabricated sample after the tri-layer deposition, the inset shows an enlarged and tilted view of a portion of the sample.

rough surface on the other side of the metamaterial structures did not permit much direct transmittance. The reflectance spectra were normalized with respect to the reflectance from a smooth gold film. The angle-dependent and polarization dependent reflectance spectra were measured using uncooled Deuterated Triglycine Sulfate (DTGS) detector mounted in the spectrometer.

Figs. 5.4(a) and (b) show the measured reflectance spectra at different incident angles for the TE and TM polarizations, respectively. The minimum of reflectance spectra decreases around the $9\ \mu\text{m}$ wavelength with increasing the angle of incidence in the case of TE polarization, whereas it remains almost constant with slight red-shift in the case of TM polarization. A small minimum appears in the reflectance spectra in both polarizations around $5\ \mu\text{m}$ wavelength, and it remains almost constant with increasing the angle of incidence in the case of TE polarization whereas in the case of TM polarization, the minimum is increasing with increasing the angle of incidence. There is an appearance of an extra minimum in the reflectance spectra around the $5.5\ \mu\text{m}$ wavelength with increasing the angle of incidence in the case of TM polarization.

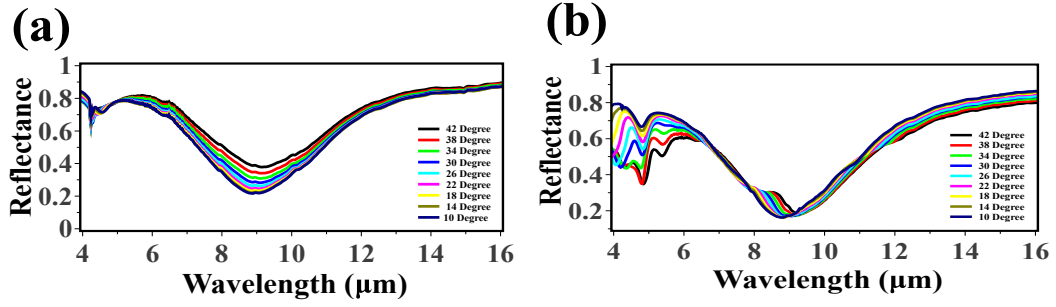


Figure 5.4: The measured reflectance spectra of the fabricated sample for the (a) TE polarization, (b) TM polarization at different incident angles.

5.2 Electromagnetic simulations

The structure consists of photoresist disk arrays on silicon substrate on which thin films of metal, dielectric and metal are sequentially deposited in a snowfall deposition as shown schematically in Fig. 5.1. The structural geometrical parameters used for simulations correspond to the fabricated sample whose AFM image is shown in Fig. 5.2. The unit cell consists of a photoresist disk with a height of 500 nm on a silicon substrate, with consecutive layers of 160 nm thick gold, 300 nm thick ZnS and 30 nm thick gold on the top of both the photoresist disk as well as on the parts of the silicon substrate not covered by the disk. In essence, the structure consists of three disks, two out of which are gold disks and one is ZnS disk placed on the photoresist disk with continuous thin films of Au/ZnS/Au containing holes filled with the photoresist at the substrate. Due to the tri-layer deposition, a cavity is formed between the bottom layer of gold on the top of photoresist disk and silicon layer at the bottom of the disk, because the refractive index of the photoresist is lower than that of silicon and gold, which is highly reflecting in any case. There is a formation of a waveguide in the ZnS layer sandwiched between the top and bottom gold layers on the silicon substrate. As the schematic diagram of the unit cell of the metamaterial absorber with illustration of different existing modes has already shown in Fig. 5.1.

The COMSOL Multiphysics software was used to calculate the electromagnetic fields in the structure. Periodic boundary conditions were used along the x and y directions to simulate an infinite array of unit cells to reduce the complexity of the simulation. Perfectly matched layers (PML) were used along the propagation direction (z -direction) to prevent the reflection of the waves from the top and bottom domain boundaries. The dispersive refractive indices (real and imaginary parts) of evaporated gold, ZnS and silicon were taken from Refs [19,21] and [20], respectively. The refractive index of the photoresist in the simulations is taken to be 1.58. The transmittance (T) and reflectance (R) of the structure are calculated by using port conditions at a plane above the structure in the air and below the structure in the silicon substrate. The absorbance is calculated using energy conservation as $A = 1 - R - T$ at each wavelength.

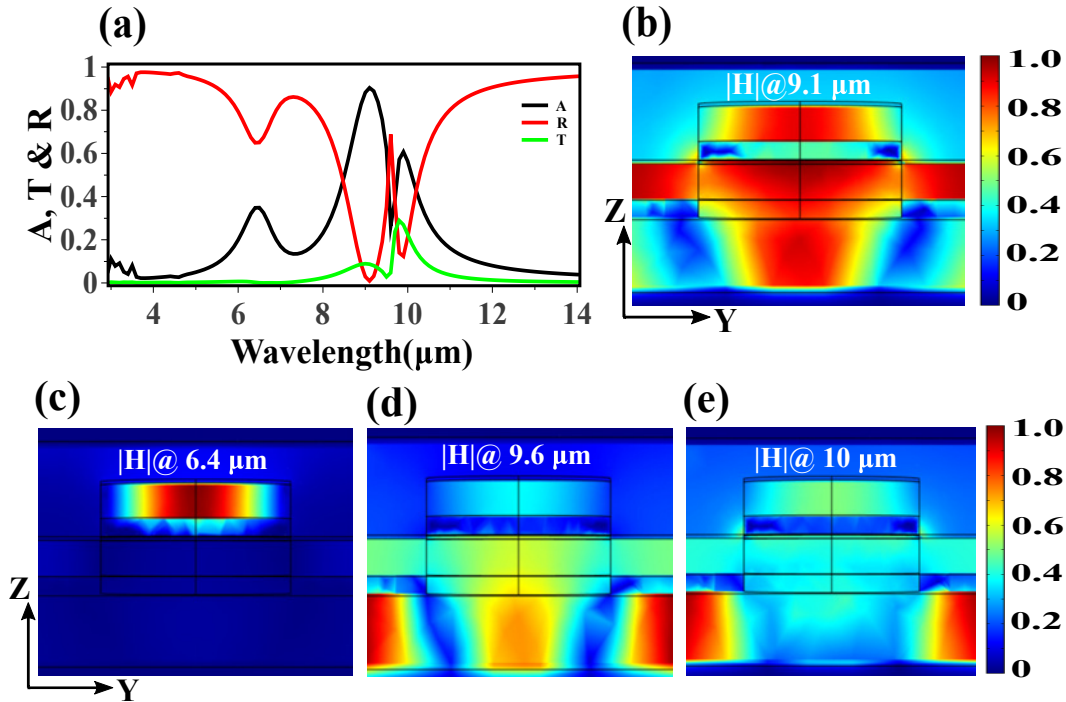


Figure 5.5: (a) Simulated reflectance, transmittance and absorbance spectra corresponding to the metamaterial absorber, (b–e) color plot of the normalized magnetic field at resonant wavelengths 9.1 μm , 6.4 μm , 9.6 μm , 10.0 μm . Parameters used for simulations: periodicity of the disk array, height of the disk, diameter of the disk, thickness of the bottom Au layer, thickness of the ZnS layer and thickness of the top Au layer are 2.8 μm , 0.5 μm , 1.68 μm , 160 nm, 300 nm and 30 nm, respectively.

The simulated reflectance, transmittance and absorbance spectra of the metamaterial are shown in Fig. 5.5(a). The transmittance spectrum consists of two peaks at wavelengths $9.8\ \mu\text{m}$ and $9\ \mu\text{m}$. The reflectance spectrum consists of three minima at wavelengths of $6.4\ \mu\text{m}$, $9.1\ \mu\text{m}$ and $9.85\ \mu\text{m}$. The absorbance spectrum consists of three maxima at wavelengths of $6.4\ \mu\text{m}$, $9.1\ \mu\text{m}$ and $10\ \mu\text{m}$. Color maps of the normalized magnetic field at different resonant wavelengths $9.1\ \mu\text{m}$, $6.4\ \mu\text{m}$, $9.6\ \mu\text{m}$ and $10\ \mu\text{m}$ are shown in Figs. 5.5(b), (c), (d) and (e), respectively. It is clear from Fig. 5.5(b) that the fields are strongly confined in the waveguide as well as in the cavity at a wavelength of $9.1\ \mu\text{m}$. The field is highly localized in the ZnS layer between the two layers of gold on the top of photoresist disk at wavelength of $6.4\ \mu\text{m}$. Figs. 5.5(d) and (e) show the normalized magnetic field maps at the peak and dip of the corresponding transmittance spectrum, respectively. It is clear from Fig. 5.5(d) that the fields are distributed along the Au/Si interface and weakly within the cavity. The fields are distributed along the Au/Si interface and not localized within the cavity at $10\ \mu\text{m}$ wavelength (see Fig. 5.5(e)). It is clear that there is no contribution of the resonance at wavelength $6.4\ \mu\text{m}$ in the resultant interfering resonances at $9.1\ \mu\text{m}$ wavelength. In order to understand the contribution of the different resonances in the interfering resonance at $9.1\ \mu\text{m}$, the resonance at $6.4\ \mu\text{m}$, which is not close to $9.1\ \mu\text{m}$ can be eliminated by removing the top layer gold and ZnS from the photoresist disk.

The simulated reflectance, transmittance and absorbance spectra of the corresponding unit cell without the ZnS and top Au layers on the disk is shown in Fig. 5.6(a). The corresponding schematic diagram of the unit cell without the top gold and ZnS layer on the top of the photoresist disk is shown in the inset of Fig. 5.6(a). Fig. 5.6(b) shows the normalized time average power flow in color map, and to understand the power flow in the system, the arrow volume plot of the time-averaged power was plotted in the same image. It is clear that the power flows into the cavity and the waveguide as well as along the interface of gold and silicon. The color maps of the normalized magnetic fields at wavelengths of $9.1\ \mu\text{m}$ and $10\ \mu\text{m}$ are shown in Figs. 5.6(c) and (d),

respectively.

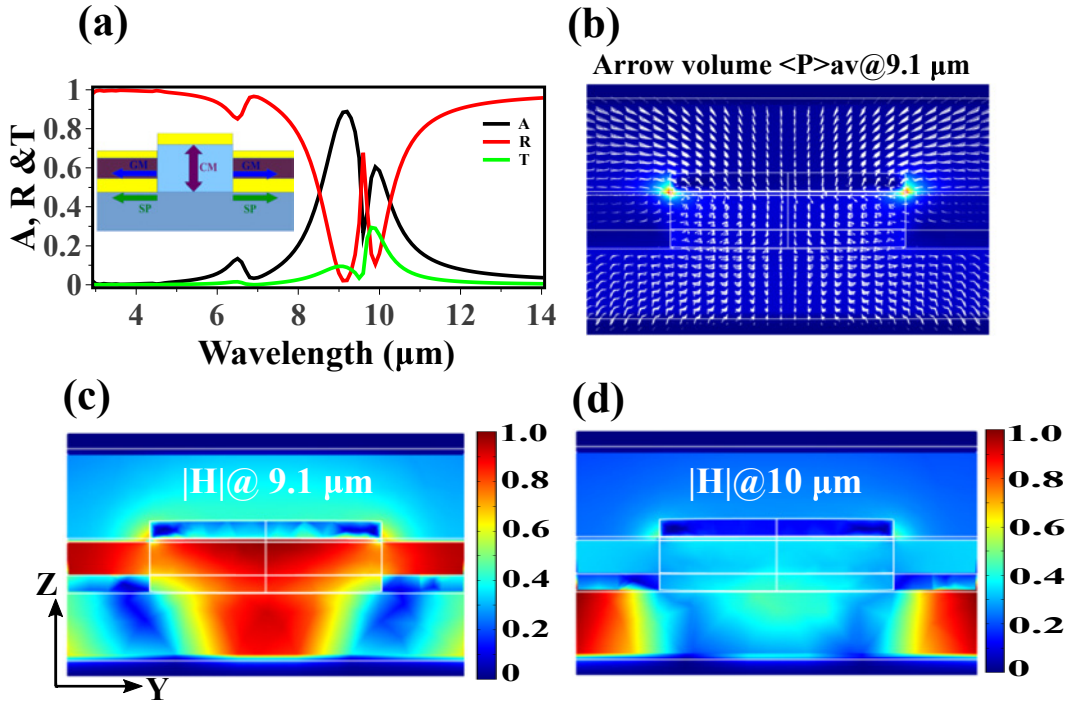


Figure 5.6: (a) Simulated reflectance, transmittance and absorbance spectra corresponding to the metamaterial absorber without top Au and ZnS layers on the disk, where the schematic diagram of the unit cell without the top gold and ZnS layers on the top of photoresist disk is shown in the inset, (b) color plot of the normalized time average power with Poynting vector field lines at resonant wavelength $9.1 \mu\text{m}$, (c–d) color plot of the normalized magnetic field at the resonant wavelength of $9.1 \mu\text{m}$ and $10.0 \mu\text{m}$. Parameters used for simulations: periodicity of the disk array, height of the disk, diameter of the disk, thickness of the bottom Au layer, thickness of the ZnS layer and thickness of the top Au layer are $2.8 \mu\text{m}$, $0.5 \mu\text{m}$, $1.68 \mu\text{m}$, 160 nm , 300 nm and 30 nm , respectively.

Fig. 5.7 shows the transmittance, reflectance and absorbance spectra for different periodicities of the photoresist disk array. The other parameters like the thickness of the bottom and top gold layer, ZnS layer and height of the photoresist disk are kept constant. With increasing the periodicity of the disk array, an extra resonance appears. The extra resonance position shifts towards longer wavelengths with increasing the periodicity of photoresist pillar array. But, the resonance corresponding to the cavity mode remains almost independent of the periodicity of the disk array. There is an asymmetric resonance for a fixed value of periodicity $2.8 \mu\text{m}$, which arises due to

the overlap of the fixed resonance (cavity resonance) and the resonance is caused by changing the periodicity (Guided-mode resonance) of the disk array [Fig. 5.7(b)]. The interfering resonances corresponding to the different modes separate when the period of the disk array becomes $4\ \mu\text{m}$ (see in Fig. 5.7(c)). At the periodicity of $2\ \mu\text{m}$, only one resonance appears that arises due to the confinement of fields into the cavity, whereas at $5\ \mu\text{m}$ periodicity an extra resonance appears around $12.4\ \mu\text{m}$.

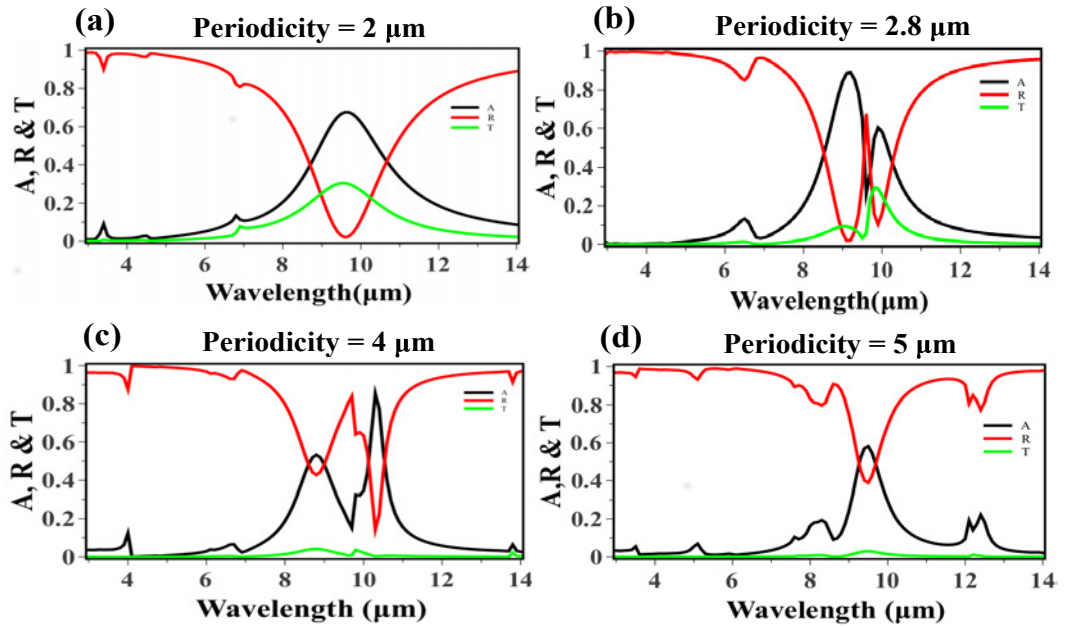


Figure 5.7: Simulated reflectance, transmittance and absorbance spectra at normal incidence for the different periodicity of the photoresist disk array. The parameters used for simulations: disk height, disk diameter, bottom Au layer thickness, ZnS layer thickness and top Au layer thickness are $0.5\ \mu\text{m}$, $1.68\ \mu\text{m}$, $160\ \text{nm}$, $300\ \text{nm}$ and $30\ \text{nm}$, respectively.

Fig. 5.8 shows the color map of the normalized magnetic field and arrow volume plot of the normalized time average power flow at different resonance wavelengths for $4\ \mu\text{m}$ periodicity of the disk array. Fig. 5.8(a) shows the color plot of the normalized magnetic field at $8.8\ \mu\text{m}$ wavelength, and at this resonance wavelength field is only localized in the cavity formed between gold layers on the photoresist disk and Si substrate. The corresponding color map of the normalized time average power and its arrow volume plot is shown in the figure 5.8(d). Fig. 5.8(b) shows the color map of the normalized magnetic field at $13.7\ \mu\text{m}$ wavelength, and at this resonance wave-

length field is only extended into the silicon substrate from the gold layer side. The corresponding color map of the normalized time average power and its arrow volume plot are shown in the figure 5.8(e). The arrow power flow indicates the power flow in the substrates along the gold and silicon interface. Fig. 5.8(c) shows the color map of the normalized magnetic field at $10.3 \mu\text{m}$ wavelength and at this resonance wavelength field is localized in the sandwiched ZnS layer between the gold layers on the top of silicon and on the ZnS layer. The corresponding color map of the normalized time average power and its arrow volume plot is shown in Fig. 5.8(f). It is clear that most of the power is flowing into the ZnS sandwiched layer.

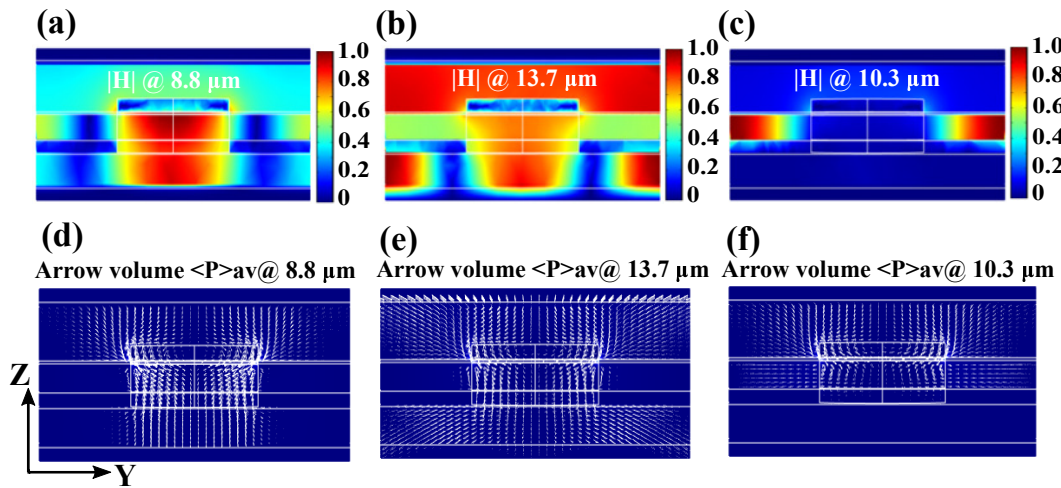


Figure 5.8: Color plots of the normalized magnetic field at resonance wavelength (a) $\lambda = 8.8 \mu\text{m}$, (b) $\lambda = 13.7 \mu\text{m}$ and (c) $\lambda = 10.3 \mu\text{m}$. The arrow volume plots of the time average power flow at resonance wavelength (d) $\lambda = 8.8 \mu\text{m}$, (e) $\lambda = 13.7 \mu\text{m}$, and (f) $\lambda = 10.3 \mu\text{m}$

Figs. 5.9(a) and (b) show the simulated reflectance spectra at different incident angles for the TE and TM polarizations, respectively. There is a slight decrement in the minimum of reflectance spectra around the $9 \mu\text{m}$ wavelength with increasing the angle of incidence in the case of TE polarization, whereas it remains almost constant with a slight redshift in the case of TM polarization. The minimum at around $10 \mu\text{m}$ wavelength in the case of TE polarization slightly decreases in amplitude with increasing the angle of incidence whereas it slightly decreases in amplitude with redshift in

the case of TM polarization. An extra minimum appears in the reflectance spectra around the $7.5 \mu\text{m}$ wavelength in the case of TM polarizations, and it shifts towards longer wavelengths with increasing the angle of incidence. The minimum in the reflectance spectra around $6.5 \mu\text{m}$ wavelength remains almost constant with increasing the angle of incidence in both polarizations. The minimum in the reflectance spectrum around $4.5 \mu\text{m}$ wavelength slightly increases in amplitude with increasing the angle of incidence for both polarizations but faster in the case of TM polarization compared to that of TE polarization. Splitting appears in the minimum at $4.5 \mu\text{m}$ wavelength with increasing the angle of incidence in the case of TM polarization, whereas there is no such splitting in the case of TE polarization.

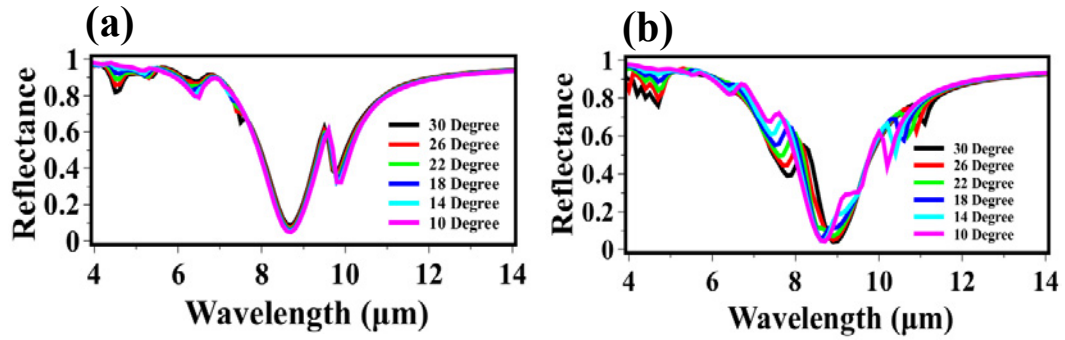


Figure 5.9: The simulated reflectance spectra of the fabricated sample for the (a) TE polarization, (b) TM polarization at different incident angles. The parameters used for simulations: disk height, disk diameter, bottom Au layer thickness, ZnS layer thickness and top Au layer thickness are $0.5 \mu\text{m}$, $1.68 \mu\text{m}$, 155 nm , 300 nm and 30 nm , respectively.

Fig. 5.10 shows the simulated electromagnetic response of the tri-layered meta-material absorber for different values of the g parameter. The value of g was changed by changing the thickness of the bottom gold layer, and the other parameters are kept constant. In the reflectance spectra [see Fig. 5.10(a)], the minimum at $9.1 \mu\text{m}$ wavelength shifts towards shorter wavelengths, and the minimum at $9.8 \mu\text{m}$ wavelength remains almost constant with increasing the gap value of g . While the minimum at $6.4 \mu\text{m}$ wavelength increases with increasing the gap. In the transmittance spectra [see Fig. 5.10(b)], the fundamental order transmission amplitude at $9.8 \mu\text{m}$ wavelength

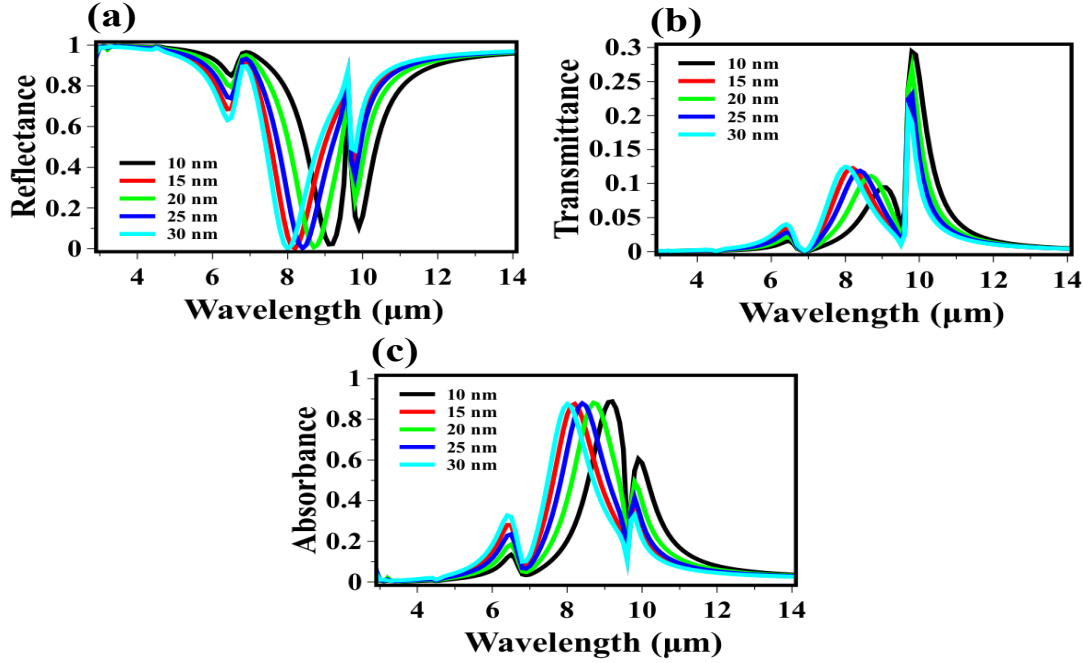


Figure 5.10: The simulated (a) reflectance, (b) transmittance and (c) absorbance spectra of the tri-layered metamaterial for different values of g as 10 nm, 15 nm, 20 nm, 25 nm and 30 nm. The other parameters such as disk height, disk diameter, ZnS layer thickness and top Au layer thickness are 0.5 μm , 1.68 μm , 300 nm and 30 nm, respectively.

decreases whereas the higher order transmission amplitude at 6.4 μm wavelength increases with increasing the gap, and both the resonances remain almost fixed in spectral position. The transmission peak at 9.1 μm wavelength shifted towards shorter wavelengths with increasing the amplitude as the gap increases. In the absorbance spectra [see Fig. 5.10(c)], the absorption peak around the 10 μm wavelength decreases with a minimal shift towards shorter wavelengths with increasing the gap. There is a shift of absorption peak around the 9 μm towards shorter wavelengths with increasing the gap whereas the absorption peak around 6.4 μm wavelength increases with increasing the gap.

Fig. 5.11 shows the simulated reflectance spectrum (black line) at normal incidence of the tri-layered system with the Fano fit (red line) using the coupled mode theory of one port and two modes. There are two minima at 9.1 μm and 9.8 μm wavelengths in the reflectance spectrum, which corresponds to the cavity mode resonance

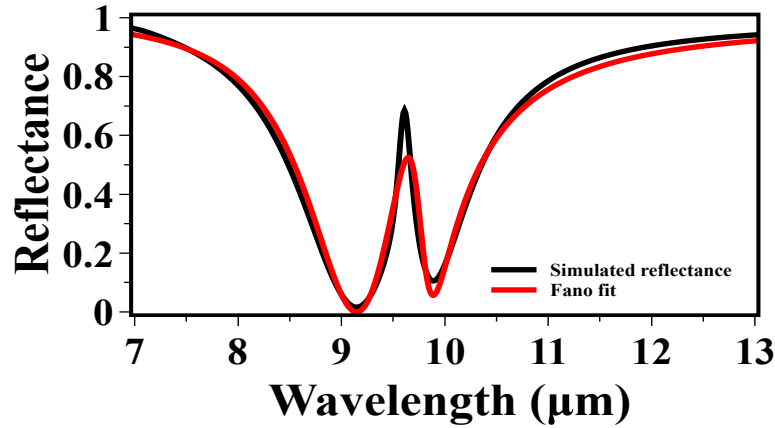


Figure 5.11: Simulated reflectance spectrum (black line) with Fano fit (red line). The parameters used for simulations: periodicity of the disk array, disk height, disk diameter, bottom layer Au thickness, ZnS layer thickness and top layer Au thickness are $2.8 \mu\text{m}$, $0.5 \mu\text{m}$, $1.68 \mu\text{m}$, 160 nm , 300 nm and 30 nm , respectively.

and guided mode resonance, respectively.

Fig. 5.12 shows the Fano fitting corresponding to the individual resonance. The individual resonance plot was plotted using the same fitting parameters as used to fit the asymmetric reflectance spectrum in Fig. 5.11. The individual response was plotted by switching off the corresponding other resonance. For example for CM resonance, the value of $\omega_2 = 0$, and similarly for GMR, the value of $\omega_1 = 0$ [see Eq. 5.1].

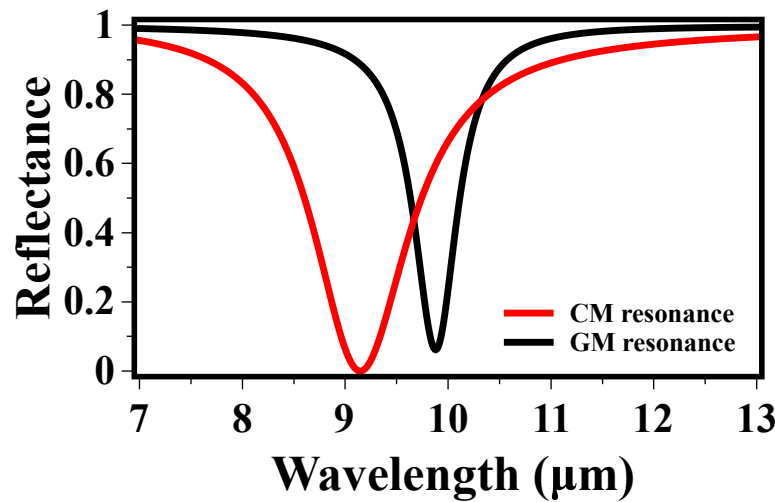


Figure 5.12: Fano fitted reflectance spectra of the corresponding individual resonance.

5.3 Discussion

The mechanism of absorption of the electromagnetic wave can be understood from the illustration of different excited modes, shown in the schematic diagram of the unit cell of the metamaterial absorber [see Fig. 5.1]. Formation of a cavity between the bottom layer gold on the top of photoresist disk and silicon substrate occurs because of the lower refractive index of the photoresist than that of silicon. The diffracted wave from the disk gets multiply reflected between the gold layer and the silicon substrate and causes the trapping of the electromagnetic wave into the photoresist medium [75, 77, 189, 190]. There is a formation of a waveguide in the ZnS layer between the gold layers on the silicon substrate and ZnS itself. Waves diffracted from the different disks enter through the gap between the bottom layer of gold on the photoresist disk and top layer gold on the ZnS layer on uncovered portions of the substrate by the photoresist disk. The diffracted light, which enters through the gap couple into the cavity mode as well as to the waveguide mode [37], and some parts of it just propagate at the interface of silicon and gold layers. The same happens by coupling through the gap with other disks. Thus, diffracted coupled waves travel in forward and backward directions in the waveguide, and cause the formation of standing waves. The diffracted waves propagating along the plane at the interface between gold and silicon get absorbed, and do not contribute to the transmittance, and the corresponding phenomenon is known as Wood's anomaly [171, 191].

Fig. 5.5(a) shows the calculated electromagnetic response of the metamaterial absorber. The asymmetric electromagnetic response is caused by the simultaneous excitation and interaction of the cavity mode, the guided mode and the Wood's anomaly resonances, which results in a Fano resonance. This Fano resonance arises due to the interference of the bright mode (cavity mode resonance) and the dark mode (guided mode resonance and Wood's anomaly) resonances. The calculated absorption spectrum

consists of three peaks at wavelengths $6.4\ \mu\text{m}$, $9.1\ \mu\text{m}$ and $10\ \mu\text{m}$. The peak at a wavelength of $6.4\ \mu\text{m}$ corresponds to the metamaterial absorption peak due to the presence of the tri-layer (Au/ZnS/Au) on the top of the photoresist disk [75, 76, 192]. There is no contribution of this resonance in the Fano resonance, so it was neglected in the further simulations by not including the top gold and ZnS layer on the photoresist disk in the simulation.

Fig. 5.6 shows the calculated electromagnetic response without considering the top gold and ZnS layer on the photoresist disk. However, there is an appearance of a peak in the absorption spectrum at $6.4\ \mu\text{m}$ which is due to the localized surface plasmons at the corner of the gold disk placed on the top of the photoresist disk. There is no effect of the removal of the top gold and ZnS layers from the photoresist disk on the other resonances, which can be seen in Fig. 5.6(a). The arrow plot of the normalized time average power flow with its color map is shown in Fig. 5.6(b). The simultaneous excitation of cavity mode, guided mode and Wood's anomaly can be seen through the coupling of power flow into each mode. The simultaneous excitation of all these modes can be seen in the color map of the normalized magnetic fields in Fig. 5.6(c). The propagation of the diffracted wave at the interface of gold and silicon can be seen in Fig. 5.6(d), which results in almost zero transmittance.

To understand the Fano resonance better and to elucidate the contribution of different modes in the Fano resonance, the simulations were carried out for different periodicities of the photoresist disk array which are shown in Fig. 5.7. Only the cavity mode resonance exists in the case of photoresist disk array with $2\ \mu\text{m}$ periodicity. The existence of this mode is independent of the periodicity of the disk array and is always associated with the unit cell size, and hence regarded as bright mode (super-radiant mode), whereas the existence of the guided mode resonance and Wood's anomaly is conditional and hence regarded as the dark mode (sub-radiant mode). Interference of the bright and dark modes is conditional, and it only happens at $2.8\ \mu\text{m}$ periodicity (Fig. 5.7b). For periodicity of $4\ \mu\text{m}$, these interfering modes get separated in frequency

(Fig. 5.7c), and the modes corresponding to the resonance wavelengths of $8.8 \mu\text{m}$, $10.3 \mu\text{m}$ and $13.7 \mu\text{m}$ are the cavity mode, guided mode and Wood's anomaly, respectively. The existence of the cavity mode can be seen even at $5 \mu\text{m}$ periodicity (Fig. 5.7d).

The color maps of the normalized magnetic field and normalized time average power flow with its arrow volume plot at different resonant wavelengths corresponding to $4 \mu\text{m}$ periodicity of disk array are shown in Fig. 5.8. Excitation of cavity mode resonance can be understood by confinement of the magnetic field in the cavity and arrow volume plot of the time average power from Figs. 5.8(a) and (d), respectively. The guided mode resonance can be understood by confinement of the magnetic field in the waveguide and arrow volume plot of the time average power from Figs. 5.8(c) and (f). Similarly, the Wood's anomaly resonance can be understood from Figs. 5.8(d) and (e).

The coupled mode theory (CMT) has been used to describe the Fano asymmetric line profile which arises due to the interference of bright and dark resonances in the metamaterial absorbers [185, 193]. Since our system contains mainly two resonances; one is cavity resonance and other is GMR, so the CMT with the one-port and two modes resonator model can be used to describe the asymmetric reflectance spectra of the metamaterial absorber [176, 194]. The reflectance r corresponding our metamaterial absorber is

$$r = -1 + \frac{2(W_1\gamma_2 + W_2\gamma_1 - 2\gamma_0\sqrt{\gamma_1\gamma_2})}{(W_1W_2 - |\gamma_0|^2)} \quad (5.1)$$

where $W_i = j(\omega - \omega_i + \gamma_i + \gamma'_i)$, ($i = 1, 2$), ω_i is resonant frequency corresponding to the i^{th} mode, γ_i is the radiation loss rate due to the interaction between the i^{th} mode and the outgoing wave, γ'_i is the intrinsic loss rate associated with the i^{th} mode, and γ_0 is the coupling between the modes. The first two terms of the numerator of the second part of Eq. 5.1 describe the responses of two modes independently after coupling modulation, whereas the last term $\sqrt{\gamma_1\gamma_2}$ describes the responses of the cross-coupling between the two modes after coupling modulation. For the metamaterial absorber, the radiation

losses for the two modes are $\gamma_1 = 6.42$ THz and $\gamma_2 = 1.86$ THz. The intrinsic loss rates of the two modes are $\gamma'_1 = 6.4$ THz and $\gamma'_2 = 3.0$ THz. The coupling between modes occurs at $\omega_0 = 6.53$ THz. The resonant frequencies of the two modes are $\omega_1 = 65.6$ THz and $\omega_2 = 60.73$ THz.

The fitting parameters match well with the expected parameters such as the spectral position of resonances, bandwidth of the individual resonance, etc. Now, it is clear that the asymmetric profile is caused by the interference of mainly the CM resonance and the GM resonance. The responses of the individual resonance using the same fitting parameters as for the fitting of the reflectance spectra [see in Fig. 5.11] are plotted in Fig. 5.12.

The simulated reflectance spectra [see Fig. 5.9] follow the same trend as the measured ones [see Fig. 5.4] for both polarizations. However, some smaller features such as minima in the reflectance spectra around the $7.5 \mu\text{m}$ and $10 \mu\text{m}$ are readily seen in the measured reflectance spectra as those appear in the simulated reflectance spectra for both polarizations. In the simulation, the gap between the gold layers on the photoresist disk and the ZnS layer is considered to be 15 nm to avoid the sharp peak in the middle of reflection deep as observed for 10 nm gap. The magnitude of the minima in the measured reflectance spectra is lesser than that predicted in the simulations. The measured reflectance bandwidth is also substantially larger than that in the simulated reflectance spectra which points to

- Inhomogeneous broadening of the resonance caused by the slightly varying sizes and shapes of the photoresist disks. This can be attributed to the experimental error as expected in the interference lithography.
- Averaging over the angular response due to the approximately 10° angular widths of the infrared beam in the FTIR spectrometer.

In the measured reflectance spectra, there is no appearance of the tri-layer resonance

at wavelength $6.4 \mu\text{m}$ which appear in that of simulated one. It is clear from the AFM topographical map [see Fig. 5.2] and the SEM image [see Fig. 5.3] of the fabricated sample after tri-layer deposition, after the consecutive deposition of gold, ZnS and gold layers, the top portion of the disk is no longer flat. Due to the smaller size of the top metallic disk, the resonance arises due to the tri-layer (Au/ZnS/Au) on the top of disk shifted towards the much lower wavelengths [76], and hence, there is no appearance of the resonance in the measured reflectance spectra. The minimum in the simulated reflectance spectra that appear at $9.8 \mu\text{m}$ wavelength is also not clearly distinguishable in the measured one. Again this could be the reason of the non-sharpness in the corner of the deposited tri-layer on the photoresist disk as well as on the substrate that may not leave the sharp gap between the gold layers on the photoresist and on the ZnS layer. Also note that we have considered a finite transmittance through the silicon substrate in the simulations whereas in the experiments, we have used single sided polished silicon substrate and the transmittance through the sample cannot be measured.

5.4 Conclusions

We have proposed a very simple design of metamaterial absorber with band selective absorptivity/emissivity that is suitable for large area fabrication. FEM based simulations were used to cross-check the physical phenomena happening in the system as well as to estimate the geometrical parameters and to understand the mechanisms for the absorption. The origin of absorption as well as the asymmetric nature of the absorption profile has been understood. The absorption is caused due to the simultaneous excitation of the cavity and guided mode resonances in the structures whereas the asymmetric profile is caused due to the interference of the bright mode (cavity mode), dark mode (guided mode and Wood's anomalies). Our approach can easily be adopted for the large areas fabrication on the industrial level. Thus, a simple method

for rapid production of designer metamaterial absorbers for large areas has been presented. The spectral position of the resonance can be tuned without structural size and shape modification just by the changing the gap between the gold layers on the top of photoresist pillar and the ZnS layer at the substrate. Another advantage of this structure is that it reduces the fabrication complexity by separating the structuring and deposition processes and making them sequential, as well as avoiding expensive lift-off and etching processes.

Chapter 6

Microstructuring using two photon polymerization with a sub-nanosecond laser

6.1 Introduction

The enhanced transmittance through a sub-wavelength hole array mounted with dielectric micro-domes structures was reported in Chapter 3, where the micro-domes were fabricated by back exposure through the substrate using UV laser. Due to the transparency of the substrate it was possible to fabricate the micro-domes using back exposure with UV laser, however, it will not be possible to fabricate the micro-domes array on the holes array in the case of opaque substrate as well as for the real applications like mounting on the detector surface. In that case, the direct laser writing technique can be used to fabricate the micro-domes on the top of each hole selectively on transparent as well as on the opaque substrate. Multi-photon absorption lithography is a direct laser writing technique, which enables local writing using polymerization in photosensitive materials inside as well as on surfaces. We have developed a TPALS for fabrication of different shaped micro/nanostructures for different applications.

Micro/nano fabrication techniques have a significant contribution to the development of micro-and nanodevices, which have many advantages over their macro-scale counterparts. For example, miniaturization allows manufacturing of easily portable, hand-held, implantable and even injectable devices [120, 195–199]. In addition to the minute sizes, these devices result in savings in the input materials and time for mass production. The growing demands of micro/nano structured materials have become important because of the ever-decreasing dimensions of devices, including those used in electronics, photonics, optical components, biological sensors and electromechanical components [200–202]. During the past few decades, several micro/nano fabrication techniques such as electron beam lithography (EBL), focused ion beam (FIB) milling and photo lithography have been developed for the fabrication of simple as well as complex micro/nano-structures [134, 203, 204]. Conventional laser writing and FIB milling have been only partially successful for fabrication of 3D micro/nano-structures. The requirement of high vacuum for the EBL and FIB methods can be disadvantageous. Micro-stereo lithography is an alternative method for 3D micro fabrication [205], but has its limitations in terms of spatial resolution and speed of writing. Multi-photon lithography can be highly advantageous over the other techniques due to the localized nature of the polymerization that can be employed for fabrication of highly complex 3D microstructures with the spatial resolution far smaller than 100 nm [135, 140]. This technique has found numerous applications in the fields of memory devices, plasmonics, micro-electro-mechanical systems (MEMS), photonic devices, chemical and biosensors [101, 196, 206–208].

Martin Wegener's group at the Karlsruhe Institute of Technology has reported several research articles on the fabrication of truly 2D/3D microstructures by two photon polymerization using a commercially available nanoscribe system [120, 145, 209–211]. In fact, M. Wegner is one of the co-founders of the nanoscribe company. The system has been showing the great potential for fabrication of even very complex shape microstructures. Maria Farsari's group at FORT in Greece has also reported several

articles on the multi-photon polymerization for different medical applications using the nanoscribe system [196, 212–214]. Maria Farsari et al. have reported three photon polymerization in a combination of organic-inorganic hybrid ORMOCER (Micro Resist Technology) material and photoinitiator Irgacure 369 (Ciba) using femtosecond laser operating at wavelength 1028 nm [215]. The photosensitive materials used by the nanoscribe system are proprietary in nature.

Much of multi-photon laser writing has been carried out using Ti: sapphire femtosecond lasers operating at 780 nm wavelength. Although the ultra-short pulses are very efficient for multi photon polymerization, they come with an associated high equipment cost. This can be off-set by picosecond or sub-nanosecond lasers and using photoinitiators with large two photon absorption cross section to obtain sub-wavelength resolution. Baldeck et al. have reported 3D micro-structuring using a low cost Q-switched Nd:YAG microlaser [148, 216, 217]. He et al. [149] have reported a series of multi-photon absorbing materials, that can be used for multi-photon polymerization using picosecond and sub-nanosecond lasers. Other groups have utilized hybrid organic-inorganic resist such as SZ2080 (ORMOSIL) for the fabrication of high resolution structures with picosecond lasers. 2, 4, Diethyl-9H-thioxanten-9-one was shown to be effectively work as a photoinitiator with SZ2080 photoresist using 8 ps laser pulses [147].

Mostly, the TPP technique has been used for the fabrication of complex shaped dielectric 2D/3D microstructures. Metallization of the fabricated devices is a little bit more challenging due to the complexity of the structures. However, some groups have come up with different processes to metallize the fabricated structures, and it still remains a challenge for scientific communities. The electroless deposition has been mostly used for metallization of the fabricated structures using two photon polymerization for different applications [112, 218–221]. Baldeck et al. have reported the direct fabrication of the metallic structures by the multi-photon polymerization using metal particles in the photosensitive materials. Ioanna Sakellari et al. have recently reported

the fabrication of 3D Chiral plasmonic metamaterials using direct laser writing [222].

These results clearly laid a route for low-cost fabrication systems and moving towards industrial rapid production. We also note that the single photon absorption can also be used for fabrication of 3D micro-structuring by very tightly focused laser beam at low intensity using the exposure threshold of photo sensitive materials for fine development [223]. But the writing speeds are comparatively very small due to the long exposure time required. The details of the multi-photon polymerization and recent research activities using the multi-photon polymerization can be found in the recent review article [224].

In this Chapter, we discuss the TPA, TPP and the optimization of the TPALS for the fabrication of micro/nano-structures in different photosensitive materials. New combinations of commercially available negative photoresists such as SU-8 and AR-N 4340 [225, 226], ma-N 1405 and the photoinitiator (2,4-Diethyl-9H-thioxanten-9-one) have been proposed and optimized for fabrication of microstructures. Systematic studies of resolution dependence on the laser power, writing speed and fabrication parameters have been carried out for the fabrication of complex as well as simple microstructures. Finally, it is shown that our system is competitive with commercially available systems based on expensive femtosecond lasers and proprietary photosensitive materials.

Chapter is organized as follows: a brief introduction about the two photon polymerization system and its current status are discussed in Section 6.1. The basic introduction of TPA and TPP are discussed in Sections 6.2 and 6.3, respectively. The photosensitive materials and optimization of different parameters such as laser dose, dwell time, writing speed, concentration of photoinitiator, etc. have been discussed in Section 6.4. Further, the sample fabrication in different photosensitive materials and the role of truncation by substrates in voxel resolution and adhesion issues on the substrates have been explored in Section 6.5. Next, the characterization and calibration of

the fabricated microstructures have been discussed in Section 6.6. Section 6.7 contains the details of theoretical estimation of the voxel dimensions, and finally conclusions are given in Section 6.8.

6.2 Fundamentals of two photon absorption

Two photon absorption (TPA) is a nonlinear optical process where there is a simultaneous absorption of two photons in a single quantum event by atoms or molecules resulting in the molecule transiting to an excited state. It was theoretically predicted by Maria Göppert Mayer in 1931 during her doctoral research [138]. The experimental realization of the phenomenon become possible only after the invention of the laser that made available the required intensities, and it took almost thirty years. The first experimental verification of the TPA was confirmed by Kaiser et al. [137], and that was the fluorescence signal emitted by a europium-doped crystal whose electrons were excited by two-photon absorption.

The TPA process is schematically shown in Fig. 6.1 (a), where an intermediate virtual state is created due to the interaction of electromagnetic field with matter, and the sum of the energies of individual photon need to match the energy of the electronic transition. According to the energy-time uncertainty relation, there can be some time scale associated with the transition given by $\hbar/\Delta E$, where ΔE is the energy difference between virtual state and the closest real state and \hbar is the Planck constant. In other words, the absorption of two photons does not need to be instantaneous, and it can occur within the interval given by the energy-time uncertainty relation. The difference between the virtual level and closest real state depends on the energy of the first photon that arrives in the molecule or atom. The probability for the two photons will be higher if they arrive closer together in time.

To increase the probability of such an absorption process, a high density of pho-

tons is required. Such a high density of photons can be obtained by spatially and temporally confining photons using high numerical aperture (NA) objectives and pulsed lasers, respectively. The spatial and temporal confinement of photons using high NA objective and picosecond pulse laser are shown in Figs. 6.1 (b) and (c), respectively. In a continuous laser, there is a uniform distribution of photons over the time with low intensity, but in pulsed laser, a large number of photons are confined in a short laser pulse [shown in Fig. 6.1(c)]. In light-matter interactions, energy and momentum

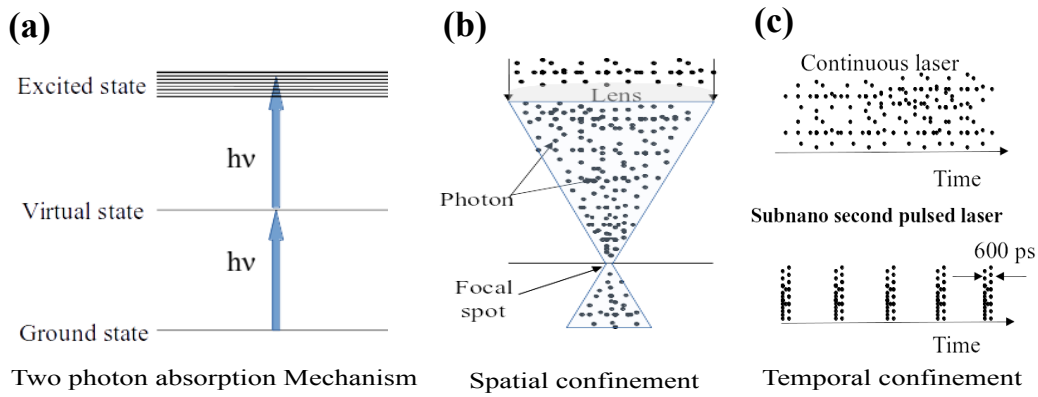


Figure 6.1: (a) Mechanism of two photon absorption when photons are simultaneously excited. An illustration of the methods for increasing the probability of two photon absorption by increasing the density of photons by (b) spatial confinement using objectives with high numerical aperture and by (c) temporal confinement of photons using pulse laser.

are exchanged between the optical fields and atoms/molecules through absorption and emission. In such a process, the energy transfer from the optical fields to a medium is proportional to the imaginary part of the nonlinear susceptibility. The change in light-matter interaction energy per unit time and per unit volume can be written as

$$\frac{dW}{dt} = \left\langle \vec{E} \cdot \dot{\vec{P}} \right\rangle, \quad (6.1)$$

where \vec{E} and \vec{P} are the electric field and the material polarization, respectively. The bracket indicates a time average. The value of the material polarization P can be written as:

$$P = \epsilon_0 [\chi^{(1)} E + \chi^{(2)} E^2 + \chi^{(3)} E^3 + \dots], \quad (6.2)$$

where $\chi^{(1)}, \chi^{(2)}, \chi^{(3)}$ are second, third, and fourth rank tensors, representing linear, second-order and third-order optical susceptibilities, respectively. For the centrosymmetric molecule having a centre of symmetry at the centre or isotropic materials such as liquids, glasses or polymers, even order susceptibilities like $\chi^{(2)}, \chi^{(4)}$ can be neglected. Therefore, the nonlinear absorption is described by the imaginary parts of $\chi^{(3)}, \chi^{(5)}$ of which typical effects are two-photon and three-photon absorptions, respectively. In the case of degenerate two photon absorption, the energy absorption rate can be written as

$$\frac{dW}{dt} = \frac{8\pi^2 h\omega}{c^2 n^2} I^2 \text{Im} \left[\chi^{(3)} \right], \quad (6.3)$$

where $\frac{dW}{dt}$ is the change in energy density per unit time, ω , c , n , I and $\chi^{(3)}$ are the angular frequency, the speed of light in vacuum, refractive index of the medium, laser intensity and the third-order non-linear optical susceptibility of the medium, respectively. It is clear that in the case of TPA, the rate of absorption is directly proportional to the square of the laser intensity, whereas in the case of single photon absorption, it is directly proportional to the laser intensity only.

Two photon absorption can dominate over the linear absorption and changes the properties of photosensitive materials within the focal volume. The minimum feature size that can be achieved in linear absorption is typically limited to the full width at half maximum (FWHM) of the laser beam. In contrast, the spatial feature size can be lesser than the FWHM of the corresponding laser intensity profile by a factor of $\sqrt{2}$ due to the I^2 dependence in the case of TPA (see Fig. 6.2(a)). Further, the material change and development processes require a minimum threshold dose of light, which may be used to restrict the region of changed material to sizes much smaller than the wavelength (see Fig. 6.2(b)). In the view of resolution and damage threshold of the photosensitive material, the intensity should be close to the polymerization threshold, too much intensity will increase the polymerization volume and reduce the resolution, and also may further damage the samples by thermal or photochemical effects. These

are some of the characteristics that have made two photon laser writing technique very appealing in the last few years.

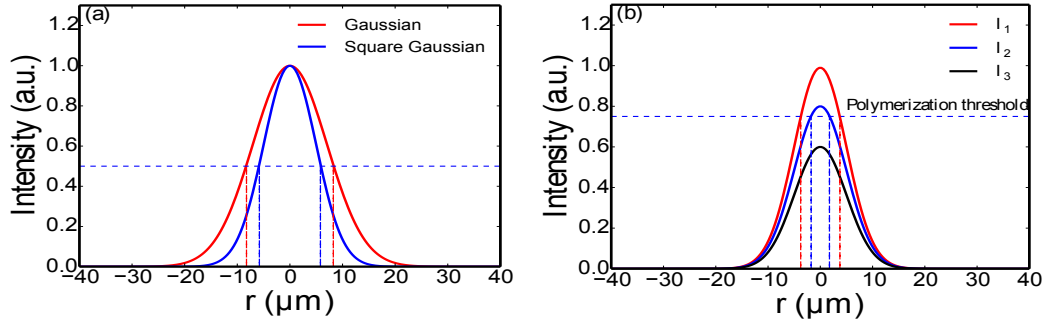
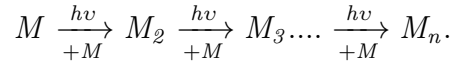


Figure 6.2: (a) Comparison of the spatial full width at half maximum of a Gaussian shaped beam intensity and its squared (I^2) profile, (b) schematic explaining a threshold intensity for photosensitive materials with a threshold assumed to be at horizontal dashed line. As the peak intensity gets closer to the threshold from above, the voxel width decreases.

6.3 Two photon polymerization

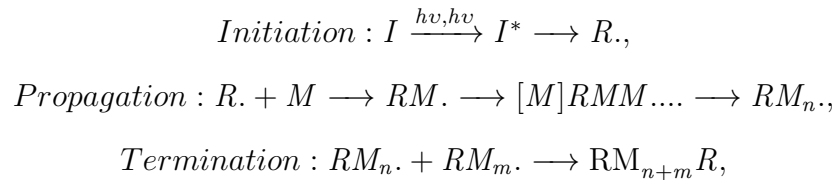
Photopolymerization is a chemical reaction that converts molecules of low molecular weight (monomers/oligomers) into macro-molecules consisting of repeating units of monomers/oligomers by using light as the reaction triggering agent [227]. Upon excitation by the light, monomers or oligomers undergo through the photo rectification by two means: polymerization and cross-linking [228–230]. In polymerization, there is a formation of macro-molecules by means of chain reaction whereas in cross-linking, there is a formation of cross-links with chemical bonds. The main difference between these two kinds of reactions lies in their quantum yield, which is defined as the ratio of the number of polymerized monomer/oligomer units to the number of photons that are needed to cause this polymerization. In the case of photo cross-linking, the addition of each monomer unit requires absorption of a photon, resulting in quantum yield less than 1. In contrast, polymerization is realized via chain reactions, so the quantum yield can reach several thousand.

The photo cross-linking can be understood from the following chemical reaction [227]:



Here, M is the monomer or oligomer unit and M_n is the macro-molecule containing n monomer units. In each step, there is a requirement of absorption of a photon to carry on the further cross-linking, so the quantum yield is lesser than unity. In general, the quantum yield of monomer/oligomer is low. To increase the initiating efficiency of the monomers/oligomers, few low-weight molecules which are more sensitive to light irradiation are added. They start the reaction by converting themselves into initiating radicals or cations by absorbing photons. Such small molecules are known as photoinitiators.

In single photon polymerization, radical species can be formed by conventional light sources (as UV lamps or laser with large photon energy) but not in the case of two photon polymerization (TPP). In TPP, a highly intense laser beam is tightly focused into the photosensitive material that results in the formation of free monomer radicals. These monomer radicals react with other monomers through a polymerization chain reaction until two such monomer radicals meet and finally terminate as polymer [227]. The TPP process can be described as follow:



where the absorption of two photons by the photoinitiator (I) causes the formation of the intermediate state (I^*) of radicals ($R.$) which combine with monomers (M) and form the monomer radicals ($RM.$). The monomer radical combines with new monomers, and form a polymeric chain of monomer radical ($RM_n.$ or $RM_m.$).

Thus, these radicals combine to each other and finally terminate as a polymer chain (RM_{n+m}R).

6.4 Photosensitive materials

Usually, the photosensitive materials used for two photon polymerization using sub-nanosecond/femtosecond lasers are proprietary in nature [147]. Nanoscribe company is providing a series of photoresists such as; P-Dip, IP-L 780, IP-G 780 and IP-S for different specific applications, and all are proprietary in nature. We have used commercially available negative photoresists SU-8-3005 (Micro-chem Corp., USA), AR-N 4340 (Allresist, Germany) and ma-N 1405 (Micro-resist, Germany). SU-8 has an optimum cross-linking response in the wavelength range of 350-400 nm. AR-N 4340 has an optimum response in the wavelength range of 300-390 nm, especially for the Hg i-line and also responds to the deep-UV (248-265 nm) and g-line (436 nm) as well. Thus AR-N 4340 shows the extremely good response for polymerization by TPA at 532 nm and can be used even without a photoinitiator. The photoresist ma-N 1405 has a response in the wavelength range of 240–450 nm. The photoinitiator (2,4, Diethyl-9H-thioxanten-9-one) (THIO) which has an absorption maximum at 255 nm [231] was used with the given photoresists to enhance the TPA at 532 nm wavelength. The amount of photoinitiator used in this work is typically 3% by the weight of photoresist.

We have used SU-8, ma-N 1405 and AR-N 4340 negative photoresists. The different combinations of photoresist with different weighted concentrations of photoinitiator were prepared and checked for the optimum parameters. It was noticed that AR-N 4340 photoresist undergoes polymerization even without adding the photoinitiator. The optimum parameters for micro-line arrays fabricated at different average laser powers without the PI and with different weighted concentration of the PI in AR-N 4340 photoresist are discussed in Appendix-C.

6.5 Sample fabrication

In general, SU-8 has poor adhesion on glass substrates. So HMDS (hexamethyldisilazane) was used as a promoter to enhance the adhesion with the glass substrate. Thoroughly cleaned glass substrates were coated with a thin layer of HMDS at 6000 RPM for 45 seconds and baked on a hot plate at 120°C for 2 minutes. After cooling at room temperature, the photosensitive resist (SU-8 with PI@3 %) was coated at 2000 RPM for 1 minute and pre-baked at 65°C for 2 minutes and at 95°C for 3 minutes, and finally exposed to laser in the laser writing system operating at 532 nm wavelength. After that post-exposure bakes were carried out for 3 minutes at 65°C and 5 minutes at 95°C to complete the polymerization, consequently the exposed portions harden. Again after cooling to room temperature, the development of the polymerized structures was carried out in propylene glycol methyl ether acetate for 20 seconds and followed by a wash in isopropyl alcohol for 1 minute. During development, the unexposed portions wash away leaving behind the polymerized structures. The development time depends on the thickness of the coated material, and it is typically longer for thicker photoresist.

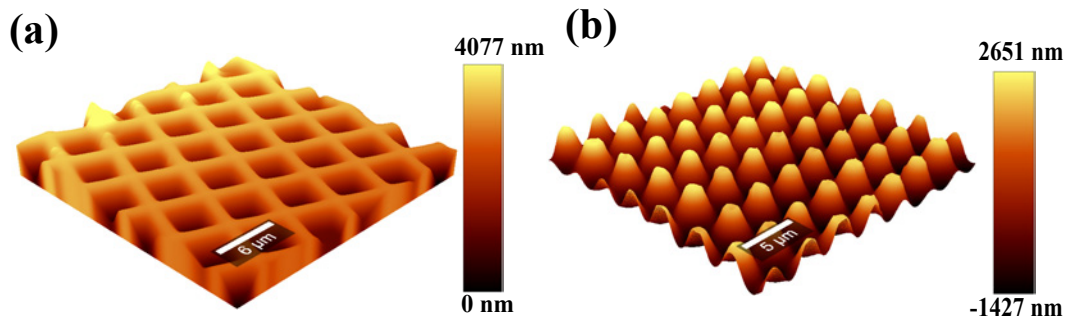


Figure 6.3: 3D view of AFM topographical maps of (a) 2D grating and (b) 2D micro disk array fabricated in SU-8. The experimental parameters used for fabrication of these microstructures are: 1.2 mW laser average power, 100 $\mu\text{m/s}$ writing speed, 10 kHz rep rate and 0.8 NA objective.

Fabrication of microstructures in AR-N 4340 was carried out as follow: cleaned glass substrates were coated with AR-N 4340 photoresist at 2000 RPM for 1 minute, and pre-baked at 85°C for 2 minutes, and exposed to laser under the laser writing

system. After a post-exposure bake carried out for 5 minutes at 95°C, the exposed portions harden. After cooling down to room temperature, the development of the polymerized structures was carried out in the developer (AR-300-475) for 20 seconds and followed by a wash in DI water for 1 minute and dried by blowing dry nitrogen. During development the unexposed portions wash away leaving behind the cross-linked structure.

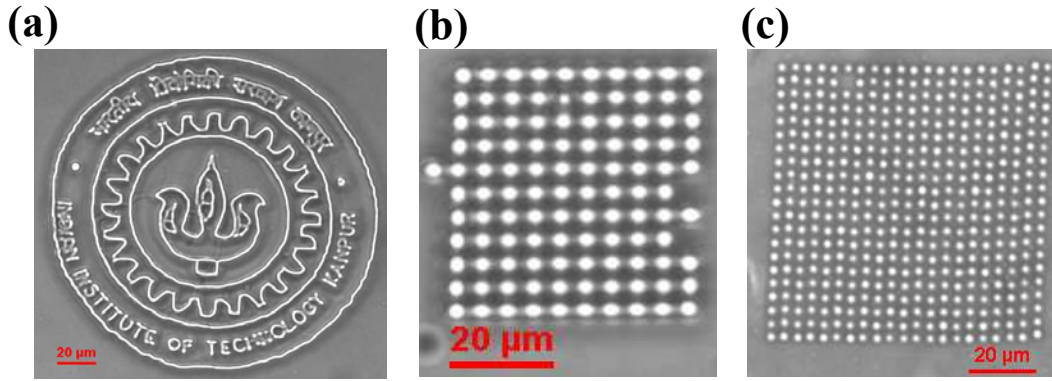


Figure 6.4: Optical microscopy images of (a) logo of IIT Kanpur fabricated in SU-8, (b) an array of micro-pillars of height 6 μm fabricated in SU-8, (c) 2D disk array fabricated in AR-N 4340. All these microstructures are fabricated using the parameters: 1.2 mW laser average power, 100 $\mu\text{m/s}$ writing speed, 10 kHz rep rate and 0.8 NA objective.

Fabrication of 2D grating in ma-N 1405 was carried out as follows: cleaned glass substrates were coated with ma-N 1405 photoresist at 2000 RPM for 1 minute, and pre-baked at 100 °C for 1 minute, and exposed to laser under the laser writing system. The exposed portions of the photoresist get polymerized during exposure under the laser system due to the formation of chemical bond among monomers/oligomers in the negative resist. After cooling down to room temperature, the polymerized structures were developed in ma-D 533 for 30 seconds and followed by a wash in DI water for 1 minute and dried by blowing dry nitrogen. During development, the unexposed portions get washed away leaving behind the cross-linked structure.

Figs. 6.3 (a) and (b) show the 3D view of AFM maps of a 2D line grating and a 2D array of 2D disks array fabricated in SU-8 photoresist. Control of the stage motion can enable the formation of complex micro structures: for example, Figs. 6.4(a) and

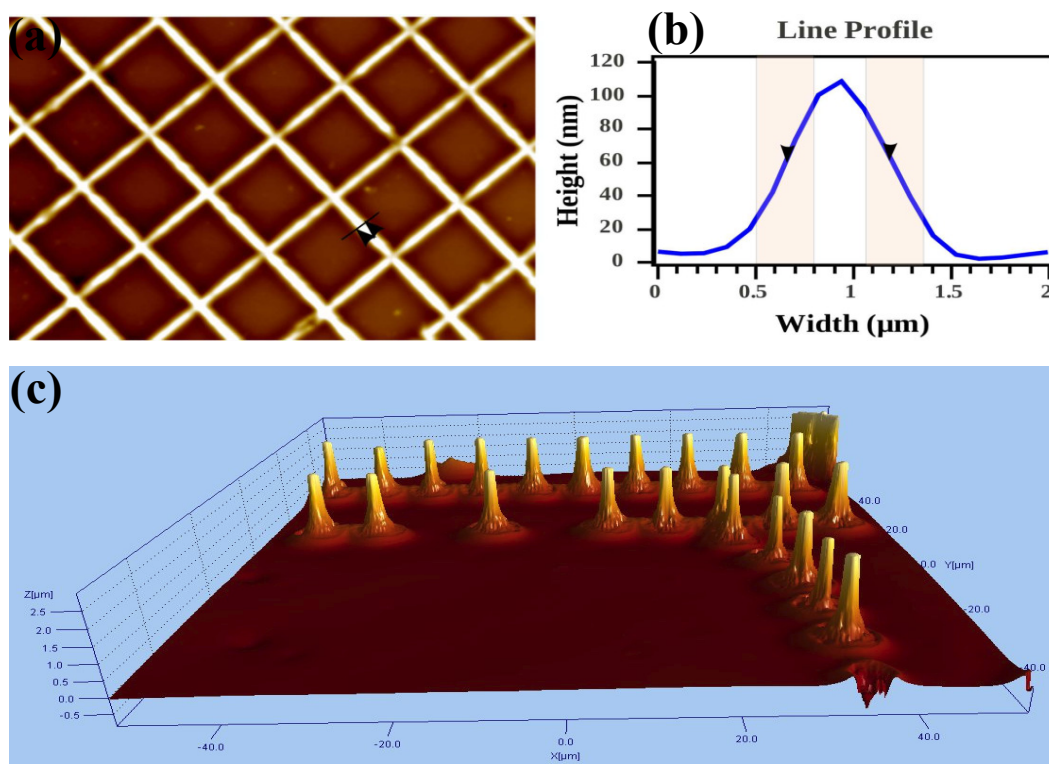


Figure 6.5: AFM topographical map of a 2D grating fabricated using $100\times$ oil immersion objective in SU-8, (b) the line profile of the selected portion of the micro-line in the sample, and FWHM of the corresponding line profile is around 500 nm. (c) 3D view of optical profiler image of the pillar array fabricated in SU-8.

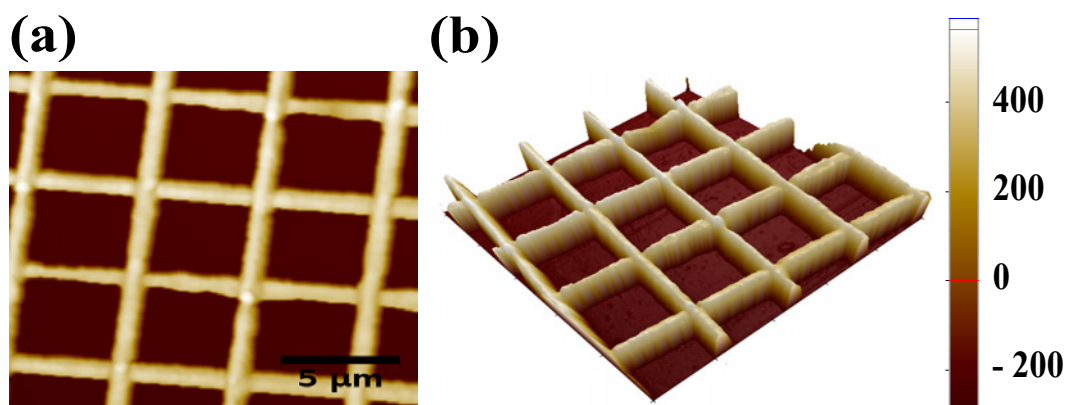


Figure 6.6: AFM topographical map of a 2D grating fabricated using $50\times$ magnification objective in ma-N 1405 negative photoresist, (b) 3D view of figure (a). This grating is fabricated using parameters: 1.2 mW laser average power, 1000 $\mu\text{m/s}$ writing speed, 10 kHz rep rate and 0.8 NA objective.

(b) show the optical microscopy images of the logo of IIT Kanpur and an array of 3D pillars fabricated in SU-8 photoresist. Fig. 6.4(c) shows the 2D disks array fabricated in AR-N 4340 photoresist with 3 % weighted concentration of PI. These microstructures

(Figs. 6.3 (a, b)) and (Figs. 6.4(a–c)) were fabricated using the parameters of 1.2 mW laser average power, 100 $\mu\text{m/s}$ writing speed, 10 kHz rep rate and 50 \times objective with 0.8 NA . Resolution of the fabricated structures highly depends on the NA of the objective. We used a 100 \times oil immersion objective with 1.3 NA for fabricating the microstructures and obtained spatial resolution around 500 nm for well defined lines as shown in Fig. 6.5(a). This 2D grating is fabricated in SU-8 using the parameters of 1.0 mW laser average power, 200 $\mu\text{m/s}$ writing speed, 10 kHz rep rate and 1.3 NA oil immersion objective. The optical profiler image of the fabricated pillars in SU-8 photoresist of height around 3 μm is shown in Fig. 6.5(c).

6.5.1 Role of voxel truncation in resolution and adhesion

In the TPP, resolution of the structure not only depends on the material, laser and fabrication parameters but also depends on the amount of truncation of the voxel dimension by the substrate. The truncation effect, a so-called ascending scan technique was first reported by Sun et al. [232]. This required to perform a point by point beam exposure of the resin while the sample holder is lowered/raised depending on the system configuration and translated. During the process, a critical height is found at which a voxel is generated at the interface between the substrate and resin, and it remains tethered to the surface after development. The truncation of the voxel by the substrate is schematically shown in Fig. 6.7(a). The proper adjustment of the laser focal spot on the sample is very important in the sense of adhesion on the substrate and control over the resolution. Some pillars topple down and some are washed away in the process of development and rinsing if the laser beam is not focused precisely just above the substrate. The toppling down and collapsing of the pillars due the improper focusing adjustment of the laser spot on the substrate are shown in Fig. 6.8(a). Most of the pillars have toppled down and some have collapsed and formed a big chunk of the resist.

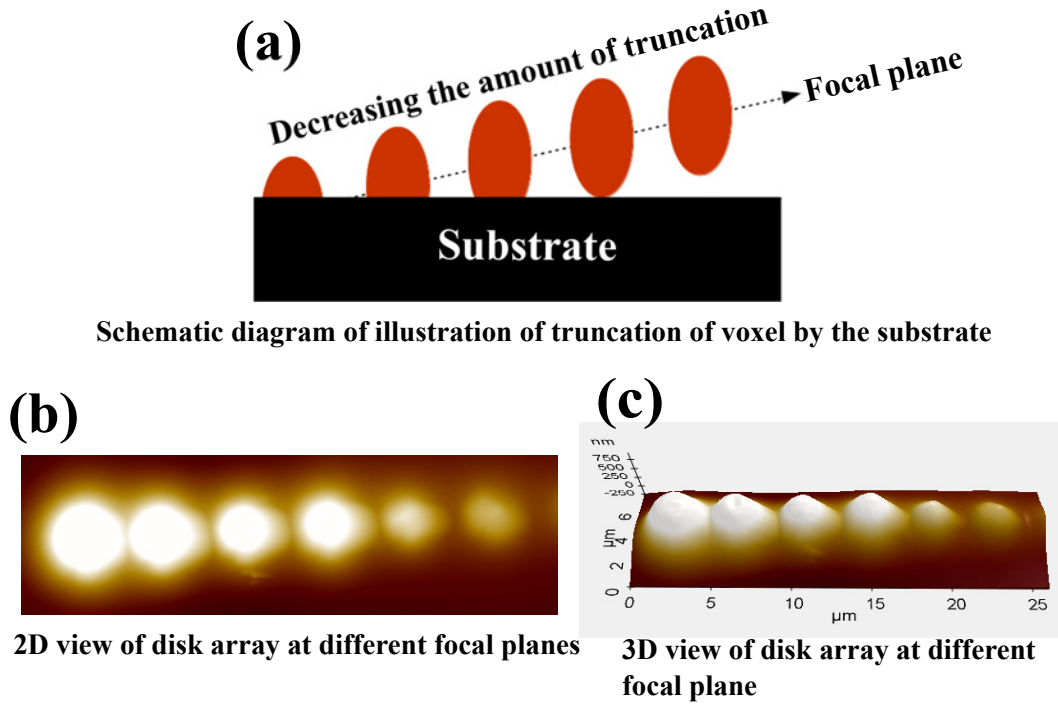


Figure 6.7: (a) Schematic diagram illustrating the truncation of the voxel by the substrate, (b) AFM topographical map of the pillars at a different height from the substrate. (c) 3D view of the AFM topographical map of the figure (b).

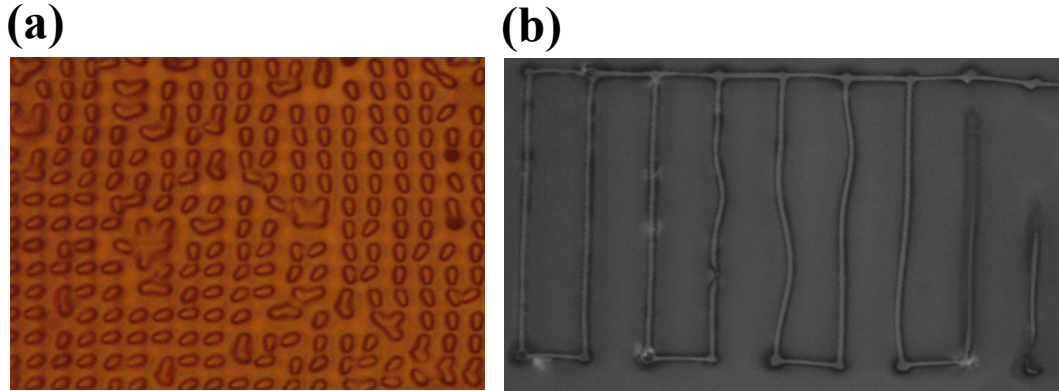


Figure 6.8: (a) Optical microscope image of the SU-8 pillar array topple down on the substrate during the development process, (b) Optical image of distorted micro-lines.

The amount of truncation also affects the shapes and dimension of the fabricated structures. When only a small part from the substrate side of the focal spot (i.e. most of the focal spot is truncated by the substrate) is in the volume of resist, fine line patterns are created and tightly tethered to the substrate. The line width of the fabricated structures can also be controlled by proper adjustment of the focal spot inside the resist. When most of the parts of the focal spot lie in the resist, the fabricated lines

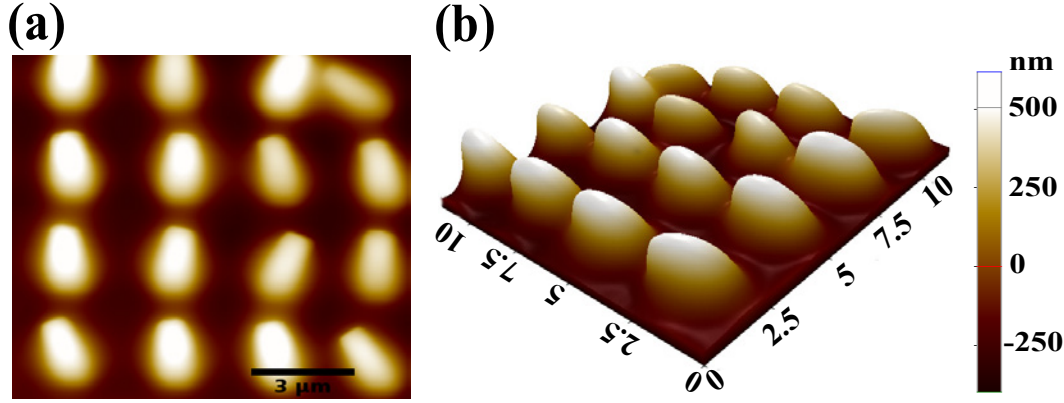


Figure 6.9: (a) 2D AFM topographical map of the SU-8 pillar array topple down on the substrate during the development process. (b) 3D AFM topographical view of the figure (a).

tend to topple over and the polymerized line begins to become wavy due to interaction with the developer during the development process. So, the critical distance between the substrate and the focal spot has to be maintained for optimum resolution and to adhere the structure with the substrate. The distortion in the line shapes and dimensions occur due to the lack of proper adjustment of the laser spot on the substrate as well as due to the interaction with developer during the development process, and some lines are even completely washed away in the development process [two lines from the right side in Fig. 6.9(b)]. Figs. 6.9(a) and (b) show AFM topographical maps of the SU-8 pillars array topple down on the substrates in 2D and 3D views, respectively.

6.6 Characterization and calibration of microstructures

Atomic force microscopy (WITec, Park System) and optical microscopy (Eclipse Ti-s, Nikon) were used to characterize the microstructures. The AFM was used in a non-contact mode with pyramidal-shaped tips (radius < 10 nm). Figs. 6.3 (a) and (b) show the 3D view of WITec AFM topographical maps of a 2D grating and a 2D disks array fabricated in the SU-8 photoresist. Fig. 6.5(a) shows the Park AFM topographical

maps of a 2D grating fabricated in the SU-8 photoresist. Figs. 6.6 (a) and (b) show the AFM topographical maps of a 2D grating and its 3D view fabricated in ma-N 1405 photoresist, respectively. Fig. 6.4 and Fig. 6.8 show the optical microscopy images of the fabricated samples in the SU-8 photoresist. Figs. 6.7(b) & (c) show the Park AFM topographical maps of dots at the different vertical height from glass substrate fabricated in SU-8 photoresist. Figs. 6.9(a) and (b) show the 2D and corresponding 3D park AFM topographical maps of the SU-8 pillars array topple down on the substrate during the development process, respectively. Figs. 6.10(a) and (b) show WITech AFM topographical maps of the micro-lines, which were fabricated at different peak intensities and different writing speeds in SU-8 photoresist using $50\times$ microscope objective, respectively.

We experimentally studied the effects of laser peak intensity, writing speed and dwell time on the width of micro-lines (see Fig. 6.10). It was noticed that the width of micro-lines increases with increasing the dwell time and peak intensity, that validates the theoretical prediction (see Fig. 6.13(a)). The damage to the photosensitive resin at higher laser powers can be seen in the first two lines (from the left in Fig. 6.10(a)). For pulsed energy below the threshold, the definition of the line is not complete. Thus a fine control over the peak intensity is necessary. We have also checked the effect of the writing speed on the line width and it also matches quite well with the theoretical prediction (see Fig. 6.13(b)).

Figs. 6.10(c) and (d) below the images show the corresponding height profiles of the lines drawn at various laser peak intensities and writing speeds, respectively. Figs. 6.11(a) and (b) show the measured line widths (FWHM) versus the peak intensity and the writing speed, respectively.

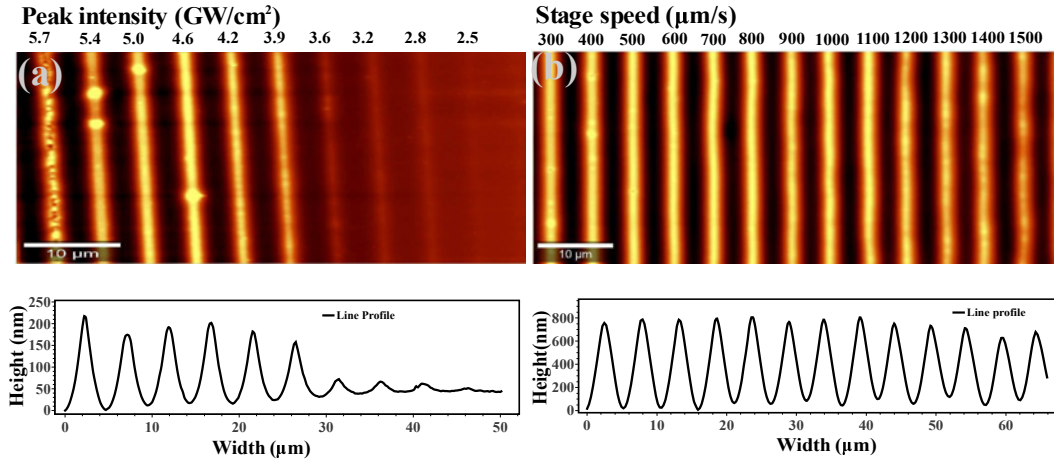


Figure 6.10: AFM topographical maps of (a) micro-lines array fabricated in the SU-8 at constant writing speed 100 $\mu\text{m/s}$ with decreasing peak intensity of 5.7 GW/cm^2 to 2.5 GW/cm^2 (from left to the right) and micro-lines array fabricated in the SU-8 at constant peak intensity 4.6 GW/cm^2 with increasing writing speed of 300 to 1600 $\mu\text{m/s}$ (from left to the right). The corresponding line profiles of the AFM maps are shown beneath the individual map.

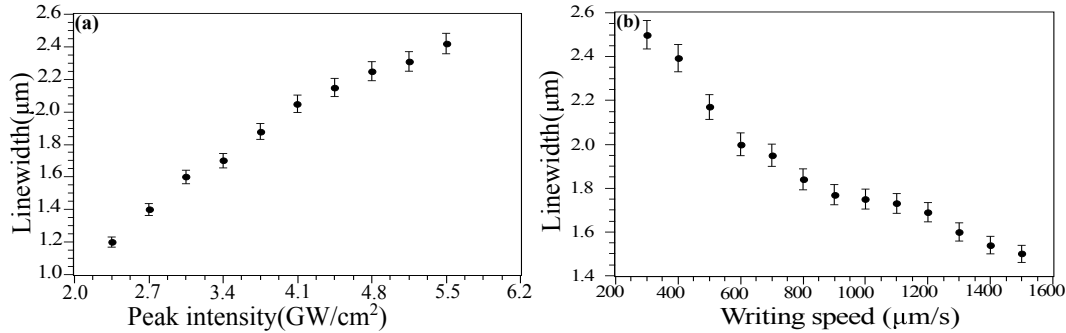


Figure 6.11: Line width (of Figs. 6.10 (a) and (b)) versus (a) peak intensity, (b) writing speed. Data points represent FWHM of the corresponding line profiles, while error bars show the variance in the line width.

6.7 Theoretical estimation of the voxel dimensions

A voxel is defined as the unit element of a three dimensional object corresponding to a pixel in a two-dimensional picture. In the case of two photon polymerization, the voxel dimensions depend on many fabrication conditions and system parameters such as laser power, pulse repetition rate, pulse width, exposure time, numerical aperture (NA) of the focusing lens and the two photon absorption cross-section of photosensitive

materials. Visualization of the formation of a voxel in our TPALS is shown in Fig. 6.12, in which the laser beam is focused through the microscope lens in the resin where the voxel formation takes place. An enlarged view of the voxel is shown to the right side of figure. Due to the threshold intensity that is required to form a stable structure,

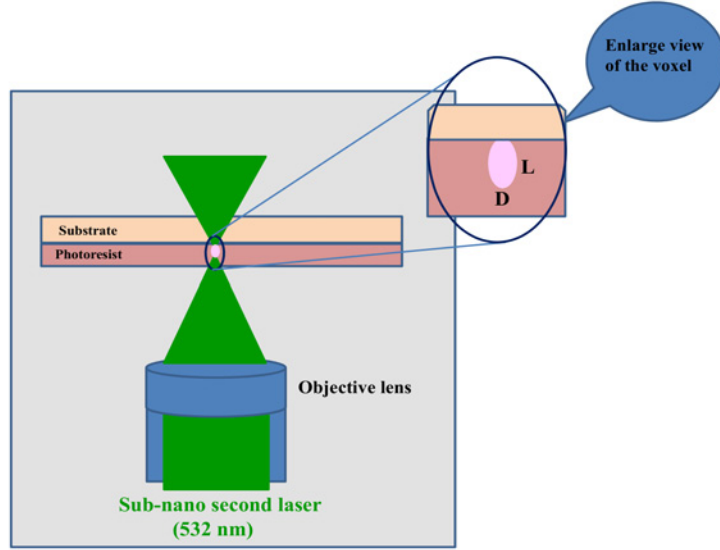


Figure 6.12: Schematic diagram used for visualization of the voxel formation in our TPALS.

the polymerization threshold can be estimated as [233]

$$I_{th}^2 \beta \tau f t \geq E_{th}, \quad (6.4)$$

where I_{th} , τ , f , t , β , and E_{th} are threshold laser intensity, pulsed duration, repetition rate, dwell time, absorption coefficient of photosensitive material and threshold energy per unit volume, respectively. The intensity distribution of a Gaussian laser beam is

$$I(r, z) = \frac{2P}{\pi w(z)^2} \exp\left[-2\left(\frac{r}{w(z)}\right)^2\right], \quad (6.5)$$

the amplitude is defined as $I(z) = 2P/(\pi w(z)^2)$, where P is the average laser power, $w(z)$ is the spot radius at the z plane and $r = \sqrt{x^2 + y^2}$ is the radial coordinate in

$x - y$ plane.

At the focal plane, ($z = 0$). We define $I_0 = I(z = 0)$ and $w_0 = w(z = 0)$ as the beam waist. The beam width elsewhere is

$$w(z) = \frac{\lambda}{\pi \tan[\sin^{-1}(\frac{NA}{n})]} \left[1 + \left(\frac{z\lambda}{\pi w_0^2} \right)^2 \right]^{1/2}, \quad (6.6)$$

where n is the refractive index of the medium, λ is the wavelength and NA is the numerical aperture of the lens used to focus the beam. The voxel width (D) and voxel depth (L) along the beam direction can be obtained from Eqs. (6.4 – 6.6) as

$$D(t, NA, P_{av}, f) = \frac{\lambda}{\pi \tan[\sin^{-1}(\frac{NA}{n})]} \left[\ln \left(\frac{4\pi^2 P_{av}^2 f t [\tan(\sin^{-1}(\frac{NA}{n}))^4]}{\lambda^4 E'_{th}} \right) \right]^{1/2} \quad (6.7)$$

and

$$L(t, NA, P_{av}, f) = \frac{2\lambda}{\pi \tan[\sin^{-1}(\frac{NA}{n})]} \left[\left(\frac{4\pi^2 P_{av}^2 f t [\tan(\sin^{-1}(\frac{NA}{n}))^4]}{\lambda^4 E'_{th}} \right)^{1/2} - 1 \right]^{1/2}, \quad (6.8)$$

respectively, where $E'_{th} = E_{th}/(\beta\tau)$. Since the writing speed of the stage is inversely proportional to the beam dwell time at a point, the dependence of the voxel dimensions on the writing speed can be obtained by replacing the dwell time with the inverse of stage speed times the spot size in Eq. (6.7).

The width of the fourth micro-line from the left in Fig. 6.10(b) was used along with the fabrication parameters to fit E'_{th} in Eq. (6.7) [234]. The fabrication parameters of the micro-line are: λ , NA , n , f , P_{av} are 532 nm, 0.8, 10 kHz, and 1.2 mW, respectively. The fitted value of E'_{th} ($6.6 \times 10^{-73} \text{ W}^2/\text{m}^4$) was used to plot Figs. (6.13)(a–c). The theoretical fits describe the observed trends in Fig.(6.10) very well.

Figs. 6.13(a), (b) and (c) show the dependence of the voxel width on the dwell time and stage speed and NA of the focusing lens, respectively as predicted by Eq. (6.7).

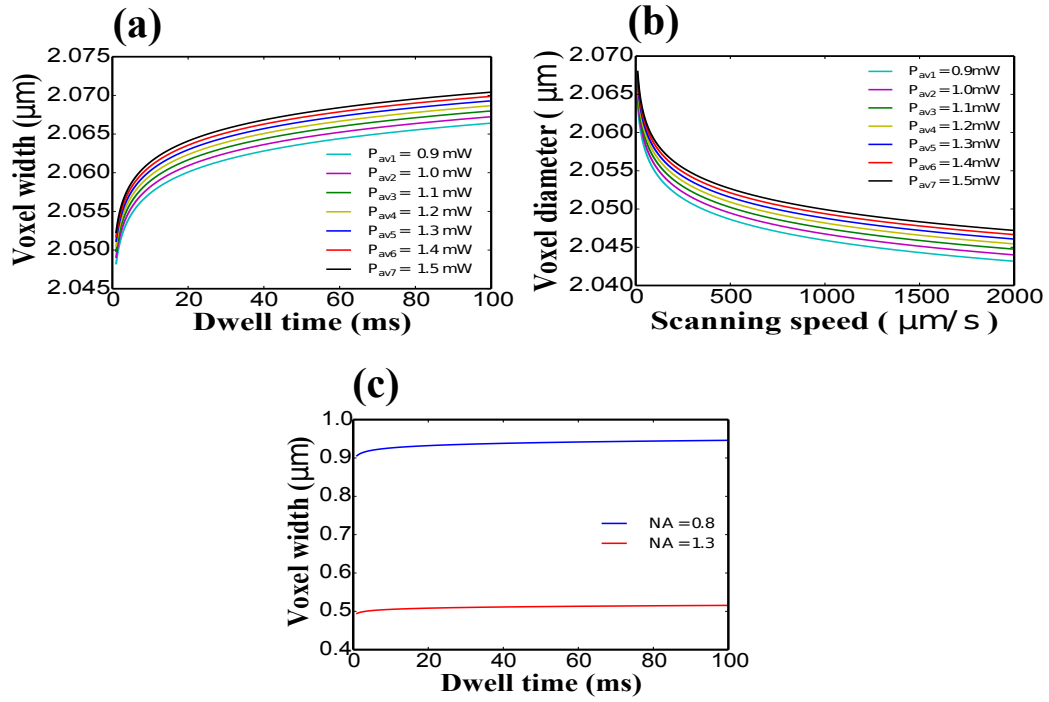


Figure 6.13: (a) Evolution of voxel width with dwell time and average laser power, (b) Evolution of voxel width with scanning speed and average laser power (c) Change in voxel width with the numerical aperture (NA) of the objectives and dwell time. The parameters used to plot these figures λ , NA , n , f , P_{av} , E'_{th} , are 532 nm, 0.8, 10 kHz, 1.2 mW and $6.6 \times 10^{-73} \text{ W}^2/\text{m}^4$, respectively.

Fig. 6.13(c) clearly shows that high resolution can be obtained using a high NA objective. Fig. 6.13(a) shows that the focusing parameters and dwell time are more critical to obtain a small voxel dimension than the laser power due to the fine focusing conditions here. Thus the theoretical predictions clearly show that high spatial localization of a voxel can be obtained using precise control over the laser power just above the polymerization threshold for less than 20 ms dwell times and 1 mW of average laser power.

There are some unique properties associated with two-photon polymerization technique which make this technique appealing for micro/nano-structuring for simple as well as complex shapes structures:

- It has intrinsic ability to produce 3D micro/nano-structures due to the localized threshold behaviour of the phenomenon, which happens only when intensity is

sufficient. In addition to this, due to the nonlinear process, the use of pulses reduces the chance of thermal damaging of the photosensitive materials.

- There is less scattering of light in this case compared to single photon polymerization due to the requirement of longer wavelengths that enables deeper penetration of the light into resists.
- It does not require any vacuum for fabrication like EBL, FIB that makes it easier to operate and maintain the system.
- There is no requirement of mask/mold for fabrication. It directly converts the CAD designs into the matter structures which allows one to quickly iterate and modify resin according to the input designs.

6.8 Conclusions

A TPALS with sub-micrometer resolution based on a sub-nanosecond pulsed laser has been developed. A detailed study and optimization of different processing parameters such as average laser power, writing speed, laser spot dwell time, concentration of PI and truncation of the laser focus spot by the substrate on the voxel have been performed. SU-8 and AR-N 4340, maN-1405 photoresists in combination of photoinitiator (2,4-Diethyl-9H-thioxanten-9-one) of large two photon absorption cross section at 532 nm wavelength have been used for fabrication of different microstructures. It has been noticed that the photoresist AR-N 4340 undergoes polymerization even without adding of the photoinitiator, implies having enough two photon absorption cross-sectional area at 532 nm wavelength. The feature size resolution as small as about $0.5\ \mu\text{m}$ (FWHM) and 3D pillars of about $6\ \mu\text{m}$ height have been demonstrated. The structural deformation and collapsing of longer height pillar have been noticed, which are suspected due to the improper exposure during the writing process, less tensile strength of the resist and development issue. The system based on an inexpensive sub-nanosecond laser and

commercially available photoresist materials promises an inexpensive substitute for expensive femtosecond laser based writers. It has also much higher capabilities for 2D micro-structuring in term of aspect ratio than conventional 2D laser micro writers.

Chapter 7

Summary and future aspects

Summary

Metamaterials and plasmonics have the potential to facilitate the fabrication of novel optical devices as well as to improve the performance of the existing ones. Metamaterial absorbers have potential applications in modern devices such as thermal imagers, selective thermal emitters, sensors, spatial light modulators, IR camouflage, use in thermophotovoltaics, and wireless communication. Metamaterial absorbers can be used to improve the performance of thermal camouflage which is used for defence applications. Thermal camouflage is used to make any object thermally indistinguishable from its surroundings. Due to the spectral tunability, compatibility with flexible and rough surfaces, metamaterial absorbers pave the way for thermal camouflage application.

Plasmonics micro/nano structures have opened a wealth of opportunities for the potential applications such as switches, sensors, filters, etc. In particular, EOT which occurs at specific frequencies imposed by the geometrical design, polarization, angle of incident light, and permittivity of the surrounding medium has been of a great area of research due to the different potential applications such as an optical coupler, nanophotonic devices, chemical and biological sensors, sub-wavelength photolithography,

near-field optics, filters, etc. Optical coupler is one the potential applications of EOT where the perforated metal film is mounted on the top of detector's active surfaces, and it has got particular attention by researchers globally due to the extraordinary performance in the coupling of light and enhancing the efficiency of photodetectors and solar cells.

In this thesis, plasmonic microstructures and metamaterials have been designed, fabricated and demonstrated for tuning the electromagnetic properties of infrared radiations as enhanced infrared transmitters and absorbers, respectively. For enhancing the transmittance through sub-wavelength hole array, SU-8 micro-domes were mounted on each hole by a unique back exposure technique through the substrate using UV laser. The SU-8 micro-domes mounted sub-wavelength hole array in a thin film show an enhanced transmittance compared to that of the without the micro-domes. The experimental observations with and without the micro-domes structures were confirmed by electromagnetic wave simulations. The dielectric micro-domes mounted on sub-wavelength holes in the thin metal film work as scatterers which scattered the incident electromagnetic radiation and help in the coupling of the incident radiation with the surface plasmon generated on the thin gold film. Transmittance through sub-wavelength holes array depends on the coupling of incident radiation and more coupling implies more transmittance. Thus, the transmittance through the sub-wavelength hole array is enhanced by mounting the dielectric micro-domes on the holes.

A simple bi-layered metamaterial absorber based on the localized spoof surface plasmons and cavity mode resonances have been designed, fabricated and demonstrated as a candidate for the thermal camouflage application. The spectral resonance of the metamaterial absorber can be easily tuned by changing the diameter of the photoresist disk. The metamaterial absorber has been fabricated on very rough surfaces like emery paper, unpolished aluminium sheet and flexible surface like kapton sheet as well as over the large areas. The experimental observations were confirmed using electromagnetic wave simulations. This design can be easily implemented for fabrication of metamate-

rial absorbers over large areas as well on flexible and rough surfaces, and it is suitable for the role to role fabrication on the industrial scale.

Another simple tri-layered metamaterial absorber based on the combined effect of the cavity mode, guided mode and Wood's anomalies is designed, fabricated and characterized. In this design, the spectral resonance can be easily tuned without changing the dimensions of the microstructures by just controlling the thickness of the deposited materials. The asymmetric resonance profile caused by Fano resonance is observed, due to the interference of bright (cavity mode) and dark mode resonances (guided mode and Wood's anomalies) arise in the system. This design can be used to fabricate the metamaterial absorbers over a large area, and is also suitable for industrial scale production.

A two photon absorption lithography system with sub-micrometer resolution based on a sub-nanosecond pulsed laser has been developed. The system with photosensitive materials has been optimized for different processing parameters such as average laser power, writing speed and laser spot dwell time, concentration of PI and truncation of the laser voxel by the substrate. The system has been used for fabrication of microstructures with different shapes even with sub-micrometer resolution. The system based on an inexpensive sub-nanosecond laser and commercially available photoresist materials promise to be an inexpensive substitute for expensive femtosecond laser writers. It has also much higher capabilities for two-dimensional micro structuring in term of aspect ratio than conventional laser micro writers.

We finally note that our use of gold for the conducting layer in the metamaterial is only for convenience, as gold probably would be unacceptable for most applications from the perspectives of adhesion, low scratch resistance, high optical reflectivity, etc. Other metals like silver, copper or chromium would also face some of the above problems and additionally suffer from long term oxidation and corrosion. In this context, infrared metamaterials have been demonstrated [235] using transparent conducting oxides

such as indium tin oxide. Conducting materials like aluminium doped zinc oxide, indium tin oxide, fluorine doped tin oxide and Titanium nitride, etc. may also be used for the construction of robust and rugged infrared metamaterials [236].

Future Aspects

The work discussed in the whole thesis is mainly concentrated on design, fabrication and characterizations of metamaterials and plasmonic microstructures for infrared applications as well as custom made inexpensive laboratory equipment for micro/nanofabrication. The extraordinary optical transmission has been used for many applications such as sensors, photovoltaic, detectors, etc. For sensing applications, there is a need of a sharp resonance to enable the detection of even small resonance shift whereas for photovoltaic and detector applications the efficiency of devices must be optimum to enhance their performance. Up to 30% enhancement in the detectivity of an InAs quantum dot infrared photodetector with a perforated metal film integrated on top of the detectors active region has been reported by S. Krishna's group. The performance of the quantum dot infrared photodetector can be further enhanced by mounting our proposed design as sub-wavelength hole array mounted dielectric microdomes on the top of detector's surface.

As far as different applications of the metamaterial absorbers are concerned, we have proposed a simple and robust design of double-layers metamaterial absorber for very rough, flexible surfaces and for large areas. The metamaterial absorbers have also been characterized for their emissivity properties in addition to reflectivity and found exactly matching with absorptivity. This design can be used for defence applications to hide the object from IR detectors, night vision cameras. The other proposed design of the tri-layered metamaterial absorber is also very simple and can be easily fabricated over large areas. We have also developed a TPALS using a sub-nanosecond laser. The

system is still undergoing improvements and can be further developed for the fabrication of more complex shaped microstructures.

The following things can be done for the further development of the system:

- Our present system is compatible with only transparent substrates, it can be further designed for fabrication of structures on transparent as well as opaque substrates.
- The issues of collapsing and toppling down voxels and micro-line can be avoided by further development in the system for an auto-focusing arrangement.
- We have used a limited number of the photoresists and photoinitiator combination for fabrication of microstructures. As we have discussed a lot of properties of the microstructures depend on the photosensitive materials. There are many possibilities for trying new combinations of photoresists and photoinitiators.

Apart from these mechanical aspects, this system can be used for fabrication of symmetric, asymmetric and cylindrical shaped metamaterials and plasmonic structures for different applications, as well as in general micro/nanofabrication for MEMS and NEMS.

Appendix-A

Operation procedures of the two photon absorption lithography system

There are some steps which have to be followed by users to operate the system.

1. Switch “ON” the main power supply from which all the components are connected. Then switch on power supply for computer, AO modulator driver, laser driver, nano-positioning stage, camera and microscope.
2. There are two software programs for controlling the motion of the stage, one is for manual feeding the co-ordinates values and the other reads the data from the files, the appropriate one can be chosen among the two.
3. If one has chosen to feed the data manually, then there is requirement to open the front panel of the corresponding software, and go to the servo mode selection option and switch it to “ON” state.
4. Select the axis to move, for x, y and z axes fill up 1, 2 and 3, respectively.
5. Define the speed of stage in $\mu\text{m/s}$, and its maximum range is $2000 \mu\text{m/s}$.
6. Define the position in μm , and it should be less than $200 \mu\text{m}$ in all axes.
7. Now system is ready for operation, mount the sample in such a way that the coated face should face the objective of the microscope.
8. Focus the sample using microscope ocular or CCD camera, or it can be done in reverse order first mount and focus the sample and follow the steps starting from second one.

One may want to operate the system in automatic mode by feeding the data in the text format, then one needs to extract the coordinates of the design in the text format and follow the next steps of the system operation.

1. One should follow the same procedures of the operation for manual data feeding. Switch on the system as mentioned in the above operation procedure.
2. There is an extra icon in this front panel, that is for loading the data. Load the data just by clicking on the icon and run the program as usual by clicking on the icon of the LabView start button.

Appendix-B

Important steps involved in design and simulations.

- **Defining the parameters and variables:**

The parameters icon can be selected from the home toolbar of COMSOL or by right clicking on the global definition setting. The parameters setting generally contains the terms like the refractive index of the working media, angle of incidence, angle of refraction, dimension of domain, etc. Similarly the variables icon can be selected from the home toolbar or by right-clicking on the icon of the definition setting. This setting contains of the components of wave vectors with appropriate units.

- **Drawing of geometry:**

The different shapes geometry like rectangular, elliptical, spiral, spherical, cylindrical and many more can be selected from the home toolbar or by right clicking on the geometry icon on the left side panel. There are some options inbuilt in the COMSOL, like extrude which helps in converting a 2D design into 3D and also to make some complex designs. Again it depends on the complication of the domain. If it is not possible to design in the COMSOL then the geometry designed in AutoCAD can be imported into the COMSOL.

- **Defining the Physics:**

The Physics setting like the electromagnetic wave simulation and frequency domain were already selected during the selection of module. However, the other settings like wave equations, boundary conditions, ports, perfectly matched layer (PML), etc. are done during defining the physics. The wave equation can be set as per requirement of the problems in the individual domain. Periodic boundary conditions are used along the x and y directions to simulate an infinite array

of unit cells to reduce the complexity of the simulation. In our case, the Floquet periodic boundary condition is used along x and y directions. PMLs were used along the propagation direction (z -direction) to prevent the reflection of the waves from the top and bottom domain boundaries. Two ports are defined at the top and bottom layers of the simulation domain for excitation of the system and receiving the electromagnetic responses.

- **Setting materials:**

The material setting icon can be selected from the left side panel in the home. As it enables the freedom of choosing material on selective domain the basis, so it is possible to fill the different domain with required material. Some materials parameters are available in the COMSOL menu, and the domain can be filled from there. The parameters of the material which are not available in the COMSOL can be imported from external sources.

- **Meshing:**

Meshing is very important in any FEM based simulations, the accuracy of results highly depends on the meshing of domains. The mesh generator discretizes the domains into tetrahedral, hexahedral, prismatic, pyramidal mesh elements. The FEM calculations are mainly based on the values of variables. The more accurate results can be obtained generally with more variables. But it also increases the number of calculations and the computation time as well as errors beyond a point. There are two options for meshing the geometry, one is physics control meshing and other is user control meshing. The user control meshing is more efficient in which the individual domains can be meshed as per the dimensions of domain. It is recommended for efficient meshing to increase the number of elements in the domains with large changes (or gradients) of variables, and decrease the number with smaller changes of variables.

- **Solving:**

After setting the needed parameters, the program can be run by selecting the study option and clicking on compute icon. The computation can be performed under direct or iterative methods. There are some set of solvers in direct method like MUMPS, PARDISO, SPOOLES, dense matrix. In our work, we have used direct method with MUMPS solver to performed the simulations.

• Results analysis

The physics behind different responses of the simulation domain can be understood by plotting the different physical quantities like electric fields, magnetic fields, current densities, time average power flow, etc. in the electromagnetic simulation (frequency domain) of the RF module. Similarly the different results can be understood by plotting of relevant physical quantities in other modules.

In the RF module, the reflection and transmission coefficients are calculated in term of the S parameters from the port boundary conditions. The S parameters are defined as

$$S_{11} = \frac{\int_{port1} [(E_c - E_r) \cdot E_r^*] dA_1}{\int_{port1} (E_r \cdot E_r^*) dA_1}, \quad (7.1)$$

and

$$S_{21} = \frac{\int_{port2} (E_c \cdot E_t^*) dA_2}{\int_{port1} (E_t \cdot E_t^*) dA_2}, \quad (7.2)$$

where E_c , E_r and E_t are the computed electric fields at the ports, corresponding to the incident, reflected and transmitted electric fields, respectively.

Appendix-C

Optimization of the combination of photoresist and photoinitiator

In this work, we have used SU-8, ma-N 1405 and AR-N 4340 negative photoresists. The different combinations of photoresist with different weighted concentrations of photoinitiator were prepared and checked for the optimum parameters. It was noticed that AR-N 4340 photoresist gets polymerized even without the photoinitiator. The micro-line arrays fabricated at different average laser powers without the PI and with a different weighted concentration of the PI in AR-N 4340 photoresist are shown in Fig. 7.1. The micro-line width gets broadened with an increase in the concentration of the PI up-to 3%, and further starts decreasing with the further increase of concentration due to the radical quenching [147]. Similarly, different weighted concentrations of the PI were tried with SU-8 photoresist. The optimum weighted concentration of the PI with SU-8 is found to be 3 %, and it was used throughout the work with SU-8.

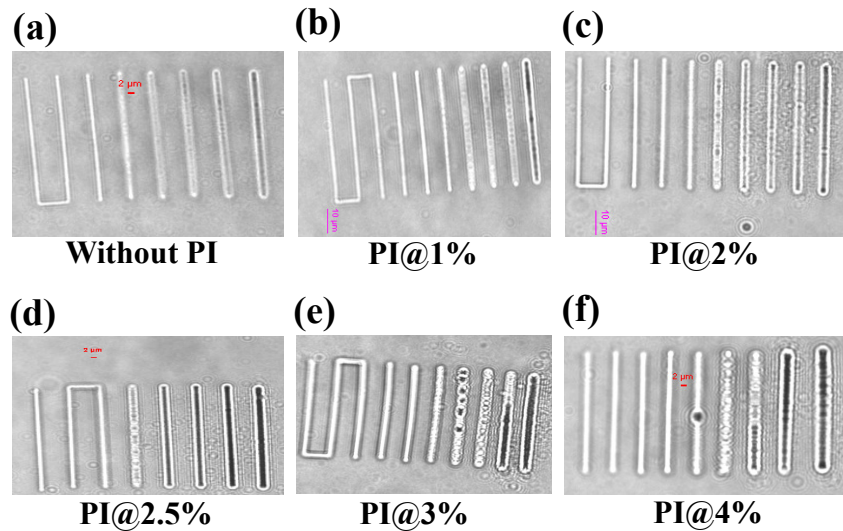


Figure 7.1: Micro-lines array fabricated at different average powers without the PI and with a different weighted concentration of the PI in AR-N 4340 photoresist.

Bibliography

- [1] S. A. Maier, *Plasmonics: fundamentals and applications* (Springer Science & Business Media, Berlin, 2007).
- [2] H. Raether, *Surface plasmons on smooth and rough surfaces and on gratings* (Springer, Berlin Heidelberg New York, 1988), pp. 91–116.
- [3] B. E. Saleh, M. C. Teich, and B. E. Saleh, *Fundamentals of photonics* (Wiley, New York, 1991), Vol. 22.
- [4] A. Yariv and P. Yeh, *Oxford University* **22**, 24 (2006).
- [5] S. A. Ramakrishna and T. M. Grzegorzczuk, *Physics and applications of negative refractive index materials* (CRC press, Boca Raton, 2008).
- [6] W. Cai and V. M. Shalaev, *Optical metamaterials* (Springer, Berlin, Heidelberg, New York, 2010), No. 6011.
- [7] A. Turner, I. Karube, and G. S. Wilson, *Biosensors: fundamentals and applications* (Oxford university press, Oxford, UK, 1987).
- [8] A. Boisen and T. Thundat, *Materials today* **12**, 32 (2009).
- [9] M. A. Green, K. Emery, Y. Hishikawa, and W. Warta, *Progress in photovoltaics: research and applications* **19**, 84 (2011).
- [10] A. G. Aberle, *Progress in Photovoltaics: Research and applications* **8**, 473 (2000).
- [11] K. Sakoda, *Optical properties of photonic crystals* (Springer Science & Business Media, Berlin, 2004), Vol. 80.
- [12] J. D. Joannopoulos, S. G. Johnson, J. N. Winn, and R. D. Meade, *Photonic crystals: molding the flow of light* (Princeton university press, New Jersey, United States, 2011).
- [13] V. G. Veselago, *Soviet physics uspekhi* **10**, 509 (1968).
- [14] S. Ogawa, K. Okada, N. Fukushima, and M. Kimata, *Applied Physics Letters* **100**, 021111 (2012).
- [15] X. Liu, T. Tyler, T. Starr, A. F. Starr, N. M. Jokerst, and W. J. Padilla, *Physical Review Letters* **107**, 045901 (2011).
- [16] N. Liu, T. Weiss, M. Mesch, L. Langguth, U. Eigenthaler, M. Hirscher, C. Sonnichsen, and H. Giessen, *Nano letters* **10**, 1103 (2009).

- [17] P. B. Johnson and R.-W. Christy, Physical review B **6**, 4370 (1972).
- [18] A. D. Rakić, A. B. Djurišić, J. M. Elazar, and M. L. Majewski, Applied optics **37**, 5271 (1998).
- [19] R. L. Olmon, B. Slovick, T. W. Johnson, D. Shelton, S. H. Oh, G. D. Boreman, and M. B. Raschke, Phys. Rev. B **86**, 235147 (2012).
- [20] H. Li, Journal of Physical and Chemical Reference Data **9**, 561 (1980).
- [21] M. Debenham, Applied Optics **23**, 2238 (1984).
- [22] I. H. Malitson, J. Opt. Soc. Am. A: **55**, 1205 (1965).
- [23] J. L. Digaum, J. J. Pazos, J. Chiles, J. DArchangel, G. Padilla, A. Tatulian, R. C. Rumpf, S. Fathpour, G. D. Boreman, and S. M. Kuebler, Opt. Express **22**, 25788 (2014).
- [24] G. Behera, P. Mandal, and S. A. Ramakrishna, Journal of Applied Physics **118**, 063104 (2015).
- [25] D. Pines and D. Bohm, Physical Review **85**, 338 (1952).
- [26] J. D. Jackson, *Classical electrodynamics* (John Wiley & Sons, New Jersey, United States, 2012).
- [27] U. Kreibig and M. Vollmer, *Optical properties of metal clusters* (Springer, Berlin Heidelberg, New York, 1995), pp. 13–201.
- [28] C. F. Bohren and D. R. Huffman, *Absorption and scattering of light by small particles* (John Wiley & Sons, New Jersey, United States, 2008).
- [29] J. Pendry, L. Martin-Moreno, and F. Garcia-Vidal, Science **305**, 847 (2004).
- [30] A. P. Hibbins, B. R. Evans, and J. R. Sambles, Science **308**, 670 (2005).
- [31] S. A. Maier, S. R. Andrews, L. Martin-Moreno, and F. Garcia-Vidal, Physical Review Letters **97**, 176805 (2006).
- [32] Z. Gao, X. Zhang, and L. Shen, Journal of Applied Physics **108**, 113104 (2010).
- [33] B. J. Yang, Y. J. Zhou, and Q. X. Xiao, Optics Express **23**, 21434 (2015).
- [34] Z. Li, B. Xu, L. Liu, J. Xu, C. Chen, C. Gu, and Y. Zhou, Scientific reports **6**, 27158 (2016).
- [35] Y. J. Zhou, C. Zhang, L. Yang, and Q. X. Xiao, JOSA B **34**, D9 (2017).
- [36] M. Born and E. Wolf, *Principles of optics: electromagnetic theory of propagation, interference and diffraction of light* (Elsevier, Amsterdam, Netherlands, 2013).
- [37] D. Rosenblatt, A. Sharon, and A. A. Friesem, IEEE Journal of Quantum electronics **33**, 2038 (1997).
- [38] S. Wang, R. Magnusson, J. S. Bagby, and M. Moharam, JOSA A **7**, 1470 (1990).
- [39] S. Wang and R. Magnusson, Applied optics **32**, 2606 (1993).
- [40] R. H. M. Michael T. Gale, Karl Knop, Zero-order diffractive microstructures for security applications, 1990.

- [41] P. Priambodo, T. Maldonado, and R. Magnusson, *Applied physics letters* **83**, 3248 (2003).
- [42] D. Wawro, S. Tibuleac, and R. Magnusson, *Optical Imaging Sensors and Systems for Homeland Security Applications* (Springer, New York, 2006), pp. 367–384.
- [43] Y. H. K. Robert Magnusson, *Guided-mode resonance nanophotonics: fundamentals and applications*, 2016.
- [44] R. C. Rumpf and E. G. Johnson, *Optics Express* **15**, 3452 (2007).
- [45] U. Fano, *Il Nuovo Cimento* (1924-1942) **12**, 154 (1935).
- [46] U. Fano, *Physical Review* **124**, 1866 (1961).
- [47] M. I. Rabinovich and D. Trubetskov, *Oscillations and waves: in linear and non-linear systems* (Springer Science & Business Media, Berlin Heidelberg, New York, 2012), Vol. 50.
- [48] Y. S. Joe, A. M. Satanin, and C. S. Kim, *Physica Scripta* **74**, 259 (2006).
- [49] C. Wu, A. B. Khanikaev, R. Adato, N. Arju, A. A. Yanik, H. Altug, and G. Shvets, *Nature materials* **11**, 69 (2012).
- [50] M. Rybin, A. Khanikaev, M. Inoue, K. Samusev, M. Steel, G. Yushin, and M. Limonov, *Physical review letters* **103**, 023901 (2009).
- [51] B. Luk'yanchuk, N. I. Zheludev, S. A. Maier, N. J. Halas, P. Nordlander, H. Giessen, and C. T. Chong, *Nature materials* **9**, 707 (2010).
- [52] R. Singh, I. A. Al-Naib, M. Koch, and W. Zhang, *Optics Express* **19**, 6312 (2011).
- [53] V. Fedotov, M. Rose, S. Prosvirnin, N. Papasimakis, and N. Zheludev, *Physical review letters* **99**, 147401 (2007).
- [54] M. Rahmani, B. Luk'yanchuk, and M. Hong, *Laser & Photonics Reviews* **7**, 329 (2013).
- [55] Y. Ma, Z. Li, Y. Yang, R. Huang, R. Singh, S. Zhang, J. Gu, Z. Tian, J. Han, and W. Zhang, *Optical Materials Express* **1**, 391 (2011).
- [56] T.-T. Tang *et al.*, *Nature nanotechnology* **5**, 32 (2010).
- [57] A. E. Miroshnichenko, S. Flach, and Y. S. Kivshar, *Reviews of Modern Physics* **82**, 2257 (2010).
- [58] H. A. Bethe, *Physical review* **66**, 163 (1944).
- [59] T. W. Ebbesen, H. J. Lezec, H. Ghaemi, T. Thio, and P. Wolff, *Nature* **391**, 667 (1998).
- [60] H. Ghaemi, T. Thio, D. Grupp, T. W. Ebbesen, and H. Lezec, *Physical review B* **58**, 6779 (1998).
- [61] L. Martín-Moreno, F. J. García-Vidal, H. J. Lezec, K. M. Pellerin, T. Thio, J. B. Pendry, and T. W. Ebbesen, *Phys. Rev. Lett.* **86**, 1114 (2001).
- [62] L. Martin-Moreno, F. Garcia-Vidal, H. Lezec, K. Pellerin, T. Thio, J. Pendry, and T. Ebbesen, *Physical review letters* **86**, 1114 (2001).

- [63] L. Martin-Moreno and F. Garcia-Vidal, *Optics Express* **12**, 3619 (2004).
- [64] H. Gao, J. Henzie, and T. W. Odom, *Nano Lett.* **6**, 2104 (2006).
- [65] P. Lalanne and J. P. Hugonin, *Nature Physics* **2**, 551 (2006).
- [66] R. Gordon, D. Sinton, K. L. Kavanagh, and A. G. Brolo, *Acc. Chem. Res.* **41**, 1049 (2008).
- [67] T. Y. Chang, M. Huang, A. A. Yanik, H. Y. Tsai, P. Shi, S. Aksu, M. F. Yanik, and H. Altug, *Lab Chip* **11**, 3596 (2011).
- [68] X. Luo and T. Ishihara, *Opt. Express* **12**, 3055 (2004).
- [69] B. Hecht, B. Sick, U. P. Wild, V. Deckert, R. Zenobi, O. J. F. Martin, and D. W. Pohl, *J. Chem. Phys.* **112**, 7761 (2000).
- [70] A. Pors, E. Moreno, L. Martin-Moreno, J. B. Pendry, and F. J. Garcia-Vidal, *Phys. Rev. Lett.* **108**, 223905 (2012).
- [71] F. Garcia-Vidal, L. Martin-Moreno, and J. Pendry, *J OPT A PURE APPL OP* **7**, S97 (2005).
- [72] A. Hajiaboli, M. Kahrizi, and V.-V. Truong, *Journal of Physics D: Applied Physics* **45**, 485105 (2012).
- [73] G. Behera and S. A. Ramakrishna, *Journal of Nanophotonics* **8**, 083889 (2014).
- [74] A. Degiron, H. Lezec, W. Barnes, and T. Ebbesen, *Applied Physics Letters* **81**, 4327 (2002).
- [75] N. I. Landy, S. Sajuyigbe, J. Mock, D. Smith, and W. Padilla, *Physical Review Letters* **100**, 207402 (2008).
- [76] G. Dayal and S. A. Ramakrishna, *Optics Express* **20**, 17503 (2012).
- [77] C. M. Watts, X. Liu, and W. J. Padilla, *Advanced Materials* **24**, (2012).
- [78] S. Guddala, R. Kumar, and S. A. Ramakrishna, *Applied Physics Letters* **106**, 111901 (2015).
- [79] J. K. Pradhan, S. A. Ramakrishna, B. Rajeswaran, A. M. Umarji, V. G. Achanta, A. K. Agarwal, and A. Ghosh, *Optics Express* **25**, 9116 (2017).
- [80] R. A. Shelby, D. R. Smith, and S. Schultz, *Science* **292**, 77 (2001).
- [81] D. Schurig, J. Mock, B. Justice, S. A. Cummer, J. B. Pendry, A. Starr, and D. Smith, *Science* **314**, 977 (2006).
- [82] J. B. Pendry, *Physical Review Letters* **85**, 3966 (2000).
- [83] N. Mattiucci, M. Bloemer, N. Aközbek, and G. D'aguanno, *Scientific reports* **3**, 3203 (2013).
- [84] B. Zhu, C. Huang, Y. Feng, J. Zhao, and T. Jiang, *Progress In Electromagnetics Research* **24**, 121 (2010).
- [85] H. Tao, N. I. Landy, C. M. Bingham, X. Zhang, R. D. Averitt, and W. J. Padilla, *Optics express* **16**, 7181 (2008).

- [86] Y. Avitzour, Y. A. Urzhumov, and G. Shvets, *Physical Review B* **79**, 045131 (2009).
- [87] K. Bhattarai, S. Silva, K. Song, A. Urbas, S. J. Lee, Z. Ku, and J. Zhou, *Scientific Reports* **7**, 10569 (2017).
- [88] W. Zhou, Y. Wu, M. Yu, P. Hao, G. Liu, and K. Li, *Optics letters* **38**, 5393 (2013).
- [89] R. Ameling, L. Langguth, M. Hentschel, M. Mesch, P. V. Braun, and H. Giessen, *Applied Physics Letters* **97**, 253116 (2010).
- [90] M. K. Hedayati, F. Faupel, and M. Elbahri, *Materials* **7**, 1221 (2014).
- [91] J. Rhee, Y. Yoo, K. Kim, Y. Kim, and Y. Lee, *Journal of Electromagnetic Waves and Applications* **28**, 1541 (2014).
- [92] C. Wu, B. Neuner III, J. John, A. Milder, B. Zollars, S. Savoy, and G. Shvets, *Journal of Optics* **14**, 024005 (2012).
- [93] K. Yao and Y. Liu, *Nanotechnology Reviews* **3**, 177 (2014).
- [94] L. F. Thompson, *An introduction to lithography* (ACS Publications, Washington, DC, 1983).
- [95] S. Reyntjens and R. Puers, *Journal of micromechanics and microengineering* **11**, 287 (2001).
- [96] J. P. Silverman, *Journal of Vacuum Science & Technology B: Microelectronics and Nanometer Structures Processing, Measurement, and Phenomena* **15**, 2117 (1997).
- [97] B. Wu and A. Kumar, *Journal of Vacuum Science & Technology B: Microelectronics and Nanometer Structures Processing, Measurement, and Phenomena* **25**, 1743 (2007).
- [98] C. Lu and R. Lipson, *Laser & Photonics Reviews* **4**, 568 (2010).
- [99] C. L. Haynes and R. P. Van Duyne, *Nanosphere lithography: a versatile nanofabrication tool for studies of size-dependent nanoparticle optics*, 2001.
- [100] J. C. Hulteen and R. P. Van Duyne, *Journal of Vacuum Science & Technology A: Vacuum, Surfaces, and Films* **13**, 1553 (1995).
- [101] B. H. Cumpston *et al.*, *Nature* **398**, 51 (1999).
- [102] J. Spallas, A. Hawryluk, and D. Kania, *Journal of Vacuum Science & Technology B: Microelectronics and Nanometer Structures Processing, Measurement, and Phenomena* **13**, 1973 (1995).
- [103] Y. Xia and G. M. Whitesides, *Annual review of materials science* **28**, 153 (1998).
- [104] J. A. Rogers and R. G. Nuzzo, *Materials today* **8**, 50 (2005).
- [105] L. Wu, Y. Zhong, C. T. Chan, K. S. Wong, and G. P. Wang, *Applied Physics Letters* **86**, 241102 (2005).
- [106] J.-H. Seo, J. H. Park, S.-I. Kim, B. J. Park, Z. Ma, J. Choi, and B.-K. Ju, *Journal of nanoscience and nanotechnology* **14**, 1521 (2014).

- [107] D. Tan, Y. Li, F. Qi, H. Yang, Q. Gong, X. Dong, and X. Duan, Applied physics letters **90**, 071106 (2007).
- [108] C. M. Soukoulis and M. Wegener, nature photonics **5**, 523 (2011).
- [109] A. Ostendorf and B. N. Chichkov, Photonics spectra **40**, 72 (2006).
- [110] K. Kaneko, H.-B. Sun, X.-M. Duan, and S. Kawata, Applied physics letters **83**, 2091 (2003).
- [111] J. Serbin, A. Ovsianikov, and B. Chichkov, Optics Express **12**, 5221 (2004).
- [112] F. Formanek, N. Takeyasu, T. Tanaka, K. Chiyoda, A. Ishikawa, and S. Kawata, Optics express **14**, 800 (2006).
- [113] S. Kawata, T. Tanaka, and N. Takeyasu, Two-photon fabrication of three-dimensional metamaterials, 2009.
- [114] W. R. H. W. W. En-Shinn Wu, James H. Strickler, Two-photon lithography for microelectronic application, 1992.
- [115] S. Jariwala, B. Tan, and K. Venkatakrisnan, Journal of Micromechanics and Microengineering **19**, 115023 (2009).
- [116] D. Wu, Q.-D. Chen, L.-G. Niu, J.-N. Wang, J. Wang, R. Wang, H. Xia, and H.-B. Sun, Lab on a Chip **9**, 2391 (2009).
- [117] P. Galajda and P. Ormos, Journal of Optics B: Quantum and Semiclassical Optics **4**, S78 (2002).
- [118] L. Amato, Y. Gu, N. Bellini, S. M. Eaton, G. Cerullo, and R. Osellame, Lab on a Chip **12**, 1135 (2012).
- [119] A. Spangenberg, N. Hobeika, F. Stehlin, J.-P. Malval, F. Wieder, P. Prabhakaran, P. Baldeck, and O. Soppera, *Updates in Advanced Lithography* (InTech, ADDRESS, 2013).
- [120] M. Deubel, G. Von Freymann, M. Wegener, S. Pereira, K. Busch, and C. M. Soukoulis, Nature materials **3**, 444 (2004).
- [121] Z.-B. Sun, X.-Z. Dong, W.-Q. Chen, S. Nakanishi, X.-M. Duan, and S. Kawata, Advanced materials **20**, 914 (2008).
- [122] W.-K. Wang, Z.-B. Sun, M.-L. Zheng, X.-Z. Dong, Z.-S. Zhao, and X.-M. Duan, The Journal of Physical Chemistry C **115**, 11275 (2011).
- [123] A. Ovsianikov, B. Chichkov, P. Mente, N. Monteiro-Riviere, A. Doraiswamy, and R. Narayan, International journal of applied ceramic technology **4**, 22 (2007).
- [124] F. Klein, B. Richter, T. Striebel, C. M. Franz, G. v. Freymann, M. Wegener, and M. Bastmeyer, Advanced materials **23**, 1341 (2011).
- [125] S. Maruo and J. T. Fourkas, Laser & Photonics Reviews **2**, 100 (2008).
- [126] W. Bogaerts, V. Wiaux, D. Taillaert, S. Beckx, B. Luyssaert, P. Bienstman, and R. Baets, IEEE Journal of selected topics in quantum electronics **8**, 928 (2002).
- [127] C. Vieu, F. Carcenac, A. Pepin, Y. Chen, M. Mejias, A. Lebib, L. Manin-Ferlazzo, L. Couraud, and H. Launois, Applied surface science **164**, 111 (2000).

- [128] F. Watt, A. Bettiol, J. Van Kan, E. Teo, and M. Breese, *International Journal of Nanoscience* **4**, 269 (2005).
- [129] S. Y. Chou, P. R. Krauss, and P. J. Renstrom, *Journal of Vacuum Science & Technology B: Microelectronics and Nanometer Structures Processing, Measurement, and Phenomena* **14**, 4129 (1996).
- [130] A. Bertsch, S. Jiguet, and P. Renaud, *Journal of micromechanics and microengineering* **14**, 197 (2003).
- [131] M. Walther, A. Ortner, H. Meier, U. Löffelmann, P. J. Smith, and J. G. Korvink, *Applied Physics Letters* **95**, 251107 (2009).
- [132] C. Pacholski, A. Kornowski, and H. Weller, *Angewandte Chemie International Edition* **41**, 1188 (2002).
- [133] X. Zhou, Y. Hou, and J. Lin, *AIP Advances* **5**, 030701 (2015).
- [134] K.-S. Lee, R. H. Kim, D.-Y. Yang, and S. H. Park, *Progress in Polymer Science* **33**, 631 (2008).
- [135] M. Emons, K. Obata, T. Binhammer, A. Ovsianikov, B. N. Chichkov, and U. Morgner, *Optical Materials Express* **2**, 942 (2012).
- [136] V. F. Paz, M. Emons, K. Obata, A. Ovsianikov, S. Peterhänsel, K. Frenner, C. Reinhardt, B. Chichkov, U. Morgner, and W. Osten, *Journal of Laser Applications* **24**, 042004 (2012).
- [137] W. Kaiser and C. Garrett, *Physical review letters* **7**, 229 (1961).
- [138] M. Göppert-Mayer, *Annalen der Physik* **401**, 273 (1931).
- [139] S. Maruo, O. Nakamura, and S. Kawata, *Optics letters* **22**, 132 (1997).
- [140] S. Kawata, H.-B. Sun, T. Tanaka, and K. Takada, *Nature* **412**, 697 (2001).
- [141] M. V. Rybin, I. I. Shishkin, K. B. Samusev, P. A. Belov, Y. S. Kivshar, R. V. Kiyani, B. N. Chichkov, and M. F. Limonov, *Crystals* **5**, 61 (2015).
- [142] R. J. Narayan, A. Doraiswamy, D. B. Chrisey, and B. N. Chichkov, *Materials Today* **13**, 42 (2010).
- [143] S. Maruo, *Multiphoton Lithography: Techniques, Materials, and Applications 1960* (2016).
- [144] A. Koroleva, A. Gill, I. Ortega, J. Haycock, S. Schlie, S. Gittard, B. Chichkov, and F. Claeysens, *Biofabrication* **4**, 025005 .
- [145] M. S. Rill, C. Plet, M. Thiel, I. Staude, G. Von Freymann, S. Linden, and M. Wegener, *Nature materials* **7**, 543 (2008).
- [146] J.-F. Xing, M.-L. Zheng, and X.-M. Duan, *Chemical Society Reviews* **44**, 5031 (2015).
- [147] M. Malinauskas, P. Danilevičius, and S. Juodkazis, *Optics express* **19**, 5602 (2011).
- [148] T.-T. Chung, C.-L. Tseng, C.-P. Hung, C.-L. Lin, and P. L. Baldeck, *Journal of Neuroscience and Neuroengineering* **2**, 48 (2013).

- [149] G. S. He, L.-S. Tan, Q. Zheng, and P. N. Prasad, Chemical reviews **108**, 1245 (2008).
- [150] F. Terenziani, C. Katan, E. Badaeva, S. Tretiak, and M. Blanchard-Desce, Advanced Materials **20**, 4641 (2008).
- [151] Y. Xia, J. A. Rogers, K. E. Paul, and G. M. Whitesides, Chemical reviews **99**, 1823 (1999).
- [152] D. Qin, Y. Xia, and G. M. Whitesides, Nature protocols **5**, 491 (2010).
- [153] *COMSOL Multiphysics 4.4, Finite element methods simulation software* (COMSOL AB, Stockholm, Sweden, 2014).
- [154] S. G. Rodrigo, L. Martín-Moreno, A. Y. Nikitin, A. Kats, I. Spevak, and F. Garcia-Vidal, Optics letters **34**, 4 (2009).
- [155] R. H. Fan, R. W. Peng, X. R. Huang, J. Li, Y. Liu, Q. Hu, M. Wang, and X. Zhang, Adv. Mater. **24**, 1980 (2012).
- [156] C. C. Chang, Y. D. Sharma, Y. S. Kim, J. A. Bur, R. V. Shenoi, S. Krishna, D. Huang, and S. Y. Lin, Nano Lett. **10**, 1704 (2010).
- [157] S. Krishna, J Phys D Appl Phys. **38**, 2142 (2005).
- [158] D. A. Miller, Quantum Dynamics of Simple Systems, ed. G.-L. Oppo, SM Barnett, E. Riis, and M. Wilkinson (Institute of Physics, London, 1996) 239 (1996).
- [159] W. Wu, A. Bonakdar, and H. Mohseni, Appl. Phys. Lett. **96**, 161107 (2010).
- [160] Y. D. Sharma, Y. C. Jun, J. O. Kim, I. Brener, and S. Krishna, Opt. Commun. **312**, 31 (2014).
- [161] S. Giudicatti, F. Marabelli, A. Valsesia, P. Pellacani, P. Colpo, and F. Rossi, J. Opt. Soc. Am. B: **29**, 1641 (2012).
- [162] H. L. Chen, S. Y. Chuang, W. H. Lee, S. S. Kuo, W. F. Su, S. L. Ku, and Y. F. Chou, Opt. Express **17**, 1636 (2009).
- [163] R. Liu, X. Zhao, C. Roberts, L. Yu, P. K. Mohseni, X. Li, V. Podolskiy, and D. Wasserman, Adv. Mater. **28**, 1441 (2016).
- [164] W. Fan, S. Zhang, B. Minhas, K. J. Malloy, and S. Brueck, Phys. Rev. Lett. **94**, 033902 (2005).
- [165] W. Fan, S. Zhang, K. Malloy, and S. Brueck, Opt. Express **13**, 4406 (2005).
- [166] A. Ward and J. Pendry, J. Mod. Opt. **44**, 1703 (1997).
- [167] C. Robin and K. Jonnalagadda, J. Micromech. Microeng. **26**, 025020 (2016).
- [168] K. Bhattarai, S. R. Silva, A. Urbas, S. J. Lee, Z. Ku, and J. Zhou, IEEE J. Sel. Top. Quantum Electron. **23**, 1 (2017).
- [169] B. Gao, M. M. Yuen, and T. T. Ye, Scientific reports **7**, 45108 (2017).
- [170] Y. Yoo, J. Hwang, and Y. Lee, Journal of Electromagnetic Waves and Applications **31**, 663 (2017).
- [171] D. Maystre, Theory of Woods anomalies, 2012.

- [172] R. Kumar and S. A. Ramakrishna, Journal of Physics D: Applied Physics **51**, 165104 (2018).
- [173] J. Cao, T. Sun, and K. T. Grattan, Sensors and Actuators B: Chemical **195**, 332 (2014).
- [174] B. Gallinet and O. J. Martin, Physical Review B **83**, 235427 (2011).
- [175] M. Galli, S. Portalupi, M. Belotti, L. Andreani, L. OFaolain, and T. Krauss, Applied Physics Letters **94**, 071101 (2009).
- [176] W. Zhou *et al.*, Progress in Quantum Electronics **38**, 1 (2014).
- [177] A. Johnson, C. M. Marcus, M. Hanson, and A. Gossard, Physical review letters **93**, 106803 (2004).
- [178] F. Hao, Y. Sonnefraud, P. V. Dorpe, S. A. Maier, N. J. Halas, and P. Nordlander, Nano letters **8**, 3983 (2008).
- [179] K.-L. Lee, H.-Y. Hsu, M.-L. You, C.-C. Chang, M.-Y. Pan, X. Shi, K. Ueno, H. Misawa, and P.-K. Wei, Scientific reports **7**, 44104 (2017).
- [180] L. Zhou and A. W. Poon, Optics letters **32**, 781 (2007).
- [181] K. Nozaki, A. Shinya, S. Matsuo, T. Sato, E. Kuramochi, and M. Notomi, Optics express **21**, 11877 (2013).
- [182] Y. Zhang, Y.-R. Zhen, O. Neumann, J. K. Day, P. Nordlander, and N. J. Halas, Nature communications **5**, 4424 (2014).
- [183] M. Kroner *et al.*, Nature **451**, 311 (2008).
- [184] C. Wu, A. B. Khanikaev, and G. Shvets, Physical review letters **106**, 107403 (2011).
- [185] A. B. Khanikaev, C. Wu, and G. Shvets, Nanophotonics **2**, 247 (2013).
- [186] J. Gu *et al.*, Nature communications **3**, 1151 (2012).
- [187] R. Singh, C. Rockstuhl, F. Lederer, and W. Zhang, Physical Review B **79**, 085111 (2009).
- [188] M. Pu, C. Hu, C. Huang, C. Wang, Z. Zhao, Y. Wang, and X. Luo, Optics Express **21**, 992 (2013).
- [189] A. Artar, A. A. Yanik, and H. Altug, Applied Physics Letters **95**, 051105 (2009).
- [190] B. Lee and Z. Zhang, Journal of Applied Physics **100**, 063529 (2006).
- [191] A. Hessel and A. Oliner, Applied optics **4**, 1275 (1965).
- [192] Y. Cui, Y. He, Y. Jin, F. Ding, L. Yang, Y. Ye, S. Zhong, Y. Lin, and S. He, Laser & Photonics Reviews **8**, 495 (2014).
- [193] S. Fan, W. Suh, and J. D. Joannopoulos, JOSA A **20**, 569 (2003).
- [194] W. Suh, Z. Wang, and S. Fan, IEEE Journal of Quantum Electronics **40**, 1511 (2004).

- [195] P. Fan, U. K. Chettiar, L. Cao, F. Afshinmanesh, N. Engheta, and M. L. Brongersma, *Nature Photonics* **6**, 380 (2012).
- [196] M. Farsari and B. N. Chichkov, *Nature photonics* **3**, 450 (2009).
- [197] K. Kumari, H. Ghadi, D. Samudraiah, and S. Chakrabarti, *Current Science* (00113891) **112**, (2017).
- [198] J. W. Judy, *Smart materials and Structures* **10**, 1115 (2001).
- [199] A. Susarrey-Arce, Á. G. Marín, S. Schlautmann, L. Lefferts, J. G. Gardeniers, and A. van Houselt, *Journal of micromechanics and microengineering* **23**, 025004 (2012).
- [200] K. Busch, G. Von Freymann, S. Linden, S. Mingaleev, L. Tkeshelashvili, and M. Wegener, *Physics reports* **444**, 101 (2007).
- [201] M. Suter, L. Zhang, E. C. Siringil, C. Peters, T. Luehmann, O. Ergeneman, K. E. Peyer, B. J. Nelson, and C. Hierold, *Biomedical microdevices* **15**, 997 (2013).
- [202] A. K. Nguyen and R. J. Narayan, *Materials Today* (2017).
- [203] R. Yang, S. A. Soper, and W. Wang, *Sensors and Actuators A: Physical* **135**, 625 (2007).
- [204] L. Li and J. T. Fourkas, *Materials Today* **10**, 30 (2007).
- [205] A. Goswami, A. Phani, A. Umarji, and G. Madras, *Review of Scientific Instruments* **83**, 095003 (2012).
- [206] C. Reinhardt, R. Kiyan, S. Passinger, A. Stepanov, A. Ostendorf, and B. Chichkov, *Applied Physics A* **89**, 321 (2007).
- [207] C. Schizas, V. Melissinaki, A. Gaidukeviciute, C. Reinhardt, C. Ohrt, V. Dedousis, B. N. Chichkov, C. Fotakis, M. Farsari, and D. Karalekas, *The International Journal of Advanced Manufacturing Technology* **48**, 435 (2010).
- [208] A. Doraiswamy, C. Jin, R. Narayan, P. Mageswaran, P. Mente, R. Modi, R. Auyeung, D. Chrisey, A. Ovsianikov, and B. Chichkov, *Acta Biomaterialia* **2**, 267 (2006).
- [209] M. Deubel, M. Wegener, A. Kaso, and S. John, *Applied physics letters* **85**, 1895 (2004).
- [210] M. Deubel, M. Wegener, S. Linden, G. Von Freymann, and S. John, *Optics letters* **31**, 805 (2006).
- [211] J. Fischer, J. B. Mueller, J. Kaschke, T. J. Wolf, A.-N. Unterreiner, and M. Wegener, *Optics express* **21**, 26244 (2013).
- [212] F. Claeysens *et al.*, *Langmuir* **25**, 3219 (2009).
- [213] V. Melissinaki, A. Gill, I. Ortega, M. Vamvakaki, A. Ranella, J. Haycock, C. Fotakis, M. Farsari, and F. Claeysens, *Biofabrication* **3**, 045005 (2011).
- [214] N. Vasilantonakis, K. Terzaki, I. Sakellari, V. Purlys, D. Gray, C. M. Soukoulis, M. Vamvakaki, M. Kafesaki, and M. Farsari, *Advanced Materials* **24**, 1101 (2012).
- [215] M. Farsari, G. Filippidis, and C. Fotakis, *Optics letters* **30**, 3180 (2005).

- [216] C.-Y. Liao, M. Bouriauand, P. L. Baldeck, J.-C. Léon, C. Masclet, and T.-T. Chung, *Applied Physics Letters* **91**, 033108 (2007).
- [217] I. Wang, M. Bouriau, P. L. Baldeck, C. Martineau, and C. Andraud, *Optics letters* **27**, 1348 (2002).
- [218] Y. Yan, M. I. Rashad, E. J. Teo, H. Tanoto, J. Teng, and A. A. Bettiol, *Optical Materials Express* **1**, 1548 (2011).
- [219] K. Terzaki, N. Vasilantonakis, A. Gaidukeviciute, C. Reinhardt, C. Fotakis, M. Vamvakaki, and M. Farsari, *Optical Materials Express* **1**, 586 (2011).
- [220] L. Vurth, P. Baldeck, O. Stéphan, and G. Vitrant, *Applied Physics Letters* **92**, 171103 (2008).
- [221] T. Tanaka, A. Ishikawa, and T. Amemiya, Three-dimensional two-photon laser fabrication for metals, polymers, and magneto-optical materials, 2015.
- [222] I. Sakellari, X. Yin, M. L. Nesterov, K. Terzaki, A. Xomalis, and M. Farsari, *Advanced Optical Materials* **5**, (2017).
- [223] M. Thiel, J. Fischer, G. Von Freymann, and M. Wegener, *Applied Physics Letters* **97**, 221102 (2010).
- [224] H.-B. Sun and S. Kawata, Two-photon photopolymerization and 3D lithographic microfabrication, 2004.
- [225] A. del Campo and C. Greiner, *Journal of Micromechanics and Microengineering* **17**, R81 (2007).
- [226] H.-Z. Cao, M.-L. Zheng, X.-Z. Dong, F. Jin, Z.-S. Zhao, and X.-M. Duan, *Applied Physics Express* **6**, 066501 (2013).
- [227] J.-P. Fouassier, *Photoinitiation, photopolymerization, and photocuring: fundamentals and applications* (Hanser, Munich Vienna, New York, 1995).
- [228] G. Odian, *Principles of Polymer Science*, 1991.
- [229] A. Reiser, *Photoreactive Polymers: The Science and Technology of Resists*, Feb. 1989, 409 pages.
- [230] J. F. Rabek and J.-P. Fouassier, *Lasers in polymer science and technology: applications* (Crc press, Boca Raton, USA, 1989), Vol. 1.
- [231] M. Malinauskas, V. Purlys, M. Rutkauskas, and R. Gadonas, Two-photon polymerization for fabrication of three-dimensional micro-and nanostructures over a large area, 2009.
- [232] H.-B. Sun, T. Tanaka, and S. Kawata, *Applied Physics Letters* **80**, 3673 (2002).
- [233] R. Kumar and S. A. Ramakrishna, *Current Science* **112**, 1668 (2017).
- [234] Y. Liu, D. D. Nolte, and L. J. Pyrak-Nolte, *Applied Physics A* **100**, 181 (2010).
- [235] G. Dayal and S. A. Ramakrishna, *Optics Express* **22**, 15104 (2014).
- [236] G. V. Naik, V. M. Shalaev, and A. Boltasseva, *Advanced Materials* **25**, 3264 (2013).